6 June 2008 | $10

Science

Unmasking the Indus

AAAS

Volume 320, Issue 5881

COVER

A bearded, horned terra cotta mask, about 5 centimeters in height, found at Mohenjo Daro, Pakistan. The artifact, which may have been attached to a puppet, offers a rare glimpse into the 5000-year-old Indus civilization. See page 1276.

Image: J. M. Kenoyer/Courtesy of the Department of Archaeology and Museums, Government of Pakistan

DEPARTMENTS

EDITORIAL

NEWS OF THE WEEK

NEWS FOCUS

Unmasking the Indus

LETTERS

BOOKS *ET AL.*

POLICY FORUM

1302

PERSPECTIVES

CONTENTS continued >>

Science

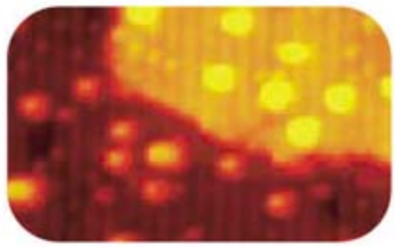

SCIENCE EXPRESS

www.sciencexpress.org

PSYCHOLOGY

BREVIA: Serotonin Modulates Behavioral Reactions to Unfairness
M. J. Crockett, L. Clark, G. Tabibnia, M. D. Lieberman, T. W. Robbins
Individuals with low levels of brain serotonin are less likely to accept an unfair offer of money from other players in a laboratory game.
10.1126/science.1155577

ECOLOGY

Animal Versus Wind Dispersal and the Robustness of Tree Species to Deforestation
D. Montoya, M. A. Zavala, M. A. Rodríguez, D. W. Purves
In Spanish forests, tree species with seeds that are dispersed by animals are more resilient in a fragmented forest than those with wind-dispersed seeds.
10.1126/science.1158404

CHEMISTRY

The Role of Interstitial Sites in the Ti3*d* Defect State in the Band Gap of Titania
S. Wendt et al.
Scanning tunneling microscope data and calculations show that near-surface titanium sites, not bridging oxygen vacancies, determine the useful electronic properties of TiO_2.
10.1126/science.1159846

EVOLUTION

Natural Selection Shapes Genome-Wide Patterns of Copy-Number Polymorphism in *Drosophila melanogaster*
J. J. Emerson, M. Cardoso-Moreira, J. O. Borevitz, M. Long
A high-resolution analysis of gene copy number in *Drosophila* species shows that most variations are deleterious but a few for resistance to toxins are being positively selected.
10.1126/science.1158078

TECHNICAL COMMENT ABSTRACTS

GEOPHYSICS

Comment on "Intermittent Plate Tectonics?" 1291
J. Korenaga
full text at www.sciencemag.org/cgi/content/full/320/5881/1291a

Response to Comment on "Intermittent Plate Tectonics?"
P. G. Silver and M. D. Behn
full text at www.sciencemag.org/cgi/content/full/320/5881/1291b

REVIEW

GEOLOGY

Rise of the Andes 1304
C. N. Garzione et al.
>> News story p. 1275

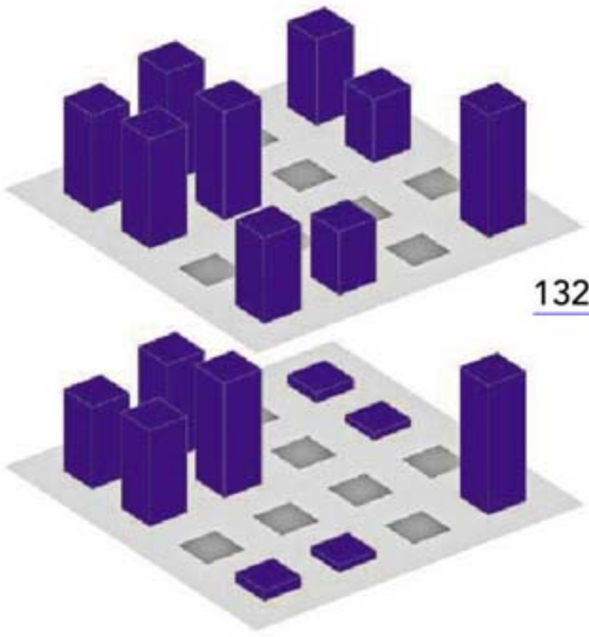

1326

BREVIA

PHYSICS

Fine Structure Constant Defines Visual Transparency of Graphene 1308
R. R. Nair et al.
The transparency of sheets of graphene is quantized in a way that allows a simple determination of the fine structure constant, which relates light and relativistic electrons.

RESEARCH ARTICLES

ASTRONOMY

An Eccentric Binary Millisecond Pulsar in the Galactic Plane 1309
D. J. Champion et al.
A rapidly rotating pulsar has a highly eccentric orbit about its companion star, not the usual circular orbit, challenging ideas on how such binary systems form. *>> Perspective p. 1298*

MICROBIOLOGY

Predictive Behavior Within Microbial Genetic Networks 1313
I. Tagkopoulos et al.
Predictable sequences of environmental signals can be exploited by bacteria so that they learn to anticipate future metabolic needs and thereby gain a competitive edge. *>> Perspective p. 1297*

REPORTS

ASTRONOMY

A Transient Radio Jet in an Erupting Dwarf Nova 1318
E. Körding et al.
Detection of a radio jet in a dwarf supernova shows that production of synchrotron radiation during accretion of a disk is a ubiquitous source of astrophysical jets.

CONTENTS continued >>

REPORTS *CONTINUED...*

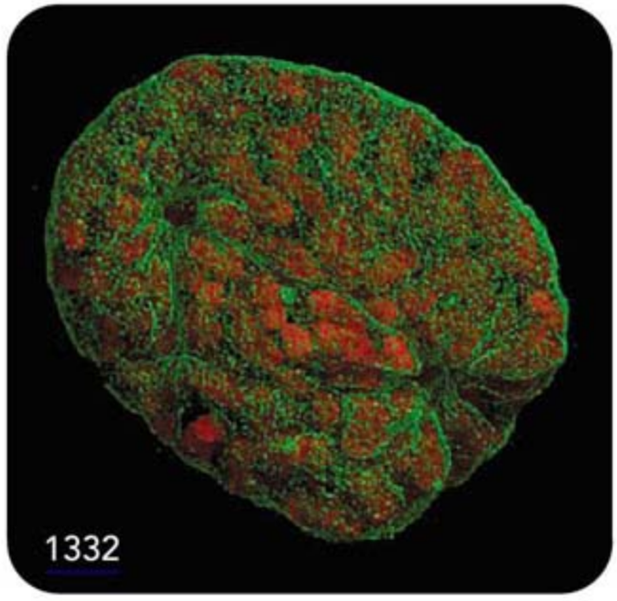

AAAS
ADVANCING SCIENCE, SERVING SOCIETY

SCIENCE (ISSN 0036-8075) is published weekly on Friday, except the last week in December, by the American Association for the Advancement of Science, 1200 New York Avenue, NW, Washington, DC 20005. Periodicals Mail postage (publication No. 484460) paid at Washington, DC, and additional mailing offices. Domestic individual membership and subscription (51 issues): $144 ($74 allocated to subscription). Domestic institutional subscription (51 issues): $770; Foreign postage extra: Mexico, Caribbean (surface mail) $55; other countries (air assist delivery) $85. First class, airmail, student, and emeritus rates on request. Canadian rates with GST available upon request, GST #1254 88122. Publications Mail Agreement Number 1069624. **Printed in the U.S.A.**

Change of address: Allow 4 weeks, giving old and new addresses and 8-digit account number. **Postmaster:** Send change of address to AAAS, P.O. Box 96178, Washington, DC 20090–6178. **Single-copy sales:** $10.00 current issue, $15.00 back issue prepaid includes surface postage; bulk rates on request. The identification code for *Science* is 0036-8075. *Science* is indexed in the *Reader's Guide to Periodical Literature* and in several specialized indexes.

CONTENTS continued >>

No place like home.

SCIENCE**NOW**

www.sciencenow.org

HIGHLIGHTS FROM OUR DAILY NEWS COVERAGE

Smallest Extrasolar Planet Portends Other Earths
Newly discovered world only three times as large as ours, orbits tiny sun.

Rodent Bones of Contention
Rat fossils may settle dispute over when humans reached New Zealand.

Mutation Spells Bad News for Breast Cancer Patients
Defect in *NQO1* gene dramatically reduces survival rates, responsiveness to treatment.

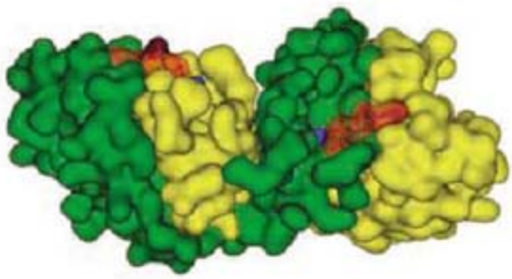

Dimeric GTPase domains of the kinase LRRK2.

SCIENCE **SIGNALING**

www.sciencesignaling.org

THE SIGNAL TRANSDUCTION KNOWLEDGE ENVIRONMENT

PERSPECTIVE: ROCO Kinase Activity Is Controlled by Internal GTPase Function
B. Weiss
The guanosine triphosphatase (GTPase) domain of leucine-rich repeat kinase 2 (LRRK2) mediates LRRK2 homodimerization and controls its protein kinase activity.

PERSPECTIVE: Dual Functions of the KNOTTED1 Homeodomain—Sequence-Specific DNA Binding and Regulation of Cell-to-Cell Transport
N. Bolduc, S. Hake, D. Jackson
A single domain confers different subcellular localizations of the homeodomain protein KN1.

TEACHING RESOURCE: Physiological and Pathological Actions of Calpains in Glutamatergic Neurons
J. Liu, M. C. Liu, K. K. W. Wang
A pair of animations illustrates how neuronal calpains contribute to synaptic plasticity or neuronal toxicity.

Iraq and Afghanistan veterans return to campus.

SCIENCE **CAREERS**

www.sciencecareers.org/career_development

FREE CAREER RESOURCES FOR SCIENTISTS

Student-Veterans Come Marching Home: Their Return to Studies
A. Kotok
A group of Iraq and Afghanistan veterans tells about their new lives as science and engineering students.

Student-Veterans Come Marching Home: A New G.I. Bill for Scientists
A. Kotok
Can the proposed G.I. Bill do for Iraq and Afghanistan veterans what the original G.I. Bill did for World War II veterans?

Taken for Granted: Over Here
B. L. Benderly
Science and technology fields offer professional opportunities for veterans who choose wisely.

June 2008 Funding News
GrantsNet Staff
Learn about the latest in research funding, scholarships, fellowships, and internships.

SCIENCE**PODCAST**

www.sciencemag.org/about/podcast.dtl

FREE WEEKLY SHOW

Download the 6 June *Science* Podcast to hear about climate-driven impacts on marine life, impulsivity and cocaine addiction, new insights into the Indus civilization, and more.

CREDITS: (SCIENCE NOW) NASA; (SCIENCE CAREERS) CODY WATERS; (SCIENCE SIGNALING) BERTRAM WEISS, BAYER SCHERING PHARMA AG13342, BERLIN, GERMANY

Separate individual or institutional subscriptions to these products may be required for full-text access.

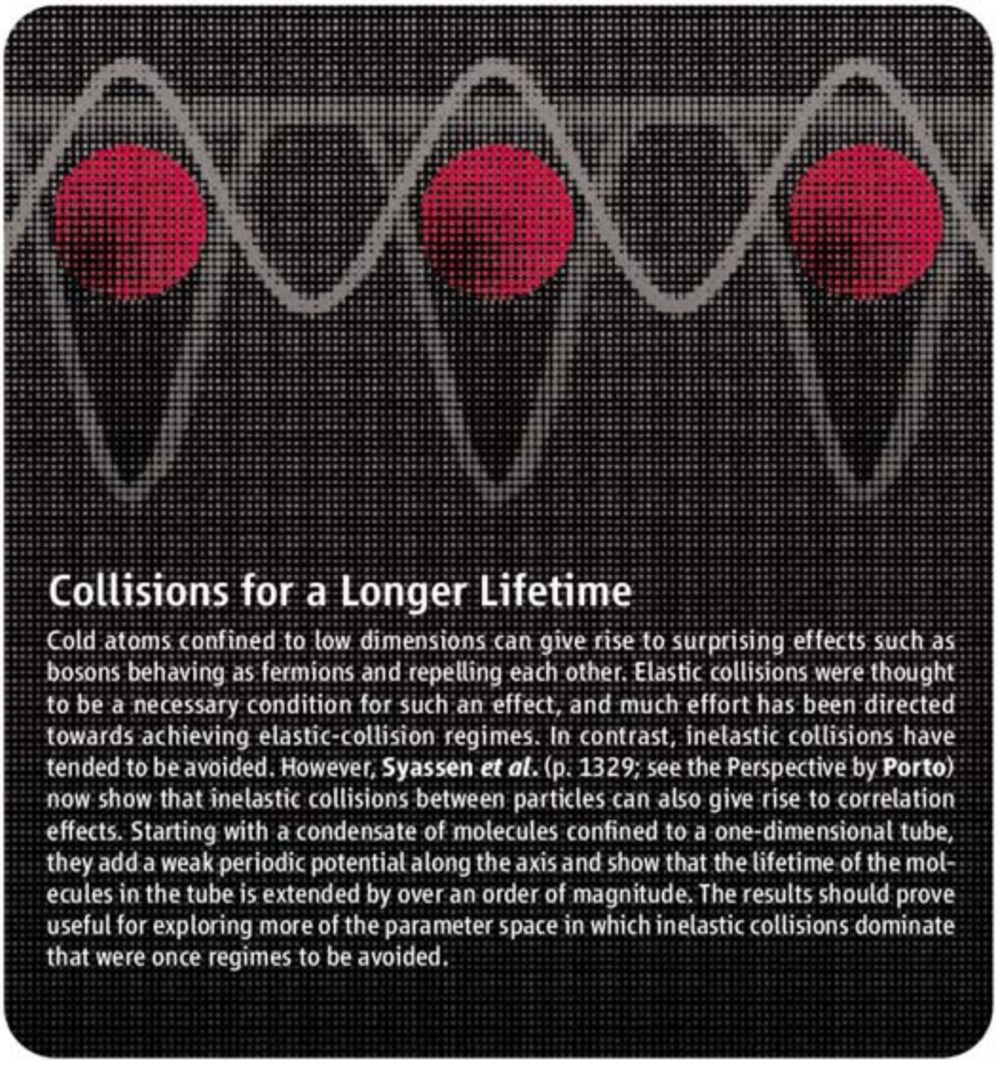

Collisions for a Longer Lifetime

Cold atoms confined to low dimensions can give rise to surprising effects such as bosons behaving as fermions and repelling each other. Elastic collisions were thought to be a necessary condition for such an effect, and much effort has been directed towards achieving elastic-collision regimes. In contrast, inelastic collisions have tended to be avoided. However, **Syassen *et al.*** (p. 1329; see the Perspective by **Porto**) now show that inelastic collisions between particles can also give rise to correlation effects. Starting with a condensate of molecules confined to a one-dimensional tube, they add a weak periodic potential along the axis and show that the lifetime of the molecules in the tube is extended by over an order of magnitude. The results should prove useful for exploring more of the parameter space in which inelastic collisions dominate that were once regimes to be avoided.

Mountain High

The Andes represent one of the longest, highest mountain ranges on Earth. Their topography affects the climate of much of South America, and their uplift history thus impacts the ecological development of the continent. **Garzione *et al.*** (p. 1304) review recent evidence for their history of uplift. Before about 10 million years ago, the Andes were of moderate elevation. Between 10 and 6 million years ago, the elevation of the Andes increased abruptly, perhaps because dense material at the base of the crust detached and subsided into the mantle.

Earthquake Running at the Speed of Sound

Some particularly destructive earthquakes, which produce sound waves, seem to rupture at faster than the local speed of sound through the crust. **Bouchon and Karabulut** (p. 1323) now show that the aftershocks of these tremors are also different. Instead of clustering on the fault plane, as is common, they cluster on secondary structures. The lack of aftershocks on the fault plane shows that friction along the fault plane itself is relatively uniform.

Foresight Among *E. coli*

Many natural signals progress in a readily predictable sequence. For instance, after being eaten, a bacterium will perceive a sudden temperature rise followed by a drop in oxygen levels. **Tagkopoulos *et al.*** (p. 1313, published online 8 May; see the Perspective by **Baliga**) investigated *E. coli*'s predictive powers in a combination of in silico and chemostat experiments. On exposure to a large temperature change, *E. coli* can shift from aerobiosis to anaerobiosis even in the presence of 18% oxygen. This might seem maladaptive, but it means that the organism will have a competitive edge as soon as it encounters the zoo of microorganisms in the oxygen-starved lower gut. Furthermore, the authors were able to "train" the organisms to adapt metabolically to "unnatural" sequences of events, e.g., elevated temperature followed by high oxygen.

Exploring Alternatives in Catalysis

Many industrial catalytic systems are based on precious metals, and the search is on for substitute catalysts based on less expensive and more abundant metals and alloys. **Studt *et al.*** (p. 1320) have examined one reaction, the selective hydrogenation of acetylene, and show how insights from density functional theory (DFT) could be used to identify a candidate alloy. Acetylene, a trace contaminant of the commodity chemical ethylene, is hydrogenated to ethylene by palladium catalysts that do not convert the ethylene to ethane. By examining trends in the heats of adsorption of hydrocarbons on metals and alloys, the authors identified zinc-nickel alloys as possible alternatives and demonstrate their selective hydrogenation activity in experimental studies of these alloys dispersed on oxide supports.

Eccentric Pulsar Performance

Binary pulsars are rapidly spinning neutron stars that emit a beam of radio waves that co-rotate with a companion star. Two main types have been seen, one spinning more slowly with an eccentric orbit around the companion star, the other spinning rapidly with a circular orbit. **Champion *et al.*** (p. 1309, published online 15 May; see the Perspective by **van den Heuvel**) have now discovered a rapidly spinning pulsar with a highly eccentric orbit that does not fit into these classes and thus challenges models for formation of pulsars. Possible alternative models for the formation of this pulsar include a triple stellar system.

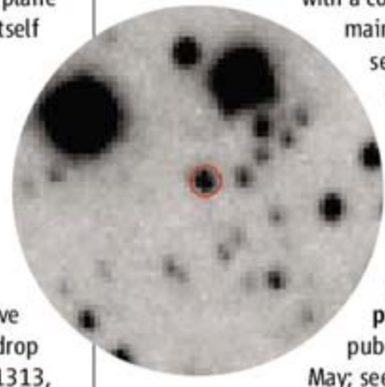

Continued on page 1259

CREDITS (TOP TO BOTTOM): SYASSEN *ET AL.*; CHAMPION *ET AL.*

Continued from page 1257

Observing Cataclysmic Variables

A variety of astrophysical objects such as binary stars involve one star accreting matter from another. In many cases, the collected matter heats up and is ejected in the form of a powerful jet. But some accreting objects, in particular so-called cataclysmic variables, seem to show no jet activity. **Körding *et al.*** (p. 1318) have gathered radio observations on the prototypical dwarf nova, SS Cyg, that show all the earmarks of an astrophysical jet. The American Association of Variable Star Observers sent out an alert that triggered data collection from the Very Large Array radio telescope. The results suggest that jet activity and the underlying mechanisms are similar in all accreting objects.

Entangling Diamond

Entanglement is a key ingredient in quantum information processing and quantum computation. While entanglement has been demonstrated for photons, cold atoms systems, and quantum dots at cryogenic temperatures, there are efforts to look to other systems that can extend entanglement to room temperature in solid state systems. By demonstrating the ability to generate and detect 2-qubit and 3-qubit entangled states with the optically active nitrogen vacancies in diamond, **Neumann *et al.*** (p. 1326) show that diamond can meet these requirements.

Poring over the Nuclear Pore

Light microscopy is a powerful tool in cell biology, and the view is improving with "super-resolution" techniques that have broken the 200- to 300-nm resolution barrier. Now **Schermelleh *et al.*** (p. 1332) describe the application of three-dimensional structured illumination microscopy (3D-SIM), an imaging technique that can produce multicolor images of whole cells with enhanced resolution in both the lateral and axial directions. They used the technique to simultaneously map nuclear pores, nuclear lamins, and chromatin at a resolution of about 100 nm and observed several features not detected by conventional microscopy.

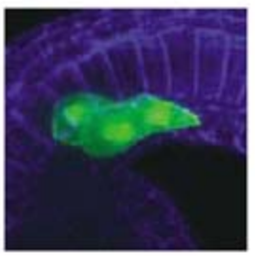

Flexible Organ Building Blocks

Building an animal with distinct organs requires the coordination of cell identity and cell behavior during embryogenesis. **Christiaen *et al.*** (p. 1349) have tracked expression of genes controlling migration of the heart precursor cells in the sea squirt, *Ciona intestinalis*. In order to move forward, migrating cells must be polarized, extend protrusions, adhere to the substrate, and then detach. Heart regulatory factors control these events by regulating only subsets of genes to specify the combination of cellular activities required for migration. These properties of the regulation and behavior interface may account for the morphogenetic diversity observed in development and evolution.

CREDIT: CHRISTIAEN *ET AL.*

Dissecting X Inactivation

The silencing of one of the two X chromosomes in mammalian females is regulated by the noncoding RNAs Xist and Tsix. These RNAs overlap for at least part of their length, leading to the speculation that RNA interference (RNAi), a pervasive gene silencing mechanism that targets double-stranded RNA, might be involved in X inactivation. **Ogawa *et al.*** (p. 1336) show in mouse cells that Xist and Tsix do indeed form an RNA duplex that can be targeted by Dicer, the RNA endonuclease at the heart of the RNA interference machinery, and give rise to small RNA species. Knocking down Dicer prevents Xist from coating the inactive X chromosome, which would generate heterochromatic marks. Thus X inactivation and RNA interference are mechanistically linked.

From Impulsive to Compulsive

Individual differences in impulsivity and sensation-seeking are related to vulnerability to drug use and abuse. Compulsive cocaine use has been thought to result from a failure in top-down executive control over maladaptive habit learning. However, whether the enhanced impulsivity observed in drug addicts predates the onset of compulsive drug use or is a consequence of protracted exposure to drugs is not clear. **Belin *et al.*** (p. 1352) now show in rats that an impulsive behavioral trait that is associated with reduced dopamine receptors in the nucleus accumbens predicts the switch to compulsive cocaine use and addiction.

Calestous Juma is a professor of the Practice of International Development at the Kennedy School of Government, Harvard University, Cambridge, MA. E-mail: calestous_juma@harvard.edu.

Elisabeth Moyer is an assistant professor in the Department of Geophysical Sciences at the University of Chicago and a former lecturer at the African Institute for Mathematical Sciences. E-mail: moyer@uchicago.edu.

Broadband Internet for Africa

IMAGINE A MAJOR RESEARCH UNIVERSITY WITH TENS OF THOUSANDS OF STUDENTS TRYING to access the Internet through a single U.S. household connection. That is the present situation in most African universities. Students there theoretically have access to *Science* through several journal archives for the developing world. In practice, most could never download it.

Sub-Saharan Africa is the most digitally isolated region in the world, with a bandwidth per capita that is only 1% of the world average and 0.2% of that in the United States. Not surprisingly, sub-Saharan Africa also has among the highest connectivity costs in the world. Its universities pay some 50 times more for bandwidth than do similar institutions in the United States, and connectivity cost per gross domestic product is almost 2000 times higher than in the United States. The resulting isolation of Africa's students from the remainder of the world is a serious impediment to both education and economic development.

The challenges the continent faces—meeting human needs, participating in the global economy, managing the environment, and improving governance, all outlined in the 2007 report *Freedom to Innovate*, commissioned by African presidents—require engineers, doctors, scientists, and businesspeople, all products of Africa's universities. For years, strategies to address these challenges centered on providing direct assistance for combating disease and poverty and for providing food and water. But living conditions in Africa cannot be improved without sustained long-term economic growth. That goal in turn requires connecting Africa to the rest of the world. The 3 million college students in sub-Saharan Africa need the same resources and access to knowledge as students anywhere. Next month, when the G8 summit opens in Japan, this aspect of African development should be a priority.

Africa's isolation is the result of both lack of infrastructure and lack of competition in telecommunications. West Africa is connected to the rest of the world through a single fiber-optic cable (SAT-3/WASC), which runs along the coast. The country of Senegal, home of one of Africa's foremost universities, has a total available fiber bandwidth of 1.2 gigabits per second, one-tenth that of Harvard University or the University of Chicago, and that capacity is further shared with four neighboring countries. East Africa is completely unconnected other than by expensive satellite links. Costs are further driven up by national telecommunications companies with monopoly (or at best duopoly) licenses on the sale of bandwidth, who are often content with "high-cost, low-volume" business strategies.

In recent years, African governments are realizing that connectivity is important for economic development, Internet use by African consumers is growing explosively, and industry is recognizing potential markets. The result is a boom in the construction of national fiber networks and proposals for new international submarine cables for East and South Africa. Nascent movements against anticompetitive practices have also helped bring down prices. But inefficient regulatory environments, lack of coherent regional infrastructure policies, and political interference have slowed progress. Efforts to bring affordable connectivity to Africa in general, and to its universities in particular, should be supported by the international policy community.

First, low-cost university access should be secured by making subsidized rates for universities a condition of any license granted to new cable operators. Although West Africa may be limited by the bottleneck of SAT-3/WASC, a new glut of capacity in East Africa, if it truly materializes, would allow allotting bandwidth to support university education. The Association of African Universities called for this initiative in 2007.

Second, helping to underwrite the costs of infrastructure should be a central goal of international development cooperation. International support should also come with requirements for open access; that is, bandwidth must be sold at a fair price to all buyers rather than only to consortium members with national monopolies. Next month's G8 summit should commit itself to making this a reality.*

– Calestous Juma and Elisabeth Moyer

10.1126/science.1161105

*This editorial is based on remarks by C. Juma at the G8 Dialogue organized by the United Nations University in Tokyo, Japan, on 23 May 2008.

CREDITS: (TOP LEFT) MARTHA STEWART; (BOTTOM LEFT) UNIVERSITY OF CHICAGO; (RIGHT) K. KRAUSE/SCIENCE (IMAGES: JUPITER)

EDITED BY GILBERT CHIN AND JAKE YESTON

PSYCHOLOGY

Social Preferences

The quotidian activity of playing cards (or kibitzing) can just as well be regarded as a self-sustaining institution within which individuals behave according to a shared set of incentives. As such, their behaviors become susceptible to game theoretic analysis, where strategies are formulated on the basis of estimated payouts, even those as intangible as a reputation for selfishness.

Yamagishi *et al.* have adopted this framework in analyzing the motivations for choices made by Japanese and Americans in a simple task. When offered a single colored pen from a group of five pens as a token payment for filling out a survey, Hokkaido students were less likely than Wolverines (Michigan students) to take a particular pen if it were the only one of that color available—that is, they would avoid reducing the scope of choice for subsequent people and thus, by incurring the cost of passing up the uniquely colored pen, not run the risk of making a negative impression on others. In contrast, a cultural psychological assessment would explain this outcome as revealing the preference (higher valuation) that East Asians place on conformity as opposed to the affinity of Westerners for individualism. When the choice task was expanded to include situations where the student was told explicitly that he was the first or the last of the five students to receive pens, the East-West difference disappeared; both Japanese and Americans were less likely to take the uniquely colored if they were the first and more likely (equally so) if they were the last to choose. — GJC

Psychol. Sci. **19**, 578 (2008).

APPLIED PHYSICS

Filling the THz Gap

At frequencies below a few hundred GHz, electrons are the information carriers of choice. For frequencies above a few THz, including infrared, the visible, and ultraviolet wavelengths, optical technologies prevail. The frequency range in between is referred to as the THz gap. Natural materials do not show much response in this gap range, even though there are many expected applications in the areas of biosensing, imaging, communication, and security. To help fill this gap, Tao *et al.* present a metamaterial—an artificial structure in which the electromagnetic response can be engineered by design—which has a strong response in the THz regime. By engineering a bilayer structure comprising a composite of metallic split-ring resonators, wires, and a polyimide spacer, they show that the electric permittivity and magnetic susceptibility response can be tuned separately. Such designed materials illustrate the potential of accessing a frequency range normally inaccessible to natural materials. — ISO

Opt. Express **16**, 7181 (2008).

CHEMISTRY

Choice of Phenyls

The formation of carbon-carbon bonds in the synthesis of organic compounds has become relatively straightforward when the sites being coupled are respectively substituted with an electronegative halide and an electropositive boron or tin moiety. The drawback of this approach is the necessity of appending these reactive groups to a precursor skeleton that consists predominantly of C-H bonds. The past decade has seen substantial progress in direct catalytic activation of C-H bonds, in certain cases eliminating the need for either the halide, the boronate, or both. One remaining hurdle is the achievement of enantioselectivity across a wide range of substrates. Shi *et al.* present progress in this vein with a chiral palladium catalyst that selectively couples a boron-substituted alkyl group to one of two phenyl rings bound to a central carbon, thereby desymmetrizing the compound. The carbon center also bears a pyridine group to direct the catalyst orientation by coordination to the Pd center. Successive trial experiments revealed that the amino acid leucine N-substituted with a menthyl ester proved the most effective ligand, resulting in high yields and enantiomeric excesses as high as 95%. Preliminary studies with a different ligand—an amino acid substituted with a bulky cyclopropyl group— also induced asymmetric coupling to one of the methyl groups in isopropyl pyridine, supporting the potential of this approach for sp^3 as well as sp^2 C-H site activation. — JSY

Angew. Chem. Int. Ed. **47**, 10.1002/anie.200801030 (2008).

PHYSIOLOGY

A Backup Source of Energy

The quality of mammalian semen is often judged by sperm motility, and the impaired movement of sperm toward egg is a common cause of infertility. Prior studies have claimed that the energy (ATP) for spermatozoan flagellar movement originates

CREDITS (TOP TO BOTTOM): THE METROPOLITAN MUSEUM OF ART/ART RESOURCE, NY; TAO *ET AL.*, *OPT. EXPRESS* 16, 7181 (2008)

from glycolysis or from mitochondrial oxidative phosphorylation; however, the primary pathway for producing ATP may in fact differ across species. Hung *et al.* use the glycolysis inhibitor alpha-chlorohydrin (ACH) or oxidative phosphorylation inhibitor pentachlorophenol (PCP) to determine the source of energy in rhesus monkey sperm. ACH interfered with whiplash motility and sperm velocity, and additional assays showed that glycolysis is the major energy source for sperm motility, hyperactivation, and protein tyrosine phosphorylation. Although flagellar mitochondrial ATP did not appear to be sufficient to sustain sperm motility and hyperactivation, ATP from glycolysis or oxidative phosphorylation did support sperm capacitation and binding to the zona pellucida. — BAP

Biol. Reprod. **78**, 10.1095/biolreprod.107.066357 (2008).

GEOCHEMISTRY

Team Effort

Reactions between water and mineral surfaces control nearly all of Earth's surface environment—they affect weathering and thus the chemistry of the oceans and atmosphere and soil development, and are critical for understanding remediation and waste disposal. Villa *et al.* provide an experiment that reveals the potential complexity of these reactions, suggesting that simple models of reactions with mineral surfaces may need to be reconsidered. They used ^{17}O nuclear magnetic resonance spectroscopy to follow the isotope exchange and dissociation reactions of a niobate cluster with seven distinct oxygen positions in aqueous solution. Analysis showed that all seven sites participate in the isotope exchange reactions in ways not easily predictable from the structure. Depending on pH, dissociation of part of the complex in some cases occurred faster than the isotope exchange reactions at most of the sites. These results suggest that the extended structure of minerals and their surface complexity need to be considered in modeling and evaluating their reactions with water. — BH

Angew. Chem. Int. Ed. **47**, 10.1002/anie.200801125 (2008).

BIOTECHNOLOGY

A Particulate Sandwich

Using a highly sensitive procedure for the detection of proteins, Kim *et al.* report an enhanced diagnostic test for the presence of HIV in human plasma. In their approach, the HIV p24 Gag protein was trapped between magnetic microparticles, which had been functionalized with sheep antibodies to p24, and gold nanoparticles, which had been decorated with a mix of mouse antibodies directed against p24 or a DNA bar code. The microparticles were then removed from solution magnetically, and the associated DNA was quantified. The sensitivity of this method was an order of magnitude greater than that of standard enzyme-linked immunoassays; the particle-based analysis was performed in solution, which allowed for homogeneous mixing and improved binding kinetics. Furthermore, careful design of the peptides used to raise the mouse and sheep antibodies enabled detection of the six most prevalent HIV subtypes. — BJ

Nanomedicine **3**, 293 (2008).

Science Signaling

AAAS

<< Degrading Polyamines for Migration

Integrins are heterodimeric transmembrane proteins that mediate cell adhesion and migration. The α9 subunit binds the spermidine/spermine-N^1-acetyltransferase SSAT, which induces the breakdown of the higher-order polyamines spermidine and spermine to the lower-order polyamine putrescine, and this interaction is required for migration mediated by the α9β1 integrin. DeHart *et al.* show that α9 recruitment of SSAT to focal adhesions affects cell migration by modulating the activity of an inward rectifier K^+ (Kir) channel. The expression of catalytically inactive SSAT inhibited migration, suggesting that polyamine metabolism is important for α9-dependent migration. Higher-order polyamines inhibit Kir channels, and inhibition or knockdown of the Kir4.2 channel inhibited migration of the cells on α9-specific substrates but did not impair migration on fibronectin. Although α9 was present in focal adhesion–like structures throughout the cell surface, Kir4.2 only colocalized with α9 in focal adhesion–like structures at the leading edge of the cell. Thus, the authors propose that local changes in polyamine concentrations are mediated by SSAT that is recruited to the α9 subunit of integrins; the inhibition of Kir channels allows a localized K^+ efflux, which stimulates migration. — AMV

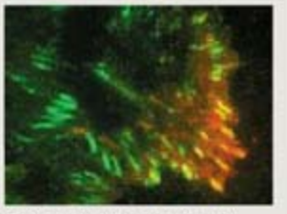

Colocalization (yellow) of integrin and potassium channel.

CREDIT: DEHART ET AL., PROC. NATL. ACAD. SCI. U.S.A. 105, 7188 (2008)

Proc. Natl. Acad. Sci. U.S.A. **105**, 7188 (2008).

www.sciencemag.org

Science

1200 New York Avenue, NW
Washington, DC 20005
Editorial: 202-326-6550, FAX 202-289-7562
News: 202-326-6581, FAX 202-371-9227
Bateman House, 82-88 Hills Road
Cambridge, UK CB2 1LQ
+44 (0) 1223 326500, FAX +44 (0) 1223 326501

Subscription Services For change of address, missing issues, new orders and renewals, and payment questions: 866-434-AAAS (2227) or 202-326-6417, FAX 202-842-1065. Mailing addresses: AAAS, P.O. Box 96178, Washington, DC 20090-6178 or AAAS Member Services, 1200 New York Avenue, NW, Washington, DC 20005

Institutional Site Licenses please call 202-326-6755 for any questions or information

Reprints: Author Inquiries 800-635-7181
Commercial Inquiries 803-359-4578

Permissions 202-326-7074, FAX 202-682-0816

Member Benefits AAAS/Barnes&Noble.com bookstore www.aaas.org/bn; AAAS Online Store http://www.apisource.com/aaas/ code MKB6; AAAS Travels: Betchart Expeditions 800-252-4910; Apple Store www.apple/eppstore/aaas; Bank of America MasterCard 1-800-833-6262 priority code FAA3YU; Cold Spring Harbor Laboratory Press Publications www.cshlpress.com/affiliates/aaas.htm; GEICO Auto Insurance www.geico.com/landingpage/go51.htm?logo=17624; Hertz 800-654-2200 CDP#343457; Office Depot https://bsd.officedepot.com/portalLogin.do; Seabury & Smith Life Insurance 800-424-9883; Subaru VIP Program 202-326-6417; VIP Moving Services http://www.vipmayflower.com/domestic/index.html; Other Benefits: AAAS Member Services 202-326-6417 or www.aaasmember.org.

science_editors@aaas.org (for general editorial queries)
science_letters@aaas.org (for queries about letters)
science_reviews@aaas.org (for returning manuscript reviews)
science_bookrevs@aaas.org (for book review queries)

Published by the American Association for the Advancement of Science (AAAS), *Science* serves its readers as a forum for the presentation and discussion of important issues related to the advancement of science, including the presentation of minority or conflicting points of view, rather than by publishing only material on which a consensus has been reached. Accordingly, all articles published in *Science*—including editorials, news and comment, and book reviews—are signed and reflect the individual views of the authors and not official points of view adopted by AAAS or the institutions with which the authors are affiliated.

AAAS was founded in 1848 and incorporated in 1874. Its mission is to advance science and innovation throughout the world for the benefit of all people. The goals of the association are to: foster communication among scientists, engineers and the public; enhance international cooperation in science and its applications; promote the responsible conduct and use of science and technology; foster education in science and technology for everyone; enhance the science and technology workforce and infrastructure; increase public understanding and appreciation of science and technology; and strengthen support for the science and technology enterprise.

Information for Authors

See pages 634 and 635 of the 1 February 2008 issue or access www.sciencemag.org/about/authors

THE ANDROGYNOUS LOOK

For a short time, visitors to London's Natural History Museum can inspect a living, newly hatched gynandromorph, a half-male, half-female moth. Male on the right and female on the left, this *Antheraea frithi*, a silk moth native to Thailand, is divided right down the middle, including its reproductive organs. Museum scientists said this exceedingly rare condition—which occurs in perhaps 1 in 50,000 moths and butterflies—results from an error involving the sex chromosomes in the first cell division.

Boating With The Phoenicians

In 600 B.C.E., the Greek historian Herodotus wrote a century and a half later, the king of Egypt commissioned Phoenicians, the lords of the Mediterranean, to sail around Africa. Philip Beale, an adventurer and former London investment manager, wants to show how they could have accomplished the feat.

On 8 August, Beale plans to embark with a crew of 20 from the Syrian island of Arwad in a Phoenician-style boat. They will head through the Red Sea and down the coast, rounding the perilous Cape of Good Hope in January and arriving in Alexandria, Egypt, by early summer. They'll be equipped with no engine or running water and little modern equipment other than that for navigation and communications.

The 21-meter vessel (above) is modeled on Phoenician sailing ships based on data from shipwrecks and other artifacts. It's being built of Aleppo pine, with 10 rowing stations on each side. It will have a single square sail of linen, which means the ship can't sail into the wind but does best with a following wind. Beale says "one of the key questions" to answer is whether the ship can get up Africa's West Coast in the face of northeasterly winds and currents pushing it out into the Atlantic.

Four years ago, Beale, 47, led another ancient replay, helming the Borobudur ship, a replica of an 8th-century double outrigger, to show that traders could have sailed from Indonesia to the West coast of Africa.

An Alien Hello?

Scientists searching for radio or light signals from extraterrestrials may be barking up the wrong tree. Aliens might send almost-undetectable particles called neutrinos, argue physicists John Learned and Sandip Pakvasa of the University of Hawaii, Manoa, and Anthony Zee of the University of California, Santa Barbara. If so, detectors currently under construction, such as the massive Ice Cube array at the South Pole, might spot those signals, they write in a paper posted to the arXiv preprint server.

Unlike radio and light waves, neutrinos will pass straight through almost anything, and their signals couldn't be confused with emissions from stars because nothing naturally produces very high-energy neutrinos, Zee says. By tuning the neutrinos' energy to 6.3 peta–electron volts, tech-savvy E.T.s could set up a particularly strong interaction in earthly particle detectors. All they would need would be particle accelerators that reach energies 6300 times higher than the highest energy achieved by a humanmade accelerator.

Even if aliens could produce such accelerators, would they use them to send signals into the void in hopes of getting a reply millennia later? "It's not the first thing that I would do," says David Rubin, an accelerator physicist at Cornell University. Still, Zee says, if aliens are sending such signals, they'll be in the data that Ice Cube will collect anyway, so "you might as well look" for them.

High Science

Despite stormy winds and temperatures below −17°C, Italian climbers last month successfully installed the world's highest automated climate station on Mount Everest.

Three alpinists and six Sherpas set out from the Pyramid, an Italian research station 5400 meters high in the Khumbu Valley, carrying 50 kilos of equipment, wires, and poles. They anchored the station to the rock at an altitude of 8000 meters, less than 900 meters from the summit.

With a network of ground-based monitoring stations in the Himalayas, scientists are tracking the movements of the so-called ABCs (atmospheric brown clouds) that waft through the mountains from the industrial plains. "The new station will help us to trace pollutants that we have unexpectedly monitored" since 1990, such as industrial aerosols and organic compounds, says project director Paolo Bonasoni, a physicist at Italy's Institute of Atmospheric Sciences and Climate in Bologna. The weather station is now sending hourly data to the Pyramid on solar radiation as well as weather conditions. "Reliable records of temperature trends in the upper troposphere [between 6000 and 11,000 meters] are still lacking," says Veerabhadran Ramanathan of Scripps Institution of Oceanography in San Diego, California. "Temperatures at this high-altitude station can be one of the most fundamental measures of global warming."

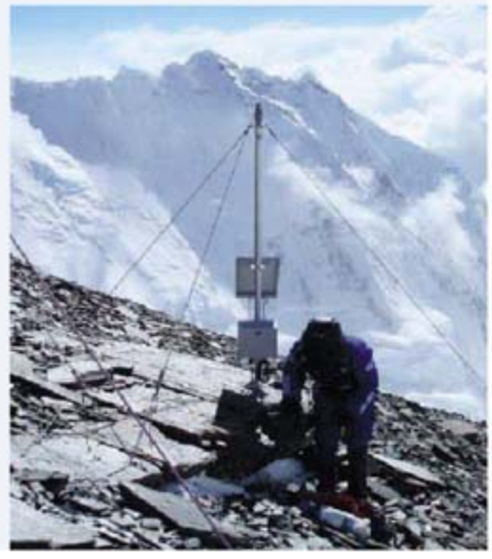

CREDITS (TOP TO BOTTOM): NATURAL HISTORY MUSEUM; COURTESY OF THE PHOENICIAN SHIP EXPEDITION; EVEREST-K2-CNR

In the News

DEFENDING CAPTIVITY. Is Jane Goodall in favor of keeping animals in zoos or isn't she?

Last month, the celebrated primatologist and animal-rights activist found herself under fire from animal-welfare advocates for remarking that chimpanzees might be better off in zoos than in the wild. "If I were a chimpanzee, I know what I would choose," she said in a 19 May speech at the opening of a new monkey enclosure at the Edinburgh Zoo in the U.K., contrasting the safety and comfort of zoos to the dangers of poaching and habitat loss in the wild. Her words put her at odds with Advocates for Animals, a U.K. organization that Goodall herself has led since 1998.

"I would prefer that zoos did not exist," she explained in a 25 May letter to the London *Times*, which ran a story about the event. But rather than condemn all zoos, "I choose to praise those that are doing the best job."

Goodall has stepped down as president of Advocates for Animals but says her resignation is unrelated to the controversy. "I just don't have time for them," she told *Science*, adding that she's on the road 300 days per year. Last week, for example, she was in Brussels presenting a petition asking the European Union to abandon experimentation with animals.

AWARDS

FIRST KAVLI PRIZES. Researchers from the United States, the United Kingdom, Japan, and Sweden have won inaugural $1 million prizes from the Kavli Foundation. The awards are for accomplishments in nanoscience, neuroscience, and astrophysics, fields that Norwegian-born philanthropist Fred Kavli wants to boost.

Louis Brus of Columbia University and Sumio Iijima of Meijo University in Nagoya, Japan, win the nanoscience prize: Brus for his work on nanocrystal semiconductors and Iijima for his research on carbon nanotubes. Maarten Schmidt of the California Institute of Technology in Pasadena and Donald Lynden-Bell of the University of Cambridge in the U.K. share the astrophysics prize for work related to quasars. And Sten Grillner of the Karolinska Institute in Stockholm, Sweden, Pasko Rakic of Yale University School of Medicine, and Thomas Jessell of Columbia University are co-winners of the neuroscience prize: Grillner for spelling out how patterns of neuronal circuitry affect locomotion and Rakic and Jessell for work on how neurons develop in the embryonic brain and spinal cord, respectively.

CALCULUS OF PEACE. David Mumford, one of three winners of the 2008 mathematics prize from the Israel-based Wolf Foundation, is donating his share of the $100,000 award to Palestinian causes. Mumford, professor emeritus of mathematics at Brown University, will give half of his award to Birzeit University in the West Bank and half to the Tel Aviv–based human rights organization Gisha, which works for freedom of movement of Palestinians in Gaza.

A pioneer in algebraic geometry who previously won the Fields Medal, mathematics' highest honor, the 70-year-old Mumford says his donations were inspired by a trip to Israel and Palestine 4 years ago, when he saw how difficult it was for Palestinians to study abroad. Sari Bashi, director of Gisha, says Israeli restrictions on travel from Gaza are particularly hard on science students: "There are many advanced degrees that don't exist in Gaza. Hundreds of students are trapped there and can't reach their studies."

Mumford stresses that he is "not doing this as a criticism of Israel. This is in Israel's interest as well. Educated Palestinians can be better partners for peace than uneducated ones." A full list of Wolf Prize winners is at www.wolffund.org.il.

Three Q's >>

VIENNA, AUSTRIA—On a visit here last week, Nobelist **Eric Kandel** attended the debut of *In Search of Memory*, a film about his life and work, dined with Austrian President Heinz Fischer, and urged officials to rename a boulevard that bears the name of a 19th century mayor known for his anti-Semitic views. Kandel, who fled Nazi-controlled Austria in 1938 at the age of 9, is now a member of the newly built Institute of Science and Technology Austria.

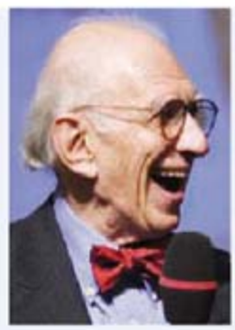

Q: How did Austria lure you back?
Of course, I had distrust of the Viennese. The Catholics here nearly took my life. Unlike Germany, where they've confronted their [anti-Semitic] history very transparently, Austria has never dealt with it. I remember a Viennese woman said to me at the time, in a very typical comment, "You know, they weren't all bad." So when I won the Nobel, I stuck it to the Austrians by saying that it was certainly not an Austrian Nobel; it was a Jewish-American Nobel. After that, I got a call from the [former] Austrian president [Thomas Klestil], asking me, "How can we make things right?"

Q: What are your goals here?
First, Doktor-Karl-Lueger-Ring should be renamed. Lueger was mayor of Vienna [1897 to 1910] and a notorious anti-Semite. Hitler even cited him in *Mein Kampf*. The fact that the University of Vienna is on this street is offensive. Second, I would like to see the Jewish intellectual community brought back to Vienna. There need to be scholarships for Jewish students and researchers.

Q: Who will pay for it?
I'm talking to a private donor. Public money, private money, … I don't care. The Jewish community here was incredibly vibrant. Imagine bringing that back. Wouldn't it be nice?

CREDITS (TOP TO BOTTOM): AP; JOHN ABROMOWSKI/BROWN UNIVERSITY; GEORG DUMIC/I.S.T. AUSTRIA

Francis Collins on personal genomics 1272

The rise of the Andes 1275

RUSSIAN SCIENCE

Russian Academy President Narrowly Wins Reelection

MOSCOW—Despite unprecedented opposition, which included fellow academicians calling for him to step aside, Yuri Osipov was reelected last week to a fourth term as president of the Russian Academy of Sciences (RAS). The election, in which two candidates who challenged Osipov received a combined 46% of the secret ballots, made clear that RAS is split at a time when many members feel its future is insecure. Osipov's return "will bring the academy to deep stagnation," says academician Alexandr Spirin, who had made a public call for the 71-year-old mathematician not to seek reelection.

It's not clear, however, how long Osipov will actually serve. A source in the academy told *Science* that Osipov earned the support of the RAS Presidium, a key management body, only after agreeing to leave his post shortly after the elections so that Mikhail Kovalchuk, director of the Kurchatov Institute, can take his place. Some discount such gossip, however. "I know these rumors about Osipov to be replaced by Kovalchuk, but I doubt it is true," says Nikolay Ponomarev-Stepnoy, the Kurchatov Institute's vice president.

Kovalchuk was expected by many to win Osipov's seat this year, in large part because the government has placed nearly $8.5 billion of nanotechnology funding under his institute's control and because former Russian president and now Prime Minister Vladimir Putin is seen as his champion. Indeed, Putin paid a rare visit to RAS to announce new science funding measures, including higher salaries for academicians, corresponding members, and RAS researchers.

Power couple. At the Russian Academy of Sciences, Prime Minister Vladimir Putin (*left*) chats with RAS President Yuri Osipov.

But many RAS members, skeptical that the nanotechnology money will actually fund academic research, weren't swayed by Putin's lobbying. Two years ago, Kovalchuk failed to get elected to a full academician membership, and last week, academy members again declined to approve his membership, dooming any plans for him to run for election to be the next RAS president. The apparent rebuke to Putin could threaten the independence of RAS, as recent legislation has given the Russian government authority to claim some of the academy's valuable property.

Still, even without Kovalchuk in the running, Osipov's victory was close. In past elections, he had no official challengers. But this time, the Power Industry, Machine-Building, Mechanics and Control Processes branch of RAS nominated its head, Vladimir Fortov. A significant personality in Russian science, Fortov headed the Russian Foundation for Basic Research and was the country's science minister in the 1990s.

Citing the need for regular turnover of top positions, academician Vladimir Zakharov, head of the RAS Research Center in Chernogolovka, had written a letter to Power Industry branch officials suggesting Fortov. "Fortov is a prominent scientist, who won many international prizes. … He is well-known all over the world, and his presidency ▶

UNIVERSITIES

Breaking With Tradition, France Picks Future Elite Schools

The French government has selected six university clusters to receive up to €500 million each for drastic renovation and expansion of facilities on their aging campuses. Although the money is for buildings only, the move is part of a broader plan to transform the selected schools into top-notch research universities that can compete on the global level and boost France's poor showing in university rankings.

Each of the six winning proposals comes from collections of universities and other schools in individual cities—Toulouse, Grenoble, Strasbourg, Montpellier, Lyon, and Bordeaux—that have agreed to merge or at least strike up tight collaborations that will increase their clout and attractiveness. "We have never received amounts like this before," says Alain Beretz, president of the University Louis Pasteur in Strasbourg, one of the winners.

Most of the €5 billion for "Operation Campus" comes from the government's sale of shares in the electricity company EDF. The eight-member panel that selected the six winners asked seven others to rework their proposals and compete for four remaining slots to be awarded in July. One or more clusters from the Paris region are widely expected to be among the winners in that round.

The plan, a 2007 campaign promise of President Nicolas Sarkozy, resembles Germany's prior effort to elevate nine universities to elite status (*Science*, 20 October 2006, p. 400). It's also a controversial break with France's traditionally egalitarian funding system. "The government is creating rich universities so it can forget about the others," says Alain Trautmann, the founder of Sauvons la Recherche, a researchers' movement, who argues that a "Marshall Plan" is needed to spruce up all campuses across the country.

–MARTIN ENSERINK

CREDIT: ALEXANDER SAVERKIN/ITAR-TASS/LANDOV

would strengthen the Academy's international status," noted Zakharov. The Far-Eastern Branch of the academy also proposed a candidate, Valery Chereshnev, head of the RAS Urals Branch.

A couple of weeks before the elections, Spirin, former director of the RAS Protein Institute, sent a public letter to Osipov asking him to withdraw his candidacy. "In the recent years the authority of our Academy, as well as your personal authority as the president, has strongly gone down in the broad scientific community and continues to fall," wrote Spirin.

At the RAS meeting in Moscow, Zakharov and Spirin again presented their arguments. Supporters of Osipov countered that he had managed the academy successfully for 17 years and was accepted in high government circles. "In these 17 years, Osipov has more than once saved the academy from elimination," says RAS Vice President Alexandr Nekipelov.

When the votes were counted, Osipov had received 52%, whereas Fortov got 39% and Valery Chereshnev 7%. "I think we are now witnessing a critical moment in the history of our academy," says Spirin. "This is an unprecedented situation that so many people voted against the president."

–ANDREY ALLAKHVERDOV AND VLADIMIR POKROVSKY

Andrey Allakhverdov and Vladimir Pokrovsky are writers in Moscow.

ECOLOGY

Seaweed Invader Elicits Angst in India

NEW DELHI—An effort in southern India to raise coastal farmers out of poverty by paying them to cultivate red algae for a food additive has gone awry. Last month, botanists reported that the alga, *Kappaphycus alvarezii*, has invaded coral reefs in a marine reserve in the Bay of Bengal. Experts are trying to establish who let the seaweed escape into the wild: a government lab, a multinational company, or careless farmers.

The saga began in 1996, when the Central Salt and Marine Chemicals Research Institute (CSMCRI) in Bhavnagar launched a project to grow the algae in perforated bags in the open sea and extract carrageenan, a gelatinous compound used to stabilize or add texture to products as diverse as toothpastes and mocha lattes. In 2000, CSMCRI transferred the technology to PepsiCo India Holdings Private Limited in Gurgaon, whose executive vice president, Amit K. Bose, told *Science* that since 2001 the company has been "supporting and subsidizing" local farmers to cultivate the alga offshore. The seaweed is grown on tethered rafts in shallow water; algae is harvested and dried and exported to countries such as Malaysia and the Philippines, which extract the carrageenan.

The commercial cultivation is near the edge of the Gulf of Mannar Marine National Park, a 560-square-kilometer reserve that's home to more than 100 species of corals and mammals such as sea cows and dolphins. Off Kurusadai Island in the reserve, "no part of the coral reefs was visible in most invaded sites, where [the algae] doomed the entire colonies and occupied almost all ridges and valleys of the coral landscape," a team led by botanist S. Chandrasekaran of Thiagarajar College in Madurai reported in the 10 May issue of *Current Science*. It's not clear if the alga has spread to other parts of the reserve.

This isn't the first time the alga, native to the Philippines, has invaded new turf: In 1999, it colonized coral reefs in Hawaii, according to the University of Hawaii, Manoa. For that reason, some prominent researchers, including M. S. Swaminathan, an agricultural scientist at M. S. Swaminathan Research Foundation in Chennai who now serves in Parliament, had opposed bringing the alga to India in the first place.

No one has taken responsibility for *K. alvarezii*'s escape. Whoever is deemed responsible could be prosecuted for damaging habitat under the Indian Wild Life Protection Act of 1972, says P. K. Manohar, a lawyer with Legal Action for Wildlife and Environment in New Delhi.

Moving in. *Kappaphycus alvarezii* growing on coral in the Gulf of Mannar Marine National Park.

CREDIT: S. CHANDRASEKARAN/THIAGARAJAR COLLEGE, MADURAI

Bose acknowledges that PepsiCo promoted contract farming of the algae to serve the community by helping impoverished farmers. The company guarantees that it will buy all the farmers' annual production of *K. alvarezii*, amounting to 100 to 200 metric tons of dry seaweed; all the dry seaweed is exported, Bose says. He denies that PepsiCo played a role in the alga's escape into the marine reserve. Instead, he suggests that CSMCRI's cultivation trials are "the root cause for its bioinvasion at [Kurusadai]."

CSMCRI's director, Pushpito K. Ghosh, says he is "quite puzzled as to what may have happened." He and his colleagues argue that strong currents could have swept algal twigs from commercial farms near Kurusadai or from his institute's trial cultivation site. "Another possibility, which must not be ruled out, is clandestine experimentation by unscrupulous elements," Ghosh says, without elaborating. Chandrasekaran calls that an "outlandish explanation" and notes that no one is allowed to visit Kurusadai Island without written permission from reserve authorities. No matter how the seaweed colonized Kurusadai, Ghosh says, "there is no question of CSMCRI disowning responsibility."

PepsiCo has said it will pay for a wider survey of *K. alvarezii* in the marine reserve as well as measures to scoop it up. But it may be too late to get rid of the algae, says Swaminathan: "All that we can now do is restrict the extent of bioinvasion."

–PALLAVA BAGLA

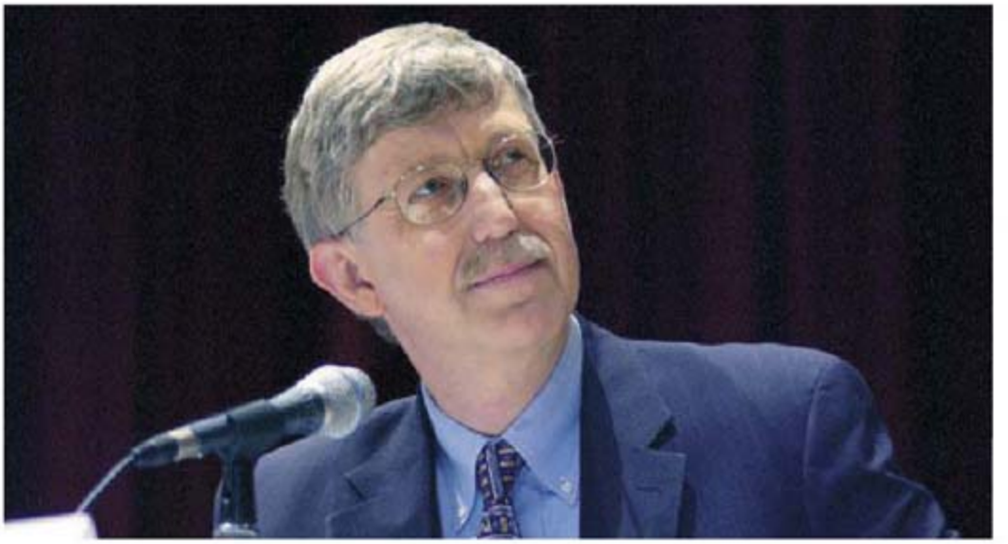

CREDIT: ERNIE BRANSON/NIH

FRANCIS COLLINS INTERVIEW

Departing U.S. Genome Institute Director Takes Stock of Personalized Medicine

For 15 years, Francis Collins has been the face of the public effort to decipher the human genome. So it came as a surprise last week when the physician-geneticist announced he will step down as director of the U.S. National Human Genome Research Institute (NHGRI) on 1 August. He plans to write a book on personalized medicine and launch a broad job search.

Since taking the helm of NHGRI—then a center—in 2003, Collins led a then-controversial 10-year effort to sequence the 3 billion bases of the human genome, ushering in "big biology." The Human Genome Project sparked a debate about whether genomic data should be freely available, an argument Collins championed and ultimately won. He has also been a tireless advocate of legislation to protect people from genetic discrimination. The passage of such a law last month was one "signal" that it was time to leave, he says.

The timing of Collins's departure has prompted speculation that he wants to advise one of the presidential campaigns, a possibility he says would interest him. Which side is not clear: He told *Science* only that he considers himself an independent. Collins is an evangelical Christian who wrote a 2006 book about his beliefs.

Collins reflected on the state of genomic medicine and his plans in a telephone interview last week. His remarks, edited for brevity, follow. A longer version, including his thoughts on dealing with the egos involved in the human genome program, is available at www.sciencemag.org.

–JOCELYN KAISER

Q: Genomewide association studies are turning up many new genetic risk variants for common diseases. Yet when people have their DNA scanned for these markers through companies like 23andMe, they learn that they have slightly elevated risks for diseases that they are at only modest risk of developing in the first place. If this is personalized medicine, it seems disappointing.

F.C.: I co-wrote a paper back in 1997 in *Science* basically arguing for the International HapMap Project [to map human genetic diversity] and for the potential that would have to reveal genetic risk factors in common disease. There were people saying HapMap was basically a welfare program for the genome centers. So the successes that you now see pouring out of the pages of journals are exhilarating. At latest count, I think 165 genetic variants associated with a common disease have been discovered in the last 2 years.

Online
sciencemag.org
Longer version of this interview.

But let's be frank about it. The discoveries still only account for a fraction of the heritability of diabetes or heart disease. A lot of people have been speculating that variants that are less common—1% or 2% or 3%—will have a larger effect in people that are carrying them. So I think in another 6 or 8 years [when rare variants are known], the predictive power will ratchet up substantially.

I'm of two minds here. I'm actually quite excited to see all these discoveries that many people are interested in taking advantage of. But I'm also worried that the public might become disillusioned and say, "Is that all there is?" And that could set the field back.

Q: How will personalized medicine work 10 years from now?

F.C.: I think we'll be at the point where sequencing your genome or mine could be done in an hour for under $1000, and people will say, "No big deal; why did they ever think this was hard?" But we'll still have this question of, "Okay, we can now make a pretty good prediction about your risk. What should you do about *it*?"

And here is one of my major frustrations. We desperately need, in this country, a large-scale, prospective, population-based cohort study. And we need to enroll at a minimum half a million people. We would need to have their environmental exposures carefully monitored and recorded, their DNA information recorded, their electronic medical records included, and have them consented for all sorts of other follow-ups.

I tried very hard to get some enthusiasm for this at high levels in the Congress and the [Bush] Administration, but as soon as people realize that this is genome project–like in terms of its cost, they shake their heads and say, "Well, it's not the right time." It would be $300 [million] or $400 million a year to run this study.

Q: Do you think the day will come when the large sequencing centers supported by NHGRI are no longer needed?

F.C.: Yes. They're incredibly valuable right now, but I do look forward to a time, maybe 5 years from now, maybe 7 years, where DNA sequencing is so exportable, and so much of a plug-and-play operation, that the need for these very large, complex centers fades away.

Q: Why are you resigning now and moving, as you put it, into "the white space of unemployment"?

F.C.: At age 58, I'm restless to see what other challenges might be out there waiting for me. I want some time to reflect on all that's happened, to step out of the pressures of a 90-hour work week, and see where is all this going. Maybe there's something I can do in global health or something that relates to the real applications of genomics to medicine—given my physician background, that's where my heart is.

This sort of systematic [job] search, where you talk to lots of people, is pretty untenable when you're an NIH institute director. That is especially true now with the very high scrutiny towards conflicts of interest.

ARCHAEOLOGY

Runoff Threatens Early Human Site

PRETORIA, SOUTH AFRICA—Wastewater runoff from a golf-course irrigation system is threatening research at caves along South Africa's southern coast that contain the earliest evidence of humans exploiting marine resources, scientists say. To their disappointment, a judge here declined last week to issue an injunction designed to protect the archaeological site.

Due to the area's water shortage, the golf course has been using a "gray water" effluent to nurture its greens, but a drainage system intended to prevent leaching into the 15 caves below hasn't worked as planned. The Wildlife and Environment Society of South Africa (WESSA), a party to the original agreement under which the golf course was supposed to protect the caves from leaching, had asked a high court judge of Western Cape province to order that the irrigation be stopped or diverted.

Water hazard. Researchers are using plastic mats and sandbags to try to protect prized caves from leaching damage caused by runoff from a golf course.

"The cave we are now excavating has been badly affected by the effluent leaching," says archaeologist Curtis Marean of Arizona State University's Institute of Human Origins in Tempe, who heads an international project investigating the so-called Pinnacle site and nearby caves near Mossel Bay. He says the caves at Pinnacle "were dry as a bone" when he first saw them in 1998; he and other scientists noticed the leaching, which includes greenish and yellowish deposits from chemicals in the effluent, after the golf course opened in 2006.

Dozens of scientists from South Africa and countries around the world have conducted archaeological research in caves at the site, first excavated in 2000. The site has provided evidence that people in the caves included shellfish and other marine resources in their diet about 164,000 years ago, as shown by the dating of mussel shells and a whale barnacle found in the caves. The caves also revealed an early use of pigment and the production of bladelet stone tool technology (*Science*, 19 October 2007, p. 377).

Marine biologist Steve du Toit, who directs conservation efforts for WESSA in the Western Cape, says that the organization wanted the court to take quick action "to ensure there is no further damage to the archaeological resources or the environment of the site." But the judge said local homeowners, whose property values could be affected by a halt in irrigation, were "entitled to be heard" as part of any court decision. WESSA plans to appeal.

The developer of the golf course, the Pinnacle Point Golf Estate, says it is trying to correct the leaching problem. It stopped irrigating the practice green and two holes of the course this week and—if the province's environment department approves—plans to install a new membrane and drainage system, says the development director, Lance Kinnear. But du Toit and other scientists worry that this won't stop all the leakage, and they fear additional cave damage.

As part of a wider project focused on southern Africa's ancient climate, environment, ecology, and anthropology, scientists are analyzing stalagmites in the caves to help determine rainfall and vegetation patterns in the region between 50,000 and 90,000 years ago and help develop climate models. Marean calls the effort "the first large transdisciplinary project to target the southern reaches of the Southern Hemisphere in an attempt to develop a unified record of climate and environmental change over the last 400,000 years." But Marean says that the leaking effluent may have already contaminated the geochemistry of some stalagmites, irrevocably altering that valuable record.

–ROBERT KOENIG

CREDIT: STEVE DU TOIT/WESSA

NASA Suppressed Science

NASA's inspector general (IG) has confirmed allegations made 2 years ago that political appointees in the agency's press office suppressed discussion of climate change research.

Fourteen senators requested the IG investigation after NASA climate change researcher James Hansen told *The New York Times* in January 2006 that he had been muzzled. In a 2 June report, the IG finds that from fall 2004 through early 2006, the NASA headquarters public affairs office "reduced, marginalized, or mischaracterized climate change science." The 48-page report also confirms that NASA barred Hansen from being interviewed by National Public Radio partly because of concerns that he would discuss policy.

However, the IG found no evidence that research activities were suppressed at NASA's research centers. Rather, the problems involved "a few key senior employees" in the central NASA public affairs office, not NASA leaders or Bush Administration officials outside the agency. NASA spokesperson Michael Cabbage notes that once senior NASA officials became aware of the problem, they issued a new media policy allowing openness (*Science*, 7 April 2006, p. 32). –JOCELYN KAISER

Banking on Europe's Biobanks

Europe urgently needs to coordinate its biobanks, according to a report released 27 May by the European Science Foundation (ESF). Several European countries have "an enormously rich resource" of tissue samples and health records stretching back decades, the report says, but varying standards and regulations prevent scientists from combining different collections. ESF calls for harmonizing sample storage and record keeping and for countries to draw up laws and regulations that make international collaborations possible.

Earlier this year, the European Union awarded €5 million to the Biobanking and Biomolecular Resources Research Infrastructure (BBMRI), which aims to integrate Europe's existing biobanks into a single network. That's an important first step, says Frank Skorpen of the Norwegian University of Science and Technology in Trondheim, co-chair of ESF's expert group, but ultimately much larger sums will be needed. To attract sustained funding, says Kurt Zatloukal of the Medical University of Graz in Austria, coordinator of BBMRI, researchers need to estimate the economic impact of a pan-European biobank. "We need to quantify the potential return on investment."

–GRETCHEN VOGEL

GENOMICS

Read All About It—The First Female Genome! Or Is It?

Dutifully hailing it as a victory for equality, hundreds of newspapers, TV stations, and Web sites noted last week that scientists had finally sequenced the genome of a woman. A 34-year-old red-haired clinical geneticist from the Netherlands had joined living DNA legend James Watson and genome entrepreneur J. Craig Venter in the exclusive club of people whose entire DNA sequence has been unraveled. The story had a funny twist, too: Her name is Marjolein Kriek. A Watson and a Kriek, united by DNA again.

But the announcement raised eyebrows as well, because the data have not been put in the public domain nor analyzed, let alone published. "As far as I can tell, this whole story is about perception with no reality involved," *PLoS Biology* editor Jonathan Eisen, an evolutionary biologist, wrote in his blog. Indeed, Leiden University Medical Center (LUMC), which presented the research at a 26 May meeting in Amsterdam, wasn't really the first to claim a female genome—not even the second.

Scientifically, it made sense to sequence the male genome first because women lack the Y chromosome, says John Edwards, who studies the genomics of breast cancer at Columbia University. But sequencing female genomes, especially when coupled with medical histories and clinical data, will be "vital for shedding new light on women's diseases," he says.

Such considerations aside, when LUMC bought a top-line sequencer from Illumina in San Diego, California, last year, it realized that the first female genome could make a splash, says team leader Gert-Jan van Ommen. The

In the spotlight. Clinical geneticist Marjolein Kriek is among the first women to have her entire genome sequenced.

team recruited Kriek, he says, because of her name's resemblance to that of Watson's colleague Francis Crick, who died in 2004.

The PR machine started humming in earnest when Van Ommen agreed to present the genome effort at a 1-day meeting of Dutch researchers and science journalists organized by the Netherlands Organisation for Scientific Research (NWO). To promote that meeting, NWO issued an embargoed press release for science reporters around the globe promising "world news."

But Illumina itself said in a 6 May press release that it had sequenced three unidentified Nigerian people: a man, a woman, and their son. And on that same day, a team from Washington University in St. Louis, Missouri, announced at a meeting at Cold Spring Harbor Laboratory that, as part of a project to understand the genetics of acute myeloid leukemia, it had read the genome of a female cancer patient.

Van Ommen says he wasn't aware of those claims. "If we had known, we would not have presented it this way," he says. He does plead guilty to Eisen's charge of "science by press release," noting, however, that his team is hardly the only perpetrator: For example, Watson's genome sequence was hailed publicly months before *Nature* published a paper on it.

Illumina isn't the least bit miffed at the Leiden team's priority claim, a company spokesperson says. Perhaps that's because the LUMC press release noted that Kriek's DNA was cracked using Illumina's equipment.

–MARTIN ENSERINK

U.S. SCIENCE FUNDING

Encourage Risk, Help Young Researchers, Panel Advises

Tight budgets have done more than restrict research; they're damaging morale by making people afraid to take chances, just when it's more important than ever to invest in what could be "transformative" research, a new report from the American Academy of Arts and Sciences argues. "The constant hunt for dollars is fostering conservative thinking" and thus making a bad situation worse, according to a panel headed by Thomas Cech, president of the Howard Hughes Medical Institute in Chevy Chase, Maryland.

Formed to look at "alternative models for the federal funding of science," the 22-person committee "quickly drilled down" to two messages, says panel member Keith Yamamoto of the University of California, San Francisco: the need to foster early-career scientists and to encourage high-risk research. Released this week, the white paper *Advancing Research in Science and Engineering* is styled as a follow-on to a National Academy of Sciences report (*Rising Above the Gathering Storm*) issued in 2005. "This report addresses a very serious set of problems," says Robert Berdahl, president of the Association of American Universities in Washington, D.C.

The panel notes that young investigators are struggling as training times lengthen and competition for grants gets tougher. The statistics are "scary," Yamamoto says: In 1980, 86% of new faculty members won a grant the first time they applied for one; now only 18% do. At the same time, they're getting older: The average Ph.D. gets his or her first real job at age 38 and first R01-type grant at 42.

It's time to encourage the next generation by various means, including supplying day-care for their young children and offering generous first-time grants that will keep a researcher afloat through tenure review time, the panel says.

In what Cech calls its "single most controversial recommendation," the report says institutions should find ways to help researchers with their salaries rather than relying on them to support themselves entirely with grant money—an arrangement that makes them more risk averse.

The report eschews calls for increased funding, focusing instead on how to get the most out of existing research dollars. One suggestion to universities: "Limit excessive building programs" in order to make more money available for promising investigators.

–CONSTANCE HOLDEN

CREDIT: LEIDEN UNIVERSITY MEDICAL CENTER

High, but how fast? The central Andes may have risen rapidly after shedding some weight.

CREDIT: ANDERS RYMAN/CORBIS

GEOCHEMISTRY

The Andes Popped Up by Losing Their Deep-Seated Rocky Load

Mountains grow so slowly that no one would notice—or so conventional thinking would have it. But a group of geoscientists is arguing that about 8 million years ago, the central Andean plateau, at least, sprang upward so fast that modern surveying techniques could have revealed the uplift in a few years. It happened, they think, when the deep root of dense rock that anchored the Andes rapidly fell away. The new geochemical evidence of rapid uplift "is really beautiful stuff," says tectonophysicist Peter Molnar of the University of Colorado, Boulder. Lovely or not, the new paleo-elevation data will be facing some tests of their own.

Mountains rise because Earth's outer skin gets squeezed. Across the Andes, an oceanic tectonic plate drives against the western edge of South America as the plate dives beneath the continent. A slow, steady squeeze gradually compresses and thickens the crust. Because the crust is less dense than underlying rock, that thickening buoys it, causing the mountains to rise. Tectonophysicists assumed that the rise of the Andes had been as protracted as their 50-million-year-long compression, but the geologic record of uplift left the speed ambiguous.

In recent years, geochemists have exploited a more detailed record of elevation change locked in the isotopic composition of the oxygen, hydrogen, and carbon of minerals formed as mountains rise. On page 1304 of this issue of *Science* and in a paper in press in *Earth and Planetary Science Letters*, Carmala Garzione and Gregory Hoke, both of the University of Rochester, New York, and their colleagues report new geochemical paleo-elevation data. Combined with existing isotopic data, the new data point to rapid uplift. In one technique they used, isotopes can reflect uplift because as atmospheric moisture moves up a mountainside, isotopically heavy molecules tend to precipitate out sooner than lighter ones. That leaves relatively less of the heavy molecules in the rain and snow that falls on the mountaintop, where the isotopes are locked into minerals. The higher the mountaintop, the lighter the isotopes. From the isotope data, Garzione and her colleagues infer that the Andean plateau shot up by 1.5 kilometers in as little as 1 million years.

Crustal compression doesn't happen that fast, but Garzione and her colleagues say an indirect effect can explain the rapid rise. Compression thickens not only the crust but also the cold, dense mantle rock immediately beneath. The central Andes seem to have lost this so-called mantle lithosphere, the group says, removing a weight from the lighter crust. Without that ballast, the crust could rise. The timing and style of volcanism in the central Andes suggest that the mantle lithosphere fell away suddenly—as a huge drop dripping off the crust or as a layer peeling away—just when the isotopic data indicate a punctuated uplift, the group writes.

The Andean paleo-elevation data all but clinch the case for that scenario, says tectonophysicist David Rowley of the University of Chicago in Illinois. But first the paleo-elevation data need to be tested further, says Todd Ehlers of the University of Michigan, Ann Arbor. Garzione and colleagues state that the climate under which new minerals recorded elevation change resembled the modern climate, he says, "but they've never tested it." Ehlers reported at last December's American Geophysical Union meeting that in a climate model, the rise of the Andes themselves alters climate—for example, by changing the source and therefore the isotopic composition of precipitation. That could give a false paleo-elevation, he says. He would like to see more work with models rather than in the field.

–RICHARD A. KERR

SCIENCESCOPE

More Clouds Over Fermilab

The United States's last dedicated particle physics laboratory faces a bleak future if Congress doesn't come through with new money, say advisers to the U.S. Department of Energy (DOE). Fermi National Accelerator Laboratory (Fermilab) in Batavia, Illinois, is already feeling a budget crunch (*Science*, 30 May, p. 1148). But last week, DOE's Particle Physics Project Prioritization Panel reported that if DOE's current $688 million budget for high-energy physics remains flat, then Fermilab researchers will have to wait an extra 3 to 5 years, to roughly 2017, to start building a high-intensity proton source that would be the lab's new centerpiece. Also, the lab's particle smasher, the Tevatron, would have to close in 2009, a year earlier than hoped, giving it less time to beat a new machine in Europe at finding the prized Higgs boson.

Lab spokesperson Judy Jackson says she is optimistic that "many members [of Congress] understand the plight of high-energy physics" and will act accordingly. However, Congress has not followed through with proposed increases for two straight years and last year cut the particle physics budget by $64 million.

–ELI KINTISCH

Rock Art Dustup

A new federal analysis could halt controversial plans to expand gas development in Utah's archaeologically rich Nine Mile Canyon. The remote canyon, which features an estimated 10,000 rock art images, also holds major reserves of natural gas. In 2004, the Bureau of Land Management (BLM) permitted drilling projects to commence in Nine Mile. A recent BLM-commissioned study supports archaeologists' fears that the rock art is being damaged by dust from trucks and rigs plying an unpaved road (*Science*, 25 January, p. 394).

Now the Environmental Protection Agency (EPA), as part of its review of a BLM plan to allow 600 new gas wells, has entered the fray. Last week, EPA found BLM's draft Environmental Impact Statement "unsatisfactory" because it did not "adequately assess" potential ozone pollution. EPA also expressed concern that dust is compromising the "physical integrity" of the rock art. The EPA evaluation "reaffirms that we're not the only ones who think something is amiss," says archaeologist Jerry Spangler, executive director of the Colorado Plateau Archaeological Alliance, an antiquities preservation group. BLM has agreed to conduct more air-quality testing, which could delay the new wells indefinitely.

–KEITH KLOOR

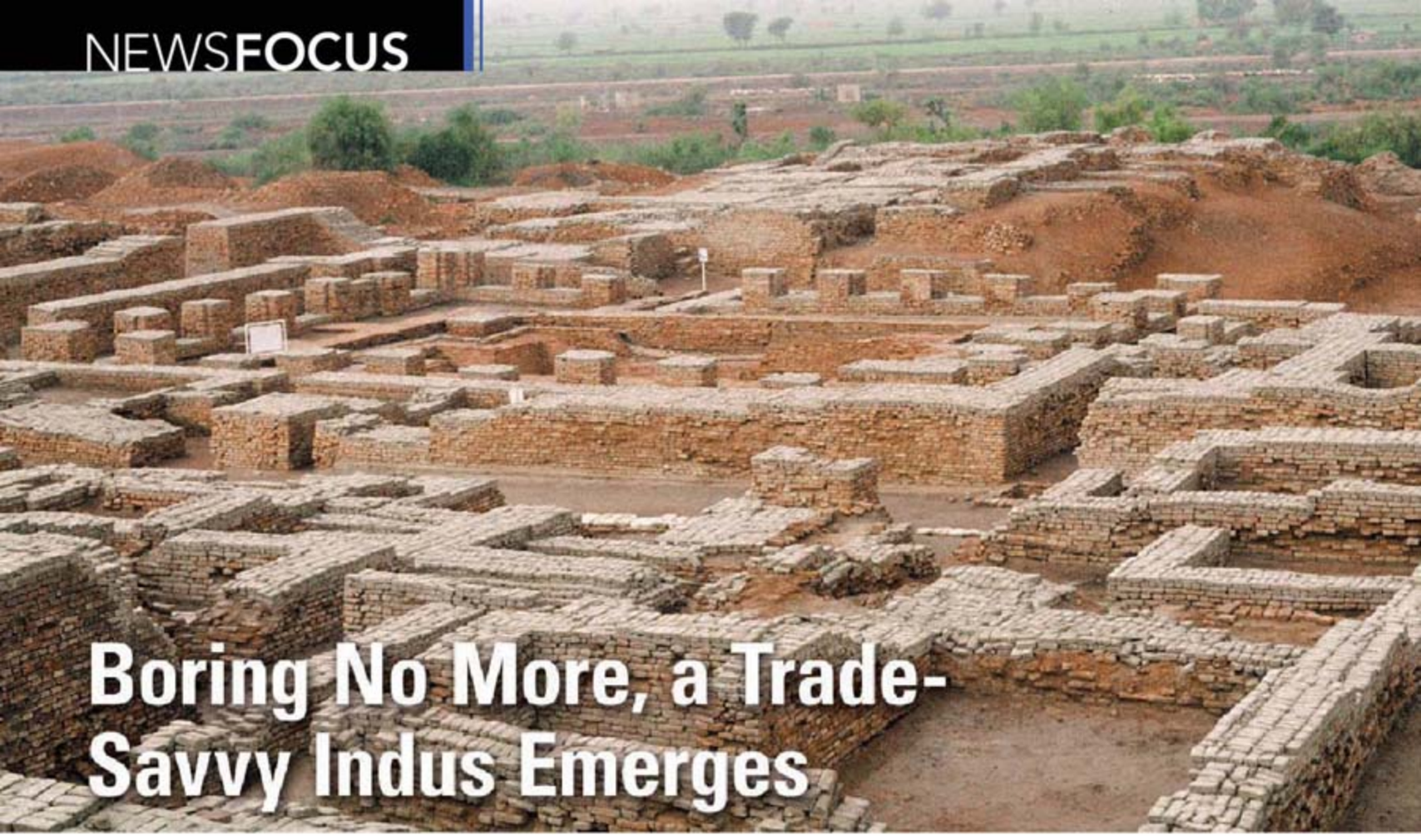

Boring No More, a Trade-Savvy Indus Emerges

Long in the shadow of its sister civilizations to the west, the Indus is emerging as the powerhouse of commerce and technology in the 3rd millennium B.C.E. But political and economic troubles dog archaeologists' efforts to understand what made this vast society tick

THAR DESERT, PAKISTAN—Egypt has pyramids, temples, and mummies galore. Ancient Mesopotamians left behind the dramatic saga of Gilgamesh, receipts detailing their most prosaic economic transactions, and the occasional spectacular tomb. But the third of the world's three first civilizations had, well, good plumbing. Even the archaeologists who first discovered the Indus civilization in the 1920s found the orderly streetscapes of houses built with uniform brick to be numbingly regimented. As recently as 2002, one scholar felt compelled to insist in a book that the remains left behind by the Indus people "are not boring."

Online
sciencemag.org
Podcast interview with the author of this article.

Striking new evidence from a host of excavations on both sides of the tense border that separates India and Pakistan has now definitively overturned that second-class status. No longer is the Indus the plain cousin of Egypt and Mesopotamia during the 3rd millennium B.C.E. Archaeologists now realize that the Indus dwarfed its grand neighbors in land area and population, surpassed them in many areas of engineering and technology, and was an aggressive player during humanity's first flirtation with globalization 5000 years ago. The old notion that the Indus people were an insular, homogeneous, and egalitarian bunch is being replaced by a view of a diverse and dynamic society that stretched from the Arabian Sea to the foothills of the Himalaya and was eager to do business with peoples from Afghanistan to Iraq. And the Indus people worried enough about the privileges of their elite to build thick walls to protect them. "This idea that the Indus was dull and monolithic—that's all nonsense," says Louis Flam, an archaeologist at the City University of New York who has worked in Pakistan. "There was a tremendous amount of variety."

This radical overhaul of the Indus image, which has gone largely unnoticed by the larger archaeology community, emerges from recent visits to key excavations in India and Pakistan, including previously unknown sites here in the desert, and interviews with dozens of Indus scholars around the world. During the past decade, archaeologists have uncovered entire Indus cities previously unknown, some with unique features such as major fortifications. New methods have spurred the first detailed analyses of everything from climate to settlement patterns to butchered animal bones. Growing interest in the role of the ancient economy in spreading goods and ideas has scholars tracing a vast trade network that reached to Mesopotamia itself, where at least one Indus interpreter went native.

Faces from the past. These small figurines are rare examples of Indus human or deity statuary.

Even well-combed sites are still full of surprises: The city of Harappa may be 1000 years older and Mohenjo Daro far larger than once thought. And the dramatic "Buddhist stupa" adorning Mohenjo Daro's high mound may in fact date back to the Indus

CREDITS (TOP TO BOTTOM): © J. M. KENOYER, COURTESY DEPT. OF ARCHAEOLOGY AND MUSEUMS, GOVERNMENT OF PAKISTAN

Ancient alleyways. The 5000-year-old massive brick structures of Mohenjo Daro, including the Great Bath (*center*), still rise from the plains of Pakistan.

heyday around 2000 B.C.E. (see sidebar, p. 1280). "What has changed is the mass of evidence from the past 15 years," says archaeologist Rita Wright of New York University (NYU), assistant director of the Harappa dig. "There is more data from landscapes and settlements, not just the cities."

But piecing together a cohesive new picture is hampered by the political discord between India and Pakistan. Many foreign archaeologists steer clear of Pakistan because of political instability, while India's government—scarred by colonialism—often discourages researchers from collaborating with European or American teams. A virtual Cold War between the two countries leaves scientists and sites on one side nearly inaccessible to the other (see p. 1282). And although Indus sites are finally receiving extensive attention, many unexcavated mounds face destruction from a lethal combination of expanding agriculture, intensive looting, and unregulated urban development (see p. 1284). The small coterie of archaeologists from Pakistan, India, America, Europe, and Japan who study the Indus admit that they also share some of the blame. Often slow to publish, this community can be reluctant to work together and lacks the journals and tradition of peer review common to colleagues who focus on other parts of the world. "We're at fault," says one Indus researcher. "We should be pushing harder to publish and collaborate."

Despite these challenges, the wave of fresh material is leading to a deeper understanding of a culture once considered obscure and impenetrable. The new data paint a far more vibrant and complex picture of the Indus than the old view of a xenophobic and egalitarian society that lasted for only a few centuries before utterly vanishing. "We are rewiring the discussion," says archaeologist Gregory Possehl of the University of Pennsylvania. Adds Wright: "The Indus is no longer just enigmatic—it can now be brought into the broader discussion of comparative civilizations."

The faceless place

The very existence of the Indus wasn't recognized until more than 100 years after digs began in Egypt and Mesopotamia. It was only in 1924 that archaeologists announced they had found two great cities from a previously unknown urban society that flourished at the same time as the Old Kingdom pyramids and the great ziggurats of Sumer. The cities, Mohenjo Daro and Harappa, thrived for nearly 1000 years along the floodplain of the Indus River, which like the Nile, Tigris, and Euphrates irrigates vast swaths of land that otherwise would be desert (see map, p. 1278).

The discovery in what was then British India was stunning: Mohenjo Daro covered at least 200 square hectares and may have housed from 20,000 to 40,000 people. Harappa, 400 kilometers to the north, was only slightly smaller. Both were comparable in size to contemporary cities such as Memphis on the Nile and Ur in today's Iraq. Unlike Egyptian and Mesopotamian cities of the time, however, the Indus builders created well-ordered streets and homes with sophisticated water and sewer systems unmatched until Roman times. The Indus penchant for precise standardization—from tiny weights to bricks to houses to entire cities—was unique in the early historic period. And at Mohenjo Daro, they used expensive baked brick rather than the cheaper mud brick favored in the Middle East, thus leaving behind the only Bronze Age city on Earth where it is still possible to stroll down ancient alleys shaded by intact walls.

CREDIT: A. LAWLER/SCIENCE

Yet despite the impressive remains, there were bafflingly few clues to the political or religious systems behind the urban complexes, which seemed to lack the grandeur of Egypt and Mesopotamia. There are no remaining life-sized statues, extensive wall carvings, or elaborate building decorations. The Indus used a still-undeciphered script, but chiefly on small seals, and some scholars believe it was not a script at all (*Science*, 17 December 2004, p. 2026). Indus scribes did not leave the vast libraries of clay tablets or carved stone inscriptions that have yielded such insight into Mesopotamia and Egypt. Most burials include only a few modest goods, in contrast to the riches of Egyptian tombs. And archaeologists could find no obvious temples or palaces. The few monumental buildings—though given nicknames like "the Granary" and "the Monastery"—had functions still hotly debated.

Unlike the many pharaohs, kings, architects, and merchants who show up in sculpture and texts in Egypt and Mesopotamia, few Indus individuals were recorded. Only a few small statues show individuals, such as seated men wearing tunics and a tiny, lithe dancer. The Indus "is something of a faceless sociocultural system," says Possehl.

This led some early and mid–20th century archaeologists to consider the Indus a nonhierarchical society. Others postulated rigid control by a small elite. Given the lack of data to support either interpretation, these ideas may have had more to do with socialist and totalitarian ideas popular at the time than with the ancient past.

Picking at the past. Workers at Farmana in India uncover clues to Indus architecture.

That first generation of archaeologists did agree that the Indus was an impressive but brief flash in the pan without deep roots. Because there was no evidence of previous settled life in the region, they surmised at the time that the Indus people absorbed urban ideas from Mesopotamia—2500 kilometers to the west—and rapidly created a quirky two-city state around 2600 B.C.E., which then vanished equally abruptly by 1800 B.C.E. The 1947 partition of India, creating the new nations of India and Pakistan, drew a line through the Indus heartland and left Indus archaeology largely an academic backwater for nearly a half-century.

Round to square

The assumption that the Indus did not spring from local culture began to unravel in the 1970s, when a French-led team excavated a Neolithic site called Mehrgarh dating to 7000 B.C.E. in the Baluchistan hills on the western fringe of the Indus valley. The town included many of the trappings of later Indus life, from mud-brick houses and copper tools to wheat, barley, sheep, goats, and cattle. Although some plants may have

arrived from the Near East, goats and cattle were likely domesticated locally, and possibly sheep as well. A partially worked elephant tusk demonstrates that craft specialists were already plying their trade, and lapis lazuli jewelry from Afghanistan and marine shells from the distant coast show long-distance trade networks.

The site is now widely accepted as a precursor to the Indus and clear proof of the indigenous nature of the later civilization. That idea gets new support from surveys here in the Thar Desert, on the eastern edge of the Indus valley. This area was long assumed to have been largely uninhabited before the rise of the Indus cities. But hundreds of small sites now show that humans lived here on the plains, not just in the Baluchistan hills, for several millennia prior to the rise of the Indus, says archaeologist Qasid Mallah of Shah Abdul Latif University in Khairpur. Taking a reporter on a tour across dunes covered in scrub, he pointed out huge piles of chert used to make blades by the Neolithic predecessors of the Indus.

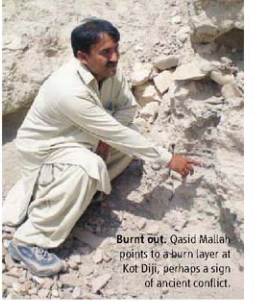

Burnt out. Qasid Mallah points to a burn layer at Kot Diji, perhaps a sign of ancient conflict.

Still, the sudden appearance of fully formed urban areas remains a puzzle. Indus cities appeared starting about 2600 B.C.E.—600 years after the first cities sprouted in Mesopotamia—and typically arose on virgin soil rather than atop earlier settlements. Some older towns date back about a millennium earlier, but most of these appear to have suffered catastrophic fires and were abandoned at the dawn of the new urban era. A site called Kot Diji a short drive from the Thar Desert shows the scars, says Mallah. The mound is an archaeological layer cake built up over centuries, with a dark layer of ash distinctly visible in a band several meters above the plain.

Some scholars argue that these burn layers record conflict between the earlier towns and new cities. But Mallah and many of his colleagues say there is not enough evidence to make that leap. Whoever constructed the cities did make distinct changes, creating new pottery styles and introducing metal forms such as razors and fishhooks. But they also drew on the long cultural history of the region and don't appear to be outside invaders, says Mallah.

In fact, new evidence suggests that not all the major cities were built from scratch. At an ongoing dig at Harappa, led by Richard Meadow of Harvard University and Jonathan Kenoyer of the University of Wisconsin, Madison, the team has found evidence of occupation dating to as early as 3700 B.C.E. By 3300 B.C.E., Harappa was a modest village of 10 square hectares but with streets running in a gridlike pattern and bricks of two standard sizes—clear foreshadowing of orderly Indus construction. "And they were trading lapis, shells from the coast, copper, and carnelian across a vast area," says Kenoyer. One of his graduate students, Randall Law, just published a dissertation pinpointing for the first time the far-flung origin of the many varieties of stone used by Indus artisans.

At a site called Farmana in the intensely farmed region west of Delhi, across the Pakistan border from Harappa, this evolution from a village of huts to sophisticated urban architecture is remarkably visible. At this previously unexcavated site, Vasant Shinde of Deccan College in Pune and his team have uncovered remains of an oval-shaped hut dating to about 3500 B.C.E., a pit dwelling made with wattle and daub and plastered walls, of a type seen today in the region. A few meters away is a level from 1000 years later where the houses have morphed

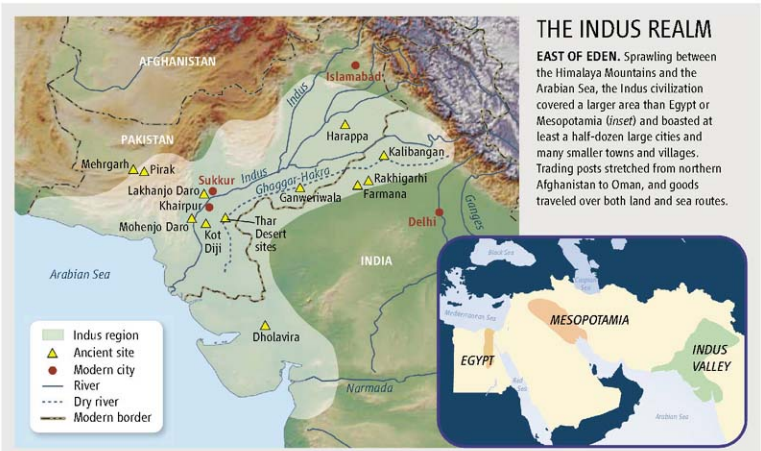

THE INDUS REALM

EAST OF EDEN. Sprawling between the Himalaya Mountains and the Arabian Sea, the Indus civilization covered a larger area than Egypt or Mesopotamia (*inset*) and boasted at least a half-dozen large cities and many smaller towns and villages. Trading posts stretched from northern Afghanistan to Oman, and goods traveled over both land and sea routes.

CREDIT: A. LAWLER/SCIENCE

into a rectangular shape and resemble those of the later Indus, except for postholes on the periphery that may have held up a roof. A few meters and 2 centuries from that trench is classic urban Indus: the clear outline of a large house with more than a dozen rooms, including a plastered bathroom, and a 20-meter-long wall fronting a long street nearly 4 meters wide. "You can see how beautifully this was planned," Shinde says, pointing at the fine brickwork and straight lines. "There are no postholes, and the bricks are of the same ratio as at Harappa." Thus from both sides of the border, the newest evidence not only underscores the local origins of the Indus, it also reveals in situ evolution. Says Mallah, "We believe that urbanization was a gradual process."

Gated communities

For the first half-century after its discovery, the Indus was virtually synonymous with Mohenjo Daro and Harappa. No other major cities were known. But along with 1000 smaller sites, archaeologists now count at least five major urban areas and a handful of others of substantial size. These sites reveal new facets of Indus life, including signs of hierarchy and regional differences that suggest a society that was anything but dull and regimented.

Take Dholavira, 800 kilometers south of Harappa in the Indian state of Gujarat. Covering 60 square hectares, it thrived for nearly 1000 years with perhaps seasonal access to the Arabian Sea. Evidence from excavations during the 1990s reveals a city that apparently included different classes of society. "Here you have meticulous planning, monumental and aesthetic architecture, a large stadium, and an efficient water-management system," says R. S. Bisht, the Archaeological Survey of India scientist who oversaw the digs. Although still largely unpublished, archaeologists around the world say Bisht's finds are truly extraordinary.

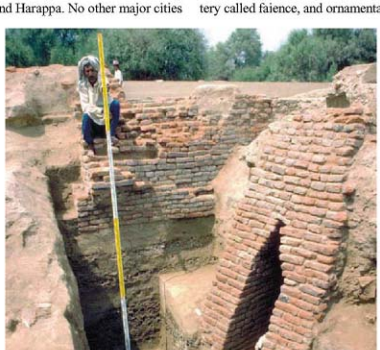

Water works. This drain from Harappa is part of a sophisticated water system that set the Indus apart from its Mesopotamian and Egyptian cousins.

CREDIT: © J. M. KENOYER, COURTESY DEPT. OF ARCHAEOLOGY AND MUSEUMS, GOVERNMENT OF PAKISTAN

In Dholavira's central citadel is an enormous structure—which Bisht dubs "the castle"—with walls that are an astounding 18.5 meters wide at their base. Next to it is an enclosed area Bisht calls "the bailey" that may have housed an elite. "This shows that Harappan [Indus] society was highly structured," says Bisht. "There was a hierarchy." Nearby is a huge mud-brick platform adorned with rare pink-and-white clay decoration and what Bisht believes was a multipurpose stadium ground stretching nearly the length of three football fields and including terraces to seat thousands of people. No structures of similar size are found at other Indus cities. And though the acropolis of an Indus city is usually walled, Dholavira's acropolis, middle town, lower town, and a series of water tanks are surrounded by an enormous wall measuring nearly 800 meters on one side and more than 600 meters on the other.

The finds at Dholavira are part of a growing body of data that lay to rest the idea of an egalitarian or a totalitarian society. For example, although most Indus graves are modest, at Kalibangan in India the remains of an elderly man lie in a mud-brick chamber beside 70 pottery vessels. At Harappa, another elderly man shares his tomb with 340 steatite beads plus three beads of gold, one of onyx, one of banded jasper, and one of turquoise. Another high-status Harappan went to rest in an elegant coffin made of elm and cedar from the distant Himalayas and rosewood from central India.

Urban house sizes also vary much more dramatically than early excavators thought, says Wright, who works on the Harappa team. Then, as now, location was a matter of status: She notes that whereas some larger dwellings have private wells and are next to covered drains, more modest houses face open drains and cesspools.

Like elites everywhere, high-status Indus people were able to acquire high-quality goods from master craftsmen to denote their wealth. They owned finely crafted beads made in a wide variety of stone, glazed pottery called faience, and ornamentation in gold, silver, copper, lead, tin, and electrum (a gold and silver alloy). For those with less means, beaded necklaces of cheap terra cotta imitated those of semiprecious stone. Anthropologist Heather Miller of the University of Toronto in Canada and Massimo Vidale, a visiting professor at the University of Bologna in Italy, concluded in a 2001 paper that the Indus were capable of "technological virtuosity." A recent find at Harappa tentatively dated to 1700 B.C.E. may prove to be the world's oldest glass, says Kenoyer.

Such goods are found across the region, including at newly discovered cities. For example, recent excavations at Rakhigarhi, 340 kilometers southeast of Harappa in rural India, turned up a bronze vessel decorated in gold and silver along with a foundry containing thousands of semiprecious stones, demonstrating extensive craft production and bolstering the notion of an elite. At another new site called Ganweriwala, deep in the desert region south of Harappa, preliminary fieldwork by Farzand Masih of Punjab University in Pakistan has yielded finely made shell bangles and a variety of agate, terra cotta, and steatite beads.

Yet despite the trappings of wealth for some, there is little evidence of the vast divide that separated pharaoh from field hand in Egypt. "This was an enormously innovative civilization," says Michael Jansen of RWTH Aachen University in Germany. "Rather than spend their time on monuments as in Egypt, they built practical things that benefited the inhabitants."

The newly discovered cities also reveal a surprisingly diverse urban life. Rakhigarhi contains the usual Indus amenities—paved streets, brick-lined drains, orderly planning—that are conspicuously lacking in the current town that covers the highest mound. But instead of following a grid, the ancient streets radiate from the city's east gate. As at Harappa, there is evidence of settlement centuries before the urban explosion rather than the clean-slate approach typical of other Indus cities. Dholavira has its own peculiarities, including large amounts of dressed stone from a local quarry in addition to the standard baked or

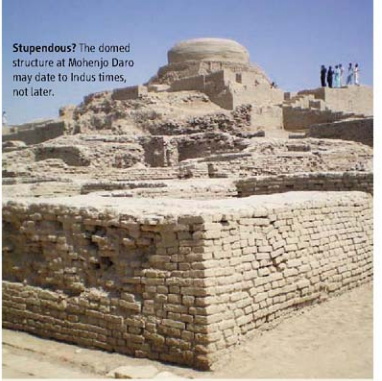

Stupendous? The domed structure at Mohenjo Daro may date to Indus times, not later.

BUDDHIST STUPA OR INDUS TEMPLE?

MOHENJO DARO, PAKISTAN—On the highest mound here rises a ruined dome—the most dramatic structure in the center of the largest Indus city, set in a courtyard once surrounded by buildings. But since the 1920s, archaeologists have considered the dome to be a much later Buddhist stupa ringed by cells of monks, built using Indus bricks 2 millennia after the city's demise. Now, University of Naples archaeologist Giovanni Verardi says that this magnificent structure may actually be a monument from Indus times. If he's right, it will force Indus scholars to rethink the religious and political nature of the civilization, long thought to lack grand temples and palaces (see main text).

The original excavators assumed the dome was Buddhist in large part because buried coins dating to the Kushan Empire of the 2nd and 3rd century C.E. were found at the site. They did note that the stupa was not aligned in typical fashion, that the plinth was of unusual height, and that certain pottery shards predated the Kushan. Verardi, who carefully examined both the site and the original archaeological reports, argues that the coins likely were buried later and therefore are of little value in dating the structures. Based on preliminary excavation of the mound, he even theorizes that the original structure may have been a series of platforms, perhaps similar to the Ur ziggurat in Mesopotamia built around 2100 B.C., near the height of Indus urban life. Such platforms were common from Mesopotamia to Turkmenistan during that era, but none have been clearly identified in the Indus region.

Other scholars are wary of the ziggurat idea but agree that the evidence supporting a stupa is slim. "I'm quite sure Verardi is right," says Michael Jansen of RWTH Aachen University in Germany, who has worked here for years. "We did a very careful survey of the area around the citadel and found not a single Kushan shard." Jansen also notes that Buddhist monks' cells of that period are not usually arranged around a stupa. "What's needed now is careful restudy," says Jansen, who hopes to excavate at the site. After 2 decades, restoration work has at last stabilized the crumbling brick, and officials plan to reopen excavations (see p. 1284). "If it is indeed [Indus], then this will turn our interpretations upside down."

–A.L

mud brick. A 10-symbol signboard was posted on the gate leading into the citadel, an unusual use of a script typically found only on small seals or pots. Grave rites also seem diverse. At Mohenjo Daro, there is no evidence for formal burials at all. At Dholavira, Bisht found a set of tomblike chambers containing an unusual variety of grave goods such as beads and pots but no traces of skeletons; he speculates that the bodies may have been cremated.

How the Indus people viewed life after death remains elusive. And the lack of temples adds to the difficulties in understanding their overall religious beliefs. A rare clue to religious practice may have emerged from now-barren Ganweriwala, which once bloomed thanks to the ancient Ghaggar-Hakra River. In his preliminary work there last year, Masih found a seal with the figure of a person or god in a yogalike pose and an apparent devotee below; on the reverse side is Indus script. The seal is similar to others found at Mohenjo Daro and dubbed "proto-Shiva" by some for its similarity to the Hindu deity. The seal has fueled speculation that the religious traditions of the Indus lived on beyond the urban collapse of 1800 B.C.E. and helped lay the basis for Hinduism (see p. 1281). Horned figures on a variety of artifacts may depict gods, as they often do in Mesopotamia.

The frustrating lack of evidence has fueled other theories that remain tenuous. Jansen and Possehl suggest that the Indus obsession with baths, wells, and drains reveals a religious ideology based on the use of water, although other scholars are skeptical.

Masters of trade

While evidence accumulates from Indus cities, other insights are coming from beyond the region, as artifacts from Central Asia, Iraq, and Afghanistan show the long arm of Indus trade networks. Small and transportable Indus goods such as beads and pottery found their way across the Iranian plateau or by sea to Oman and Mesopotamia, and Indus seals show up in Central Asia as well as southern Iraq. An Indus trading center at Shortugai in northern Afghanistan funneled lapis to the homeland. And there is strong evidence for trade and cultural links between the Indus and cities in today's Iran as well as Mesopotamia.

Holding a pose? This rare seal may hint at the ancient origins of yoga and the Hindu god Shiva.

CREDITS: (TOP TO BOTTOM) A. LAWLER/SCIENCE; © J. M. KENOYER, COURTESY DEPT. OF ARCHAEOLOGY AND MUSEUMS, GOVERNMENT OF PAKISTAN

Textual analysis of cuneiform tablets coupled with recent excavations along the Persian Gulf also show that Indus merchants routinely plied the Arabian Sea and Persian Gulf, likely in reed boats with cotton sails. "They were major participants in commercial trade," says Bisht, who sees Dholavira and other sites along the coast as trading centers thanks to monsoon winds that allowed sailors to cross 800 kilometers of open waters speedily. "These people were aggressive traders, there is no doubt about it," adds Possehl, who has found Indus-style pottery made from Gujarat clay at a dig in Oman. Archaeologist Nilofer Shaikh, vice chancellor of Latif University, takes that assertion a step further, arguing that "the Indus people were controlling the trade. They controlled the quarries, the trade routes, and they knew where the markets were."

She points out that although Indus artifacts spread far and wide, only a small number of Mesopotamian artifacts have been found at Indus sites. Evidence suggests that some Indus merchants and diplomats lived abroad, although the trade was certainly two-way. An inscription from the late 3rd millennium B.C.E. refers to one Shu-

ilishu, an interpreter from Meluhha, reports NYU's Wright in a forthcoming book. What may be Shu-ilishu and his wife are featured on a seal wearing Mesopotamian dress. There is some evidence for a village of Indus merchants between 2114 and 2004 B.C.E. in southern Iraq. And "a man from Meluhha" knocked out someone's tooth during an altercation and was made to pay a fine, according to a cuneiform text, hinting at a life that was neither faceless nor boring.

Indus archaeologists still confront fundamental research questions, including how a far-flung array of cities adopted standardized measures. There is little or no data on how the Indus people governed themselves, what language they spoke, and whether they engaged in war. Some researchers envision a collection of city states, while others imagine regional powers that jockeyed for influence but generally cooperated. What is clear is that the organization differed from the pharaonic ways of Egypt and the rival kingdoms of Mesopotamia. "We don't need to use the models from the Near East," says Kenoyer. "What was once seen as a monolithic state was actually a highly diverse set of multiple centers of power that negotiated across a large landscape."

With barely one-tenth of the 1000-plus known Indus sites examined, archaeologists say the next frontier is the smaller sites that could reveal more about day-to-day life. That could fill in the gaps about how the Indus people worshipped, traded, and governed themselves. "There are thousands of villages," says Shinde during lunch break at the Farmana dig. "And it is our fault that we only go to the big sites." Researchers are also bringing the latest archaeological tools to bear on Indus artifacts, closely examining the origins of stone used in beadwork, the prevalence of certain animals and plants, and even the methods used in butchering. Archaeologists also recognize an urgent need to chart climate change throughout the region during the Indus era. "It's a great tragedy," says Bisht. "It is a book waiting to be read." Whatever archaeologists uncover in coming years, the revised story of the Indus civilization is sure not to be a dull read. **–ANDREW LAWLER**

Indus Collapse: The End or the Beginning of an Asian Culture?

The puzzling downfall of an ancient civilization more than 3 millennia ago sparks debate today in both scientific and political circles

While Egypt was in chaos and the Akkadian Empire in Mesopotamia collapsed in the 22nd century B.C.E., the marketplaces of Mohenjo Daro in today's Pakistan were booming. Carts pulled by water buffalo jauntily decorated in henna carried luxury goods along the city's wide, paved streets. Artisans worked lapis lazuli from distant Afghanistan into beads and shaped local steatite into delicately carved seals. Citizens drew water from one of the city's 700 wells or relaxed under the colonnades around a large brick-and-tar lined bath in the center of town.

Yet 2 centuries later, the carefully planned metropolis was abandoned, and the number of settlements on its outskirts dwindled from 86 to a mere half-dozen. The cultures of Egypt and Mesopotamia recovered in time, but not so the Indus. Mohenjo Daro and other great cities were never rebuilt, a set of sophisticated symbols was forgotten, and vibrant urban life vanished from the Indian subcontinent until much later.

This anomaly is the most puzzling and controversial issue surrounding the Indus civilization, which thrived from 2600 B.C.E. until 1900 B.C.E. (see timeline). Droughts, floods, tectonic shifts, ideological turmoil, and foreign invasions have all been invoked to explain a spectacular collapse that long appeared both sudden and total. But new research suggests that the end may not have been as dramatic or complete as scholars long assumed. Some cities lingered for up to 500 years after others were deserted, and the next wave of urbanism arose far earlier than once thought.

The rise of Hindu nationalism in today's India has thrust this scholarly debate into the political spotlight. Hindu nationalists' push to see the roots of their religion in the 5000-year-old Indus civilization creates yet another barrier between Indian archaeologists and their mostly Muslim counterparts in Pakistan (see sidebar, p. 1282). "There is no place in the world where the people and culture of the 3rd millennium B.C.E. are more important," says archaeologist Gregory Possehl of the University of Pennsylvania.

Archaeologists have theorized about the end of the Indus for decades. In the 1940s, excavator Mortimer Wheeler suggested that Aryan tribes who swept in from the northwest triggered the

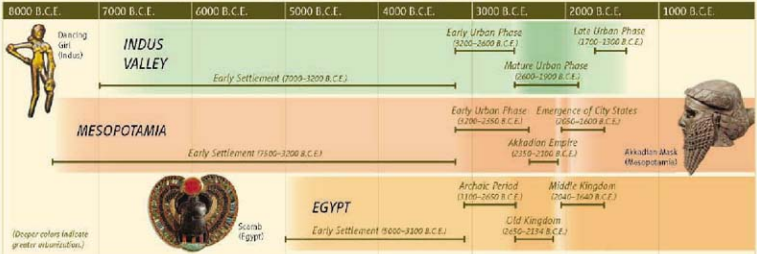

CREDITS: (LEFT) HARAPPA.COM; (BOTTOM AND RIGHT) GIANNI DAGLI ORTI/CORBIS

downfall. These Aryans were long thought to have brought Vedic culture—considered the root of Hindu tradition—to India at the expense of the Indus people. "Indra stands accused," Wheeler famously wrote, referring to the chief Aryan deity. But there is no archaeological evidence for an invasion during this period. Many scholars agree that people did migrate into the region from north and east but not until after the decline of the Indus.

More recently, some researchers have proposed that climate indirectly affected the Indus. They postulate that the drought-related collapse of Egypt and Mesopotamia and the loss of those markets at the turn of the 2nd millennium B.C.E. led to an economic crisis that upended the Indus system a century or two later. Mentions of Meluhha, presumed to refer to the Indus, vanish from Mesopotamian texts about 2000 B.C.E., says Harvard University Assyriologist Piotr Steinkeller.

Climate may have hit the Indus directly as well. According to a 2003 paper, cores drilled from the Arabian Sea indicate that during the 22nd century B.C.E., the Indus River and its tributaries discharged significantly less water, a sign of drought. By 2000 B.C.E., people near Harappa in today's Pakistan were trying to cope with a drying climate by planting different crops, according to recent research led by Rita Wright of New York University (*Science*, 18 May 2007, p. 978). "People were making adjustments; there was a change in their way of life," Wright says, although she cautions against making sweeping claims because her data are from only one region.

Although Wright and others argue that climate and society are deeply intertwined, Possehl scoffs at the idea that drought explains the collapse. "We should stop thinking about the physical world and start looking at the fabric of society," he suggests. He believes that the end of the Indus was primarily a matter of ideology, like the collapse of the Soviet Union. Possehl and Michael Jansen of RWTH Aachen University in Germany note that the Great Bath at the center of Mohenjo Daro was abandoned a century or two before the city, suggesting change in a society that they say emphasized water-related rituals.

In the end, Wright, Possehl, and other scholars acknowledge that they can't be sure what caused the Indus decline. "There are a lot of theories but little evidence," complains Harvard archaeologist Richard Meadow, who co-directs current excavations at Harappa.

Spinning wheel. Modern carts in today's Pakistan resemble toy carts (*inset*) crafted by Harappans thousands of years ago.

But the collapse was likely as varied as the civilization itself. Mohenjo Daro and the region of Cholistan, between that city and Harappa, declined dramatically after 1900 B.C.E. However, while rural settlements near Harappa contracted from 18 to four at this time, life in the city surprisingly continued for at least another 500 years, says archaeologist Jonathan Kenoyer of the University of Wisconsin, Madison, co-director of the Harappa dig. And to the northeast, in today's India, the number of sites increased rapidly from 218 to 853 after 1900 B.C.E., according to data from surveys gathered by Possehl.

In Gujarat in southwestern India, urban life and even trade with the Arabian side of the Persian Gulf appears to have continued well

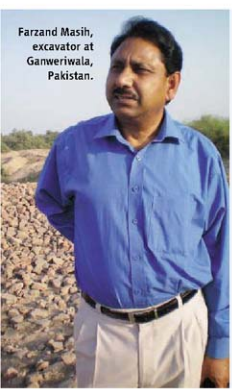

Farzand Masih, excavator at Ganweriwala, Pakistan.

TRENCH WARFARE: MODERN BORDERS SPLIT THE INDUS

FARMANA, INDIA—Vasant Shinde and Farzand Masih work a mere 200 kilometers apart, each perhaps an hour or so from the border between India and Pakistan. But neither archaeologist can visit the site of the other. "I'm excavating at Farmana," says Shinde of Deccan College in Pune, India. "On the other side is Ganweriwala—but I can't know what's going on there or talk to the archaeology team." Masih of Punjab University in Lahore, Pakistan, leads that team and says he's eager for international collaboration, but for now including Indians is beyond his power. Nor can he visit Shinde's site.

That's because the fault line resulting from the bitter partition of British India in 1947 runs through the middle of what was once the Indus civilization, one of the world's first great urban societies from 2600 B.C.E. to its puzzling collapse in about 1800 B.C.E. (see main text). Back then, Indus merchants may have traveled freely over the region's plains and hills. But today the Indus's 1 million square kilometers are split between Pakistan and western India (see map, p. 1278). The cities of Mohenjo Daro, Harappa, and Ganweriwala are in Pakistan, while Dholavira, Rakhigarhi, and Farmana lie just across the border in India. Hundreds of other settlements are spread across the Indus plain in one nation or the other.

Each country has fought serious skirmishes in the Himalaya, built nuclear weapons with their adversary in mind, and laid claim to the Indian state of Kashmir. The politics make it difficult if not impossible for archaeologists from one side to roam the countryside of the other. "Secret police would follow us every step—if we could get a visa," says one South Asian archaeologist.

Scientists on both sides say that a host of research topics would make more sense if done collaboratively. For example, understanding the complex geomorphology of the Indus and its

CREDITS: (TOP TO BOTTOM): A. LAWLER/SCIENCE; © J. M. KENOYER, COURTESY DEPT. OF ARCHAEOLOGY AND MUSEUMS, GOVERNMENT OF PAKISTAN; A. LAWLER/SCIENCE

into the 2nd millennium B.C.E., although exactly how long is a matter of dispute. At the site of Pirak in eastern Baluchistan in today's Pakistan, a small town appears to have thrived continuously from 1800 B.C.E. to as late as the arrival of Alexander the Great in India in 325 B.C.E., says Meadow. Later settlements, however, lack the sophisticated urban planning of even smaller sites from the mature Indus phase.

The persistence of settlements raises the question of how much of the Indus culture survived the urban decline. For decades, most archaeologists assumed that the Indus's abrupt end and long hiatus in urban life meant that few if any of its traditions survived. But now it appears that the Indus collapse drove people to the east, into the watershed of the Ganges, which spreads as far as the Bay of Bengal. Excavations along the Gangetic plain show that cities began to arise there starting about 1200 B.C.E., just a few centuries after Harappa was deserted and much earlier than once suspected. That means that some continuity between the first and second wave of Indian civilization is conceivable, says Possehl.

Climate chronicler. Rita Wright tracks the Indus response to drought around Harappa.

There is no doubt that the hallmarks of the Indus disappeared with its cities, including its unique set of specific symbols, sophisticated standardization of weights and bricks, and rectilinear urban planning. Later urban areas along the Ganges are radically different in layout; the new writing system that eventually emerged is unrelated to Indus symbols; and standardization is missing.

But archaeologists such as Possehl see deeper connections. "There is continuity," he says. A handful of Indus seals showing a deity with three faces in a yogic-style posture may link today's Hindu god Shiva and yoga practices with the Indus civilization. And a variety of technologies and traditions, such as tandoori ovens, oxcarts pulled by water buffalo, and cattle marked with henna are a regular part of village life around Mohenjo Daro even today. Traces of all these scenes can be found at Indus archaeological sites and imprinted upon seals.

Did the Indus directly seed what eventually grew into the second wave of Indian civilization? That is a hot political as well as scholarly topic. "This plays a significant role in today's India," says Possehl. The Bharatiya Janata Party (BJP), which ruled India from 1998 to 2004, declared the Indus to be the progenitor of Hindu civilization, a controversial claim in a country with a large Muslim population. While in power, BJP pumped additional funding into Indus-related digs, and its influence over archaeological matters remains strong. Last fall, the Archaeological Survey of India (ASI) was harshly criticized in Parliament for asserting in a report that the underwater ridge connecting India and Sri Lanka was natural rather than the remains of a bridge built by the traditional hero Rama. Under pressure, ASI suspended two senior employees involved in the report. In May, members of India's Supreme Court expressed sympathy for a lower court decision ordering ASI to investigate the formation.

Some Indian scholars argue that early Hindu texts can be used as guides, much as the Bible has been used in Near Eastern archaeology. Respected ASI archaeologist R. S. Bisht, who excavated Dholavira and can quote long passages from Hindu scripture, suggests that the Indus people were one and the same as the Aryans whom Wheeler saw as invaders. That theory finds little purchase with foreign scholars. And one Western archaeologist complains that such talk makes for a volatile mix of science and religion that is "needlessly inflammatory to our Pakistani colleagues."

The intense emotion surrounding the debate is exacerbated by the many questions that remain about the Indus's decline. "There is no silver bullet; there were clearly multiple factors," says Meadow. "And we still don't know what was the trigger." But, he says, recognizing that complexity is itself a big step forward.

–ANDREW LAWLER

tributaries can't be done without cross-border studies. Comprehensive analyses of ancient climate require regional sampling. And because the research communities are so divided, discoveries in one country may go unnoticed in the other; archaeologists say they have little knowledge of what takes place across the border. Given the lack of published papers and personal connections, even digital and virtual collaboration is rare.

Foreigners can make the trip between the two countries with relative ease, and a few European, Japanese, and American researchers frequently work on both sides. But archaeologists from India and Pakistan have only rare and fleeting opportunities to meet, such as at international conferences. "We need to be able to put together all the pieces," says Qasid Mallah, a professor at Shah Abdul Latif University in Khairpur, Pakistan. "That includes the Indian portion too." Adds Shinde: "It would be more beneficial if we could all work in both India and Pakistan, particularly for the students."

Politicians and administrators in both countries have shown little interest in using archaeology as a tool for détente. The director general of the Archaeological Survey of India, Anshu Vaish, says her organization has no plans to push for more cooperation. And the recent elections in Pakistan, which resulted in an uneasy coalition, make dramatic initiatives from that side unlikely.

To circumvent the political reality, Shinde helped create the Society of South Asian Archaeologists in 2005. Most Indian and Pakistani archaeologists couldn't afford to go to international conferences, so he proposed a new organization—registered under the Indian government but classed as a private group—to hold meetings closer to home. For the first conference in Mumbai in 2006, a few Pakistanis secured visas, although others did not. The second meeting was held 25 to 27 May in Shiraz, Iran, on neutral ground, and the next gathering is to be held in Sri Lanka in 2010. Shinde says that despite growing pains, the group now has 400 members from six countries. In the meantime, he and Masih will go about their respective business, so close, and yet so far. **–A.L.**

Vasant Shinde, excavator at Farmana, India.

CREDITS: (TOP TO BOTTOM) SUSAN WRIGHT; A. LAWLER/SCIENCE

Rescue squad. A Latif University team digs at Lakhanjo Daro, a site now largely destroyed.

Trying to Make Way for the Old

Archaeologists battle looters and sometimes locals in both Pakistan and India as they seek to excavate before modern development swallows Indus cities

SUKKUR, PAKISTAN—It's dusk in a grim industrial area on the outskirts of this southern Pakistani city, and archaeologist Qasid Mallah of Shah Abdul Latif University in Khairpur stands in a vacant lot, full of anger and dismay. "This is the murder of heritage," he says bitterly, gesturing at the metal rebar sprouting from recently dug trenches. "In spite of all our efforts, this will be gone." Just a few months ago, the construction site was a barren field containing some of the last remains of a 5000-year-old city known as Lakhanjo Daro. Now, even this last patch is threatened by development; the work is a harbinger of yet another factory.

Destroying ancient sites to make way for the new is old business here. In the 1860s, before the Indus city of Harappa was even excavated, British engineers seized thousands of baked bricks to build a railway bed and passenger stations. Only later did archaeologists recognize the site as one of the premier metropolises of an ancient civilization. But the threat to what remains of the Indus comes not just from development. Rakhigarhi, a recently excavated site in western India, supports a lively trade in looted antiquities. And at Mohenjo Daro in Pakistan, where scientists have recently managed to stop water-related destruction, thieves brazenly raided the site museum in 2002. Such varied dangers threaten the heritage of both countries and pose yet another challenge for Pakistan's struggling archaeological community (see sidebar, p. 1285).

Despite its large size, Lakhanjo Daro wasn't even recognized as an Indus site until the 1980s, when local students brought material to Latif in nearby Khairpur. The Indus River squeezes through the stony Rohri Hills here, making the location a strategic center. The area around Lakhanjo Daro was set aside for industrial development in the 1980s, when the population surged above 500,000; it is now at 1.8 million.

When government officials moved to protect the area, local developers used political connections and lawsuits to oppose the move. So Latif archaeologist and current Vice Chancellor Nilofer Shaikh compromised by setting aside specific vacant lots. "I had to demark some limits, or we would not have gotten anything," Shaikh says. A Latif team, including Shaikh and Mallah, spent four seasons from 1994 to 2006 probing five mounds as factories sprang up around them, uncovering shell bangles, terra cotta animal figurines, and a rare copper spearhead along with the rectilinear architecture and pottery typical of an Indus site. Now construction is encroaching on even those remaining lots.

The researchers have only hints of what is being lost to development. Climbing through thorny brush in a nearby ravine, Mallah points his flashlight at a dressed limestone block—an unusual feature for an Indus site—alongside Indus-style bricks. "This city could have been 1 square kilometer in size, or even larger," he says. "But it is going fast." He says further excavation is unlikely, given how disturbed the area is now.

Fifty kilometers to the southwest, the largest of Indus cities, Mohenjo Daro, confronts a different set of problems. In 1980, the year it was named a World Heritage Site, a United Nations report warned that the city was "in danger of total destruction" due to rising water levels. UNESCO began a massive project to divert the Indus River and drain water from the site, involving more than 50 costly water pumps and later a series of canals. But high soil moisture continued to draw out salts that ate away at the brick foundations. Officials spent years arguing over what to do. In the meantime, new digs at the site—less than 10% of which has been excavated—were banned.

Researchers eventually discovered that the soil moisture was due primarily to cold, humid air during the winter. The pumps were turned off in 2003, and workers put a thin layer of clay over the original bricks. Now when salt crystallizes in the heavy dews of winter, it eats away this layer instead. "I'm extremely happy; the site is very stable," says Michael Jansen, a member of the UNESCO team and an archaeologist at RWTH Aachen University in Germany, who visited the site in March. "It is the first time in 20 years that there's not a newly endangered wall." Pakistan's director general for archaeology, Fazal Dad Kakar, says he intends to lift the ban on excavations now that the crisis is over.

But expanding villages pose a new threat. While diverting water from the site in the late 1980s, workers uncovered evidence of Indus-era buildings 1.5 kilometers from the city center. And throughout the area, workers digging wells have found Indus-era bricks, suggesting a city potentially twice as large as the 150 hectares long estimated. "Mohenjo Daro is far larger than we anticipated," says Jansen. "If the city is 300 hectares in size, it is enormous, comparable to Ur" at the same period in Mesopotamia. Archaeologists from UNESCO, Pakistan, and other countries hope to begin a series of test drills to determine the city's extent, but the project has been hampered by lack of funding and repeated bureaucratic delays.

Hidden treasure. Wazir Chand Saroae, with Indus figurine, says looting continues at Rakhigarhi.

The site faces an even more complex challenge from lawlessness. In 2002, thieves were bold enough to steal 40 seals and copper tablets from the Mohenjo Daro museum, where a sign now warns that "Weapons are not allowed in the museum." A curator says the site is not fenced and admits that there is "some looting." Although a relatively peaceful area,

CREDITS: (TOP TO BOTTOM) LATIF UNIVERSITY; A. LAWLER/SCIENCE

PAKISTANI ARCHAEOLOGY FACES ISSUES OLD AND NEW

KHAIRPUR, PAKISTAN—Ghulam Mohiuddin Veesar doesn't have to commute to find remains of the past. Just a short walk beyond his mud-brick village in southeastern Pakistan rises a small mound covered with stone tools, pottery shards, and the occasional shell bead fashionable during the glory days of the Indus civilization. A 47-year-old archaeologist at nearby Shah Abdul Latif University, the quiet and wiry Veesar has led Pakistani and Italian colleagues to hundreds of ancient sites here on the edge of the rugged Thar Desert, without needing global positioning systems, survey maps, or other tools. This is home turf. As a teenager, he rode his motorcycle up and down these sand dunes.

The finds are opening a new window on the Indus civilization, showing that this remote region was settled for thousands of years. Veesar's Latif colleague and friend Qasid Mallah argues that the enormous variety of sites offers a rich opportunity to understand the Indus hinterland. What's needed, Mallah says, are massive surveys and pinpointed excavations, as well as a way to protect sites from development and looting (see main text). Given the size of the area and its harsh terrain, "it's really a huge task," Mallah says. With support from their vice chancellor Nilofer Shaikh, herself an Indus archaeologist, they have begun the job and hope to lure foreign archaeologists to assist. "Tell people to come and research," Mallah says. "Everyone is welcome."

The optimism and enthusiasm at Latif, a growing rural university that is 2 decades old, is one of a few bright spots for archaeology in Pakistan. The University of the Punjab in Lahore, the country's largest, recently organized its first archaeology department, and a scattering of other universities conduct excavations, mostly working with foreign teams. But Pakistan has long been hampered by loss of expertise when the country was created in 1947 and severed ties with the Archaeological Survey of India. "We had to start from scratch," says Anjum Javaid, assistant curator at the Lahore Fort in the northern city of Lahore.

Now Pakistani researchers face new problems. "We get peanuts for excavations, we're losing all our experienced archaeologists, and the new generation is not getting trained," frets Javaid. Most recently, Pakistan's provinces have been pressuring the federal government in Islamabad to abolish national control over archaeological sites. Javaid fears this could lead to abolition of the central archaeology department, which would likely diminish the budget and authority of archaeologists and make it more difficult to protect sites, he says.

Already, there are tight constraints on where archaeologists can operate. Most foreign researchers steer clear of the country at the moment. And some areas rich in sites—such as Baluchistan to the west and the North-West Frontier Province—are off-limits to both Pakistani and foreign excavators. But here in Sindh province and in other areas in the east, the countryside remains relatively peaceful. Whether or not foreigners come, Veesar says he will continue to seek new sites to catalog and dig in the Thar Desert, rattling over high sand dunes in an old jeep with Mallah. "This is not only our heritage, it's the world's," he says. **–A.L.**

Nomad's land. Ghulam Veesar (*right*) consults with a local shepherd in the Thar Desert.

CREDIT: A. LAWLER/SCIENCE

local officials say bandits and the occasional terrorist make roads unsafe after nightfall.

At Harappa, nearly 600 kilometers to the north, the problems are more prosaic but just as challenging. Local villagers own half the land area of the sprawling ancient city and are loath to be bought out by the government. They have begun to turn part of the land into a cemetery, and a mosque built 5 centuries ago with Indus brick sits on a prominent spur of the ancient city. Those areas will remain off-limits to archaeologists. "When it comes to religion, people get emotional," says Aasim Dogar, who directs the site. Passing by the mosque, an old man shouts an epithet at Dogar, who grumbles in reply—a sign of the contentious relationship between officials and locals. But Dogar is optimistic the deal will be closed soon, allowing a fence to be put in place to protect the mounds.

Across the border in India, villagers are similarly resentful of archaeologists. Half of the large Indus city of Rakhigarhi is in the hands of private owners, and the town covers several of the largest mounds. Excavations by the Archaeological Survey of India (ASI) began in 1997 but ground to a halt in 2000, partly because of disputes with inhabitants. "The villagers are afraid that the government will grab their land," says Tejas Garge, who worked as a graduate student for ASI excavating at the site. He recalls village women throwing stones at him: "It was horrible. At one point, a dozen villagers came with sticks and ordered us to stop." The team eventually abandoned their effort. Fences are going up around unoccupied mounds, and one senior ASI official says the goal is to buy out the locals and remove the village. "Only then can you dig," he says, adding that the bureaucratic and financial obstacles to doing so are huge.

Meanwhile, archaeologists say there has been extensive looting here over the years; according to one recent rumor, a villager found and sold 30 Indus seals. That traffic has almost stopped, insists the site's lone guard. But local schoolteacher Wazir Chand Saroae disagrees. In his modest home nearby, he shows off an impressive array of pots, bangles, ivory and lapis lazuli beads, and animal figurines carefully wrapped in newspaper and numbered according to his own archival system. Saroae is an outspoken advocate for site protection and says he does not sell his finds. "The situation has not improved much," he says ruefully. "Villagers are still digging, and the single watchman is not effective over such a large area."

Some archaeologists call for tougher penalties for looting, but others say the key is to educate the population. "At least one man in the village has developed a passion for this," Garge says optimistically as he leaves Saroae's home. Just a few meters away, he points out a 17-meter-high cliff studded with 5000-year-old potsherds and bricks; an ancient mound has been sliced away for a village road. Pigeons are busy roosting, digging holes into the layers. But the site is owned by villagers and so strictly off-limits to the spades of archaeologists.

–ANDREW LAWLER

LETTERS

edited by Jennifer Sills

Working Toward Meritocracy in Italy

I READ WITH ANGUISH THE "OPEN LETTER TO SENATOR RITA LEVI-Montalcini" by R. Clementi *et al.* (21 March, p. 1615), which was signed by 776 Italian researchers holding temporary contracts, lamenting the lack of stability and meritocracy. As a researcher, clinician, and academician who has worked under different systems in Italy and abroad, I share their concerns. I am fully aware of the heavy limitations of the Italian system. However, as the past Chair of the Health Committee of the Italian Senate, I must take exception to their statement that the left-wing government's intent never went beyond mere words. In my capacity as Senator, I have promoted measures that enhance transparency and meritocracy in the selection of projects and that allocate dedicated resources to young investigators. The 2007 national budget law allocated €15 million to projects submitted by biomedical researchers under 40 years of age. The projects are to be selected by an international committee composed of scientists who are also under 40, and who will judge the proposals strictly on their merits. Another measure, inserted in the 2008 national budget law, designates €81 million to projects presented, again, by researchers under 40 in all areas of intellectual endeavor.


The Italian Senate

True, in spite of the above-mentioned total of €96 million, Italy is still behind in research investment. We invest only 1.1% of the GDP in research, less than the average 2% for Europe, which already compares poorly with the 2.7% for the United States and over 3% for Japan.

Without minimizing the rightful complaint of the Italian researchers, I do not believe that the correct way to proceed is to hire everyone who is currently working with temporary contracts, but to start applying the rules of peer review consistently. By evaluating only on the basis of merit, we will give dignity to valuable scientists, and we will promote the intellectual, economic, and cultural growth of Italy.

IGNAZIO R. MARINO

Jefferson Medical College, Philadelphia, PA 19107, USA.

The Emerging World of Wikis

WE NOTED WITH INTEREST THE LETTER "Preserving accuracy in GenBank," (M. I. Bidartondo *et al.*, 21 March, p. 1616) and the related News of the Week story "Proposal to 'wikify' GenBank meets stiff resistance" (E. Pennisi, 21 March, p. 1598). David Lipman's fears that wikifying GenBank "would be chaos" are widely shared, but those fears should be balanced by the realization that individual curators cannot fully encompass the collective expertise of the larger scientific community. Serious users of GenBank use it as a starting point for in-depth analysis with new bioinformatic tools and reviews of more recent work. These users often learn more about the data than the initial depositors or curation staff. This valuable information—hidden in notebooks and rarely published—is being lost to future researchers. A parallel wiki-based structure provides one way of capturing these data.

We are working on such systems, including EcoliWiki (*1*), the community annotation component of EcoliHub (*2*), and a Gene Ontology Normal Usage Tracking System (GONUTS) (*3*), a browser and annotation system for Gene Ontology (*4*). We regard these and similar efforts (*5*–*8*) as experiments to test wiki-based curation. So far, the challenge is not chaos but lack of participation. Thus, we are also experimenting with curation by undergraduates supervised by an experienced scientist. Integrating annotation and genomics education leverages how we teach critical thinking about the literature, accelerates the pace of curation, and provides institutional incentives for established scientists to participate.

Nevertheless, we understand that changing the GenBank model should not be done lightly. There are well-established expectations about GenBank, and wikifying it could be quite disruptive. Perhaps GenBank could support an arm's length relationship to wikis via the LinkOut service. We look forward to ongoing discussion of how community curation could be added to GenBank. In the meantime, we encourage the 250 scientists who signed the Bidartondo *et al.* letter to help us build wiki-based fungal curation via GO at GONUTS.

JAMES C. HU,[1] RODOLFO ARAMAYO,[2] DAN BOLSER,[3] TYRRELL CONWAY,[4] CHRISTINE G. ELSIK,[5] MICHAEL GRIBSKOV,[6] THOMAS KELDER,[7] DAISUKE KIHARA,[6,8] THOMAS F. KNIGHT JR.,[9] ALEXANDER R. PICO,[10] DEBORAH A. SIEGELE,[2] BARRY L. WANNER,[4] ROY D. WELCH[11]

[1]Department of Biochemistry and Biophysics, Texas A&M University, College Station, TX 77843–2128, USA. [2]Department of Biology, Texas A&M University, College Station, TX 77843–3258, USA. [3]The BioFoundation, 52 Eoeun-dong, Yuseong-gu, Daejeon, 305-333, Korea. [4]Advanced Center for Genome Technology, University of Oklahoma, Norman, OK 73019, USA. [5]Department of Biology, Georgetown University, Washington, DC 20057, USA. [6]Department of Biological Sciences, Purdue

University, West Lafayette, IN 47907–2054, USA. [7]BiGCaT Bioinformatics, Maastricht University, Maastricht, 6229 ER, Netherlands. [8]Department of Computer Science, Purdue University, West Lafayette, IN 47907, USA. [9]Computer Science and Artificial Intelligence Laboratory 32-312, Massachusetts Institute of Technology, Cambridge, MA 02139, USA. [10]Gladstone Institute of Cardiovascular Disease, San Francisco, CA 94158, USA. [11]Department of Biology, Syracuse University, Syracuse, NY 13244, USA.

References

1. Ecoliwiki (http://ecoliwiki.net).
2. Ecolihub (http://ecolihub.org).
3. GONUTS (http://gowiki.tamu.edu).
4. M. Ashburner *et al.*, *Nat. Genet.* **25**, 25 (2000).
5. S. Mathivanan *et al.*, *Nat. Biotechnol.* **26**, 164 (2008).
6. B. L. Ashinoff *et al.*, *Nucleic Acids Res.* **35**, D422 (2007).
7. Wikipathways (www.wikipathways.org).
8. PDBWiki, a community-annotated knowledge base of biological molecular structures (http://PDBWiki.org).

Science 2.0: Not So New?

B. SHNEIDERMAN'S PERSPECTIVE, "SCIENCE 2.0" (7 March, p. 1349), is quite right to identify the value of new observations of human interaction made possible by the advent of the Internet. However, Shneiderman's assertion that these data require some radically new methodology, which he calls "Science 2.0," is apparently based on a misunderstanding of the scope of existing scientific methods.

Shneiderman says that Science 2.0 will address questions of human interaction that "cannot be studied adequately in laboratory conditions," because "the interaction among variables undermines the validity of reductionist methods." Instead, data for analysis must be "collected in real settings." This sounds exactly like approaches that are already practiced, with great success, by researchers in the fields of (to name but a few) ecology, evolutionary biology, geology, paleontology, economics, cosmology, and social science.

Indeed, what Shneiderman calls Science 1.0 has always included methods beyond simple controlled experiments, such as inference from observation of integrated natural systems and the careful use of "natural experiments" (*1*) to test and eliminate competing hypotheses.

JEREMY B. YODER

Department of Biological Sciences, University of Idaho, Moscow, ID 83844–3051, USA.

Reference

1. J. Diamond, *Science* **294**, 1847 (2001).

Letters to the Editor

Letters (~300 words) discuss material published in *Science* in the previous 3 months or issues of general interest. They can be submitted through the Web (www.submit2science.org) or by regular mail (1200 New York Ave., NW, Washington, DC 20005, USA). Letters are not acknowledged upon receipt, nor are authors generally consulted before publication. Whether published in full or in part, letters are subject to editing for clarity and space.

Response

I AGREE THAT THE NATURAL SCIENCES ARE based on more than just replicable, controlled laboratory experimental studies, and that observational methods play a key role in the natural and social sciences (*1*). However, the interventional methods as practiced in design science studies of sociotechnical systems have novel elements. In addition to "natural experiments," such as when the FaceBook managers change the deletion rules or eBay administrators update their fraud control mechanisms, I was advocating research-oriented interventions to develop predictive models.

Amazon and NetFlix designers conduct many studies to improve their user interfaces

by making changes in a fraction of accounts to measure how user behaviors change. Their goal is to improve business practices, but similar interventional studies on a massive scale could develop better understanding of human collaboration in the designed (as opposed to natural) world (*2*). For example, studies of the impact of Web-based enrollment procedures on trust and perceived privacy could facilitate more effective online health care. Developing better models of recognition and reward structures in open-source software, scientific collaboratories, or museum and library annotation projects could accelerate the adoption of these productive mechanisms. Understanding how to increase the motivation of residents to report crime, health problems, or natural disasters and then provide resident-to-resident assistance could improve community safety.

Observations of natural experiments will be important, but my point was that Science 2.0 researchers can also intervene in massive computer-mediated sociotechnical systems to measure impacts in ways that astronomers or geologists cannot. I suggest that if we, as a society, made major commitments to support these new research directions, many of our civic institutions could be dramatically improved.

BEN SHNEIDERMAN

Department of Computer Science, University of Maryland, College Park, MD 20742, USA.

References

1. J. Hatton, P. B. Plouffe, *Science and its Ways of Knowing* (Prentice-Hall, Upper Saddle River, NJ, 1997).
2. J. Horgan, *The End of Science: Facing the Limits of Knowledge in the Twilight of the Scientific Age* (Broadway Books, New York, 1997).

TECHNICAL COMMENT ABSTRACTS

COMMENT ON "Intermittent Plate Tectonics?"

Jun Korenaga

Silver and Behn (Reports, 4 January 2008, p. 85) proposed that intermittent plate tectonics may resolve a long-standing paradox in Earth's thermal evolution. However, their analysis misses one important term, which subsequently brings their main conclusion into question. In addition, the Phanerozoic eustasy record indicates that the claimed effect of intermittency is probably weak.

Full text at www.sciencemag.org/cgi/content/full/320/5881/1291a

RESPONSE TO COMMENT ON "Intermittent Plate Tectonics?"

Paul G. Silver and Mark D. Behn

Korenaga takes issue with our proposal that intermittent plate tectonics provides a solution to the thermal catastrophe paradox, arguing that the heat flux in the absence of plate tectonics is too high. We show that this flux is small enough and changes rapidly enough in response to variations in slab flux to produce a reasonable thermal history back to at least 3 billion years ago.

Full text at www.sciencemag.org/cgi/content/full/320/5881/1291b

CORRECTIONS AND CLARIFICATIONS

News of the Week: "New superconductors propel Chinese physicists to forefront" by A. Cho (25 April, p. 432). In the figure labeled "Temperature records for new compounds," subscripts for oxygen and fluorine in the chemical formulas were reversed. Instead of O_xF_{1-x}, the four formulas should read $O_{1-x}F_x$.

News of the Week: "When hobbits (slowly) walked the earth" by E. Culotta (25 April, p. 433). Arizona State University is in Tempe, not Tucson.

News of the Week: "IPCC tunes up for its next report aiming for better, timely results" by E. Kintisch (18 April, p. 300). Susan Solomon was incorrectly identified in the story. She is a senior scientist with the National Oceanic and Atmospheric Administration's Earth System Research Laboratory in Boulder, Colorado, and was co-chair of the IPCC's Working Group I.

STATISTICS AND SOCIETY

Signifying Little

Theodore M. Porter

"Repent," we are commanded in the conclusion to *The Cult of Statistical Significance*. "Sell all your goods and come with us." From Karl Pearson's "Saint Biometrika" at the beginning of the 20th century to the gospel according to Ronald A. Fisher, the cool, technical reason of statistics has also inspired messianic anticipations, and Stephen Ziliak and Deirdre McCloskey are only partly joking when they propose that we can enter the promised land of effective science only by rejecting Fisher's methods. The "standard error" of their title—the one that costs us jobs, justice, and lives—is the confusion of statistical with substantive significance. The authors do not claim much originality in recognizing this as an error; they list and discuss a distinguished roster of predecessors in statistics, philosophy, and the sciences who have called attention to it. And yet somehow the error persists, across a wide range of disciplines including some—such as pharmaceutical regulation, econometrics, and education studies—that feed directly into policy. The book was written to shake us out of our lazy habit of treating significance levels as an almost automatic criterion of scientific and practical worth.

The Cult of Statistical Significance
How the Standard Error Costs Us Jobs, Justice, and Lives

by Stephen T. Ziliak and Deirdre N. McCloskey

University of Michigan Press, Ann Arbor, 2008. 348 pp. $75, £48.95. ISBN 9780472070077. Paper, $24.95, £16.50. ISBN 9780472050079. Economics, Cognition, and Society.

If not Fisherian significance, what should be the Holy Grail of statistics? Ziliak and McCloskey (economists at, respectively, Roosevelt University and the University of Illinois at Chicago) answer: "Oomph." We should identify quantities that matter and measure them, not merely determine whether they can be distinguished from the null (meaning no effect) at some predetermined likelihood level. The validity of this point I take to be virtually self-evident. Yet statistical tests that ignore quantity remain pervasive, as the authors demonstrate through quantitative analyses of the contents of some very prestigious journals of economics, psychology, and medicine.

Of course, effective measurement requires in addition evidence as to the accuracy of the measure. The authors are not much interested in this aspect of the problem (the estimation of statistical error), and perhaps they are too willing to advise acting on the basis of inferred causal relations that, if assessed in a Fisherian way, admit serious doubt as to their very existence. At a minimum, it will normally be advisable to continue investigating when the evidence suggests, even tentatively, that a new drug causes suicides or a social program to help people find work saves three times what it costs. The book's inattention to sampling error may perhaps be forgiven as a corrective to the usual preoccupation with it.

Fisher and his disciples, I would agree, have a lot to answer for. But Ziliak and McCloskey also take some cheap shots, blaming Fisher for transgressions by medical and social researchers that he did not endorse and would not have countenanced. The most blatant of these is the supposition that a failure to demonstrate statistical significance licenses the assumption that an effect or causal relation does not exist. Ziliak and McCloskey show how often this move is made by economists running regressions and medical researchers analyzing experiments. But we should consider the following example, the main support for the assertion in the book's title that confusion about significance "costs us … lives." In a clinical trial of Vioxx in 2000, five experimental patients suffered heart attacks, compared to only one in the control group. The different did not rise to statistical significance at the 5% level, and on that basis the researchers declared there was no danger. Is this dubious reasoning to be blamed on the Fisherian statisticians? Not really. The sins of pharmaceutical trials are legion, as is now amply documented, and in this case the work was done and the paper written by Merck, which subsequently recruited phantom authors at universities willing to attach their names to the publication. Ziliak and McCloskey point out that Merck had already suppressed other data implying the riskiness of Vioxx. Most of the really harmful abuses chronicled in the rather overblown first 40 pages of this book involve statistical maneuvers that are illegitimate even by the standards of Fisher's program. We can better explain the Vioxx episode in terms of a corrupt research program than of flawed statistical tools.

The defects of Fisherian theory, it is clear, were made much worse in the practices of social and medical researchers as these were institutionalized from about 1930 to 1960. Most of the problems arose from an effort to set up inferential statistics as a set of recipes that could obviate any need for good sense of judgment. Ziliak and McCloskey argue that anxieties about subjectivity in the social and medical sciences encouraged reliance on such "magic pills." In my view, this quest for mechanized objectivity is typical of the modern adaptation of science to the state, which generally places scientists in a subordinate position when public decisions are at issue and demands of them, above all, rigorous impersonality and value-neutrality.

The book connects its statistical claims with a dubious morality tale. Even if William Sealy Gosset (who studied statistics in Karl Pearson's laboratory and worked out the basics of the *t* test) was as saintly as he is portrayed here, we might doubt the strongly implied link between his moral goodness and the correctness of his statistical program. On the chief point in question, the value of measuring effects rather than merely controlling error, he does not appear to me to be very different from that famously difficult personality and committed eugenicist—and effective founder of the 20th-century mathematical field of statistics—Pearson.

"Student" of the *t* test. William Sealy Gosset.

CREDIT: COURTESY THE GALTON LABORATORY, UNIVERSITY COLLEGE LONDON

The authors' hagiography of Gosset is counterpointed by a demonology of Fisher. Fisher's unattractive eugenic politics, refusal to give credit to colleagues and predecessors, and personal cruelty may also be genuine, but can these explain the misdirection of his statistical program? A shift in statistical practice from detecting effects to measuring them and assessing their consequences would be good for science, but it may not hasten the millennium.

10.1126/science.1160305

The reviewer is at the Department of History, 6265 Bunche Hall, Box 951473, University of California, Los Angeles, Los Angeles, CA 90095-1473, USA. E-mail: tporter@history.ucla.edu

PSYCHOLOGY

Piling On the Selection Pressure

Johan J. Bolhuis

As we approach the 150th anniversary of the publication of *On the Origin of Species*, the theory of evolution is still not without controversy in the popular domain. But it is generally considered one of the most important intellectual achievements of the modern age. It therefore seems logical to extend the theory to cognition, as Darwin himself did in *The Descent of Man* when he considered human characteristics such as morality or emotions to have been evolved. Evolutionary psychology aims to do just that: applying evolutionary theory to the human mind. Specifically, it proposes that the mind consists of cognitive modules that evolved in response to selection pressures faced by our Stone Age ancestors. The approach has a wide popular appeal, perhaps because it often addresses such exciting topics as human desire, sex, and passion.

Early in the introductory chapter of *Evolutionary Psychology as Maladapted Psychology*, Robert Richardson readily acknowledges that "[o]ur psychological capacities are evolved traits," subject to natural selection. But at the same time, he maintains that there is very little we can find out about the evolution of the mind and that the evolutionary psychology interpretation is wrong from the perspective of evolutionary biology. Richardson, a philosopher at the University of Cincinnati, is not the first to add to the selection pressure on this fledgling psychological discipline. The merit of his critique is that it is not polemic in the way those of some of his fellow critics (such as Jerry Fodor or Stephen Jay Gould) have been. Rather, Richardson wants to evaluate evolutionary psychology strictly on scientific grounds.

This approach is reminiscent of that taken by David Buller in *Adapting Minds* (*1*). Richardson often refers to his predecessor, and there are many similarities between the two authors. For a start, both are philosophers rather than psychologists or evolutionary biologists. Also, both are broadly sympathetic with an evolutionary approach to human cognition. Nevertheless, they both end up criticizing evolutionary psychology as it has been practiced to date. The most obvious difference between the two books is that Richardson's is considerably shorter. This is because he criticizes mainly the methods used by evolutionary psychologists, whereas Buller evaluated their evidence in great detail and provided alternative interpretations. Another difference is that where Buller concentrated on psychological data, Richardson weighs the approach's theoretical framework using criteria from evolutionary biology. In the end, the two books are complementary, and together they constitute a formidable critique of evolutionary psychology.

CREDIT: COURTESY MIT PRESS

Evolutionary Psychology as Maladapted Psychology

by Robert C. Richardson

MIT Press, Cambridge, MA, 2007. 225 pp. $30, £19.95. ISBN 9780262182607. Life and Mind: Philosophical Issues in Biology and Psychology.

Richardson evaluates in some detail whether particular human cognitive traits, such as language or human reasoning, can be seen as adaptations. He concludes that although it should be possible to find evidence to support such claims, evolutionary psychologists have generally failed to do so. He follows arguments by Stephen Jay Gould and Richard Lewontin (*2*) that natural selection, although of crucial importance, is not the only factor in evolution. The main problem with evolutionary psychology is that it usually does not consider alternative explanations but takes the assumption of adaptation through natural selection as given.

Evolutionary psychologists often argue for their proposals with a zest and enthusiasm that seems to convey the message that we can only understand the human mind if we consider our evolutionary history. At various places in *Evolutionary Psychology as Maladaptive Psychology*, Richardson concludes that we simply lack the historical evidence for a reconstruction of the evolution of human cognition. For human language, an "explanation" favored by evolutionary psychology is that it evolved for use in complex social groups, that is, there was a functional demand for language. Richardson rightly suggests that paleontologists are unlikely to unearth the evidence that can inform us about the social structure of our ancestral communities. I think one can go a step further. Even if we would be able to muster the evidence needed for an evolutionary psychological analysis of human cognition, it would not tell us anything about our cognitive mechanisms. The study of evolution is concerned with a historical reconstruction of traits. It does not, and cannot, address the mechanisms that are involved in the human brain. Those fall within the domains of neuroscience and cognitive psychology. In that sense, evolutionary psychology will never succeed, because it attempts to explain mechanisms by appealing to the history of these mechanisms. To use the author's words, "We might as well explain the structure of orchids in terms of their beauty." In this excellent book, Richardson shows very clearly that attempts at reconstruction of our cognitive history amount to little more than "speculation disguised as results." The book's title implies that the field is itself subject to selection pressure. Richardson is certainly piling it on.

The reviewer is in the Behavioral Biology Group, Utrecht University, Post Office Box 80086, 3508 TB Utrecht, Netherlands. E-mail: j.j.bolhuis@uu.nl

References

1. D. J. Buller, *Adapting Minds: Evolutionary Psychology and the Persistent Quest for Human Nature* (MIT Press, Cambridge, MA, 2005); reviewed by J. J. Bolhuis, *Science* **309**, 706 (2005).
2. S. J. Gould, R. C. Lewontin, *Proc. R. Soc. London Ser. B* **205**, 581 (1979).

10.1126/science.1157403

OCEAN SCIENCE

Under-Resourced, Under Threat

A coherent global vision is needed to better determine the impacts of climate change on marine systems.

Anthony J. Richardson[1,2] and Elvira S. Poloczanska[3]

The recent IPCC (Intergovernmental Panel on Climate Change) Fourth Assessment Report (*1*) noted 28,586 significant biological changes in terrestrial systems but only 85 from marine and freshwater systems. Of these few observations from aquatic systems, 99% were consistent with global warming, which suggests that aquatic systems may be extremely vulnerable to climate change. Here, we argue that the dearth of documented changes from marine systems is an artifact of the distribution of global science funding, the difficulty of disentangling multiple stressors from relatively poorly sampled systems, the disconnect between marine and terrestrial ecology, the way marine ecologists report research findings, and limitations in the existing IPCC process.

Marine research is under-resourced compared with that on land. If the number of publications (1996 to 2004, Thomson Scientific ISI) is used as a measure, less than 11% of published papers in each of the fields of ecology, conservation biology, and biodiversity research deal with marine systems (*2*–*4*). This bias arises in part because investigating the ocean realm is generally difficult, resource-intensive, and expensive.

Observational capacity is also much lower in the oceans than in terrestrial systems. Humans are far removed from much of the ocean expanse, which reduces the likelihood of observing changes there. Research forays into the oceans are transitory and concentrated in coastal waters. Inaccessibility of most marine systems precludes studies by amateur naturalists, who have provided valuable terrestrial data sets on the timing of blossoms or arrival of migratory birds. Satellite observing systems are generally restricted to the sea surface, and even shallow marine ecosystems such as seagrass meadows and coral reefs remain hidden. There are several unique avenues for generating marine time series. Fishery records and fish otoliths (used to estimate fish age and growth, akin to tree rings) provide information over interannual to decadal scales. Reconstructions from sedimentary records and coral cores afford insight over centennial and longer time scales (*5*, *6*).

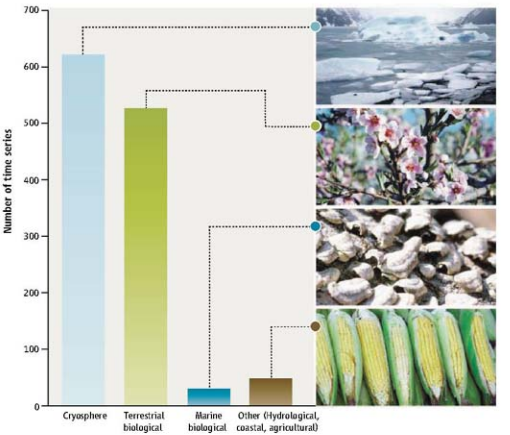

Marine undersampling. The number of time series from different environments included in the recent IPCC (Intergovernmental Panel on Climate Change) Fourth Assessment Report differ widely. Marine systems are vastly underrepresented compared with terrestrial systems (*1*).

The difficulty of disentangling multiple stressors within poorly sampled systems has also stymied the discovery of marine climate change impacts. No parts of the oceans remain unaffected by multiple human activities, such as eutrophication, fishing, habitat destruction, hypoxia, pollution, and species introductions (*7*). These multiple stressors may have masked more subtle impacts of climate change and may even have misled researchers to interpret climate change impacts as those of local environmental changes.

Furthermore, there is a profound disconnect between marine and terrestrial ecology, evident in the lack of contributions of marine ecology to general ecological theory, journals, and textbooks (*3*, *8*, *9*). Major differences in concepts (such as the size dependence of predation in marine systems), organization (marine and terrestrial ecologists are usually in different institutes), and funding have resulted in marine research being overshadowed by terrestrial ecology (*8*, *9*), and this is evident in biological climate impacts research.

Findings from the Fourth Assessment Report (*1*) reflect the dichotomy between research on marine and terrestrial biological impacts. Chapter 1 of Working Group II's report lists only 30 marine data series (biological and physical) in the synthesis of climate impacts, compared with 622 series from the cryosphere and 527 series from terrestrial biological systems (*1*). Further, only 4 out of 43 authors of this chapter were marine biologists, which results in a greater likelihood that documented changes in marine systems may be overlooked.

IPCC guidelines for inclusion in assessment reports demand that time series must be at least 20 years long and end in 1990 or later. Yet, many marine time series were halted in the late

[1]Climate Adaptations Flagship—Commonwealth Scientific and Industrial Research Organisation (CSIRO) Marine and Atmospheric Research, Post Office Box 120, Cleveland, Queensland 4163, Australia. E-mail: anthony.richardson@csiro.au; [2]University of Queensland, Department of Mathematics, St. Lucia, Queensland 4072, Australia; [3]Climate Adaptations Flagship—CSIRO Marine & Atmospheric Research, General Post Office Box 1538, Hobart, Tasmania 7001, Australia. E-mail: elvira.poloczanska@csiro.au

PHOTO CREDITS (TOP TO BOTTOM): JUPITER IMAGES

1980s, just when ocean warming was accelerating, as a consequence of a funding crisis that shifted marine research toward process-orientated studies (*10*). A possible way to bolster confidence and enhance transparency in the IPCC process would be to specifically detail each marine and terrestrial observation synthesized in the report (in an appendix), as is the norm in large published meta-analyses (*11, 12*). As well as identifying gaps, this will allow the broader scientific community to provide quality control of the data gathering and interpretation that underpin the assessment.

Marine ecologists must also accept responsibility for the paucity of evidence of climate-driven impacts on marine species. Terrestrial studies state observed changes in distribution (as kilometer per degree celsius) and timing (as number of days earlier per degree celsius) explicitly for inclusion in meta-analyses and IPCC reports; these figures are rarely provided in the marine literature. The tendency for marine researchers to report bulk responses for functional groups rather than individual species (*13, 14*) also contributes to underestimates in the number of marine biological changes. Both marine and terrestrial ecologists must develop robust yardsticks against which climate-change impacts can be measured (*15*).

The situation is made more urgent, as emerging evidence suggests that the response of marine organisms to climate change may be faster than on land, despite slower ocean warming. Range shifts of hundreds of kilometers in a few decades have been observed in phytoplankton (*16*), zooplankton (*14*), fish (*17*), and intertidal fauna (*18*). Many organisms can be dispersed widely and rapidly by ocean currents (*19*). High fecundity (for example, many bony fish spawn thousands to millions of eggs per female per year), coupled with free-floating early-life stages, allows far-ranging dispersal in a single reproductive season. Changes in life-cycle events may also be greater for marine organisms, with an advance in seasonal timing by more than 8 days per decade of the appearance of phyto- and zooplankton (*13, 20*) and breeding in sea turtles (*21*) and seabirds (*22*). Shorter life cycles of oceanic primary producers (days to weeks) compared with land plants (months to years) contribute to this rapid response.

Unfortunately, our greater knowledge of terrestrial climate impacts will not provide the means to understand marine impacts. Ocean and terrestrial (atmospheric) processes commonly operate over fundamentally different time and space scales (*8*). For example, cyclones in the atmosphere are about 1000 km across and last for a week or so, whereas their marine equivalent, ocean eddies, have diameters of about 200 km and exist for months to years. Slow ocean dynamics also means that some changes will be essentially irreversible. For example, declines in ocean pH may impact calcifying organisms, from corals in the tropics to pteropods (winged snails) in polar ecosystems (*23, 24*), and will take tens of thousands of years to reequilibrate to preindustrial conditions (*23*). Understanding and adapting to climate impacts in the oceans will require some uniquely marine solutions.

Despite these basic differences between marine and terrestrial systems, marine scientists will find many solutions by embracing general principles that transcend the division between these environments. Effects of temperature on organism traits (such as growth and life cycles) may obey similar fundamental rules in the ocean and on land. The metabolic theory of ecology, which formulates predictions on a range of ecological processes based on biophysical principles, is emerging as a unifying principle bridging the marine-terrestrial divide (*9*). Other areas of common interest include fast rates of habitat destruction and critical concepts, such as the likelihood of climatic tipping points beyond which ecosystems may experience abrupt changes. Tackling these research concepts should yield common theory that has predictive capability in both environments.

Marine ecosystems are undoubtedly underresourced, overlooked, and under threat; our knowledge of impacts of climate change on marine life is a mere drop in the ocean compared with that for terrestrial organisms. To address this disparity, a coherent vision is needed to lobby for greater resources for marine research, to focus marine investigations, and to improve marine coverage in the IPCC process. This vision should address the following points:

- encourage comparative research effort in areas where there is likely to be mutual interaction (and benefit) between marine and terrestrial biologists, such as the effects of temperature on life cycles and metabolism;
- establish multinational observing networks that extend across ocean basins to resolve the rapid and long-range shifts expected in organism ranges;
- address the multiple, interactive modes of impacts of climate change and other global change stressors on marine ecosystems and biodiversity;
- encourage marine biologists to participate more actively in the formulation and testing of general ecological principles, providing the necessary theory to interpret and predict climate impacts in marine ecosystems;
- ensure maximum inclusion of marine impacts in the IPCC process by urging marine researchers to state observed changes explicitly for each species studied;
- call for better representation by marine biologists in the IPCC process;
- recommend that the IPCC list each marine and terrestrial observation they use;
- capitalize on the unique windows into marine ecosystem changes over relatively long time scales afforded by sedimentary records.

Two meetings in Spain this year—the recent symposium on *Effects of Climate Change on the World's Oceans* (19 to 23 May) in Gijon and the upcoming *World Marine Biodiversity Conference* (11 to 15 November) in Valencia—bring together marine biologists concerned with climate change and the conservation of marine biodiversity. These meetings provide ideal opportunities to develop such a global vision.

References

1. C. Rosenzweig *et al.*, in *Climate Change 2007: Impacts, Adaptation, and Vulnerability. Contribution of Working Group II to the Fourth Assessment Report of the Intergovernmental Panel on Climate Change*, M. L. Parry, O. F. Canziani, J. P. Palutikof, P. J. van der Linden, C. E. Hanson, Eds. (Cambridge Univ. Press, Cambridge, 2007), pp. 79–131.
2. P. S. Levin, B. F. Kochin, *Conserv. Biol.* **18**, 1160 (2004).
3. K. I. Stergiou, H. I. Browman, *Mar. Ecol. Prog. Ser.* **304**, 292 (2005).
4. I. E. Hendriks, C. M. Duarte, C. H. Heip, *Science* **312**, 1715 (2006).
5. D. B. Field, T. R. Baumgartner, C. D. Charlers, V. Ferreira-Bartrina, M. D. Ohman, *Science* **311**, 63 (2006).
6. Z. V. Finkel *et al.*, *Proc. Natl. Acad. Sci. U.S.A.* **104**, 20416 (2007).
7. B. S. Halpern *et al.*, *Science* **319**, 948 (2008).
8. J. H. Steele, *J. Theor. Biol.* **153**, 425 (1991).
9. C. M. Duarte, *TREE* **22**, 331 (2007).
10. C. M. Duarte, J. Cebrián, N. Marbà, *Nature* **356**, 190 (1992).
11. C. Parmesan, G. Yohe, *Nature* **421**, 37 (2003).
12. T. L. Root *et al.*, *Nature* **421**, 57 (2003).
13. M. Edwards, A. J. Richardson, *Nature* **430**, 881 (2004).
14. G. Beaugrand, P. C. Reid, F. Ibañez, J. A. Lindley, M. Edwards, *Science* **296**, 1692 (2002).
15. M. E. Visser, C. Both, *Proc. R. Soc. London Ser. B* **272**, 2561 (2005).
16. M. Edwards, *Mar. Ecol. Prog. Ser.* **Suppl 1-2**, 1 (2004).
17. A. Sabatés, P. Martín, J. Lloret, V. Raya, *Global Change Biol.* **12**, 2209 (2006).
18. J. P. Barry, C. H. Baxter, R. D. Sagarin, S. E. Gilman, *Science* **267**, 672 (1995).
19. B. P. Kinlan, S. D. Gaines, *Ecology* **84**, 2007 (2003).
20. D. L. Mackas, R. Goldblatt, A. G. Lewis, *Can. J. Fish. Aquat. Sci.* **55**, 1878, (1998).
21. J. F. Weishampel, D. A. Bagley, L. M. Erhart, *Global Change Biol.* **10**, 1424 (2004).
22. L. E. Chambers, *The Impact of Climate on Little Penguin Breeding Success* (Research Report no. 100, Bureau of Meteorology Research Centre, Melbourne, Australia, 2004).
23. J. Raven *et al.*, *Ocean Acidification Due to Increasing Atmospheric Carbon Dioxide* (Royal Society Special Report, London, 2005).
24. J. C. Orr *et al.*, *Nature* **437**, 681 (2005).

10.1126/science.1156129

ECOLOGY

Putting the Heat on Tropical Animals

Tropical animals may be particularly vulnerable to climate warming.

Joshua J. Tewksbury,[1] Raymond B. Huey,[1] Curtis A. Deutsch[2]

Impacts of climate warming in the tropics—the cradle of biodiversity—are often predicted to be small relative to those in temperate regions (*1*, *2*), because the rate of climate warming in the tropics is lower than at higher latitudes (*3*). Yet, predictions based only on the magnitude of climate change may be misleading. Models that include organismal physiology suggest that impacts of climate warming may be more severe in the tropics than in temperate regions.

The impacts of climate warming on organisms depend not only on the magnitude of the environmental temperature shift but also on the behavior, morphology, physiology, and ecology of the organisms in question (*4*–*6*). This added complexity is daunting, but some general principles are emerging from research focused mainly on ectothermal animals (such as insects, fish, reptiles, and amphibians), which cannot maintain a constant internal body temperature. Negative impacts should be greatest on animals that are physiologically specialized with respect to temperature (*7*) and have limited acclimation capacity (*8*). Further, species living in warm climates are likely to suffer disproportionately from small increases in temperature (*9*), and species that live in aseasonal environments may be particularly vulnerable to increases in temperature, because changes in behavior and physiology are less likely to provide relief from rising temperatures (*10*).

Terrestrial ectotherms with these vulnerability traits are typically tropical (*7*, *11*, *12*). In the 1960s, Janzen (*13*) noted that tropical ectotherms should be thermal specialists (see the figure, top) and have limited acclimation capacities, relative to higher-latitude species, because they have evolved in relatively constant, aseasonal environments. These predictions have been largely validated for various terrestrial and aquatic ectotherms (*7*, *11*, *12*, *14*–*17*), yet the implications of this pattern for species vulnerabilities to climate change have rarely been investigated (*15*, *17*–*19*).

Tropical ectotherms have other traits that increase vulnerability. Because tropical organisms experience far more warm weather throughout the year than do temperate organisms, tropical animals might be expected to have greater heat tolerance. Surprisingly, that is often not the case: Heat tolerance typically varies very little across latitude in terrestrial ectotherms (*7*, *12*, *15*). Thus, many tropical ectotherms live much of the year in environments where equilibrium body ("operative") temperatures are near or above optimal temperatures for performance (*15*). Tropical forest species may be particularly vulnerable, because they live in constant shade, are not generally adapted to the high operative temperatures found in warmer open habitats, and have few behavioral options available to evade rising temperatures (*10*, *15*). Any climate-induced increase in operative temperature could cause steep declines in thermal performance and Darwinian fitness (see the figure, top).

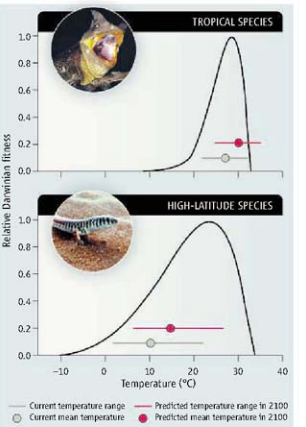

Survival in a warmer climate. Data from diverse terrestrial ectotherms suggest that tropical species living in stable aseasonal climates, such as the Amazonian lizard *Enyalioides palpebralis* (**top inset**), have narrower thermal tolerances than do higher-latitude species such as the temperate lizard *Nucras tessellata* (**bottom inset**), and also live in climates that are closer to their physiological optima. The former may thus be highly vulnerable even to modest climate warming.

To assess whether independent data support these assertions, long-term demographic data on tropical species are required. Such data are rare, but in the study of frogs and lizards in lowland Costa Rica, densities have declined by ~4% per year between 1970 and 2005 (*20*). These declines are explained by climate-driven declines in leaf litter on the forest floor over the study period.

Theoretically, these patterns can cut both ways: The same factors that make tropical ectotherms vulnerable to changing climate may benefit some temperate ectotherms (*15*) (see the figure, bottom). Empirical data tell a more complex story. During the last rapid warming event, 50 million years ago, insect damage on temperate plants did increase sharply (*21*), but data on contemporary temperate-zone insects are mixed: Some species are expanding rapidly (*22*), occasionally causing large changes to ecosystems and economies (*23*), whereas others—often specialists relying on day-length cues and species living in disappearing high-elevation habitats—are predicted to decline (*6*).

All these predictions are for terrestrial habitats, and patterns may differ elsewhere. In marine habitats, for example, thermal specialists occur both at low and high latitudes, and thermal generalists appear most common at mid-latitudes (*9*, *24*). Yet this pattern tracks the seasonality of ocean surface temperatures—polar oceans are cold but show little temperature variation throughout the year, and the largest seasonality in ocean surface temperatures are seen at mid-latitudes. Therefore, both tropical and high-latitude species live at near-stressful temperatures and could be vulnerable to warming (*24*). In intertidal habitats, which

[1]Department of Biology, University of Washington, Seattle, WA 98195, USA. [2]Department of Atmospheric and Oceanic Sciences, University of California at Los Angeles, Los Angeles, CA 90095, USA. E-mail: tewksj@u.washington.edu

CREDIT: (TOP PHOTO) LAURIE WITTJUNY OF OKLAHOMA; (BOTTOM PHOTO) RAIMOND HUEY/UNIV. OF WASHINGTON

have very sharp temperature gradients, an organism's vulnerability to warming depends on vertical position, latitude, daily time of exposure, and interactions with predators and competitors (*4*). Despite this complexity, thermal tolerance and acclimation capacity are still governed by temperature variability (*4*, *8*, *16*).

The strong association between the physiological flexibility of ectotherms and the temperature variations they experience will create serious problems in the tropics, compounding threats from habitat loss and fragmentation. We have focused on the direct impacts of changing temperature on ectotherm physiology. Equally important is the integration of these effects into a framework that includes the impacts of changing climate on species interactions, community structure, and ecosystem function. Such an integration is critical if we hope to predict the impacts of global warming on biodiversity.

References

1. T. L. Root *et al.*, *Nature* **421**, 57 (2003).
2. C. Parmesan, *Global Change Biol.* **13**, 1860 (2007).
3. Intergovernmental Panel on Climate Change (IPCC), *Climate Change 2007: The Physical Science Basis. Working Group I Contribution to the Fourth Assessment Report of the IPCC*, S. Solomon *et al.*, Eds. (Cambridge Univ. Press, Cambridge, 2007).
4. B. Helmuth, J. G. Kingsolver, E. Carrington, *Annu. Rev. Phys.* **67**, 177 (2005).
5. M. Kearney, W. P. Porter, *Ecology* **85**, 3119 (2004).
6. W. E. Bradshaw, C. M. Holzapfel, *Mol. Ecol.* **17**, 157 (2008).
7. C. Ghalambor, R. B. Huey, P. R. Martin, J. J. Tewksbury, G. Wang, *Integr. Comp. Biol.* **46**, 5 (2006).
8. J. H. Stillman, *Science* **301**, 65 (2003).
9. H. O. Pörtner, R. Knust, *Science* **315**, 95 (2007).
10. R. Ruibal, *Evolution* **15**, 98 (1961).
11. A. A. Hoffmann, R. J. Hallas, J. A. Dean, M. Schiffer, *Science* **301**, 100 (2003).
12. A. Addo-Bediako, S. L. Chown, K. J. Gaston, *Proc. R. Soc. London. Ser. B* **267**, 739 (2000).
13. D. H. Janzen, *Am. Nat.* **101**, 233 (1967).
14. F. H. van Berkum, *Am. Nat.* **132**, 327 (1988).
15. C. A. Deutsch *et al.*, *Proc. Natl. Acad. Sci. U.S.A.* **105**, 6669 (2008).
16. S. E. Gilman, D. S. Wethey, B. Helmuth, *Proc. Natl. Acad. Sci. U.S.A.* **103**, 9560 (2006).
17. P. Calosi, D. T. Bilton, J. I. Spicer, *Biol. Lett.* **4**, 99 (2008).
18. J. W. Williams, S. T. Jackson, J. E. Kutzbach, *Proc. Natl. Acad. Sci. U.S.A.* **104**, 5738 (2007).
19. P. A. Parsons, *Ambio* **18**, 322 (1989).
20. S. M. Whitfield *et al.*, *Proc. Natl. Acad. Sci. U.S.A.* **104**, 8352 (2007).
21. E. D. Currano *et al.*, *Proc. Natl. Acad. Sci. U.S.A.* **105**, 1960 (2008).
22. L. Crozier, G. Dwyer, *Am. Nat.* **167**, 853 (2006).
23. W. A. Kurz *et al.*, *Nature* **452**, 987 (2008).
24. J. R. Brett, in *Marine Ecology, Vol. 1, O.* Kinne, Ed. (Wiley, New York, 1970), pp. 515–560.

10.1126/science.1159328

SYSTEMS BIOLOGY

The Scale of Prediction

Nitin S. Baliga

A predictive model for a biological system requires capturing the network of environmental factors that affect system responses.

Interlocking architectures. The associations between environmental and biological networks facilitate predictive modeling of cellular responses. The interlocked gears within a microbial cell represent coupled biochemical processes that operate in sync with similarly coupled changes in environmental factors, also represented by interlocked gears.

The predictability of cellular responses is the basis for applications as diverse as preventive medicine and the reengineering of microbes for biotechnology. At first glance, the diversity of biological systems suggests that they can adopt a seemingly infinite number of behaviors or states. If this were true, it would severely hinder our ability to predict the responses of biological systems to new environmental changes. Fortunately, this is not the case (*1*). An individual biological system functions optimally within an environmental space (defined by the ranges in any given parameter) in which it has evolved. Furthermore, within this defined space, changes in individual factors (temperature, pH, O_2, etc.) do not occur in isolation but in a temporally coupled and nonrandom manner for physicochemical reasons. On page 1313 of this issue, Tagkopoulos *et al.* (*2*) offer theoretical simulations and experimental validation to show that even simple microbes can learn temporal interrelationships among changes in environmental factors, and thus can predict and prepare for future environmental changes, a behavior attributed to metazoans. This work not only demonstrates how biological networks (gene, protein, and metabolic) have assembled during evolution, but also explains why decoding these networks into predictive models is a tractable problem.

The progression of naturally coupled environmental changes over billions of years has been the primary selection pressure in evolution. Because these natural environmental changes occur in a coordinated manner, from the perspective of an organism they are routine and predictable. Not surprisingly, biological systems have used this to their advantage and evolved anticipatory behavior. Tagkopoulos *et al.* show that this ability to predict environmental changes lends a competitive advantage to the organism. In fact, they demonstrate that decoupling environmental changes reduces the fitness of an organism and that this fitness can be regained through evolution of new network architectures from the same original parts list. This is especially exciting because relationships among environmental factors can change markedly from one niche to another (for example, the relationship among temperature, light, and nutrient availability across the ocean surface, hypersaline lake, and hydrothermal vent environments). Given sufficient separation on evolutionary time scales, this can result in different regulatory logic in related organisms that share similar genes but have gone on to inhabit different niches (*3*) [e.g., different ecotypes of the cyanobacterium *Prochlorococcus marinus* (*4*)].

Tagkopoulos *et al.* provide insight into the process by which the architecture of an environmental network is imprinted onto the

Institute for Systems Biology, 1441 N. 34th Street, Seattle, WA 98103, USA. E-mail: nbaliga@systemsbiology.org

CREDIT: ADAPTED BY R. HUEY/SCIENCE

structure of a biological network. They make a striking observation that this rewiring process occurs rapidly (in <100 generations). This suggests that an organism can migrate to a suboptimal environment and rapidly gain fitness through rewiring. Such a marginal increase in fitness might make the organism reasonably competitive while it undergoes a much longer process (lateral gene transfers and/or spontaneous mutations followed by selection) to fully adapt to the new environment.

The fitness gain associated with internalized network changes that reflect coupled environmental changes might also partly explain why multiple environmental sensing domains are physically linked in numerous response regulatory proteins (*5*). These linkages are even apparent at a systems level and are phenomena that have been known for quite some time (*6*, *7*). Circadian rhythms, seasonal flowering, and the migratory behavior of birds are excellent examples of anticipatory behaviors over different time scales. Acclimation to an impending change upon sensing a predictive environmental cue is a systems-level phenomenon with mechanistic roots in the molecular architecture of gene and protein networks. Once decoded, the logic within the architecture of these networks that enable an organism to anticipate environmental changes should in turn help us predict its behavior.

This is not an unrealistic expectation because these complex systems-level phenomena are now tractable at a molecular level. High-throughput technologies enable the measurement of molecular changes in system-wide genetic information processing (such as RNA and protein expression levels, protein-protein and protein-DNA interactions, and protein modifications). However, it seems that to construct a predictive model we would need to make these measurements over nearly an infinite space of combinatorial perturbations in all environmental factors. Tagkopoulos *et al*. show that combinatorial perturbation experiments that couple environmental factors in an unnatural way might elicit responses that do not accurately reflect relationships that the organism has learned through evolution. If so, then a model constructed from such "unnatural" responses is unlikely to be predictive.

This argues that the combinatorial perturbations conducted in the laboratory should mimic true relationships in the natural environment. Both the paucity of detailed models for these dynamic temporal relationships in diverse environments and the complexity of mimicking them in the laboratory make this an unattainable goal. Interestingly, the same network of coupled environmental changes that has resulted in anticipatory behavior also aids in predictive modeling of these networks from a relatively modest number of systematic one-factor perturbation experiments. This is because even a simple perturbation propagates through the highly structured network of physicochemical relationships to give complex and reproducible multifactor changes. Consequently, these perturbations trigger linked and anticipatory networks within the organism, generating a structured response that can be learned and modeled (*8*).

References

1. C. L. Barrett, C. D. Herring, J. L. Reed, B. O. Palsson, *Proc. Natl. Acad. Sci. U.S.A.* **102**, 19103 (2005).
2. I. Tagkopoulos, Y.-C. Liu, S. Tavazoie, *Science* **320**, 1313 (2008); published online 8 May 2008 (10.1126/science.1154456).
3. M. W. Kirschner, *Cell* **121**, 503 (2005).
4. A. Dufresne *et al*., *Proc. Natl. Acad. Sci. U.S.A.* **100**, 10020 (2003).
5. T. Mascher, J. D. Helmann, G. Unden, *Microbiol. Mol. Biol. Rev.* **70**, 910 (2006).
6. A. N. Dodd *et al*., *Science* **309**, 630 (2005).
7. S. S. Nikaido, C. H. Johnson, *Photochem. Photobiol.* **71**, 758 (2000).
8. R. Bonneau *et al*., *Cell* **131**, 1354 (2007).

10.1126/science.1159485

ASTRONOMY

An Eccentric Pulsar: Result of a Threesome?

Observation of an eccentric millisecond binary pulsar challenges the standard model of millisecond pulsar formation.

Edward P. J. van den Heuvel

Pulsars are rapidly spinning neutron stars whose lighthouse-like beams of radio waves sweep Earth, producing highly regular pulses with periods ranging from about 1 ms to 8 s. Of the ~1600 pulsars known in the disk of our galaxy, some 5% have pulse periods shorter than 10 ms (*1*). Most of these millisecond pulsars have a companion star that is a white dwarf, and all such millisecond binary pulsars known in the galactic disk have perfectly circular orbits (*1*, *2*). Yet, on page 1309 in this issue, Champion *et al*. (*3*) report the discovery of a millisecond pulsar in the galactic disk with a highly eccentric orbit and a companion that is probably a solar-like star. The mass of this pulsar is ~30% larger than that of other binary neutron stars in the galactic disk (*2*). The discoverers suggest that the high eccentricity of this binary is due to interaction with a third star.

Neutron stars and black holes are the densest objects known in the universe and have the strongest gravitational fields. They are formed by the collapse of the burned-out core of a star exceeding eight solar masses, accompanied by a supernova explosion in which the envelope of the star is violently ejected. Weighing in at ~1.4 solar masses and with a diameter of only 20 km, a neutron star is essentially an atomic nucleus consisting of 10^{57} neutrons held together by a gravitational attraction ~11 orders of magnitude greater than on the surface of Earth. This enormous gravity allows a neutron star to spin ~1000 times per second.

In the standard model for millisecond-pulsar formation (*4*–*7*) in the galactic disk, the transfer of matter from a binary companion causes the neutron star's spin period to decrease. Although the supernova explosion initially results in an eccentric orbit for the neutron star (*8*), strong tidal effects during the subsequent mass-transfer phase produce the circular orbit.

The millisecond radio pulsars with circular orbits are the later evolutionary products of low-mass x-ray binaries (LMXBs). These consist of a neutron star and a solar-like companion star less than 1.5 solar masses (*9*). The mass transfer in these systems may last hundreds of millions of years, allowing the spin period of their neutron star to decrease to mil-

Astronomical Institute "Anton Pannekoek" and Center for High Energy Astrophysics, University of Amsterdam, 1098SJ Amsterdam, Netherlands, and Kavli Institute for Theoretical Physics, University of California Santa Barbara, CA 93106-4030, USA. E-mail: e.p.j.vandenheuvel@uva.nl

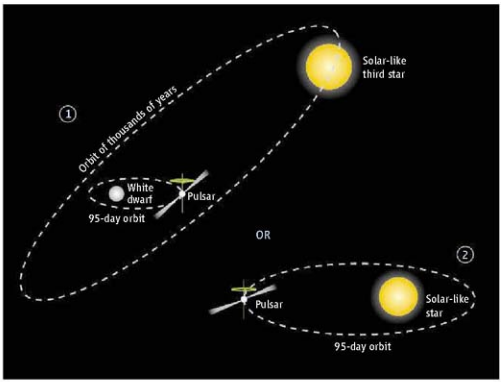

Eccentric millisecond pulsar systems. Two possible configurations of the eccentric-orbit binary millisecond pulsar system resulting from triple-star interactions. **(Model 1)** The 95-day orbit eccentric binary started out as a "normal" circular-orbit millisecond binary pulsar with a white dwarf companion. Its orbit later became eccentric due to the gravitational disturbances produced by the solar-like star seen at the pulsar's sky position, which is in a wide orbit around the inner system. **(Model 2)** The pulsar started out in a very close pulsar–white dwarf binary around which the solar-like star moved in a wider orbit. Due to its proximity, the white dwarf was evaporated by the pulsar's high-energy radiations and particle fluxes, or coalesced with it, such that the present binary remained.

liseconds and tidal forces to circularize the orbit. Indeed, in more than 20 LMXBs, millisecond spin periods were detected in the past decade (*10*–*12*), and the circular orbits were verified. The x-ray–emitting neutron star in the LMXB will become a millisecond radio pulsar once the accretion has stopped and the companion star has "died" and become a white dwarf star.

To explain the eccentric orbit observed by Champion *et al.*, something must have disturbed the initially circular orbit of the pulsar system. The possibilities include interaction with another body after formation, initial formation from three rather than two stars, or disruptive effects from gravitational forces. Such effects have been seen in globular star clusters but not in our galaxy.

In globular star clusters, LMXBs are about three orders of magnitude more common than they are in the disk of our galaxy, and the same is true for their descendants, the millisecond radio pulsars (*1*). This overabundance of neutron star binaries is a result of the relatively high star density of globular star clusters compared to our galaxy's disk. This higher density leads to more frequent stellar encounters, making it easier for a neutron star to capture a solar-like companion star. After repeating this capture and accretion process several times, the neutron star may increase its mass. Indeed, some millisecond pulsars in globular clusters are observed to have masses up to ~1.8 solar masses.

Also, an encounter of a millisecond pulsar binary with another cluster star may cause the orbit of the millisecond pulsar to become eccentric and/or its white dwarf companion to be exchanged for a solar-like cluster star. Some 10% of the millisecond pulsar binaries in globular clusters indeed have eccentric orbits, and in some cases the companions are solar-like stars (*1*). In addition, such an encounter may impart a sufficiently large velocity to the binary for it to escape from the cluster. Champion *et al.* suggest this "knock-out scenario" as one of the possible formation models for their system, estimating the formation probability to be ~10%.

As an alternative, they suggest formation in the galactic disk from a hierarchical triple system, originally composed of a "normal" circular close inner binary consisting of the millisecond pulsar and a white dwarf, plus a third distant companion, which is the observed solar-like star (see the figure, model 1). The latter star can, by its gravitational interaction with the inner binary, induce a large eccentricity in the orbit of that system. They estimate that the probability of finding at least one triple system among the known number of millisecond binary pulsars is ~50%. Although it can explain the eccentricity, there remains the problem of the observed large mass of the pulsar and also of the white dwarf [white dwarfs in circular-orbit millisecond pulsar binaries always have masses below 0.44 solar masses (*1*, *2*)]. As an alternative three-body model, they suggest that the white dwarf in the inner binary system (in this case very close) was evaporated by the pulsar's energy flux and the third (solar-like) star remained in the 95-day eccentric orbit (see the figure, model 2). This still does not explain the large mass of the pulsar.

Each of these models therefore has problems. An attractive alternative to model 2 is one in which the close inner binary system consists of a pulsar and a massive white dwarf (*13*). Due to gravitational-wave losses, such a binary will coalesce, completely disrupting the massive white dwarf (*14*). Part of the massive disk that then forms around the neutron star may be accreted, increasing its mass, the ejection of the remainder inducing an eccentric orbit.

It thus appears that viable models can be constructed to explain the observations by Champion *et al.* This eccentric system seems to confirm that in nature—to paraphrase the novelist T. H. White—"anything not forbidden is compulsory."

References and Notes

1. D. R. Lorimer, *Living Rev. Relativ.* **8**, 7 (2005).
2. I. H. Stairs, *Science* **304**, 547 (2004).
3. D. J. Champion *et al.*, *Science* **320**, 1309 (2008); published online 15 May 2008 (10.1126/science.1157580).
4. M. A. Alpar, A. F. Cheng, M. A. Ruderman, J. Shaham, *Nature* **300**, 728 (1982).
5. V. Radhakrishnan, G. Srinivasan, *Curr. Sci.* **51**, 1096 (1982).
6. D. R. Lorimer, M. Kramer, *Handbook of Pulsar Astronomy* (Cambridge Univ. Press, Cambridge, 2005).
7. P. Ghosh, *Rotation and Accretion Powered Pulsars* (World Scientific, London and Singapore, 2007).
8. B. P. Flannery, E. P. J. van den Heuvel, *Astron. Astrophys.* **39**, 61 (1975).
9. W. H. G. Lewin, M. van der Klis, Eds., *Compact Stellar X-ray Sources* (Cambridge Univ. Press, Cambridge, 2006).
10. R. Wijnands, M. van der Klis, *Nature* **394**, 344 (1998).
11. D. Chakrabarty, E. H. Morgan, *Nature* **394**, 346 (1998).
12. M. van der Klis, in *Compact Stellar X-ray Sources*, W. H. G. Lewin, M. van der Klis, Eds. (Cambridge Univ. Press, Cambridge, 2006), p. 39.
13. R. T. Edwards, M. Bailes, *Astrophys. J.* **547**, L37 (2001).
14. E. P. J. van den Heuvel, P. T. J. Bonsema, *Astron. Astrophys.* **139**, L16 (1984).
15. The author was supported by the National Science Foundation under grant NSF PHY 05-51164.

Published online 15 May 2008;
10.1126/science.1158738
Include this information when citing this paper.

PHYSICS

Improving Correlations Despite Particle Loss

As a trapped quantum gas is slowly set free, pairs of colliding molecules escape, but these collisions actually help slow further losses.

J. V. Porto

Correlations arise in systems where the behavior of any given particle depends strongly on all the other particles. Such correlations help to distinguish relatively simple gases (which are largely uncorrelated systems; over time, the average position of an atom in a gas does not depend much on the other atoms) from more complicated condensed matter systems. In traditional condensed materials, correlations arise from two effects: interactions (for example, the charge of electrons causes them to repel each other) and quantum statistics (for example, fermionic particles such as electrons cannot be in the same state, as stated in the Pauli exclusion principle). Yet, on page 1329 of this issue, Syassen *et al.* (*1*) show that in dilute quantum gases, correlations can arise through another mechanism: inelastic loss of particles from the system.

This approach uses the unusual properties of ultracold atoms that are held in optical lattices, standing waves of light created by interfering laser beams. Collisional loss allows pairs of colliding particles to escape the traps, leading to particle correlations. Despite being less dense than typical solids by a factor of 1 billion, gases of ultracold atoms provide a way to realize and study "condensed" matter physics (*2*). Trapped in a vacuum with magnetic or optical fields, these weakly interacting dilute gases can serve as nearly perfect realizations of some solid-state models and may help us understand phenomena such as high-temperature superconductivity or exotic quantum magnets. In addition, they present opportunities unavailable in traditional materials, such as the ability to precisely engineer lattice potentials to trap the atoms and to directly control the strength of atom-atom interactions.

Another important feature of trapped atom systems is that they can undergo inelastic atom loss, in which two or more particles collide to form a molecule, kicking those particles out of the trapped gas. Particles converging on the same point in space can undergo inelastic collisions and are effectively annihilated—they disappear from the trap.

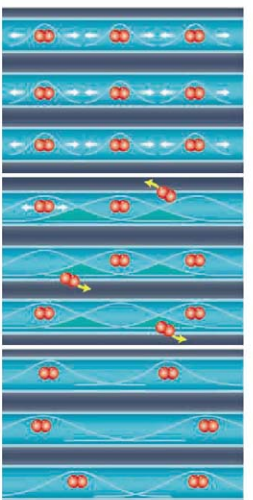

Making gains out of losses. (Top) Molecules initially isolated from one another in a lattice are released along one direction and are allowed to spread out and interact with their neighbors. **(Middle)** When the molecular wave functions spread out enough for neighboring atoms to come in contact, strong inelastic loss of particles can occur. **(Bottom)** Counterintuitively, this strong loss can actually stabilize the system against further loss.

Collisional losses are normally considered undesirable for studying many-body physics because they can lead to heating and decay. Losses, however, depend on the positions of other particles, and loss rates have been used to measure two-particle correlations in a Bose gas of ^{87}Rb atoms (*3*). Syassen *et al.* point out that these losses can generate correlated states: The remaining atoms are more likely to be arranged to avoid each other. However, this effect alone would not be enough to generate stable correlated states, because the remaining separated particles could continue to adjust their positions, and would find and collide with other atoms until all atoms had decayed away.

Quantum mechanical systems can evolve in ways counter to our classical intuition, and there is a quantum effect that can stabilize the system if the loss rate is much greater than the rate at which atoms can move from point to point in the gas. In the quantum Zeno effect, processes that strongly perturb a given state tend to inhibit the system from evolving into that state. It's as if the mere possibility of strong losses of colocated atoms tends to prevent separated atoms from moving together and annihilating. In the context of cold atoms, the quantum Zeno effect has been proposed as a means to stabilize a quantum "register" of atoms in an optical lattice (*4*).

Syassen *et al.* point toward the broader application of creating correlated many-body states. They first trapped an array of individual Rb_2 molecules into the separate sites of a three-dimensional (3D) optical lattice, which creates a correlated state (this state resembles a low-density crystal; see the figure, top panel). By decreasing the strength of the trapping lattice along just one direction, they converted the rubidium system into a 2D array of 1D gases (see the figure, middle panel). The previously isolated Rb_2 molecules were then free to move along the wires and annihilate each other (see the figure, bottom panel).

As these dynamic processes took place, Syassen *et al.* measured substantially lower particle loss than would be expected for an uncorrelated system, which shows that the particles are correlated—they avoid each other. More important, as particles disappeared, the loss rate slowed more than would be expected from the decreased number of atoms alone, which indicates that these loss processes further increase the correlations of the remaining atoms. This interpretation is supported by the authors' theoretical description of the system.

This inherently dynamic many-body problem presents some interesting theoretical

Joint Quantum Institute, University of Maryland and National Institute of Standards and Technology, Gaithersburg, MD 20899, USA. E-mail: trey@nist.gov

questions. To what extent can temperature be defined, and how do the final states depend on the initial conditions? Is the approach taken here, in which the system starts in a correlated state, different from one starting with a completely uncorrelated system and then suddenly turning on loss processes? The authors' numerical calculations indicate that the system forgets any details of its initial state quickly, and it will be interesting to further elucidate the details.

The work of Syassen *et al.* represents a first step in solving the experimental challenges to making this collision process generally useful. This technique could be used to produce other interesting states, such as fractional quantum Hall states (*5*) and systems that exhibit anyonic statistics (*6*). Here, the particle correlations create composite particles that have fractional electron charge or obey "fractional" quantum statistics somewhere between those of a boson and a fermion. Even in the absence of these applications, the present work opens up the experimental and theoretical study of a new class of interesting dynamic problems.

References

1. N. Syassen *et al.*, *Science* **320**, 1329 (2008).
2. D. Jaksch *et al.*, *Phys. Rev. Lett.* **81**, 3108 (1998).
3. T. Kinoshita, T. Wenger, D. S. Weiss, *Phys. Rev. Lett.* **95**, 190406 (2005).
4. G. K. Brennen, G. Pupillo, A. M. Rey, C. W. Clark, C. J. Williams, *J. Phys. B* **38**, 1687 (2005).
5. L. B. Laughlin, *Phys. Rev. Lett.* **50**, 1395 (1983).
6. F. Wilczek, *Phys. Rev. Lett.* **48**, 1144 (1982).

10.1126/science.1159748

MOLECULAR BIOLOGY

Refined View of the Ends

Studies in fission yeast have expanded the known repertoire of proteins that assemble at chromosomal ends to control telomere function.

Alessandro Bianchi and David Shore

The linear genomes of eukaryotes pose specific problems for the protection and replication of DNA ends, or telomeres. These challenges were overcome by the evolution of a specialized protein apparatus that, together with the short DNA repeats that recruit these proteins to chromosome ends, forms the telomeric complex (*1*, *2*). On page 1341 of this issue (*3*), Miyoshi *et al.* identify new protein components of the fission yeast telomeric complex and offer new insights into telomere function and evolution.

In yeasts and mammals, the short but highly repeated DNA motif synthesized by the telomerase enzyme is partly single-stranded, terminating in a 3′-OH overhang (enriched with the nucleotides thymine and guanine) at the tip of the telomere. Consequently, both double-stranded and single-stranded telomeric DNA binding proteins have evolved. Both sets of proteins protect chromosomes and regulate telomerase activity. The emerging picture is that the double-stranded binding factors repress telomerase through a mechanism that depends on the number of bound molecules, which is linked to telomere length; overhang-binding proteins participate in telomerase activation.

The core mammalian telomeric complex is called shelterin, for its role in telomere protection (*4*). It is delivered to telomeres by two of its components, telomeric repeat binding factor 1 (TRF1) and TRF2. TRF2 recruits an additional factor, repressor activator protein 1 (RAP1). The mammalian overhang-binding unit is a heterodimer of the protein protection of telomeres 1 (POT1) and TPP1 (previously known as TINT1/PTOP/PIP1). A sixth factor, TRF1-interacting nuclear factor 2 (TIN2), completes the core complex. Of the two well-studied yeast model systems, *Saccharomyces cerevisiae* and *Schizosaccharomyces pombe*, only the latter has orthologs of TRF1/TRF2 (called Taz1) and POT1.

Using a biochemical approach, Miyoshi *et al.* identify the Pot1-interacting partner in *S. pombe* (the TPP1 ortholog, called Tpz1). They also reveal two additional components of a Pot1 complex localized at telomeres: Poz1, a small protein of unknown function and with no obvious homologs, and coiled-coil quantitatively enriched protein 1 (Ccq1), whose multiple functions include heterochromatin formation (*5*), meiosis (*6*), and, as now reported, telomerase regulation (*3*). Tpz1, like its partner Pot1, is essential for telomere protection, and for Poz1 and Ccq1 association with the telomere. Poz1 in turn interacts with both Rap1 and Tpz1, and thus has an important architectural role in bridging the Taz1-Rap1 complex with Pot1-Tpz1 (and Ccq1). The set of mapped interactions is reminiscent of those described for the human shelterin complex, raising the question of whether Poz1 might be a TIN2 homolog. One important difference is that Poz1 in *S. pombe*, unlike TIN2 in mammals, interacts with Rap1.

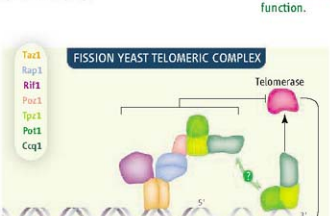

Fission yeast telomeric complex. In this model, the Pot1-Tpz1-Ccq1 complex promotes telomerase activity when bound directly to the 3′-OH overhang, but not when recruited to the Taz1-Rap1 complex by Poz1. The extent of sequestration of the Pot1-Tpz1-Ccq1 complex depends on the number of telomere-bound Taz1-Rap1 molecules, which in turn is dictated by telomere length.

Although loss of Pot1 or Tpz1 in fission yeast results in telomere deprotection and cell death, mutant cells lacking either Poz1 or Ccq1 grow normally. However, Poz1 and Ccq1 do protect telomeres, as the double mutant is inviable and loses telomere sequences rapidly. Both proteins also regulate telomerase, but in opposite ways: Poz1- and Ccq1-deficient cells have elongated and shortened telomeres, respectively. One attractive hypothesis is that the Pot1-Tpz1-Ccq1 complex (possibly together with Poz1) forms a subcomplex at telomere overhangs that recruits and activates telomerase (see the figure). This agrees with recent findings that human POT1-TPP1 interacts with telomerase in vivo and stimulates its activity in vitro when bound to its DNA substrate (*7*, *8*). Importantly, Miyoshi *et al.*, demonstrate that Tpz1 immunoprecipitates telomerase activity from yeast cells, in a Ccq1-dependent manner.

Department of Molecular Biology and the National Centres of Competence in Research "Frontiers in Genetics" Program, University of Geneva, CH-1211 Geneva 4, Geneva, Switzerland. E-mail: david.shore@molbio.unige.ch

It has been proposed that mammalian shelterin controls telomerase activity by transducing a telomere length-dependent signal to the chromosome end via POT1-TPP1 (*9*). The findings of Miyoshi *et al.* in fission yeast suggest a version of this model, in which telomerase activity is controlled by a switch in the Pot1-Tpz1-Ccq1 complex from a Taz1-Rap1–bound state, nonpermissive for telomerase recruitment and/or activation, to an overhang-bound conformation where it promotes telomerase action (see the figure). Consistent with this proposal, Poz1 and Pot1 associate with duplex telomeric DNA in cells with circularized chromosomes (thus devoid of ends), and this binding depends on Taz1 and Rap1. The proposed role of Poz1 in delivering the Pot1-Tpz1-Ccq1 complex to its Taz1-Rap1–bound "repressive" state would explain the telomere lengthening phenotype of *poz1* mutants. Further testing of this model could help elucidate the role of mammalian shelterin in telomerase control.

The work by Miyoshi *et al.* places a spotlight on Ccq1, whose many functions also include protecting telomeres, because cells lacking Ccq1 exhibit increased telomere recombination and activate the DNA damage response. It remains unclear how the various activities of Ccq1 are coordinated and whether a mammalian homolog exists.

The findings of Miyoshi *et al.* underscore the importance of structural relations and transitions within the telomeric complex in carrying out its many functions. Unraveling the architectural organization of shelterin will be a major challenge, but is only part of the task, because several accessory factors that associate only transiently with the core telomeric complex are required for telomere function. Interaction of these factors with the telomere is often mediated by RAP1 or TRF proteins. Indeed, TRF1/TRF2 and Taz1 share a conserved α-helical domain that provides a large surface for protein interactions (*10*). Structural analysis has identified short peptide motifs (bearing the consensus Tyr/Phe-X-Leu-X-Pro, where X is any amino acid) that interact with the α-helical domain of TRF1/TRF2 (*11*). For example, the consensus sequence of TIN2 interacts specifically with TRF1, and that of Apollo (a nuclease) interacts with TRF2. This motif has been identified in other human proteins involved in telomere function, indicating that they too might interact directly with TRF proteins. Whether Taz1 uses a similar docking mechanism to recruit accessory telomeric factors remains to be seen, but appears likely.

Where does this leave the budding yeast *S. cerevisiae*, long viewed as an outlier in telomere evolution? Budding yeast use Rap1 as the telomere duplex DNA binding protein, apparently relegating the TRF-like protein (called Tbf1) to a poorly defined back-up role in telomere biology. Similarly, the role of Pot1 in budding yeast seems to be carried out by a different protein [cell division cycle 13 (Cdc13)], albeit one with an overall structural similarity, namely, the presence of multiple oligosaccharide-oligonucleotide-binding (OB) folds. Cdc13 forms a trimeric complex (called the CST complex) with Stn1 and Ten1, proteins that also bear OB folds. Remarkably, two recent reports identify Stn1 orthologs in a wide range of organisms from *S. pombe* to humans (*12*, *13*), and provide direct evidence that the *S. pombe* protein does indeed play a role at telomeres (*12*). Could it be that a CST-like complex in fission yeast and mammals awaits discovery?

References

1. N. Hug, J. Lingner, *Chromosoma* **115**, 413 (2006)
2. M. P. Longhese, *Genes Dev.* **22**, 125 (2008).
3. T. Miyoshi, J. Kanoh, M. Saito, F. Ishikawa, *Science* **320**, 1341 (2008).
4. T. de Lange, *Genes Dev.* **19**, 2100 (2005).
5. T. Sugiyama *et al.*, *Cell* **128**, 491 (2007).
6. M. R. Flory, A. R. Carson, E. G. Muller, R. Aebersold, *Mol. Cell* **16**, 619 (2004).
7. F. Wang *et al.*, *Nature* **445**, 506 (2007).
8. H. Xin *et al.*, *Nature* **445**, 559 (2007).
9. D. Loayza, T. De Lange, *Nature* **423**, 1013 (2003).
10. L. Fairall, L. Chapman, H. Moss, T. de Lange, D. Rhodes, *Mol. Cell* **8**, 351 (2001).
11. Y. Chen *et al.*, *Science* **319**, 1092 (2008).
12. V. Martin, L. L. Du, S. Rozenzhak, P. Russell, *Proc. Natl. Acad. Sci. U.S.A.* **104**, 14038 (2007).
13. H. Gao, R. B. Cervantes, E. K. Mandell, J. H. Otero, V. Lundblad, *Nat. Struct. Mol. Biol.* **14**, 208 (2007).

10.1126/science.1159104

APPLIED PHYSICS

Going with (or Against) the Flow

Scientists have made great progress in controlling flow in many systems, but general strategies with feedback remain the ultimate goal.

Thomas Peacock[1] and Elizabeth Bradley[2]

Our daily lives are governed by flow control. We not only move through fluids, such as air and water, but also depend on fluid flows for transport and mixing on all scales, from the blood flow that brings oxygen to our cells, to geophysical convection and turbulence in the oceans and atmosphere. Flow control thus lies at the heart of a panoply of scientific problems, such as improving the performance of transport vehicles or managing pollution dispersion in the environment. The importance of these issues is driving new theoretical and technological advances in this diverse and challenging research field.

[1]Department of Mechanical Engineering, Massachusetts Institute of Technology, 77 Massachusetts Avenue, Cambridge, MA 02139, USA. [2]Department of Computer Science, University of Colorado, 430 UCB, Boulder, CO 80309, USA. E-mail: tomp@mit.edu

Flow control begins on the microscale (*1*); for example, fluid flows in lab-on-a-chip technology can manipulate DNA molecules through hydrodynamic focusing (*2*). In this Perspective, however, we restrict our attention to macroscale phenomena. An important example is controlling the separation of a thin boundary layer of air adjacent to moving cars and planes; this small-scale process in turn alters the macroscale flow around a vehicle, affecting the drag and lift. If this separation can be prevented or delayed, performance can be improved substantially.

Some boundary-layer control problems can be solved by turning to nature. Many aquatic creatures have evolved to become dynamically efficient through a combination of their static body profile, skin roughness, and active control of their geometry when generating propulsion (*3*, *4*). And because low-speed water flow can be equivalent to high-speed air flow, configurations that have evolved in one medium can sometimes be translated into the other. For instance, the humpback whale flipper has large rounded protuberances on the leading edge (see the figure) that delay boundary-layer separation during sharp turning maneuvers (*5*). This research has inspired prototype wind-turbine blades that generate as much power at wind speeds of 10 miles per hour as conventional turbines do at 17 miles per hour (*6*). Other recent biomimetic technologies include a low-drag, large-storage capacity Mercedes-Benz car designed to mimic the hydrodynamic profile of a boxfish (*7*), and a swimsuit made from fabrics that reduce the drag on the bodies of competitive swimmers (*8*).

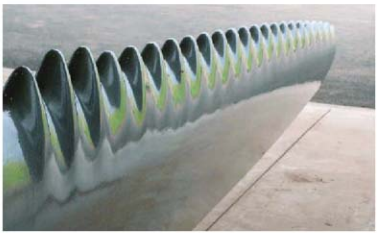

Biomimetic wind turbines. Rounded protuberances on the flippers of humpback whales (**left**) delay the dramatic loss of lift (known as "stall"). They can do so by changing the pressure distribution, which delays separation behind the bumps; the existence of vortices in the troughs between tubercles may also play a role. Prototype wind-turbine blades that mimic these features (**right**) perform much better than conventional blades at low wind speeds.

Many engineered systems operate in dynamic regimes or configurations that are foreign to biology, so biomimetics is not a universal flow-control solution. In some cases, open-loop strategies—a fixed approach based on predetermined information, such as new geometries (passive control) or surface-mounted actuators (active control)—can improve performance substantially (*9*). For example, supersonic microjets 100 to 1000 μm in size, with exit velocities in the range of 300 to 500 m/s, are used to actively control unsteady behavior in larger supersonic jets used by short-takeoff and vertical-landing aircraft (*10*).

However, these approaches are tailored to specific problems, and it remains difficult to develop a closed-loop strategy that adapts in real time, based on feedback from sensors, to control a wide range of complex flows. First, because of their many degrees of freedom, complex flows are difficult to approximate and highly sensitive to initial conditions, restricting our ability to make accurate real-time forecasts with numerical methods. Second, although the boundaries of a flow can be accessed through surface-mounted sensors and actuators, it is not practical to do so for the body of the fluid. Finally, even at the boundaries, demands on sensors and actuators are high; the technology must operate on very fine scales while being robust enough to withstand harsh conditions, such as those found on the surface of an airplane wing or the inside of a jet engine.

Despite these challenges, impressive progress is being made in all areas of closed-loop flow control. Robust actuation technology has been developed, for example, in the form of synthetic jet actuators that provide localized velocity disturbances to alter the near-wall flow (*11*). And because increased computing power alone is unlikely to enable real-time simulation in the foreseeable future, alternative prediction strategies are being developed. One promising approach, which has been demonstrated to smooth a turbulent flow in numerical simulations, is to use rigorous linear approximations of the governing equations (*12*). In complex flows, where this approach can be impractical, system identification methods provide an alternative means to obtain an approximate linear model; this technique has been used to reduce the frequency of turbulent bursting by 23% in wind-tunnel tests (*13*). Other approaches under development include low-dimensional models that approximate the full dynamics (*14*), or techniques that identify and manipulate key coherent structures, such as separation spikes (*15*). These strategies are likely to have a substantial impact for small-scale autonomous vehicles, which—like birds, insects, and fish—maneuver at speeds commensurate with the unsteady aerodynamics and exploit unsteady phenomena such as dynamic lift (that is, the lift available for a short time immediately before stall sets in).

Some of the most pressing flow-control issues faced by society exist on even larger scales. According to the Energy Information Administration, more than 5% of the total annual energy consumption of the United States goes into heating and cooling buildings (*16*). In an effort to improve efficiencies, the design of openings in buildings is being guided by experiments that use flows of stratified salt water through scaled-down models to mimic air flow in a building (*17*). In combination with computations, which are difficult because the flow is turbulent, this work is helping guide a new generation of actively controlled environments in buildings, such as the window-opening strategies employed in the Federal Building in San Francisco (*18*). There are also promising efforts using geophysical-scale forecasting to control the flow of environmental pollutants, by timing their release based on computational assimilation of field data; examples include ozone-regulatory enforcement in Arizona (*19*) and pollution dispersion in Monterey Bay (*20*). Indeed, there is a close connection between the theoretical basis for geophysical-scale forecasting and model-based flow control. By integrating the perspectives and techniques from both the aerodynamic flow control and weather forecasting communities, great fundamental advances are yet to come.

References and Notes

1. H. A. Stone, A. D. Stroock, A. Ajdari, *Annu. Rev. Fluid Mech.* **36**, 381 (2004).
2. P. K. Wong, Y.-K. Lee, C.-M. Ho, *J. Fluid Mech.* **497**, 55 (2003).
3. F. E. Fish, G. V. Lauder, *Annu. Rev. Fluid Mech.* **38**, 193 (2006).
4. M. S. Triantafyllou, A. H. Techet, F. Hover, *IEEE J. Ocean. Eng.* **29**, 585 (2004).
5. E. A. van Nierop, S. Alben, M. P. Brenner, *Phys. Rev. Lett.* **100**, 054502 (2008).
6. T. Hamilton, *MIT Tech. Rev.* (6 March 2008).
7. W. Scharfman, *Scientist* **20**, 17 (2007).
8. See www.nasa.gov/home/hqnews/2008/feb/HQ_08053_Speedo.html.
9. H. Choi, W.-P. Jeon, J. Kim, *Annu. Rev. Fluid Mech.* **40**, 113 (2008).
10. H. D. Lou, F. S. Alvi, C. Shih, *AIAA J.* **44**, 58 (2006).
11. A. Glezer, M. Amitay, *Annu. Rev. Fluid Mech.* **34**, 503 (2002).
12. J. Kim, T. R. Bewley, *Annu. Rev. Fluid Mech.* **39**, 383 (2007).
13. R. Rathnasingham, K. S. Breuer, *J. Fluid Mech.* **495**, 209 (2003).
14. C. W. Rowley, *Int. J. Bifurcation Chaos* **15**, 997 (2005).
15. M. Weldon, T. Peacock, G. Jacobs, M. Helu, G. Haller, *J. Fluid Mech.*, in press. Preprint available at web.mit.edu/peacocklab/separation.shtml.
16. See www.eia.doe.gov/.
17. G. R. Hunt, P. F. Linden, *J. Fluid Mech.* **527**, 27 (2005).
18. G. Carrilho da Graca, P. F. Linden, P. Haves, *Building Serv. Eng. Res. Technol.* **25**, 223 (2004).
19. S. M. Lee, H. J. S. Fernando, S. Grossman Clarke, *Environ. Model. Assess.* **12**, 63 (2007).
20. C. Coulliette, F. Lekien, J. D. Paduan, G. Haller, J. E. Marsden, *Environ. Sci. Technol.* **41**, 6562 (2007).

21. We thank T. Bewley for helpful discussions.

10.1126/science.1153479

Rise of the Andes

Carmala N. Garzione,[1]* Gregory D. Hoke,[1] Julie C. Libarkin,[2] Saunia Withers,[3] Bruce MacFadden,[4] John Eiler,[5] Prosenjit Ghosh,[6] Andreas Mulch[7]

The surface uplift of mountain belts is generally assumed to reflect progressive shortening and crustal thickening, leading to their gradual rise. Recent studies of the Andes indicate that their elevation remained relatively stable for long periods (tens of millions of years), separated by rapid (1 to 4 million years) changes of 1.5 kilometers or more. Periodic punctuated surface uplift of mountain belts probably reflects the rapid removal of unstable, dense lower lithosphere after long-term thickening of the crust and lithospheric mantle.

The surface uplift of mountain belts, such as the central Andes plateau, has long been thought to be the isostatic response of shortening and thickening of the continental crust. Recently developed isotopic techniques allow us to determine the uplift history of the central Andes independently from the shortening history. These results show that shortening and uplift are temporally decoupled, with shortening and thickening happening over protracted periods of time, whereas uplift occurs geologically rapidly. Thus arises a paradox: Why does slow, continuous shortening and thickening not produce slow, continuous isostatic uplift in the central Andes?

Both crustal thickening and the removal of relatively dense mantle or lower crust can generate isostatic surface uplift (*1*, *2*). Paleoelevation studies help resolve the geodynamic evolution of mountain belts because the rate and lateral extent of surface uplift depends on the processes involved. Here, we synthesize the elevation history of the central Andes, Earth's second largest mountain belt. We then compare paleoelevation estimates to histories of regional incision, sedimentation, shortening, and volcanism within the mountain belt to characterize lithospheric evolution and the geodynamic mechanisms that led to surface uplift.

The central Andean plateau (Fig. 1), with a width of ~400 km and an average elevation of ~4 km, is a typical example of an active plate margin where oceanic lithosphere is subducted beneath continental lithosphere. At its widest, the central Andean plateau consists of the internally drained Altiplano basin at an elevation of ~3800 m that is bounded by the Western and Eastern Cordilleras, where peak elevations exceed 6 km. The Western Cordillera is a chain of volcanic edifices associated with the modern Andean magmatic arc, whereas the Eastern Cordillera and Altiplano basin record a history of folding and faulting. The central Andes have a protracted crustal shortening history spanning the last 50 million years (My) (*3*–*5*) that has generated crustal thicknesses of ~70 km below the highest topography in the Eastern and Western Cordillera and 60 to 65 km below the central Altiplano (*6*). Geophysical observations suggest that eclogitic lower crust is absent beneath much of the plateau (*6*). The mantle between 16°S and 20°S shows the lowest *P* wave velocities below the Altiplano/Eastern Cordillera transition, suggesting that virtually all of the mantle lithosphere has been

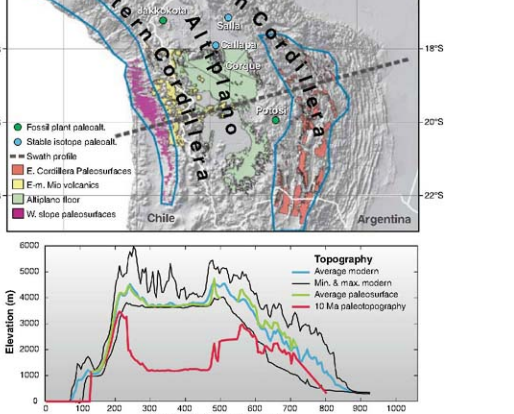

Fig. 1. Elevations of the Central Andean plateau based on Shuttle Radar Topography Mission 30 data and modern versus 10 Ma paleotopography profiles. (**Top**) Shaded relief topography of the central Andean plateau between 17.5°S and 23°S with colored areas representing the different paleosurface data used to reconstruct the topography of the Andes at 10 Ma. Regions outlined in blue show low-relief paleosurfaces that underwent rotation and incision beginning in late Miocene time. Green dots denote locations of Miocene paleobotanical estimates of paleoelevation (*20*, *21*). Blue dots indicate locations of late Miocene stable isotope paleoelevation and paleotemperature estimates shown in Fig. 2. The large gap between the pale green and red paleosurfaces corresponds to the Los Frailes ignimbrite shield. The dashed line marks the center of a 100-km-wide swath average profile across the central Andean plateau. (**Bottom**) Profiles showing the modern maximum and minimum topography (thin black lines), the average modern topography (light blue), and the average topography of the areas identified as paloesurfaces (green). The red line represents the topography of the Andes at 10 Ma based on the paleoelevation estimates given in Fig. 4 (center of plateau) and river incision-based estimates of relief generation for the eastern and western flanks of the Altiplano. The data gap created by the Los Frailes ignimbrite shield and the Subandes is filled by linear interpolations.

[1]Department of Earth and Environmental Sciences, University of Rochester, Rochester, NY 14627, USA. [2]Department of Geological Sciences, Michigan State University, East Lansing, MI 48824, USA. [3]Department of Plant Biology, Michigan State University, East Lansing, MI 48824, USA. [4]Florida Museum of Natural History, University of Florida, Gainesville, FL 32611, USA. [5]Division of Geological and Planetary Sciences, California Institute of Technology, Pasadena, CA 91125, USA. [6]Center for Atmospheric and Oceanic Science, Indian Institute of Science, Bangalore, 560 012, India. [7]Institut für Geologie, Universität Hannover, 30167 Hannover, Germany.

*To whom correspondence should be addressed. E-mail: garzione@earth.rochester.edu

removed (*7*–*9*). In addition, high $^3He/^4He$ ratios in hydrothermal fluids and gases across much of the Altiplano and Eastern Cordillera indicate the degassing of mantle asthenosphere-derived magmas (*10*). Together, these observations support previous suggestions for the southern Altiplano and Puna (*11*, *12*) that both mantle lithosphere and eclogitic lower crust were removed below much of the Altiplano and the western part of the Eastern Cordillera (*6*). Removal of lower lithosphere might occur rapidly by delamination or convective removal (*1*, *13*) or gradually by ablative subduction of foreland cratonic lithosphere (*14*, *15*). Either case results in an influx of lighter asthenosphere, generating surface uplift of several kilometers. However, rapid removal of lower lithosphere would result in surface uplift in as little as several million years, whereas gradual removal by ablative subduction would generate surface uplift over tens of millions of years, coincident with crustal shortening.

Climate Trends and Subsidence History

The Altiplano and Eastern Cordillera contain thick accumulations of Oligocene through late Miocene fluvial, floodplain, and lacustrine deposits (*16*). The oxygen ($\delta^{18}O$) and hydrogen (δD) isotopic composition of paleosol carbonates and authigenic clays from volcaniclastic units provide a record of meteoric water composition that is the basis for stable isotope paleoelevation estimates (Fig. 2). Stable carbon isotope ($\delta^{13}C$) values of paleosol carbonates provide a record of plant respiration rates that can be used as a proxy for aridity (i.e., lower plant respiration reflects a more arid climate). Depositional environments within a 3.6-km-thick succession preserved in the eastern limb of the Corque syncline include fluvial channel sandstones and floodplain mudstones in the lower 1.4 km and upper 700 m, as well as a widespread freshwater-to-playa lake system that can be traced more than 100 km along strike. Both sedimentology and carbon isotopes in this section suggest that the central Altiplano became more arid between ~10 and 6 million years ago (Ma) (*17*). Fluvial channel deposits decreased in thickness and lateral extent up-section, further suggesting a decrease in discharge. Over the same time interval, $\delta^{13}C$ values of pedogenic carbonates increased by ~3 per mil (‰), suggesting a decrease in plant-respired CO_2 (*17*). Despite evidence for increasing aridity, the $\delta^{18}O$ values of palustrine and paleosol carbonates ($\delta^{18}O_c$) decrease by ~3 ‰ (Fig. 2), a change opposite of the expected trend for higher rates of surface-water evaporation. More positive $\delta^{18}O$ values observed in the older part of the record are synchronous with observations of wetter conditions, suggesting that evaporative enrichment of ^{18}O is an unlikely cause for the trend to more negative $\delta^{18}O$ values over time.

Sedimentation rates in the Altiplano reflect rates of subsidence relative to the surrounding topography. Sedimentation rates in the central Altiplano and Puna dramatically decreased after 10 Ma (*18*) (Fig. 3). Between 13 and 9 Ma, sedimentation rates were extremely high, averaging 880 m/My (Fig. 3). During this time period, widespread lacustrine deposition suggests underfilled basin conditions. By 8.6 Ma, fluvial deposition resumed and subsidence decreased dramatically, averaging 0.12 mm/year.

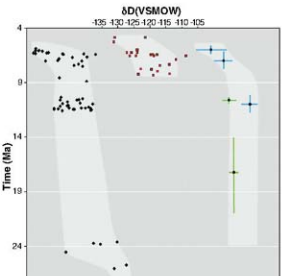

Fig. 2. Stable isotope paleoelevation proxies over time. $\delta^{18}O$ and δD values are from authigenic (paleosol and palustrine) carbonates and shallow groundwater cements. δD values are from authigenic clays in volcanic ash deposits. Paleotemperature estimates are derived from Δ_{47} measurements on pedogenic carbonates (*22*) (blue) and fossil-leaf physiognomy (*20*, *21*) (green). Horizontal error bars reflect the 1σ variation on a group of pedogenic nodules. Vertical bars represent the age range (including uncertainty) of the sample group. VSMOW, Vienna standard mean ocean water; VPDB, Vienna Pee Dee belemnite.

Paleoelevation Constraints

Shallow marine deposits of the El Molino Formation require that the Altiplano lay at sea level at the end of Cretaceous time (*19*). Paleotemperature estimates derived from fossil-leaf physiognomy in the northern Altiplano and Eastern Cordillera (Fig. 1) suggest that paleoelevations were <1.3 km at ~15 to 20 Ma (*20*) and <2 km by ~10 Ma (*21*). Both the oxygen isotopic composition of rainfall and surface temperatures vary as a function of elevation. Stable oxygen isotope values of pedogenic carbonate and carbonate cement should reflect the composition of soil water and shallow groundwater, which is a reflection of rainfall composition and near surface temperature. The abundance of ^{13}C–^{18}O bonds relative to a random distribution of carbon and oxygen isotopes in carbonate (measured by the Δ_{47} value of CO_2 extracted from carbonates) should record the soil carbonate precipitation temperature (*22*). Carbonate $\delta^{18}O$ values and Δ_{47} temperature estimates decrease with time (*17*, *22*, *23*), suggesting that elevations increased by 2.5 ± 1 km during late Miocene time, consistent with low elevation estimates from fossil leaves.

We supplement these elevation records with δD data from authigenic clays in late Miocene ash deposits in the Callapa section and $\delta^{18}O$ data from late Oligocene to early Miocene pedogenic carbonates from the Salla and Huayllapucara/Totora Formations (*16*) (Figs. 1 and 2 and tables S4 and S6). One challenge in interpreting stable isotope records of elevation is that they can be biased toward lower elevation estimates (i.e., more positive values) by increased surface-water evaporation associated with climate change. δD data of authigenic clay minerals in combination with the oxygen isotope carbonate record ($\delta^{18}O_c$) provide a qualitative assessment of this bias because of the retention and fractionation behavior of hydrogen and oxygen in soil and lake water during evaporation (*24*). δD values of smectite from volcanic ashes of the Callapa Formation parallel $\delta^{18}O_c$ values (Fig. 2) and decrease by about 10 to 20 ‰ during the late Miocene. Despite increasingly arid climate, the combined $\delta^{18}O_c$ and δD data show trends toward more negative isotopic compositions of meteoric water, supporting the inference that the decrease in $\delta^{18}O_c$ reflects a change in surface elevation of the Bolivian Altiplano.

Before the late Miocene, $\delta^{18}O_c$ values and paleotemperature estimates suggest a long history of fairly stable surface temperatures and isotopic compositions of surface waters (Fig. 2), perhaps reflecting minimal surface elevation change between ~25 and 10 Ma. Using the paleotemperature estimates from an early middle Miocene fossil-leaf assemblage (*21*), we converted the $\delta^{18}O_c$ values of late Oligocene to early Miocene soil carbonates to surface-water values ($\delta^{18}O_w$) (*25*). For the modern isotopic lapse rate of $h = 472.5\delta^{18}O_{rainfall} - 2645$ [where h = elevation in meters (*17*)], paleoelevation is <2.3 ± 1 km (*26*) between 10 and 25 Ma, broadly consistent with fossil-leaf estimates (*20*) (Fig. 4). Before 25 Ma, the only paleoelevation estimates come from paleosol carbonates of the Salla Formation. Both high $\delta^{18}O_c$ values and high paleotemperature estimates, based on Δ_{47} values (table S5), suggest elevations close to sea level. [Assuming modern temperature and $\delta^{18}O$ lapse rates, reconstructed $\delta^{18}O_w$ are similar to modern values in the Amazon foreland, and temperatures are slightly warmer than those in the foreland (Fig. 4).] The relatively positive late Oligocene to early Miocene $\delta^{18}O_c$ values cannot be explained by diagenesis of carbonate because both higher temperatures and/or diagenesis in the presence of later fluids should produce more negative $\delta^{18}O_c$ values (*27*), which are not observed. In addition, Δ_{47} values suggest reasonable temperatures for surface environments, as opposed to the higher temperatures that might result from burial diagenesis.

The $\delta^{18}O_c$, Δ_{47}, and δD compilation (Figs. 2 and 4) suggests that there was at least one discrete

pulse of rapid surface uplift of ~1.5 to 3.5 km (2.5 ± 1 km) between ~10 and 6 Ma and perhaps an earlier phase of surface uplift at ~25 Ma. However, limited data between 30 and 20 Ma preclude an understanding of the nature and extent of the older event. In the following discussion, we review geologic histories of the magmatism, shortening, and incision within the central Andean plateau that, when viewed with sedimentation rates and surface uplift history, shed light on the regional geodynamic processes that induced late Miocene surface uplift.

Magmatism and Distribution of Shortening

Widespread felsic magmatism in the Andean plateau began between 18°S and 24°S at ~25 Ma (*28*) and has been attributed to steepening of the subducting Nazca slab (*29*). Despite its wide extent, the volume of pre-late Miocene magmatism was small. Most activity (>85%) between 19°S and 23.5°S occurred between ~8.5 and 4 Ma (*30*, *31*). Mafic lavas erupted throughout the northern and central Altiplano beginning at ~7.5 to 5.5 Ma (*32*, *33*) and at ~7 to 3 Ma in the southern Altiplano and Puna (*13*, *34*) (Fig. 5D). One group of lavas that erupted between 25°S and 26.5°S shows trace element and radiogenic isotopic compositions characteristic of an asthenospheric source, inferred to reflect the removal of eclogitic lower crust and mantle lithosphere beneath the southern Altiplano and Puna plateaus (*34*).

From 30 to 10 Ma, the Andean plateau experienced east-to-west shortening by ~6 to 12 mm/year across the plateau (*3*, *5*). From 10 to 7 Ma, while elevation increased, shortening ceased and deformation propagated eastward into the Subandean zone (*4*, *35*) (Fig. 5C). This shift in the locus of shortening is consistent with surface uplift, which should decrease the horizontal deviatoric compressive stress under the plateau while applying greater force per unit length to the surrounding lowland.

Geomorphology

Changes in the relief structure of the Plateau also imply that surface uplift occurred since ~10 Ma (*36*–*38*). Paleosurfaces on both the eastern slope of the Eastern Cordillera (*36*, *37*) and the western slope of the Western Cordillera (*38*–*43*) reflect remnants of low-relief drainage systems that were active between ~7 and 12 Ma in the Eastern Cordillera (*36*, *37*) and until ~10 Ma on the western slope (*44*). Widespread incision of the paleosurfaces in the Eastern Cordillera began by ~6.5 Ma (*37*) and in the Western slope began between ~9 and 5.5 Ma (*40*, *42*, *43*). Cooling ages of minerals in the Eastern Cordillera also imply that rapid incision began between ~15 and 6 Ma in the absence of substantial shortening (*45*, *46*). Reconstructions of the relief in these incised valleys suggest ~2 km of surface uplift of the Eastern Cordillera (*47*) and ~1 to 2.5 km of surface uplift of the Western Cordillera (*40*–*42*). The western slope of the Andes (north of ~30°S) has had an arid-to-hyperarid climate since at least 15 Ma (*48*–*50*), indicative of atmospheric circulation patterns similar to the modern pattern, in which rainfall is derived predominantly from the east. Despite dramatically different climates between west and east, the similar timing of incision on the western and eastern slopes supports the notion that incision was induced by surface uplift and rotation of the slopes.

The widespread extent of incision implies that the entire width of the mountain belt—over at least 5° latitude—rose (Fig. 1A) (*51*). The regional late Miocene paleotopography can be reconstructed using surface uplift estimates in Fig. 4 (for the Altiplano) and the magnitude of relief generated during incision of the Eastern and Western cordilleras (*40*, *47*) (Fig. 1B). There is a large difference in cross-sectional area between the average modern elevation of the paleosurface and the 10-Ma reconstructed topography. For crustal thickening to account for this difference would require shortening rates in excess of 40 mm/year over the 1 to 3 My during which surface uplift occurred. This is four times greater than the observed rates in the Andean plateau over the past 40 My, which seems implausible. Flow of middle-lower crust from the Eastern and Western cordilleras to the Altiplano (*52*) fails to explain the simultaneous rise of the cordilleras, which should subside or remain the same elevation as lower crustal material flows laterally. We conclude that the rapid rate, magnitude, and regional extent of surface uplift, in addition to crustal thickening, also require a mantle contribution, most likely the isostatic response to removal of eclogite and mantle lithosphere.

Climatic responses to Andean surface uplift may extend beyond South America. For example, the presence of the Andes deflects the Intertropical Convergence Zone to north of the equator in the Pacific, which influences the strength and distribution of monsoonal climates with Pacific teleconnections (*53*). It is therefore possible that punctuated Andean surface uplift contributed to the reorganization of south Asian climate observed in the late Miocene.

Geodynamic Implications

Crustal thicknesses of 60 to 70 km in the central Andes are the result of protracted shortening and thickening over the past 50 My. Despite extensive crustal thickening, regional reconstruction of paleotopography suggests paleoelevations of <2 km in the Altiplano and 2.5 to 3.5 km in the Eastern and Western cordilleras until ~10 Ma (*51*). These anomalously low paleoelevations probably reflect the presence of dense eclogitic lower crust, which held the surface down. An analogous region today might be the western Sierras Pampeanas in Argentina, with 60-km-thick crust but average elevations of ~1 km (*54*).

Geologic observations suggest that the internal structure of the Andean lithosphere changed between ~10 and 6 Ma. During this time, the entire width of the plateau experienced surface uplift, deep incision of low-relief paleosurfaces initiated on the eastern and western slopes of the Andes, sedimentation rates within the Altiplano basin decreased dramatically while the basin

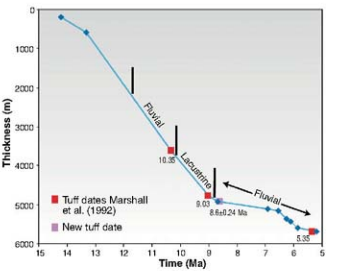

Fig. 3. Sediment thickness (nondecompacted) versus time for deposition in eastern limb of the Corque syncline. Stratigraphic thickness versus age in rocks older than 10.35 My come from (*57*). Constraints on geologic time are indicated by different symbols: red squares are dates from (*58*), the purple square is the new tuff age reported here (*16*), and blue diamonds are revised magnetostratigraphy (*16*). The blue line reflects the rate of sediment accumulation and changes in depositional environment are labeled accordingly. Note the marked decrease in accumulation rates after 9 Ma associated with a change from lacustrine to fluvial deposition.

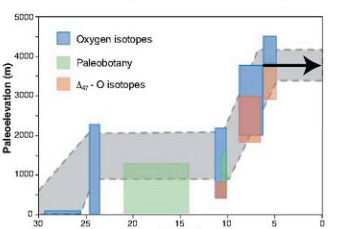

Fig. 4. Multiple proxies of elevation versus time for the central Andean plateau over the past 30 My. Paleoelevation estimates are derived from oxygen isotopes (*17*, *23*), both Δ_{47} and oxygen isotopes (*17*, *22*), and fossil-leaf physiognomy (*20*, *21*).

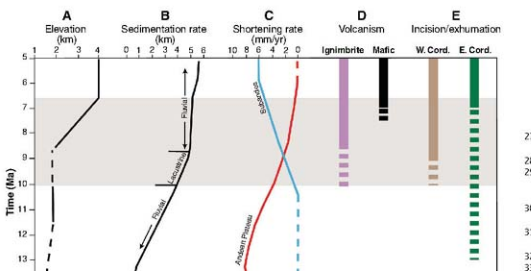

Fig. 5. Synthesis of geologic events that occurred in the central Andean plateau between ~17°S and 26° S latitude during the middle to late Miocene. **(A)** Elevation history based on the various proxies in Fig. 4. **(B)** Subsidence rate for the sediments exposed in the Corque syncline (Fig. 3). **(C)** Cumulative shortening rates for the Andean plateau (*5*) and Subandean range (*4*). **(D)** Volcanic activity (*12*, *31*). **(E)** Incision and exhumation of the eastern (*36*, *37*, *45*, *46*) and western flanks (*40*, *42*, *43*) of the central Andean plateau.

transitioned from underfilled lacustrine environments to filled fluvial/floodplain environments, shortening ceased in the plateau and propagated into the foreland, and widespread and voluminous ignimbrite eruption began, followed closely in time by mafic volcanism (Fig. 5). Together, these observations are best explained by the removal of dense eclogite and mantle lithosphere, triggering regional surface uplift of ~1.5 to 2.5 km. The amount of surface uplift requires the removal of eclogite and mantle lithosphere of ~80 to 140 km thick, an amount that fits within the geometry of the subduction zone (*51*). Removal by drips of downward-flowing lower lithosphere can explain the sedimentation history in the Altiplano in that the region above the drip should experience rapid subsidence during drip formation (*5.5*), accompanied by rapid rates of sedimentation and underfilled basin conditions. Both rapid sedimentation and underfilled lacustrine conditions are observed in the Altiplano between ~13 and 9 Ma, just before the late Miocene surface uplift (Figs. 3 and 5, A and B). We suggest that the morphology of broad, flat, high-elevation, orogenic plateaus is the product of phases of both crustal and mantle lithosphere thickening punctuated by discrete intervals of surface uplift associated with the convective removal of dense lower crust and mantle lithosphere. Between ~40 and 10 Ma, crustal shortening, lower crustal flow, and erosion/sedimentation redistributed crustal lithosphere while eclogitic lower crust and mantle lithosphere accumulated at depth. This long-term history created the conditions that resulted in lower lithosphere removal between ~10 and 6 Ma. After 6 Ma, continued lower crustal flow and erosion and sedimentation redistributed mass within the crust to enhance the low-relief landscape observed in the plateau today.

References and Notes

1. P. Bird, *J. Geophys. Res.* **83**, 4975 (1978).
2. P. A. England, G. A. Houseman, *J. Geophys. Res.* **94**, 17561 (1989).
3. N. McQuarrie, B. K. Horton, G. Zandt, S. Beck, P. G. DeCelles, *Tectonophysics* **399**, 15 (2005).
4. L. Echavarria, R. Hernandez, R. Allmendinger, J. Reynolds, *Am. Assoc. Pet. Geol. Bull.* **87**, 965 (2003).
5. K. Elger, O. Oncken, J. Glodny, *Tectonics* **24**, TC4020 (2005).
6. S. L. Beck, G. Zandt, *J. Geophys. Res.* **107**, 2230 (2002).
7. P. Wigger *et al.*, in *Tectonics of the Southern Central Andes: Structure and Evolution of an Active Continental Margin*, K. J. Reutter, E. Scheuber, P. J. Wigger, Eds. (Springer, Berlin, 1994), pp. 23–48.
8. C. Dorbath, M. Granet, *Tectonophysics* **259**, 117 (1996).
9. S. C. Myers, S. Beck, G. Zandt, T. Wallace, *J. Geophys. Res.* **103**, 21233 (1998).
10. L. Hoke, D. R. Hilton, S. H. Lamb, K. Hammerschmidt, H. Friedrichsen, *Earth Planet. Sci. Lett.* **188**, 341 (1994).
11. R. W. Kay, S. M. Kay, *Tectonophysics* **219**, 177 (1993).
12. S. M. Kay, C. Mpodozis, B. Coira, in *Geology and Ore Deposits of the Central Andes*, B. J. Skinner, Ed. (Society of Economic Geologists, Littleton, CO, 1999), vol. 7, pp. 27–59.
13. G. A. Houseman, D. P. McKenzie, P. Molnar, *J. Geophys. Res.* **86**, 6115 (1981).
14. W. C. Tao, R. J. O'Connell, *J. Geophys. Res.* **97**, 8877 (1992).
15. D. C. Pope, S. D. Willett, *Geology* **26**, 511 (1998).
16. Supporting online material is available on *Science* Online.
17. J. Quade, C. Garzione, J. Eiler, *Rev. Mineral. Geochem.* **66**, 53 (2007).
18. R. W. Allmendinger, T. E. Jordan, S. M. Kay, B. L. Isacks, *Annu. Rev. Earth Planet. Sci.* **25**, 139 (1997).
19. T. Sempere *et al.*, *Geol. Soc. Am. Bull.* **109**, 709 (1997).
20. K. M. Gregory-Wodzicki, *Geol. Soc. Am. Bull.* **112**, 1091 (2000).
21. K. M. Gregory-Wodzicki, K. Velasquez, W. C. Macintosh, *J. South Am. Earth Sci.* **11**, 533 (1998).
22. P. Ghosh, C. N. Garzione, J. M. Eiler, *Science* **311**, 511 (2006).
23. C. N. Garzione, P. Molnar, J. C. Libarkin, B. J. MacFadden, *Earth Planet. Sci. Lett.* **241**, 543 (2006).
24. A. Maltch, C. P. Chamberlain, *Rev. Min. Geochem.* **66**, 89 (2007).
25. S.-T. Kim, J. R. O'Neil, *Geochim. Cosmochim. Acta* **61**, 3461 (1997).
26. Uncertainties are estimated as in (*56*) by assuming that the modern climate captures the characteristics of the rainout process in the past. Using a bootstrap simulation approach, errors are propagated by incorporating the scatter in empirical data that constrain the $\delta^{18}O_w$-versus-altitude gradient, uncertainty of ±5°C on the temperature of carbonate precipitation, and scatter in the temperature-dependent ^{18}O fractionation between water and calcite. This yields 1σ errors of ±500 m at elevations >4 km, increasing to ±1000 m at elevations of <1 km. Assuming a Rayleigh distillation process for fractionation during condensation from a vapor mass, higher-than-modern global temperature in the late Oligocene to late Miocene would lower the $\delta^{18}O_w$-versus-altitude gradient, which would cause an underestimation of paleoelevation for distillation from a vapor mass with a similar to modern starting composition (*56*).
27. C. N. Garzione, D. L. Dettman, B. K. Horton, *Palaeogeogr. Palaeoclimatol. Palaeoecol.* **212**, 119 (2004).
28. B. L. Isacks, *J. Geophys. Res.* **93**, 3211 (1988).
29. D. E. James, I. S. Sacks, B. J. Skinner, in *Geology and Ore Deposits of the Central Andes*, B. J. Skinner, Ed. (Society of Economic Geologists, Littleton, CO, 1999), vol. 7, pp. 1–25.
30. M. C. W. Baker, P. W. Francis, *Earth Planet. Sci. Lett.* **41**, 175 (1978).
31. S. L. de Silva, W. D. Gosnold, *J. Volcanol. Geotherm. Res.* **167**, 320 (2007).
32. S. Lamb, L. Hoke, *Tectonics* **16**, 623 (1997).
33. G. Carlier *et al.*, *Geology* **33**, 601 (2005).
34. S. M. Kay, B. Coira, J. Viramonte, *J. Geophys. Res.* **99**, 24323 (1994).
35. I. Moretti, P. Baby, M. E. D. Zubieta, *Petrol. Geosci.* **2**, 17 (1996).
36. T. L. Gubbels, B. L. Isacks, E. Farrar, *Geology* **21**, 695 (1993).
37. L. Kennan, S. H. Lamb, L. Hoke, in *Palaeosurfaces: Recognition, Reconstruction and Palaeoenvironmental Interpretation*, M. Widdowson, Ed. (Geological Society of London, London, 1997), vol. 120, pp. 307–323.
38. M. Farías, R. Charrier, D. Comte, J. Martinod, G. Hérail, *Tectonics* **24**, TC4001 (2005).
39. M. García, G. Hérail, *Geomorphology* **65**, 279 (2005).
40. G. D. Hoke *et al.*, *Tectonics* **26**, TC5021 (2007).
41. F. Kober, F. Schlunegger, G. Zellinger, H. Schneider, in *Tectonics, Climate and Landscape Evolution*, S. D. Willett, N. Hovius, M. T. Brandon, D. M. Fisher, Eds. (Geological Society of America, Denver, CO, 2006), pp. 75–86.
42. T. F. Schildgen, K. V. Hodges, K. Whipple, P. W. Reiners, M. S. Pringle, *Geology* **35**, 523 (2007).
43. J.-C. Thouret *et al.*, *Earth Planet. Sci. Lett.* **263**, 151 (2007).
44. G. D. Hoke, B. L. Isacks, T. E. Jordan, J. S. Yu, *Geology* **32**, 605 (2004).
45. J. B. Barnes, T. A. Ehlers, N. McQuarrie, P. B. O'Sullivan, J. D. Pelletier, *Earth Planet. Sci. Lett.* **248**, 118 (2006).
46. R. J. Gillis, B. K. Horton, M. Grove, *Tectonics* **26**, (2006); 10.1029/2005TC001887.
47. R. Barke, S. Lamb, *Earth Planet. Sci. Lett.* **249**, 350 (2006).
48. J. Houston, A. J. Hartley, *Int. J. Climatol.* **23**, 1453 (2003).
49. C. N. Alpers, G. H. Brimhall, *Geol. Soc. Am. Bull.* **100**, 1640 (1988).
50. J. A. Rech, B. S. Currie, G. Michalski, A. M. Cowan, *Geology* **34**, 761 (2006).
51. G. D. Hoke, C. N. Garzione, *Earth Planet. Sci. Lett.*, published online 22 April 2008; 10.1016/j.epsl.2008.04.008.
52. L. Husson, T. Sempere, *Geophys. Res. Lett.* **30**, 1243 (2003).
53. K. Takahashi, D. S. Battisti, *J. Clim.* **20**, 3434 (2007).
54. H. Gilbert, S. Beck, G. Zandt, *Geophys. J. Int.* **165**, 383 (2006).
55. G. A. Houseman, E. A. Neil, M. D. Kohler, *J. Geophys. Res.* **105**, 16237 (2000).
56. D. B. Rowley, C. N. Garzione, *Annu. Rev. Earth Planet. Sci.* **35**, 463 (2007).
57. P. Roperch, G. Herail, M. Forani, *J. Geophys. Res.* **104**, 20415 (1999).
58. L. G. Marshall, C. C. Swisher III, A. Lavenu, R. Hoffstetter, G. H. Curtis, *J. South Am. Earth Sci.* **5**, 1 (1992).

59. We thank D. Foster for $^{40}Ar/^{39}Ar$ analyses and R. Allmendinger and P. Molnar for suggestions that improved the paper. This work was supported by NSF EAR grants 0230232 and 0635678 (to C.N.G.) and 0350396 (to J.C.L.).

Supporting Online Material

www.sciencemag.org/cgi/content/full/320/5881/1304/DC1
Materials and Methods
SOM Text
Figs. S1 to S4
Tables S1 to S6
References

27 September 2007; accepted 18 March 2008
10.1126/science.1148615

Fine Structure Constant Defines Visual Transparency of Graphene

R. R. Nair,[1] P. Blake,[1] A. N. Grigorenko,[1] K. S. Novoselov,[1] T. J. Booth,[1] T. Stauber,[2] N. M. R. Peres,[2] A. K. Geim[1]*

There are few phenomena in condensed matter physics that are defined only by the fundamental constants and do not depend on material parameters. Examples are the resistivity quantum, h/e^2, that appears in a variety of transport experiments, including the quantum Hall effect and universal conductance fluctuations, and the magnetic flux quantum, $h/2e$, playing an important role in the physics of superconductivity (h is Planck's constant and e the electron charge). By and large, it requires sophisticated facilities and special measurement conditions to observe any of these phenomena. In contrast, we show that the opacity of suspended graphene (*1*) is defined solely by the fine structure constant, $\alpha = e^2/\hbar c \approx 1/137$ (where c is the speed of light), the parameter that describes coupling between light and relativistic electrons and that is traditionally associated with quantum electrodynamics rather than materials science. Despite being only one atom thick, graphene is found to absorb a significant ($\pi\alpha \approx 2.3\%$) fraction of incident white light, a consequence of graphene's unique electronic structure.

It was recently argued (*2*, *3*) that the high-frequency (dynamic) conductivity G for Dirac fermions (*1*) in graphene should be a universal constant equal to $e^2/4\hbar$ and different from its universal dc conductivity, $4e^2/\pi h$ [however, the experiments do not comply with the prediction for dc conductivity (*1*)]. The universal G implies (*4*) that observable quantities such as graphene's optical transmittance T and reflectance R are also universal and given by $T = (1 + 2\pi G/c)^{-2} \approx (1 + \frac{1}{2}\pi\alpha)^{-2}$ and $R = \frac{1}{4}\pi^2\alpha^2 T$ for the normal light incidence. In particular, this yields graphene's opacity $(1 - T) \approx \pi\alpha$ [this expression can also be derived by calculating the absorption of light by two-dimensional Dirac fermions with Fermi's golden rule (*5*)]. The origin of the optical properties being defined by the fundamental constants lies in the two-dimensional nature and gapless electronic spectrum of graphene and does not directly involve the chirality of its charge carriers (*5*).

We have studied specially prepared graphene crystals (*5*) such that they covered submillimeter apertures in a metal scaffold (Fig. 1A inset). Such large one-atom-thick membranes suitable for optical studies were previously inaccessible (*6*). Figure 1A shows an image of one of our samples in transmitted white light. In this case, we have chosen to show an aperture that is only partially covered by suspended graphene so that opacities of different areas can be compared. The line scan across the image qualitatively illustrates changes in the observed light intensity. Further measurements (*5*) yield graphene's opacity of $2.3 \pm 0.1\%$ and negligible reflectance (<0.1%), whereas optical spectroscopy shows that the opacity is practically independent of wavelength, λ (Fig. 1B) (*5*). The opacity is found to increase with membranes' thickness so that each graphene layer adds another 2.3% (Fig. 1B inset). Our measurements also yield a universal dynamic conductivity $G = (1.01 \pm 0.04)$ $e^2/4\hbar$ over the visible frequencies range (*5*), that is, the behavior expected for ideal Dirac fermions.

The agreement between the experiment and theory is striking because it was believed that the universality could hold only for low energies ($E < 1$ eV), beyond which the electronic spectrum of graphene becomes strongly warped and nonlinear and the approximation of Dirac fermions breaks down. However, our calculations (*5*) show that finite-E corrections are surprisingly small (a few %) even for visible light. Because of these corrections, a metrological accuracy for α would be difficult to achieve, but it is remarkable that the fine structure constant can so directly be assessed practically by the naked eye.

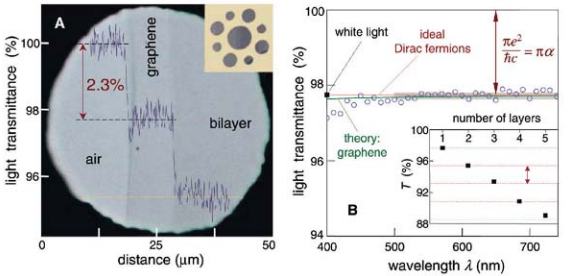

Fig. 1. Looking through one-atom-thick crystals. **(A)** Photograph of a 50-μm aperture partially covered by graphene and its bilayer. The line scan profile shows the intensity of transmitted white light along the yellow line. (Inset) Our sample design: A 20-μm-thick metal support structure has several apertures of 20, 30, and 50 μm in diameter with graphene crystallites placed over them. **(B)** Transmittance spectrum of single-layer graphene (open circles). Slightly lower transmittance for $\lambda < 500$ nm is probably due to hydrocarbon contamination (*5*). The red line is the transmittance $T = (1 + 0.5\pi\alpha)^{-2}$ expected for two-dimensional Dirac fermions, whereas the green curve takes into account a nonlinearity and triangular warping of graphene's electronic spectrum. The gray area indicates the standard error for our measurements (*5*). (Inset) Transmittance of white light as a function of the number of graphene layers (squares). The dashed lines correspond to an intensity reduction by $\pi\alpha$ with each added layer.

References and Notes

1. A. K. Geim, K. S. Novoselov, *Nat. Mater.* **6**, 183 (2007).
2. T. Ando, Y. Zheng, H. Suzuura, *J. Phys. Soc. Jpn.* **71**, 1318 (2002).
3. V. P. Gusynin, S. G. Sharapov, J. P. Carbotte, *Phys. Rev. Lett.* **96**, 256802 (2006).
4. A. B. Kuzmenko, E. van Heumen, F. Carbone, D. van der Marel, *Phys. Rev. Lett.* **100**, 117401 (2008).
5. Materials and methods are available on *Science* Online.
6. J. S. Bunch *et al.*, *Science* **315**, 490 (2007).
7. We are grateful to A. Kuzmenko, A. Castro Neto, P. Kim, and L. Eaves for illuminating discussions. Supported by Engineering and Physical Sciences Research Council (UK), the Royal Society, European Science Foundation, and Office of Naval Research.

Supporting Online Material
www.sciencemag.org/cgi/content/full/1156965/DC1
Materials and Methods
SOM Text
Figs. S1 to S5
References

25 February 2008; accepted 26 March 2008
Published online 3 April 2008;
10.1126/science.1156965
Include this information when citing this paper.

[1]Manchester Centre for Mesoscience and Nanotechnology, University of Manchester, M13 9PL Manchester, UK. [2]Department of Physics, University of Minho, P-4710-057 Braga, Portugal.
*To whom correspondence should be addressed. E-mail: geim@man.ac.uk

An Eccentric Binary Millisecond Pulsar in the Galactic Plane

David J. Champion,[1,2]* Scott M. Ransom,[3] Patrick Lazarus,[1] Fernando Camilo,[4] Cees Bassa,[1] Victoria M. Kaspi,[1] David J. Nice,[5] Paulo C. C. Freire,[6] Ingrid H. Stairs,[7] Joeri van Leeuwen,[8] Ben W. Stappers,[9] James M. Cordes,[10] Jason W. T. Hessels,[11] Duncan R. Lorimer,[12] Zaven Arzoumanian,[13] Don C. Backer,[8] N. D. Ramesh Bhat,[14] Shami Chatterjee,[15] Ismaël Cognard,[16] Julia S. Deneva,[10] Claude-André Faucher-Giguère,[17] Bryan M. Gaensler,[15] JinLin Han,[18] Fredrick A. Jenet,[19] Laura Kasian,[7] Vlad I. Kondratiev,[12] Michael Kramer,[9] Joseph Lazio,[20] Maura A. McLaughlin,[12] Arun Venkataraman,[6] Wouter Vlemmings[21]

Binary pulsar systems are superb probes of stellar and binary evolution and the physics of extreme environments. In a survey with the Arecibo telescope, we have found PSR J1903+0327, a radio pulsar with a rotational period of 2.15 milliseconds in a highly eccentric ($e = 0.44$) 95-day orbit around a solar mass ($M_\odot$) companion. Infrared observations identify a possible main-sequence companion star. Conventional binary stellar evolution models predict neither large orbital eccentricities nor main-sequence companions around millisecond pulsars. Alternative formation scenarios involve recycling a neutron star in a globular cluster, then ejecting it into the Galactic disk, or membership in a hierarchical triple system. A relativistic analysis of timing observations of the pulsar finds its mass to be 1.74 ± 0.04 $M_\odot$, an unusually high value.

The population of binary and millisecond pulsars in the disk of our Galaxy is thought to have two main formation mechanisms (*1*). Most pulsars with spin periods of tens of milliseconds have neutron star (NS) companions in orbits of high eccentricity caused by the near disruption of the system by a supernova explosion. In contrast, pulsars with spin periods less than about 10 ms (i.e., "millisecond pulsars" or MSPs) have white dwarf (WD) companions in orbits made highly circular (orbital eccentricities $e < 0.001$) by tidal effects during the recycling process. The combination of rapid spin rates and circular orbits is considered vital evidence that MSPs achieve their short periods by accretion of mass and angular momentum from binary companion stars (*2*). Here, we report the discovery of an unprecedented MSP that requires a different formation mechanism and whose potentially large mass may play an important role in constraining the equation of state of matter at supranuclear density (*3*).

Discovery and follow-up observations. We are conducting a pulsar survey of the Galactic plane using the Arecibo L-band Feed Array (ALFA) receiver on the 305-m Arecibo radio telescope in Puerto Rico (*4*). The large collecting area of Arecibo, the rapid sampling rate (every 64 μs), and the high spectral resolution (256 channels over 100 MHz, which minimizes the dispersive smearing due to free electrons along the line of sight) provide sensitivity to MSPs over a much larger volume of the Galactic disk than any previous pulsar survey.

The 2.15-ms pulsar J1903+0327 was discovered using a search pipeline based on the PRESTO suite of pulsar analysis software (*5*, *6*). It was detected as a highly significant signal with a large dispersion measure (DM) of 297 pc cm^{-3} in data taken in October 2005. Follow-up timing observations using Arecibo, the Green Bank Telescope, and the Westerbork Synthesis Radio Telescope revealed the binary orbit of the pulsar to be highly eccentric (Fig. 1). The Keplerian orbital parameters give a minimum companion mass of 0.85 to 1.07 $M_\odot$ (for pulsar masses of 1.3 to 1.9 $M_\odot$). Additional constraints come from the extensive timing of the pulsar, including a general relativistic interpretation of the measurement of the advance of periastron $\dot{\omega}$ and a detection of the Shapiro delay. As described in the supporting online material and in the caption to Table 1, the best model fit to the pulse times of arrival indicates that the companion has a mass of 1.051(15) $M_\odot$ and that the pulsar has a mass of 1.74(4) $M_\odot$. It should be noted that these masses are based on ~1.5 years of timing data that cannot yet include parameters such as proper motion, which can affect the mass measurements. Although the pulsar mass is significantly more massive than the 1.25 to 1.45 $M_\odot$ seen in most double neutron star (DNS) systems (*1*), it is comparable to the inferred masses of several recently detected pulsars in eccentric binaries in globular clusters (*7*–*9*), at least one other Galactic MSP (*10*), and the x-ray pulsar Vela X-1 (*11*). If the large pulsar mass is confirmed in future observations, it will constrain the equation of state of matter at supranuclear density and potentially rule out certain "soft" equations of state (*3*). The companion mass is compatible with those of a NS, WD, or main-sequence (MS) companion. Although the spin parameters of PSR J1903+0327 (Table 1) resemble those of other Galactic disk MSPs, the pulsar is clearly distinct when orbital eccentricity is compared as well (Fig. 2). Further details of the search pipeline, follow-up observations, and timing analysis are provided in the supporting online material.

Given the possibility that the companion could be a NS, and potentially a pulsar, we searched for pulsations from the companion using several of the Arecibo observations, but found none. These null results set an upper limit on pulsed emission at 1.4 GHz of ~20 μJy for a period of 2 ms and ~9 μJy for a period of 200 ms, assuming a pulse duty cycle of 30% of the pulse period.

To search for a MS companion, we obtained images of the pulsar field with the Gemini North telescope on July 24, 2007. The total exposure times were 10 min in the infrared J, H, and K_S bands (1.27, 1.67, and 2.22 μm, respectively). After calibrating the astrometry and photometry of the images against the Two Micron All Sky Survey (2MASS) catalog, we find a single star within the 0.13″ 1-σ frame-tie error circle at the position of the pulsar (Fig. 3). It has $J = 19.22(9)$, $H = 18.41(10)$, and $K_S = 18.03(9)$ magnitudes. Given the density of stars in this field, we estimate that the probability of finding a star in

[1]Department of Physics, McGill University, Montreal, QC H3A 2T8, Canada. [2]Australia Telescope National Facility (ATNF), Commonwealth Scientific and Industrial Research Organisation, Post Office Box 76, Epping NSW 1710, Australia. [3]National Radio Astronomy Observatory, 520 Edgemont Road, Charlottesville, VA 22903, USA. [4]Columbia Astrophysics Laboratory, Columbia University, 550 West 120th Street, New York, NY 10027, USA. [5]Physics Department, Bryn Mawr College, Bryn Mawr, PA 19010, USA. [6]National Astronomy and Ionosphere Center (NAIC), Arecibo Observatory, HC03 Box 53995, Arecibo, PR 00612, USA. [7]Department of Physics and Astronomy, University of British Columbia, 6224 Agricultural Road, Vancouver, BC V6T 1Z1, Canada. [8]Astronomy Department, 441 Campbell Hall, University of California at Berkeley, Berkeley, CA 94720, USA. [9]Jodrell Bank Observatory, Macclesfield, Cheshire SK11 9DL, UK. [10]Astronomy Department, Cornell University, Ithaca, NY 14853, USA. [11]Astronomical Institute "Anton Pannekoek," University of Amsterdam, Kruislaan 403, 1098 SJ Amsterdam, The Netherlands. [12]Department of Physics, West Virginia University, Morgantown, WV 26506, USA. [13]Center for Research and Exploration in Space Science and Technology, and X-ray Astrophysics Laboratory, NASA Goddard Space Flight Center, Code 662, Greenbelt, MD 20771, USA. [14]Swinburne University of Technology, Post Office Box 218, Hawthorn, Victoria 3122, Australia. [15]School of Physics, The University of Sydney, NSW 2006 Australia. [16]Laboratoire de Physique et Chimie de l'Environnement, Centre National de la Recherche Scientifique, UMR 6115 3A, Avenue de la Recherche Scientifique, F-45071 Orleans Cedex 2, France. [17]Harvard-Smithsonian Center for Astrophysics, 60 Garden Street, MS-10, Cambridge, MA 02138, USA. [18]National Astronomical Observatories, Chinese Academy of Sciences, Jia-20 Datun Road, Chaoyang District, Beijing 100012, China. [19]Center for Gravitational Wave Astronomy, University of Texas, Brownsville, TX 78520, USA. [20]Naval Research Laboratory (NRL), 4555 Overlook Avenue, SW, Washington, DC 20375, USA. [21]Argelander-Institut für Astronomie, University of Bonn, Auf dem Hügel 71, 53121 Bonn, Germany.

*To whom correspondence should be addressed. E-mail: David.Champion@atnf.csiro.au

the error circle by chance is 2.6%. Using MS star models (*12*) and estimating the reddening with red clump stars (*13*) at the ~6.4 kpc distance inferred from the pulsar's DM (*14*), we find that a 0.9 $M_\odot$ star of age 10 billion years (Gy) would have magnitudes similar to those observed. The uncertainties in the distance and reddening measurements also allow for a 1.05 $M_\odot$ star of age 1 to 5 Gy, making it possible that this (likely) MS star is a companion to PSR J1903+0327.

If the MS star is the pulsar's binary companion, ionized stellar winds might be detected as increases in the measured DM or as an eclipse of the pulsed flux when the companion passes between the pulsar and Earth. From multifrequency observations around the orbit, we find no evidence of an eclipse, and we limit any additional DM contribution to <0.02 pc cm^{-3}. If the companion of PSR J1903+0327 is a ~1 $M_\odot$ MS star with solar-like winds, we would expect an additional DM contribution on the order of 10^{-3} pc cm^{-3} near conjunction (*15*). Strong irradiation of the companion by the pulsar's relativistic wind, however, could lead to a substantially larger mass loss. Our DM variation limit argues against such a large mass loss.

For a system like PSR J1903+0327, a rotationally induced quadrupole moment in the companion could cause a classical periastron advance (*16*) that would contribute to the measured $\dot{\omega} = 2.46(2) \times 10^{-4}$ deg $year^{-1}$. If the companion star is a WD rotating near breakup velocity, the classical contribution would typically be on the order of 10^{-7} deg $year^{-1}$, but could be more than an order of magnitude larger for specific but unlikely system orientations. If the companion is a 1 to 2 Gy, 1.05 $M_\odot$ MS star with a typical rotational period of 8 to 10 days (*17*), the classical contribution would be 2×10^{-6} deg $year^{-1}$ for most system orientations. Such a star would need a rotational period between 1.3 and 1.5 days and/or an unlikely system orientation to account for ~10% of the measured $\dot{\omega}$, or a rotational period <0.5 day to account for all of it. These numbers suggest that the measured $\dot{\omega}$ is dominated by general relativistic effects and, given the high quality of the fit, that the use of the relativistic timing model is well justified.

Formation mechanisms. What is the origin of this unique system with a short spin period, large orbital eccentricity, and possible MS companion? According to conventional evolutionary scenarios (*1*), binary pulsars that have been recycled down to millisecond periods should always appear in circularized orbits. In contrast, pulsars in eccentric systems should be only mildly recycled or not recycled at all. Because PSR J1903+0327 does not fall into either of these broad categories, we consider three alternative scenarios. The first is that the pulsar was not recycled but was born spinning rapidly in an eccentric orbit at the time the NS was created. The second has the pulsar recycled in a globular cluster and then ejected into the Galactic disk. The third has the pulsar recycled in a hierarchical triple system.

For various reasons, it seems unlikely that the pulsar was formed spinning rapidly at the time of core-collapse with a small surface magnetic field (2×10^8 G). First, there are no pulsars like J1903+0327 in any of the more than 50 young supernova remnants in which a NS has been inferred or detected directly (*18*). Second, a "born-fast" scenario for PSR J1903+0327 would likely be expected to account for some or all of the 18 isolated MSPs detected in the Galactic disk. Although the formation of those systems is puzzling because the observed time scales for evaporating a companion star seem too long, their spin distributions, space velocities, and energetics are indistinguishable from those of recycled (i.e., not born-fast) binary MSPs, and their space velocities and scale heights do not match those of nonrecycled pulsars (*19*). Third, magnetic fields in young pulsars likely originate either from dynamo action in the proto-NS (*20*) or through compression of "frozen-in" fields of the progenitor star during collapse (*21*). If compression is the correct mechanism, then young pulsars with magnetic fields <10^{10} G are rare, as we know of none. Alternatively, the dynamo model actually requires rapidly spinning systems to have strong magnetic fields. Although core-collapse born-fast

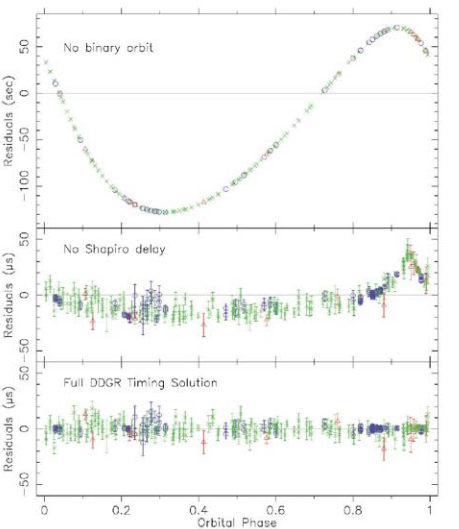

Fig. 1. Residual pulse arrival times as a function of orbital phase (mean anomaly) for PSR J1903+0327 after subtraction of the best-fit timing model. The timing residuals are from observations made with the Arecibo telescope (blue circles), the Westerbork Synthesis Radio Telescope (red triangles), and the Green Bank Telescope (green crosses) and are defined as observed minus model. **(Top)** The measured timing residuals if no orbit is accounted for. The resulting curve is the Roemer delay (i.e., the light-travel time across the orbit), and its nonsinusoidal shape shows the large eccentricity ($e = 0.44$) of PSR J1903+0327. The uncertainties on the data points would be the same as in the lower panels, but the scale is different by a factor of 10^6. **(Middle)** The same residuals as in the top panel but with the Roemer delay and all general relativistic delays except for Shapiro delay from the timing solution in Table 1 removed. **(Bottom)** The timing residuals for the full Damour and Deruelle General Relativistic (DDGR) timing model described in Table 1, which assumes that general relativity fully describes the parameters of the binary system (*32*). The weighted root-mean-square timing residual shown here is 1.9 μs.

mechanisms seem to be ruled out, the accretion-induced collapse of massive and rapidly rotating WDs to NSs might form MSPs (*22*). This collapse may be able to produce the observed orbital parameters, but the large observed pulsar mass would require the collapsing WD to be well above the Chandrasekhar mass and would also suggest that the companion should be evolved.

Globular clusters (GCs) are known to be efficient producers of MSPs, including those in eccentric binaries, as a result of interactions between NSs and other stars or binaries in their high-density cores. Of the ~130 known GC pulsars (*23*), more than 10% are in highly eccentric ($e > 0.2$) orbits. These numbers, combined with the known populations of NSs in GCs and the Galaxy, and the respective masses of GCs and the Galaxy, imply that GCs produce eccentric binary pulsars at least 1000 times more efficiently per unit mass than the Galactic disk. Furthermore, stellar interactions and exchanges can provide MS companions for MSPs, although those companions should be less massive than the most evolved MS stars currently observed in GCs (~0.8 to 0.9 $M_\odot$).

Although GCs seem a natural formation ground for PSR J1903+0327, there is no known GC located near PSR J1903+0327 on the sky, nor is there any evidence for an unknown cluster in the 2MASS catalog (*24*), in the Spitzer Space Telescope Galactic Legacy Infrared Mid-Plane Survey Extraordinaire data (*25*), or in our Gemini observations. An intriguing possibility is that PSR J1903+0327 was formed in the core of a GC and then ejected from the cluster, possibly in the same interaction that induced the orbital eccentricity we observe today. This would have to have occurred sometime within the past ~1 to 2 Gy (i.e., within the characteristic age of the MSP). Detailed simulations of NS interactions in GCs have shown that up to ~50% of recycled NSs are ejected within the ~10 Gy lifetimes of the GCs (*26*). Once the pulsar has left the cluster, it drifts far away from its parent cluster on 10^8 to 10^9 year time scales. Alternatively, the cluster could have been disrupted during orbital passages through the Galactic disk and bulge within the past ~1 Gy (*27*). Rough estimates based on the masses and densities of the GC system and the Galactic disk suggest (see supporting online material) a 1 to 10% chance that PSR J1903+0327 originated in a GC. The characteristic age of the pulsar is perhaps the biggest challenge for a GC explanation, because it requires that the newly made MSP had one or more violent interactions that replaced the star that recycled the NS, and then was displaced enough from the GC such that the GC is no longer visible to us, all within ~2 Gy.

In a third formation scenario, PSR J1903+0327 is part of a primordial hierarchical triple system. In such a system, the inner binary evolves normally. In this case, the secondary mass likely needs to be quite fine-tuned to produce a highly recycled massive MSP while still producing a high-mass (0.9 to 1.1 $M_\odot$) WD in a wide circular orbit, although no such borderline systems have been observed to date. In this scenario the WD is the companion seen in the timing. The third star in the system, now the MS star that we detect as the infrared counterpart, is in a much wider and highly inclined orbit around the inner binary. Secular perturbations in such a system can cause large oscillations of the inner-binary eccentricity and the outer-orbit inclination (so-called Kozai cycles) (*28*). Especially for a cycle period resonant with the inner-binary relativistic periastron advance at ~2×10^6 years, a 0.9 $M_\odot$ MS star ~120 astronomical units out in a highly inclined ~700-year orbit can induce large inner-binary eccentricities (*29*). Initial estimates (see supporting online material) for the formation and survival probability of such a triple system suggest that a few percent of observed NS-WD binaries could be members of hierarchical triples. As such, it seems plausible that after finding ~50 pulsar-WD binaries, we have now found the first in a hierarchical stellar triple.

A related scenario that avoids the need for formation of both a fully recycled MSP and a high-mass WD companion (which has never been observed) has PSR J1903+0327 recycled as part of a compact inner binary in a hierarchical triple, in a configuration recently suggested for 4U 2129+47 (*30*). The MSP then ablated away its WD companion and was left in a 95-day eccentric orbit around the MS star we now observe.

Further observations of PSR J1903+0327 will allow us to decide between these (or other) formation scenarios. A measurement of a large projected space velocity (>100 to 200 km s^{-1}), by long-term timing or very-long-baseline interferometry astrometry, might reflect a cluster origin given the high velocities of most GCs. Spectroscopic observations of the MS star will reveal its spectral type and metallicity, both possible indicators for or against a GC origin, and will show whether it exhibits the 95-day

Table 1. Measured and derived parameters for PSR J1903+0327. The timing parameters were measured using the DE405 solar system ephemerides (*31*) and the DDGR timing model, which assumes that general relativity fully describes the parameters of the binary system (*32*). A total of 342 pulse arrival times measured between MJDs 53990 and 54568 were fit. The numbers in parentheses are twice the TEMPO-reported 1-σ uncertainties in the least significant digit or digits quoted as determined by a bootstrap error analysis. The distance is inferred from the NE2001 free-electron density model (*14*). Ensemble distance measurements using this model have an estimated error of 25%, although errors for individual pulsars may be larger.

Timing parameters assuming general relativity	
Right ascension (J2000)	$19^h\ 03^m\ 05.^s79368(3)$
Declination (J2000)	$03^\circ\ 27'\ 19.''2220(11)$
Spin period (ms)	2.14991232984335(3)
Period derivative (s/s)	$1.879(2) \times 10^{-20}$
Dispersion measure (pc cm^{-3})	297.537(7)
Epoch of period (MJD)	54280.0
Orbital period (days)	95.1741176(2)
Projected semi-major axis (lt-s)	105.60585(11)
Eccentricity	0.436678411(12)
Longitude of periastron	$141.65779(4)^\circ$
Epoch of periastron (MJD)	54063.8402308(5)
Total system mass, M_{tot} ($M_\odot$)	2.79(5)
Companion mass, M_2 ($M_\odot$)	1.051(15)
Other parameters	
Scattering time at 1.4 GHz (ms)	0.126(1)
1.4-GHz flux density (mJy)	1.3(4)
2-GHz flux density (mJy)	0.62(5)
5-GHz flux density (mJy)	0.09(2)
Spectral index	−2.1(2)
Derived parameters	
Galactic longitude (J2000)	$37.^\circ3363$
Galactic latitude (J2000)	$-1.^\circ0136$
Mass function ($M_\odot$)	0.1396076(2)
Distance (kpc)	~6.4
Surface dipole magnetic field strength (Gauss)	2.0×10^8
Characteristic age (Gy)	1.8
Spin-down luminosity (ergs s^{-1})	7.5×10^{34}
Advance of periastron (deg yr^{-1})	$2.46(2) \times 10^{-4}$
Orbital inclination	$78(2)^\circ$
Pulsar mass, M_1 ($M_\odot$)	1.74(4)

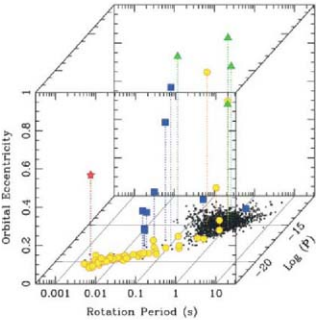

Fig. 2. Rotation periods, period derivatives, and orbital eccentricities (for binary pulsars) of pulsars in the disk of the Galaxy. The bottom face of the cube shows a plot of rotation period versus rotation period derivative for all Galactic pulsars. Colored points show the binary pulsars, projected upward from the bottom face in proportion to their orbital eccentricities. Square blue points are double neutron star systems, triangular green points are pulsars with MS or massive companions, circular yellow points are pulsars with white dwarf or subdwarf companions, and the red star is PSR J1903+0327, which occupies a unique place in the diagram.

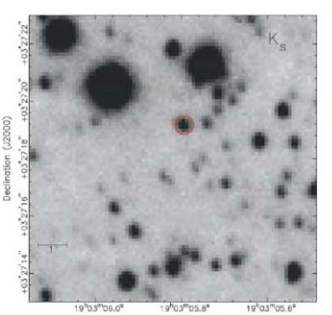

Fig. 3. A K_S-band image of the PSR J1903+0327 field taken during excellent seeing conditions (0.3 to 0.4") with the Gemini North telescope. The red circle shows the 2-σ error circle, with radius 0.32" (produced by the frame-tie uncertainties in right ascension and declination), for the position of the pulsar based on astrometric calibrations made with the 2MASS catalog. The star within the error circle is the possible MS companion to the pulsar.

orbital motion of the pulsar. If the star is the companion, the radial-velocity curve will further constrain the masses of both the pulsar and the companion. Additionally, if the MS companion is confirmed to be more massive than ~1 $M_\odot$, it will likely rule out a GC origin because MS stars of that mass in clusters have already left the MS. Finally, long-term and higher-precision timing of the pulsar will dramatically improve the relativistic parameters of the system (and therefore the derived masses) and will reveal secular changes in the spin and orbital parameters caused by the presence of a third star or by classical effects from the rotation of a MS companion.

References and Notes

1. I. H. Stairs, *Science* **304**, 547 (2004).
2. M. A. Alpar, A. F. Cheng, M. A. Ruderman, J. Shaham, *Nature* **300**, 728 (1982).
3. J. M. Lattimer, M. Prakash, *Phys. Rep.* **442**, 109 (2007).
4. J. M. Cordes *et al.*, *Astrophys. J.* **637**, 446 (2006).
5. S. M. Ransom, S. S. Eikenberry, J. Middleditch, *Astron. J.* **124**, 1788 (2002).
6. Pulsar Exploration and Search Toolkit, www.cv.nrao.edu/~sransom/presto.
7. S. M. Ransom *et al.*, *Science* **307**, 892 (2005).
8. P. C. C. Freire *et al.*, *Astrophys. J.* **675**, 670 (2008).
9. P. C. C. Freire, A. Wolszczan, M. van den Berg, J. W. T. Hessels, *Astrophys. J.*, in press, http://arxiv.org/abs/0712.3826 (2008).
10. J. P. W. Verbiest *et al.*, http://arxiv.org/abs/0801.2589 (2008).
11. H. Quaintrell *et al.*, *Astron. Astrophys.* **401**, 313 (2003).
12. L. Girardi, A. Bressan, G. Bertelli, C. Chiosi, *Astron. Astrophys. Suppl. Ser.* **141**, 371 (2000).
13. M. López-Corredoira, A. Cabrera-Lavers, F. Garzón, P. L. Hammersley, *Astron. Astrophys.* **394**, 883 (2002).
14. J. M. Cordes, T. J. W. Lazio, http://arxiv.org/abs/astro-ph/0207156 (2002).
15. X. P. You, G. B. Hobbs, W. A. Coles, R. N. Manchester, J. L. Han, *Astrophys. J.* **671**, 907 (2007).
16. N. Wex, *Mon. Not. R. Astron. Soc.* **298**, 67 (1998).
17. D. Cardini, A. Cassatella, *Astrophys. J.* **666**, 393 (2007).
18. V. M. Kaspi, D. J. Helfand, in *Neutron Stars in Supernova Remnants*, P. O. Slane, B. M. Gaensler, Eds. (2002), vol. 271 of *Astronomical Society of the Pacific Conference Series*, pp. 3–22.
19. D. R. Lorimer, M. A. McLaughlin, D. J. Champion, I. H. Stairs, *Mon. Not. R. Astron. Soc.* **379**, 282 (2007).
20. C. Thompson, R. C. Duncan, *Astrophys. J.* **408**, 194 (1993).
21. L. Ferrario, D. Wickramasinghe, *Mon. Not. R. Astron. Soc.* **367**, 1323 (2006).
22. L. Ferrario, D. Wickramasinghe, *Mon. Not. R. Astron. Soc.* **375**, 1009 (2007).
23. Pulsars in Globular Clusters, www.naic.edu/~pfreire/GCpsr.html.
24. M. F. Skrutskie *et al.*, *Astron. J.* **131**, 1163 (2006).
25. R. A. Benjamin *et al.*, *Publ. Astron. Soc. Pac.* **115**, 953 (2003).
26. N. Ivanova, C. O. Heinke, F. A. Rasio, K. Belczynski, J. M. Fregeau, *Mon. Not. R. Astron. Soc.* **386**, 553 (2008).
27. O. Y. Gnedin, J. P. Ostriker, *Astrophys. J.* **474**, 223 (1997).
28. Y. Kozai, *Astron. J.* **67**, 591 (1962).
29. E. B. Ford, B. Kozinsky, F. A. Rasio, *Astrophys. J.* **535**, 385 (2000).
30. M. S. Bothwell, M. P. Torres, M. R. Garcia, P. A. Charles, http://arxiv.org/abs/0804.1358 (2008).
31. E. M. Standish, *Astron. Astrophys.* **417**, 1165 (2004).
32. J. H. Taylor, J. M. Weisberg, *Astrophys. J.* **345**, 434 (1989).

33. We thank the staff at NAIC and ATNF for developing ALFA and its associated data acquisition systems. This work was supported by NSF through a cooperative agreement with Cornell University to operate the Arecibo Observatory. The National Radio Astronomy Observatory is a facility of the National Science Foundation operated under cooperative agreement by Associated Universities, Inc. Pulsar research at Cornell is supported by NSF grants AST 0507747 and CISE/RI 040330 and by the Center for Advanced Computing. The McGill pulsar group Beowulf computer cluster used for this work was funded by the Canada Foundation for Innovation (CFI). Pulsar research at Bryn Mawr College is funded by NSF grant AST 0647820. Basic research in radio astronomy at NRL is supported by 6.1 base funding. Pulsar research at Columbia University is supported by NSF grant AST 0507376. Pulsar research at the University of British Columbia is supported by a Natural Sciences and Engineering Research Council of Canada (NSERC) Discovery Grant and also benefits from a computer cluster funded by the CFI. V.M.K. holds a Canada Research Chair and the Lorne Trottier Chair and acknowledges support from an NSERC Discovery Grant, Canadian Institute for Advanced Research, and Fonds Québécois de la Recherche sur la Nature et les Technologies. J.W.T.H. holds an NSERC Postdoctoral Fellowship and Canadian Space Agency supplement. L.K. holds an NSERC Canadian Graduate Scholarship–Doctoral fellowship. J.v.L. is a Wells Stensen Fellow. Pulsar research at the University of Texas at Brownsville is funded by NSF grant AST 0545837. We thank O. Pols, D. Fabrycky, and G. Duchêne for helpful discussions.

Supporting Online Material

www.sciencemag.org/cgi/content/full/1157580/DC1
Materials and Methods
Fig. S1
Table S1
References

10 March 2008; accepted 29 April 2008
Published online 15 May 2008;
10.1126/science.1157580
Include this information when citing this paper

Predictive Behavior Within Microbial Genetic Networks

Ilias Tagkopoulos,[1,2]* Yir-Chung Liu,[2,3]* Saeed Tavazoie[2,3]†

The homeostatic framework has dominated our understanding of cellular physiology. We question whether homeostasis alone adequately explains microbial responses to environmental stimuli, and explore the capacity of intracellular networks for predictive behavior in a fashion similar to metazoan nervous systems. We show that in silico biochemical networks, evolving randomly under precisely defined complex habitats, capture the dynamical, multidimensional structure of diverse environments by forming internal representations that allow prediction of environmental change. We provide evidence for such anticipatory behavior by revealing striking correlations of *Escherichia coli* transcriptional responses to temperature and oxygen perturbations—precisely mirroring the covariation of these parameters upon transitions between the outside world and the mammalian gastrointestinal tract. We further show that these internal correlations reflect a true associative learning paradigm, because they show rapid decoupling upon exposure to novel environments.

Although originally conceived in the context of human physiological adaptation (*1*), homeostasis has also become the de facto framework for understanding cellular behavior. In its most essential form, the homeostatic response is an attempt to maintain the "constancy of the internal state" in response to perturbations resulting from environmental fluctuations (e.g., expression of osmoprotectants in response to osmolarity stress). When such fluctuations are essentially random (unpredictable), the cell may directly or indirectly sense the perturbation and enact the appropriate response program. On the other hand, if such variations are perfectly predictable, such as periodic changes in photon flux due to Earth's rotation, an internal model (circadian rhythm) can be used to anticipate relevant changes. The organism can then mount a "preemptive" response—for example, by gearing up the photosynthetic machinery before sunrise. The widespread use of internal circadian models, from unicellular cyanobacteria to humans (*2*), suggests that this predictive mode of behavior confers considerable fitness advantages to organisms that have evolved it.

Environmental variables that show purely random fluctuations or perfectly periodic rhythms define idealized extremes. In fact, some parameters whose fluctuations may seem random when viewed in isolation can nonetheless be highly "predictable" when considered in the temporal context of variation in other parameters (Fig. 1). As such, variations in one environmental variable can convey substantial information about variation in another. For example, a bacterium may experience strong covariation in temperature and photon flux as it traverses the upper layers of a stratified marine ecosystem. Such temporally structured correlations can exist on multiple time scales, reflecting the highly structured (non-random) habitats of free-living organisms. Temporal delays are a typical feature of these correlations. For example, an increase in temperature may herald an impending decrease in O_2 levels some 20 min later. An organism that is capable of learning (internalizing) these correlations can then exploit them in order to anticipate vital changes in the environment—for example, preparing for resource fluctuations or mounting protective responses to extreme perturbations.

Within metazoans, the basic capacity for predictive behavior requires complex neural network architecture. Here we hypothesize that an analog of this capacity, implemented by networks of biochemical reactions, exists in unicellular microbes. To demonstrate this potential, we have developed a biochemically realistic computer simulation for evolving populations of organisms under precisely defined environments where multiple time-varying signals encode information about resource abundance. Randomly evolving biochemical networks of these organisms form internal representations of their dynamic environments that enable predictive behavior. We provide experimental evidence for this capacity by revealing strong correlations in genome-wide transcriptional responses of *E. coli* to transitions in oxygen and temperature. These correlations do not reflect an essential biochemical coupling between oxygen and temperature because they are rapidly decoupled in the context of selection in a novel environment.

Emergence of predictive behavior in simulated biochemical networks. Computational simulations of biological systems are yielding unique insights into a variety of fundamental questions in biology (*3*–*10*). We developed a simulation framework, called Evolution in Variable Environment (EVE), aimed at exploring the capacity of biochemical networks to evolve predictive internal models of complex environments (*11*). Within EVE, biochemical networks are structured around the "central dogma" and they evolve in an asynchronous and stochastic manner, achieving the temporal dynamics of cascades of biochemical interactions/transformations (including transcription, translation, and protein modification) that are present in real cells (Fig. 2A). Each node in the biochemical network of an organism is parameterized by several continuous variables mapping to biological parameters such as basal expression, degradation, and regulatory strength. At any point during the simulation, random mutations (e.g., transcription rate change, node duplication, node deletion) may alter any of the organism's parameters and consequently its phenotype (Fig. 2B). Environmental signals, conveying information about resources, may couple and stochastically regulate any action (e.g., transcription, translation, or transformation) in the organism's internal network. A node can regulate any other node, although one may restrict unlikely interactions using a probabilistic model (for instance, we may choose to make RNA-mediated protein modification a rare event). Each organism possesses a generic and stable response pathway through which it can interact with the environment, whether for energy extraction or response to stress. Expression of the response pathway is modeled to have a high energy cost; thus, there is strong selection for organisms whose response correlates with the appropriate environmental event (e.g., presence of food). Organisms evolve in the context of a constant population size, where growth rate is directly proportional to the amount of energy per cell. The energy of each

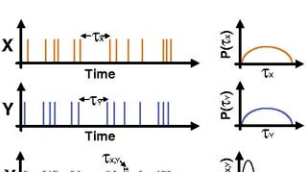

Fig. 1. Predictability emerges from temporal context of correlated random variables. When viewed in isolation, events X and Y have a random temporal structure (left) as manifested by the large uncertainty in the inter-event interval τ_x and τ_y (right). However, the occurrence of event X is highly predictable within the temporal context of event Y (left), with a relatively tight distribution of temporal delay between the two events $\tau_{x,y}$ (right).

[1]Department of Electrical Engineering, Princeton University, Princeton, NJ 08544, USA. [2]Lewis-Sigler Institute for Integrative Genomics, Princeton University, Princeton, NJ 08544, USA. [3]Department of Molecular Biology, Princeton University, Princeton, NJ 08544, USA.

*These authors contributed equally to this work.
†To whom correspondence should be addressed. E-mail: tavazoie@genomics.princeton.edu

cell depends on the energy extraction rate from the environment as well as on the metabolic demands of expressing and maintaining network components (Fig. 2C).

Within this in silico ecology, evolving organisms with random initial networks compete against each other in structured environments where signals and resources fluctuate with a distinct temporal correlation structure. In a typical experiment, the combinatorial states of multiple signals convey information about the availability of extractable energy resources in the near future. Cells that can efficiently "learn" such correlations are able to express the energy-extracting metabolic pathway at the appropriate time, giving them sizable fitness advantage over their competitors.

We conducted large-scale simulations of nine temporally structured environments across mutation rates spanning four orders of magnitude. A variety of environments were imposed, including those that selected for one of five delayed logic gates, oscillators, bistable switches, and duration inference mechanisms. Despite the complex nature of many of these environments, high-fitness organisms emerged with variable success rate in every case (table S1 and figs. S4 and S5).

The full historical documentation of the evolutionary process in EVE allowed us to connect evolutionary dynamics, phenotypic behavior, and network structure in ways that are difficult to do in naturally evolved biological systems. In a particularly challenging environment, the abundance of resource (food) is related to the signals through a delayed dynamic exclusive OR (XOR) relationship, where resources become abundant shortly (within 1000 time units) after the presence of either signal S1 or signal S2 alone, but not when they co-occur. Fitness is defined as the Pearson correlation (PC) between the abundance of resource and response pathway expression. Interestingly, the fitness trajectory of the fittest organism displays nonmonotonic behavior (Fig. 3A). In the first 5.4×10^6 time units (1100 epochs), there is no stable phenotype in the population whose response protein expression correlates well with the presence of resources in the environment (Fig. 3B, 1). However, several advantageous mutations in the next 4.5×10^5 time units (100 epochs) lead to a phenotype where the expression of the response protein loosely couples to the presence of signal S1 and the absence of signal S2 (Fig. 3B, 2). Subsequent mutations give rise to a fit (PC > 0.8) but unstable phenotype (Fig. 3B, 3) where a noisy dynamic XOR is achieved. Instead of stabilization of the fittest phenotype at the time, we observe an abrupt decline of fitness and subsequent fixation to a suboptimal fitness peak (Fig. 3B, 4). The next fitness increase occurs after 3.6×10^5 time units (800 epochs) when a gene duplication event (fig. S6) allows the newly formed gene and its protein and modified protein products to take on their own course in evolution, thus giving rise to an optimal final phenotype (Fig. 3B, 5). The evolutionary impact of gene duplication was also observed in other experiments, most of which displayed monotonically increasing fitness trajectories (figs. S7 and S8).

The evolved biochemical networks displayed a high level of redundancy, as the majority of single node/link "knockouts" did not reveal a sizable fitness effect. In an attempt to identify a "minimal network" that was sufficient to express the evolved behavior, we devised a procedure (*11*) that sequentially knocks out links until the network hits a critical mass that cannot be reduced without a large (>5%) decrease in the organism's fitness. We found that such minimal networks were considerably more informative about the relationship between network structure and function relative to the initial networks they were derived from.

The full and minimal networks belonging to the fittest organism evolved under the delayed XOR selection are displayed in Fig. 4A; the expression profile of all the nodes in the full network is shown in Fig. 4B. From a total of 31 links, only 11 were found to be essential as defined above. Signals S1 and S2 serve as direct observable environmental inputs, whereas resources can be harvested only when response protein (RP1) is expressed. The presence of S1 catalyzes the translation of RNA2 to P2, which in turn leads to the activation of G1 and subsequent translation of its RNA to P1. Once P1 is created, it can undergo modification and become response protein RP1. However, this step is not completed immediately, as P2 also inhibits P1's modification. Modification can occur after signal S1 goes down and the high degradation rate of P2 leads to its rapid drop. This in turn introduces a delay interval that is large enough to allow the expression of RP1 to coincide precisely with the presence of the resource. Once expressed, RP1, operating in a negative feedback loop, represses the expression of G1. The low degradation rate of RNA1 and self-activation of P1 contribute to the network's ability to stay in standby mode where P1 molecules are constantly replenished but not modified to RP1. With this mechanism, the time delay is easily tuned through changes in the kinetic constants of one protein, namely P2. Similarly, when only S2 is present, the response pathway is activated through P0 in an analogous fashion. However, when both signals S1 and S2 are present, P0 and P2 are unable to activate G1 transcription because the two environmental signals cross-catalyze the modification of these proteins to their inactive states (MP0 and MP2). Additionally, the high degradation rate of MP0 and MP2 makes transitions from MP0 to P0 or from MP2 to P2 unlikely.

In general, careful inspection revealed how behavior emerges from the topology and kinetics of the evolved minimal networks (*11*). However, we found variable success in the ability of standard reverse-engineering methods (*12*, *13*) to reveal network structure from behavior (figs. S14 to S16).

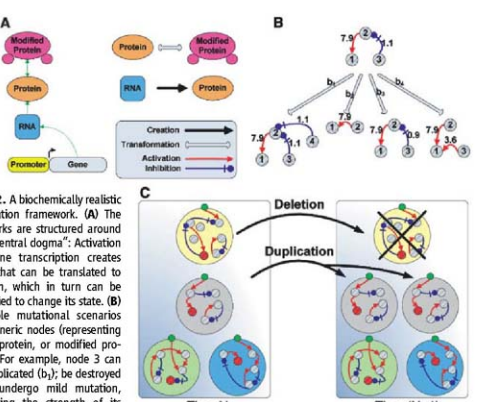

Fig. 2. A biochemically realistic simulation framework. **(A)** The networks are structured around the "central dogma": Activation of gene transcription creates RNA that can be translated to protein, which in turn can be modified to change its state. **(B)** Possible mutational scenarios for generic nodes (representing RNA, protein, or modified protein). For example, node 3 can be duplicated (b_3); be destroyed (b_0); undergo mild mutation, changing the strength of its regulation of node 2 (b_2); or mutate strongly, causing its decoupling from node 2 and coupling to node 1 (b_x). In addition to network topology, mutations may change node parameters such as basal transcription rate, degradation rate, and interaction affinity. **(C)** Organisms that accumulate enough energy undergo duplication and increase their representation in the population. Duplication is accompanied by deletion of the organism with the least energy in the population.

Correlated transcriptional responses of *E. coli* to oxygen and temperature perturbations. The evolution of predictive behavior in simulated networks suggested that this capacity might exist in naturally evolved microbial networks. Looking for evidence of such predictive modeling requires knowledge of microbial habitat structures well beyond what currently exists for most organisms. However, for some microbes, recurrent transitions in and out of a dominant niche are accompanied by deterministic correlations in important environmental variables. For example, transition from the outside environment into the oral cavity exposes the bacterium *E. coli* to an immediate increase in temperature from ambient (<30°C) to 37°C. This is followed by an impending drop in oxygen levels as the bacterium transitions into the gastrointestinal tract (Fig. 5A). The complex ecology of the mammalian GI tract imposes strong competitive selection for colonization (*14*). In this setting, appropriate expression of adaptive functions confers strong fitness advantages. From a purely homeostatic perspective, physiological transition from aerobic to anaerobic respiration should only take place immediately after a drop in oxygen levels. However, the fitness benefits of such a reflexive response will not be optimal, in terms of shutting down superfluous capacities (such as aerobic respiration) as well as the time delay required to fully express beneficial functions (such as anaerobic respiration). On the other hand, if bacteria use the immediate increase in temperature as a predictive signal of impending oxygen drop, they could respond in an anticipatory fashion and be in the optimal physiological state at the time oxygen levels drop. If this were true, we would expect that an increase in temperature may lead to a similar physiological response to a decrease in oxygen—even in the presence of maximal oxygen levels.

To test this hypothesis, we used microarray transcriptional profiling (*15*) to observe the global cellular state correlates of such physiological responses. Oxygen and temperature were precisely controlled in the context of growth within bioreactors (*11*). These experiments included temperature transitions between

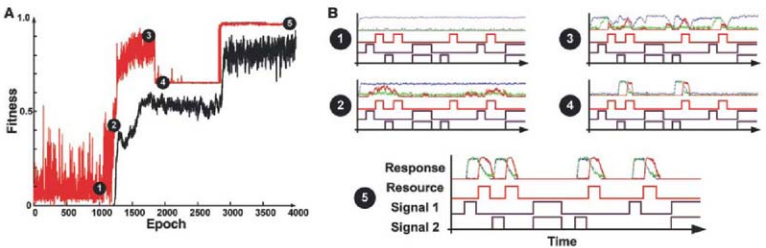

Fig. 3. Emergence of a delayed XOR phenotype. **(A)** Fitness trajectory of an experiment where the presence of one (and only one) signal indicates the future availability of resources. Red and black lines correspond to the highest and mean fitness in the population at each epoch (4500 time units), respectively. **(B)** The phenotypic behavior of the fittest organism at different points along the evolutionary trajectory. Each subplot consists of four rows. The first row depicts the abundance profiles of the RNA (blue), protein (green), and modified protein (red) of the response pathway. The second, third, and fourth rows correspond to resource abundance and environmental signals S1 and S2, respectively.

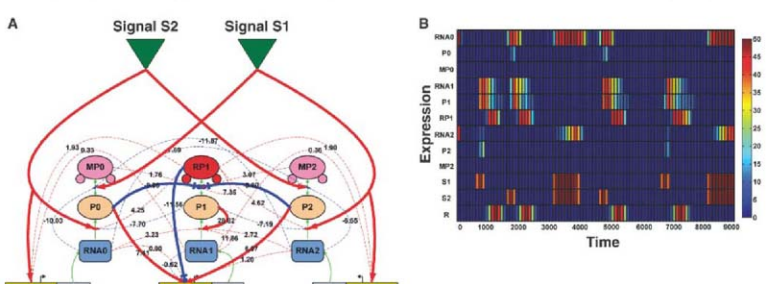

Fig. 4. Network topology and expression profiles of molecular components. **(A)** The regulatory network of an organism evolved under low mutation rate within a delayed dynamic XOR environment. Each node represents mRNA/siRNA (RNA), protein (P), or modified protein (MP). The environmental resource harvested at each time point is proportional to the number of response protein molecules (red RP1 node) and resource abundance at the time. Regulatory interactions can be positive (activating; red arrows) or negative (repressing; blue arrows). Solid lines represent essential links. **(B)** Expression profile of all nine nodes, environmental signals (S1 and S2), and resource (R) during two epochs (9000 time units). The color scale refers to the number of molecules present.

25°C and 37°C, and shifts between anaerobic (0% dissolved O_2) and aerobic (16 to 21% dissolved O_2) growth. Duplicate experiments revealed highly reproducible temperature and oxygen profiles (fig. S17) and gene expression patterns (fig. S18).

Consistent with the predictive behavioral framework above, we found a striking correlation between global transcriptional responses to temperature upshift and oxygen downshift, corresponding to the transition of *E. coli* into the GI tract (Fig. 5A). For instance, we found a highly significant overlap between the set of genes down-regulated by temperature upshift and those down-regulated by oxygen downshift (hypergeometric $P < 10^{-58}$). As predicted, these genes are highly enriched for aerobic respiration functions such as the tricarboxylic acid cycle (TCA) and glyoxylate cycle ($P < 10^{-8}$) and cytochrome bo_3 oxidase complex ($P < 10^{-4}$), the dominant electron donor under aerobic conditions (*16*).

Likewise, temperature downshift and oxygen upshift—corresponding to the transition out of the GI tract—induced strikingly similar gene expression responses ($P < 10^{-28}$) (fig. S19). We also compared the global similarity in transcriptional responses through Pearson correlation (Fig. 5B). As expected, oxygen downshift and oxygen upshift are highly anticorrelated (Pearson $r = -0.50$; $P < 10^{-148}$), as are reverse perturbations in temperature ($r = -0.56$; $P < 10^{-171}$). The strong correlation between temperature upshift and oxygen downshift was most striking ($r = +0.39$; $P < 10^{-79}$), consistent with the similarity in differentially regulated genes. The relatively small correlation between oxygen downshift and unrelated perturbations such as ultraviolet exposure (*17*) ($r = -0.06$; $P < 0.02$) and osmolarity stress (*18*) ($r = 0.11$; $P < 10^{-7}$) makes it unlikely that these correlated behaviors may be due to a generic response to external perturbations (Fig. 5B), as seen, for example, in the common "stress" response in yeast (*19*). What is remarkable is the rapid transcriptional reprogramming from aerobic to anaerobic, during temperature increase, as reflected by the strong repression of genes encoding components of the TCA cycle and cytochrome bo_3 oxidase complex (Fig. 5C). These changes are accompanied by concomitant induction of genes encoding components of cytochrome bd oxidase complex—the preferred electron donor in low-oxygen environments (*16*) (Fig. 5C). Strikingly, this anaerobic transcriptional reprogramming occurs under a highly aerobic environment (18% dissolved O_2), representing a seemingly maladaptive response—at least from the perspective of a homeostatic behavioral framework. Alternatively, the anticipatory repression of oxidative respiration seems adaptive when viewed in the context of the ecologically crucial transition of *E. coli* from the external world into the mammalian GI tract.

We observed that a temperature upshift (25°C to 37°C) led to the induction of the heat shock response regulon, a set of operons activated through the expression and activity of the σ^{32} alternative sigma factor (*20*). This robust response allowed us to explore the possibility of a reciprocal associative coupling, in which oxygen downshift leads to the induction of heat shock response in much the same way as temperature upshift causes respiratory repression. Remarkably, this is exactly what was observed (Fig. 5C).

Novel environment decouples correlated transcriptional responses. Strong correlations in the expression of distinct biochemical pathways may reflect compatibility or mutual dependence between pathway operations—as seen in the spatiotemporal separation of photosynthesis and nitrogen fixation in cyanobacteria (*21*)—rather than reflecting ecological structure per se. To show that the observed correlations are due to an "associative learning" paradigm, we evolved a population of *E. coli* under a dynamic environment where temperature and oxygen fluctuations had a temporal relationship counter to that expected in nature (Fig. 6A). Wild-type *E. coli* should perform poorly in this environment, because a temperature upshift will cause repression of aerobic respiratory pathways, just when oxygen saturation has achieved maximum levels. This inverted environment imposes strong selection for bacteria that fully or partially decouple the native behavior because it is highly maladaptive. If such a reprogramming can occur, then the originally observed correlated responses to temperature upshift and oxygen downshift cannot be due to hard biochemical constraints, but rather is a reflection of a common response to correlated changes in temperature and oxygen that has evolved over geological time scales.

Previous evolution experiments in bacteria have focused mostly on adaptation to "steady-state" conditions, with sizable fitness increases (~30%) occurring only after thousands of generations (*22*). Remarkably, we witnessed large increases in reproductive fitness occurring in fewer than a hundred generations (Fig. 6B). Population growth rate increased only marginally in the 25°C and 0% O_2 regime, but showed more than a 50% increase within the 37°C and 21% O_2 regime. We attribute this rapid increase in fitness to the strength of recurring selection occurring over many cycles. Isolation of individual bacteria and competition with the parental strain (*23*) confirmed the fitness advantage of the evolved strain (fig. S21).

To more precisely characterize the nature of the fitness gains, we monitored growth rates of the parental and evolved strains at a higher temporal resolution across a single cycle of selection (Fig. 6C). As expected, the increase in growth rate of the evolved strain was most pronounced immediately after the temperature upshift, with maximal difference occurring immediately after the upshift in O_2. This suggests that at least part of the adaptation may have been due to the expected decoupling between temperature upshift and repression of aerobic respiration. To test this possibility, we performed transcriptional profiling of parental and evolved strains in the context of a temperature upshift from 25°C to 37°C. We used Pearson correlation to measure the global similarity in transcriptional responses between the original oxygen downshift perturbation and temperature upshift. As can be seen, the strong correlation between oxygen downshift and temperature upshift is considerably

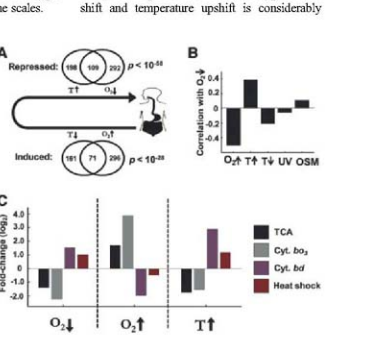

Fig. 5. Global responses to oxygen and temperature perturbations reflect ecological correlation structure. **(A)** Transition of *E. coli* between the outside environment and the mammalian GI tract is accompanied by anticorrelated changes in temperature and oxygen. Correspondingly, highly significant overlap is seen in sets of genes down-regulated by temperature upshift and oxygen downshift (transition into the GI tract; $P < 10^{-58}$). Similarly, a highly significant overlap is seen in sets of genes induced by temperature downshift and oxygen upshift (transition out of the GI tract; $P < 10^{-28}$). **(B)** Pearson correlation of global changes in gene expression between oxygen downshift and other perturbations: oxygen upshift ($r = -0.50$; $P < 10^{-148}$), temperature upshift ($r = +0.39$; $P < 10^{-79}$), ultraviolet exposure ($r = -0.06$; $P < 0.02$), and osmolarity stress ($r = 0.11$; $P < 10^{-7}$). **(C)** The average relative change ($\log_2$) of TCA (*acnA*, *acnB*, *fumB*, *gltA*, *mdhA*, *sdhA*, *sdhB*, *sucB*, *sucC*, and *sucD*), cytochrome bo_3 (*cyoA*, *cyoB*, *cyoC*, *cyoE*), cytochrome bd (*cydA* and *cydB*), and heat shock–regulated (*dpB*, *dnaJ*, *grpE*, *hslU*, *hslV*, *htpX*, and *lon*) genes displaying reciprocal cross-regulation of aerobic respiration and heat shock in response to temperature and oxygen perturbations.

reduced in the evolved strain relative to the parental strain, both at early (16 min; parental, $r = 0.53$; evolved, $r = 0.19$) and late (44 min; parental, $r = 0.39$; evolved, $r = 0.06$) time points (Fig. 6D). This global decrease in correlation in the evolved strain was accompanied by a marked reduction in repression of TCA and cytochrome bo_3 oxidase genes, as well as reduction in the activation of genes encoding cytochrome bd oxidase (Fig. 6E).

Dynamic representations and predictive behavior. Molecular interactions and catalytic transformations are the fundamental building blocks in all cellular processes. We have shown that randomly evolving networks composed of these basic elements are able to internalize dynamic representations of their complex environments, enabling predictive behavior, and that this ability explains the seemingly maladaptive responses of *E. coli* to transitions in oxygen and temperature. Although the correlated responses we observe precisely correspond to transitions of *E. coli* between the outside world and the mammalian GI tract, it is formally possible that they may be due to some other unknown ecological structure in the wild. What is critical, however, is that these correlations show "plasticity" over the course of laboratory experimental evolution. Our findings motivate an alternative interpretation of cellular responses to nominally stressful stimuli (*24*); such "stresses" may be important to the organism not because of their immediate and direct fitness consequences, but in the information that they convey about the overall state of the environment and its likely trajectory.

Here, we have focused on the utility of learning temporally phased correlations for predicting sequential events in the environment (e.g., temperature upshift followed by oxygen downshift). However, the reciprocal cross-regulation of heat shock response and respiratory repression (Fig. 5C) suggests that *E. coli* also uses the simultaneous co-occurrence of events to reinforce perception of its immediate environment. More generally, the correlation structure of the environment can be internalized as a probabilistic model in the high-dimensional space of an organism's complete sensory perception. As such, the very organization of microbial regulatory networks may, in large part, represent the physical instantiation of this probabilistic model. From this perspective, inferences regarding the functional utility of biological networks, including notions of modularity and optimality, may be incomplete, or even inaccurate, without considering habitat structure. Experiments of the flavor we have presented here may allow biologists to essentially go in the opposite direction and "reverse-engineer" ecological structure from physiological observations in the laboratory.

Although our work on *E. coli* focused primarily on parameter changes that reflect macroscopic transitions in the environment, the dominant forces shaping microbial regulatory networks are likely to arise from microscopic correlation structure present in the complex chemistry of intra- and interspecies interactions (*25*, *26*).

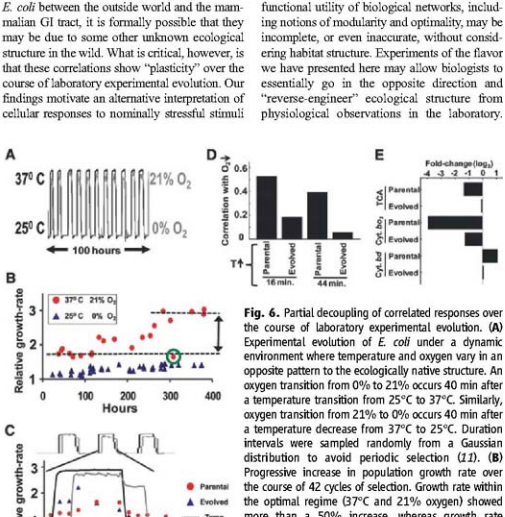

Fig. 6. Partial decoupling of correlated responses over the course of laboratory experimental evolution. **(A)** Experimental evolution of *E. coli* under a dynamic environment where temperature and oxygen vary in an opposite pattern to the ecologically native structure. An oxygen transition from 0% to 21% occurs 40 min after a temperature transition from 25°C to 37°C. Similarly, oxygen transition from 21% to 0% occurs 40 min after a temperature decrease from 37°C to 25°C. Duration intervals were sampled randomly from a Gaussian distribution to avoid periodic selection (*11*). **(B)** Progressive increase in population growth rate over the course of 42 cycles of selection. Growth rate within the optimal regime (37°C and 21% oxygen) showed more than a 50% increase, whereas growth rate increased only marginally within the 25°C and 0% oxygen regime. The measurement circled in green is an outlier. **(C)** High-resolution monitoring of growth rate in the parental and evolved strains shows that the fitness differential is maximal immediately after the oxygen upshift. **(D)** Pearson correlation of global changes in gene expression between the oxygen downshift and temperature upshift perturbations in the parental and evolved strains at 16 and 44 min after the temperature upshift. **(E)** Average relative change of gene expression for the TCA, cytochrome bo_3, and cytochrome bd gene sets at 16 min after a temperature increase in both the parental and evolved strains.

References and Notes

1. W. B. Cannon, *The Wisdom of the Body* (Norton, New York, 1932).
2. D. Bell-Pedersen *et al.*, *Nat. Rev. Genet.* **6**, 544 (2005).
3. A. Bergman, M. L. Siegal, *Nature* **424**, 549 (2003).
4. P. Francois, V. Hakim, *Proc. Natl. Acad. Sci. U.S.A.* **101**, 580 (2004).
5. P. Francois, V. Hakim, E. D. Siggia, *Mol. Syst. Biol.* **3**, 154 (2007).
6. N. Kashtan, U. Alon, *Proc. Natl. Acad. Sci. U.S.A.* **102**, 13773 (2005).
7. R. E. Lenski, C. Ofria, T. C. Collier, C. Adami, *Nature* **400**, 661 (1999).
8. G. Rodrigo, J. Carrera, A. Jaramillo, *Cent. Eur. J. Biol.* **2**, 233 (2007).
9. O. S. Soyer, T. Pfeiffer, S. Bonhoeffer, *J. Theor. Biol.* **241**, 223 (2006).
10. A. Wagner, *Proc. Natl. Acad. Sci. U.S.A.* **102**, 11775 (2005).
11. See supporting material on *Science* Online.
12. K. Basso *et al.*, *Nat. Genet.* **37**, 382 (2005).
13. D. Segre, A. Deluna, G. M. Church, R. Kishony, *Nat. Genet.* **37**, 77 (2005).
14. C. Dunne, *Inflamm. Bowel Dis.* **7**, 136 (2001).
15. M. Schena, D. Shalon, R. W. Davis, P. O. Brown, *Science* **270**, 467 (1995).
16. F. C. Neidhardt *et al.*, Escherichia coli *and* Salmonella: *Cellular and Molecular Biology* (American Society for Microbiology, Washington, DC, 1996).
17. J. Courcelle, A. Khodursky, B. Peter, P. O. Brown, P. C. Hanawalt, *Genetics* **158**, 41 (2001).
18. K. J. Cheung, V. Badarinarayana, D. W. Selinger, D. Janse, G. M. Church, *Genome Res.* **13**, 206 (2003).
19. A. P. Gasch *et al.*, *Mol. Biol. Cell* **12**, 2987 (2001).
20. T. Yura, K. Nakahigashi, *Curr. Opin. Microbiol.* **2**, 153 (1999).
21. I. Berman-Frank *et al.*, *Science* **294**, 1534 (2001).
22. R. E. Lenski, M. Travisano, *Proc. Natl. Acad. Sci. U.S.A.* **91**, 6808 (1994).
23. S. F. Elena, R. E. Lenski, *Nat. Rev. Genet.* **4**, 457 (2003).
24. G. Glaever *et al.*, *Nature* **418**, 387 (2002).
25. B. L. Bassler, R. Losick, *Cell* **125**, 237 (2006).
26. S. S. Branda, S. Vik, L. Friedman, R. Kolter, *Trends Microbiol.* **13**, 20 (2005).

27. We thank the members of the Tavazoie laboratory for helpful comments on the manuscript, Princeton's CSES team for supercomputer support, and S. Tavazoie, M. Tavazoie, and G. Vassilakis for crucial feedback throughout the preparation of this manuscript. Supported by a Burroughs Wellcome fellowship (I.T.) and by grants from the NSF Faculty Early Career Development (CAREER) Program, Defense Advanced Research Projects Agency, National Human Genome Research Institute, and National Institute of General Medical Sciences (PSO GM071508) (S.T.). The microarray data are deposited at NCBI Gene Expression Omnibus with accession number GSE10855.

Supporting Online Material

www.sciencemag.org/cgi/content/full/1154456/DC1
SOM Text
Figs. S1 to S21
Table S1
References

20 December 2007; accepted 25 March 2008
Published online 8 May 2008;
10.1126/science.1154456
Include this information when citing this paper.

A Transient Radio Jet in an Erupting Dwarf Nova

Elmar Körding,[1]* Michael Rupen,[2] Christian Knigge,[1] Rob Fender,[1] Vivek Dhawan,[2] Matthew Templeton,[3] Tom Muxlow[4]

Astrophysical jets seem to occur in nearly all types of accreting objects, from supermassive black holes to young stellar objects. On the basis of x-ray binaries, a unified scenario describing the disc/jet coupling has evolved and been extended to many accreting objects. The only major exceptions are thought to be cataclysmic variables: Dwarf novae, weakly accreting white dwarfs, show similar outburst behavior to x-ray binaries, but no jet has yet been detected. Here we present radio observations of a dwarf nova in outburst showing variable flat-spectrum radio emission that is best explained as synchrotron emission originating in a transient jet. Both the inferred jet power and the relation to the outburst cycle are analogous to those seen in x-ray binaries, suggesting that the disc/jet coupling mechanism is ubiquitous.

Jets launched by accreting objects seem to be a ubiquitous phenomenon, suggesting that accretion and jet launching may be intrinsically coupled. Jet emission from accreting white dwarfs (WDs) has been reported for supersoft sources (WDs with thermonuclear burning) (*1*) and symbiotic stars (highly accreting binary systems) (*2*). However, no jets have been found in cataclysmic variables (CVs), except perhaps after Nova eruptions (*3*). In fact, the lack of jet emission from dwarf novae (DNe), a class of weakly accreting nonmagnetic CVs, has been used as a constraint for jet-launching mechanisms of accreting objects (*4*, *5*). Radio emission, which is often used as a tracer for a jet, has only sporadically been found for nonmagnetic DNe (*6*, *7*), and the radio detections are usually not reproducible (*8*). It has thus been suggested that the radio emission is correlated with the optical outburst (*9*). X-ray binaries (XRBs), which do show jets, share many properties with DNe: The triggering of an outburst as well as the subsequent evolution of the accretion disc (for example, a truncated disc) are thought to be similar (*10*).

XRBs can be well studied throughout a full outburst cycle because the time scale from quiescence to the peak of the outburst and back ranges from weeks to months (*11*). The accretor in XRBs may be either a black hole or a neutron star. One of the main results of the study of black hole XRBs is the establishment of accretion states (*12*), through which a source moves in a predefined order (*13*), and their associated jet properties. These states can be well separated on a hardness-intensity diagram (HID) (*11*). At the beginning of the outburst, the source shows a hard x-ray spectrum and usually shows radio emission originating from a jet (the hard state, zone A in the left panel of Fig. 1) (*14*). The source brightens while staying in the hard state until it makes a transition to the soft state characterized by a soft x-ray spectrum. This transition is typically accompanied by a bright radio flare once the source crosses the jet line; after this, the core radio emission is quenched in the soft state (*13*). During the decay of the outburst the source moves back to the hard state—albeit at a lower luminosity than the hard-to-soft transition (*13*). Although the nomenclature of neutron star XRB states is different, one can map the neutron star states onto the black hole equivalents (*15*). This can be visualized in a HID, where they follow basically the same pattern (*16*) as shown in the middle panel of Fig. 1. The main difference, with respect to their radio emission, is that the radio emission is only suppressed by a factor of ~10 when the source is in the analog state of the soft state (*17*). The different behavior may be due to the existence of a boundary layer in neutron star XRBs, which does not exist in the black hole case.

The analogy between XRBs and DNe can be visualized by constructing a disc-fraction luminosity diagram (*18*) of a dwarf nova (DN) (Fig. 1, right panel), which is a generalization of the HIDs used for XRBs. For a DN, the inner region of the accretion flow is truncated by the stellar surface and its boundary layer. The boundary layer is thought to be the origin of the x-ray and extreme ultraviolet (UV) emission. The disc-fraction plotted in Fig. 1 describes the optical depth of the accretion flow for UV emission. The described analogy between XRBs and CVs suggests that radio emission from a DNe should be most prominent during the initial rise (zone A in Fig. 1) and the subsequent state transition to the soft state. However, the time scale of this rise is

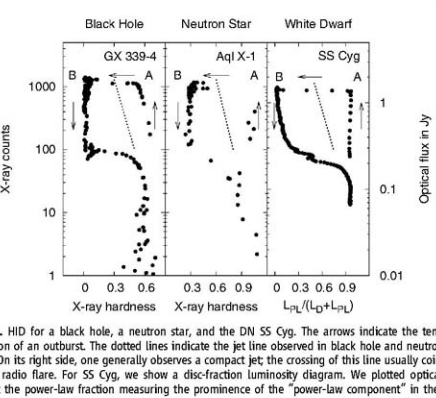

Fig. 1. HID for a black hole, a neutron star, and the DN SS Cyg. The arrows indicate the temporal evolution of an outburst. The dotted lines indicate the jet line observed in black hole and neutron star XRBs: On its right side, one generally observes a compact jet; the crossing of this line usually coincides with a radio flare. For SS Cyg, we show a disc-fraction luminosity diagram. We plotted optical flux against the power-law fraction measuring the prominence of the "power-law component" in the hard x-ray emission in relation to the boundary layer/accretion disk luminosity. This power-law fraction has similar properties to the x-ray hardness used for XRBs. The diagram is based on data from (*16*, *29*), and we used their conversion factors from extreme UV counts to disc/boundary layer luminosity L_D. The x-ray luminosity L_{PL} for SS Cyg is for the 3 to 18–keV energy range. For the other objects, the hardness ratio is defined as the ratio of the counts in the 6.3 to 10.5–keV range to the 3.8 to 6.3–keV range, and the x-ray counts represent the 3.8 to 21.2–keV counts of the Rossi X-ray Timing Explorer.

[1]School of Physics and Astronomy, University of Southampton, Southampton SO17 1BJ, UK. [2]National Radio Astronomy Observatory, 10003 Lopezville Road, Socorrow, NM 87801, USA. [3]American Association of Variable Star Observers, 49 Bay State Road, Cambridge, MA 02138, USA. [4]University of Manchester, Jodrell Bank Observatory, Macclesfield SK11 9DL, UK.

*To whom correspondence should be addressed. E-mail: elmar@phys.soton.ac.uk

usually on the order of 24 hours, making this phenomenon hard to catch.

To observe a DN in the radio band during the rise of an outburst, the American Association of Variable Star Observers (AAVSO) monitored a sample of 10 DNe on our behalf. On 13 April 2007, we received notice from the AAVSO that the prototypical DN, SS Cyg, had brightened to a magnitude of 11.3 in the V band, indicating the onset of an outburst. We subsequently triggered Very Large Array (VLA) observations at 8.6 GHz, which started ~10 hours after the initial optical observation. A typical observation (phase referenced to BL Lacertae) lasted for 2 hours and had a noise of 20 microjanskys (μJy) per beam.

We detected SS Cyg at 8.5 GHz during this long optical outburst. Slightly after the beginning of the outburst, we detected a fast rise of the radio flux to 1.1 mJy that immediately declined again to a flux of ~0.3 mJy. This flux declined further with time, though more slowly than did the optical emission (Fig. 2). During the 1.1-mJy "flare," we found upper limits for the linear polarization and circular polarization of 3.2 ± 2.7% and –3.2 ± 2.7%, respectively. During the decline of the outburst we also observed the source twice at 4.9 GHz, in addition to the 8.5-GHz observations. Both observations indicate that the source had a slightly inverted spectrum with an average spectral index of $\alpha = 0.3 \pm 0.2$ (flux $S_\nu \sim \nu^\alpha$).

We also detected SS Cyg with the Multi-Element Radio-Linked Interferometer Network (MERLIN) at 1.66 GHz as a point source with 0.79 ± 0.10 mJy, 13 hours after the detection of the radio flare with the VLA. These observations (at higher angular resolution than the VLA) indicate that the source of the radio emission is smaller than the beam size of ~0.2 arc sec. The position of the radio emission as measured by MERLIN is in agreement with the VLA position and coincides with the optical position of SS Cyg (nominal offset of 27 milli–arc sec when including proper motion). We did not detect any proper motion of the radio source associated with SS Cyg in our VLA images (average VLA beam size is 11 by 7 arc sec; nominal offsets of <2 arc sec).

The only possibilities for radio emission from a CV are optically thick or thin thermal emission, synchrotron emission, or coherent emission processes. From the angular resolution and flux of the MERLIN detection, we found a brightness temperature of at least 11,000 K. The radio spectrum of optically thick thermal emission with such high temperatures has a spectral index of ~2, which would predict an 8.5-GHz VLA flux density at the time of the MERLIN observation of >20 mJy, in contrast to the observed light-curve. Optically thin thermal free-free emission could produce the measured spectrum. As the radio light-curve does not directly follow the bolometric luminosity of the CV, it is unlikely that the emitting gas cloud is detached from the accreting system and only reprocesses the energy emitted from the CV. Thus, the emitting gas is likely to originate from the CV. In case of an uncollimated outflow (a wind), we obtained an upper limit to the 8.6-GHz flux from optically thin thermal emission of 10^{-3} mJy (*19*) by assuming that this wind carries all of the accreted material ($\sim 10^{-8}\ M_\odot$/year, where $M_\odot$ denotes a solar mass) into the emitting gas cloud. This value is far below the measured value. If we collimate the outflow (i.e., if we have a jet), we will obtain higher fluxes. However, as the jet would have to carry nearly all accreted material and be extremely highly collimated (opening angle < 0.2°) to obtain the measured flux, we consider this an unlikely explanation.

Coherent emission is seen only in line emission (e.g., masers) and very-steep-spectrum continuum emission, as is observed in pulsars or flare stars, for example (*20*). This is inconsistent with the measured flat spectrum. For gyrosynchrotron emission, we would expect a high degree of circular polarization, and our nondetection thus argues against this emission process. Additionally, the magnetic field of SS Cyg is thought to be fairly low (*21*) and should not play a dominant role in the emission mechanism: In order for the brightness temperature of the observed emission during the radio plateau not to exceed the Compton limit of $\sim 10^{12}$ K, the size of the emission region must be larger than ~60,000 km, more than 10 times the size of the central WD. The magnetosphere of SS Cyg in outburst is expected to be smaller than a few dwarf radii (*21*), if it exists at all. Thus, it is unlikely that the radio emission originates from any magnetic accretion processes near the WD. Synchrotron emission is known to produce a very high surface brightness (up to 10^{12} K) and may have spectral indices from –1.5 to 2.5, depending on optical depth. Thus, it is the best possibility for the observed emission.

As we have not resolved the emission region with our observations, it is hard to assess its geometry. The best-known geometries are expanding shells and jets. Shells are commonly seen in explosive phenomena like Novae (*22*) but have not been seen in a normal DN outburst. Any synchrotron emission from a transient shell or jet ejection has a steep spectrum during the decline, whereas we observe a flat spectrum during the decay. In a jet scenario, the observed behavior can be created by having a compact radio jet during the initial rise of the outburst, then a transient ejection followed by a restarting compact jet. This is exactly what was suggested by the analogy between CVs and XRBs (Fig. 1), which are known to be jet emitters. SS Cyg does show radio emission during its soft state; this behavior corresponds more closely to that observed in neutron stars, possibly because both neutron stars and WDs accrete onto a stellar surface and hence form a boundary layer.

For jet-emitting XRBs and active galactic nuclei (AGN), the radio emission in the hard state correlates well with the power liberated in the accretion flow (*23*). Taking into account that, for a given accretion rate, the accretion flow onto a WD liberates roughly 500 times less power than accretion onto a neutron star, we find $F_{8.6\mathrm{GHZ}} = 0.44\ \mathrm{mJy}\ (\dot{M}/10^{-8}\ M_\odot\ \mathrm{per\ year})^{1.4}$ (where F is the 8.6-GHz flux ratio, and $\dot{M}$ is the accretion rate) if the system is located at the Hubble Space Telescope (HST)–parallax distance of 166 pc (*24*). Typical DNe outbursts reach accretion rates of $\sim 10^{-8}\ M_\odot\ \mathrm{year}^{-1}$, but the HST distance and peak brightness of SS Cyg would imply an anomalously high accretion

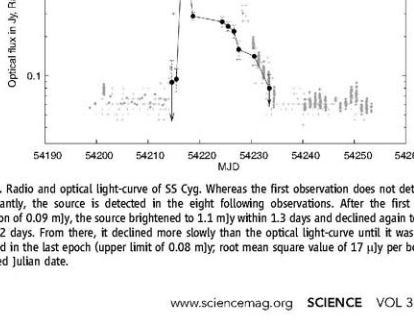

Fig. 2. Radio and optical light-curve of SS Cyg. Whereas the first observation does not detect SS Cyg significantly, the source is detected in the eight following observations. After the first significant detection of 0.09 mJy, the source brightened to 1.1 mJy within 1.3 days and declined again to 0.29 mJy within 2 days. From there, it declined more slowly than the optical light-curve until it was no longer detected in the last epoch (upper limit of 0.08 mJy; root mean square value of 17 μJy per beam). MJD, modified Julian date.

rate of ~10^{-7} $M_\odot$ year^{-1} for this system in outburst (*25*). A smaller distance of ~80 pc would be required to bring SS Cyg's peak accretion rate in line with typical values for DNe (*25*). Using this distance and an accretion rate of ~5×10^{-9} $M_\odot$ year^{-1} during the rise, we obtain a flux of ~0.7 mJy, in agreement with the observations (the uncertainty of the correlation is a factor of ~2). However, if the HST distance is correct and the accretion rate is indeed as high as ~10^{-7} $M_\odot$ year^{-1}, we have to assume an accretion rate during the rise of ~5×10^{-8} $M_\odot$ yr^{-1}. The predicted radio flux is then ~4 mJy, which is still roughly consistent with the measured values. In this case, the jet emission of SS Cyg, especially during the optical plateau, may correspond to the highest accreting states in XRBs and not to the hard state. For such high accretion rates, jet launching for CVs has been suggested by Soker and Lasota (*5*).

The similarities in the radio luminosity, as well as in the relation of the radio emission to the accretion states, suggest that we did observe a jet from a nonmagnetic DN. The detection of a jet in a DN with similar disc/jet coupling as that seen in XRBs suggests that there may be a common jet-launching mechanism in CVs and XRBs. The radii of WDs lie roughly halfway in log-space between those seen in young stellar objects (YSOs) and those of black holes, so WDs connect YSOs to XRBs. With the exception of source classes similar to soft-state XRBs, all accretion-powered jet-emitting sources from YSOs (*26*), via AGN (*27*) to gamma-ray bursts (*28*), seem to have a jet-launching efficiency (that is, the ratio of the jet power to the power liberated in the accretion flow) of ~10%. This suggests that there may be a common disc/jet coupling in all accreting objects from YSOs to gamma ray bursts.

References and Notes

1. T. Tomov, U. Munari, D. Kolev, L. Tomasella, M. Rejkuba, *Astron. Astrophys.* **333**, L67 (1998).
2. A. R. Taylor, E. R. Seaquist, J. A. Mattei, *Nature* **319**, 38 (1986).
3. T. Ijima, H. H. Esenoglu, *Astron. Astrophys.* **404**, 997 (2003).
4. M. Livio, *Phys. Rep.* **311**, 225 (1999).
5. N. Soker, J. P. Lasota, *Astron. Astrophys.* **422**, 1039 (2004).
6. A. O. Benz, E. Fuerst, A. L. Kipfinger, *Nature* **302**, 45 (1983).
7. A. O. Benz, M. Guedel, *Astron. Astrophys.* **218**, 137 (1989).
8. E. Fuerst, A. O. Benz, W. Hirth, M. Geffert, A. Kipfinger, *Astron. Astrophys.* **154**, 377 (1986).
9. A. O. Benz, M. Gudel, J. A. Mattei, in *Radio Emission from the Stars and the Sun*, Astronomical Society of the Pacific Conference Series, vol. 93, A. R. Taylor, J. M. Paredes, Eds. (Astronomical Society of the Pacific, San Francisco, 1996), pp. 188–190.
10. J. P. Lasota, *New Astron. Rev.* **45**, 449 (2001).
11. T. Belloni *et al.*, *Astron. Astrophys.* **440**, 207 (2005).
12. R. A. Remillard, J. E. McClintock, *Annu. Rev. Astron. Astrophys.* **44**, 49 (2006).
13. R. P. Fender, T. M. Belloni, E. Gallo, *Mon. Not. R. Astron. Soc.* **355**, 1105 (2004).
14. R. P. Fender, *Mon. Not. R. Astron. Soc.* **322**, 31 (2001).
15. M. Klein-Wolt, M. van der Klis, *Astrophys. J.* **675**, 1407 (2008).
16. D. Maitra, C. D. Bailyn, *Astrophys. J.* **608**, 444 (2004).
17. S. Migliari *et al.*, *Mon. Not. R. Astron. Soc.* **351**, 186 (2004).
18. E. Körding, S. Jester, R. Fender, *Mon. Not. R. Astron. Soc.* **372**, 1366 (2006).
19. A. E. Wright, M. J. Barlow, *Mon. Not. R. Astron. Soc.* **170**, 41 (1975).
20. M. Gudel, A. Benz, *Astron. Soc. Pac. Conf. Ser.* **93**, 303 (1996).
21. B. Warner, P. A. Woudt, *Mon. Not. R. Astron. Soc.* **335**, 84 (2002).
22. A. J. Mioduszewski, M. P. Rupen, *Astrophys. J.* **615**, 432 (2004).
23. E. Körding, R. P. Fender, S. Migliari, *Mon. Not. R. Astron. Soc.* **369**, 1451 (2006).
24. T. Harrison *et al.*, *Astrophys. Lett.* **515**, L93 (1999).
25. M. R. Schreiber, J. P. Lasota, *Astron. Astrophys.* **473**, 897 (2007).
26. R. J. White, L. A. Hillenbrand, *Astrophys. J.* **616**, 998 (2004).
27. E. Körding, S. Jester, P. Fender, *Mon. Not. R. Astron. Soc.* **383**, 277 (2008).
28. A. I. MacFadyen, S. E. Woosley, A. Heger, *Astrophys. J.* **550**, 410 (2001).
29. P. J. Wheatley, C. W. Mauche, J. A. Mattei, *Mon. Not. R. Astron. Soc.* **345**, 49 (2003).

30. We acknowledge all variable star observers (AAVSO and others) for their monitoring of DNe. We thank B. Warner for helpful discussions. We are grateful for the fast scheduling by the scheduling officers of the VLA and MERLIN. E.K. acknowledges support from a Marie Curie Intra-European-Fellowship. The National Radio Astronomy Observatory is a facility of NSF operated under cooperative agreement by Associated Universities. MERLIN is a National Facility operated by the University of Manchester at Jodrell Bank Observatory on behalf of the Science and Technology Facilities Council.

22 January 2008; accepted 30 April 2008
10.1126/science.1155492

Identification of Non-Precious Metal Alloy Catalysts for Selective Hydrogenation of Acetylene

Felix Studt,[1,2] Frank Abild-Pedersen,[1,2] Thomas Bligaard,[1] Rasmus Z. Sørensen,[3] Claus H. Christensen,[3] Jens K. Nørskov[1]

The removal of trace acetylene from ethylene is performed industrially by palladium hydrogenation catalysts (often modified with silver) that avoid the hydrogenation of ethylene to ethane. In an effort to identify catalysts based on less expensive and more available metals, density functional calculations were performed that identified relations in heats of adsorption of hydrocarbon molecules and fragments on metal surfaces. This analysis not only verified the facility of known catalysts but identified nickel-zinc alloys as alternatives. Experimental studies demonstrated that these alloys dispersed on an oxide support were selective for acetylene hydrogenation at low pressures.

The ethylene used in the production of polymers needs to contain less than a few parts per million of acetylene in order not to affect the polymerization process (*1*, *2*). Ethylene is produced in steam crackers and typically contains on the order of 1% of acetylene (*3*), which is removed by hydrogenation, but the hydrogenation process should not convert ethylene to ethane. The most common industrially used catalyst for this process is based on Pd modified by the addition of Ag (*4*). This system leaves ample room for improvement, particularly in terms of price. We show how alternative alloy catalysts for this reaction have been identified. Density functional theory (DFT) calculations identified why Ag promotes the selectivity of the Pd for this process. We then developed scaling relations between different adsorption energies of reactants and intermediates and used that analysis to identify a descriptor for both catalytic activity and selectivity. We screened a number of alloys as potential catalysts and singled out Ni-Zn intermetallic compounds as promising candidates. Subsequent synthesis, characterization, and catalytic testing showed these systems to have a high selectivity.

Following Sheth *et al.* (*5*–*7*), we first considered acetylene hydrogenation over Pd(111) (Fig. 1A). The process is facile (under appropriate conditions); acetylene adsorbs exothermally, and the transition-state energies for the first and second hydrogenation steps are both below the energy of gas-phase acetylene. Once ethylene is formed on the surface, it can desorb or react further; the latter outcome will lead to the unwanted formation of ethane. Ethylene from the gas phase can also adsorb on the surface and has the same possibility of further hydrogenation to ethane. A selective catalyst that hydrogenates only acetylene should have an activation barrier for the hydrogenation of ethylene that is greater than the barrier for desorption. For Pd(111), the two barriers are comparable. For PdAg(111), the barrier for desorption is smaller (Fig. 1A). However, the adsorption of acetylene is still sufficiently exothermic that its hydrogenation is facile. This analysis explains the basis for the addition of Ag to Pd in the industrial catalyst (*4*–*7*). Ag primarily changes the stability of adsorbed acetylene and

[1]Center for Atomic-scale Materials Design, Department of Physics, Building 311, Technical University of Denmark, DK-2800 Lyngby, Denmark. [2]Computational Materials Design ApS, Fysikvej, Building 307, DK-2800 Lyngby, Denmark. [3]Center for Sustainable and Green Chemistry, Department of Chemistry, Building 206, Technical University of Denmark, DK-2800 Lyngby, Denmark.

ethylene, rather than activation energies. The metal-independence of the activation barriers for hydrogenation has also been observed for a number of other hydrogenation reactions (*8*), which suggests that the stabilities of the two adsorbed species are the dominant parameters determining the potential activity and selectivity of the catalyst, as suggested previously by Bond (*9*).

The use of the acetylene and ethylene heats of adsorption, $\Delta E_{C_2H_2}$ and $\Delta E_{C_2H_4}$, as the parameters determining the turnover rate and selectivity is a large simplification. However, calculating these energies for a large number of systems is still demanding. We can simplify this problem considerably by introducing scaling relations between these adsorption energies and the adsorption energies of even simpler molecules, as illustrated in Fig. 2A. Based on calculations for a number of transition-metal surfaces, we find that the acetylene and ethylene adsorption energies scale with the methyl adsorption energies on the same metals. Such scaling relations were first established for CH_x molecules with differing numbers of H atoms (*10*). The results of Fig. 2A show that scaling relations also exist for more complicated molecules that are of interest in heterogeneous catalysis. The slope of the scaling relations is 4 for C_2H_2 and 2 for C_2H_4. This result can be viewed as a manifestation of bond order conservation for the C atoms; adsorbed CH_3 forms one σ bond to the surface, whereas C_2H_2 forms four σ bonds and C_2H_4 forms two. In this sense, the approach is related to that of Shustorovich and Bell (*11*).

A good catalyst is characterized by having a high stability of adsorbed acetylene ($\Delta E_{C_2H_2}$ as negative as possible) and a low stability of ethylene ($\Delta E_{C_2H_4}$ as positive as possible). The former determines the overall rate of acetylene removal, whereas the latter determines the selectivity. The results in Fig. 2A show that $\Delta E_{C_2H_2}$ and $\Delta E_{C_2H_4}$ are correlated, and one cannot just find a metal with a weak ethylene bond and a strong acetylene bond; the optimum catalyst is a compromise.

In Fig. 2A, we have illustrated the values of $\Delta E_{C_2H_4}$ and ΔE_{CH_3}, where the turnover rate is on the order of 1 s^{-1} at a total pressure of 1 bar, a temperature of 375 K, and 1% acetylene in the feed. More positive values of ΔE_{CH_3} should give lower rates, whereas increasing the temperature will move the value of ΔE_{CH_3} corresponding to a turnover rate of 1 s^{-1} to more positive values. In Fig. 2A, we also show the values of $\Delta E_{C_2H_4}$ and ΔE_{CH_3}, where the rates of ethylene desorption and hydrogenation are comparable. A larger value of ΔE_{CH_3} will now correspond to a more selective catalyst, because the activation barrier for the hydrogenation of ethylene, E_{hyd2}, will be greater than the desorption activation energy, $-\Delta E_{C_2H_4}$. This analysis leaves an optimum range of values of ΔE_{CH_3}. Because the DFT values used in establishing this range have an inherent uncertainty, and the model we used is simple, we allowed for a region around these values in our further search for new catalysts, as illustrated in Fig. 2B.

We screened about 70 different bimetallic compounds made from the elements for methyl binding energies (Fe, Ni, Co, Cu, Pd, Pt, Ag, Au, Zn, Cd, Hg, Ga, Tl, Ge, Sn, and Pb) (Fig. 2B). A number of alloys fall in the region of interest. Several PdAg alloys are there, as expected, and adding more Ag increases the selectivity; in fact, the commercial catalysts contain up to 80% of Ag (*4*). We also identified Pd-Ga, Pd-Pb, and Pd-Au alloys, which have recently been shown to have a good activity and selectivity for this process (*12*–*15*). Because one of the problems with

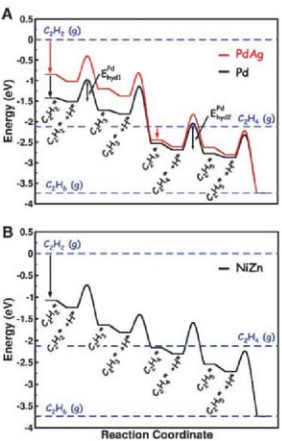

Fig. 1. Potential energy diagrams obtained from DFT calculations for the hydrogenation of acetylene to ethane on close-packed surfaces of **(A)** Pd (black) and PdAg (red) and **(B)** NiZn. In (A), the relevant hydrogenation barriers for the hydrogenation of acetylene and ethylene, respectively, are highlighted for Pd.

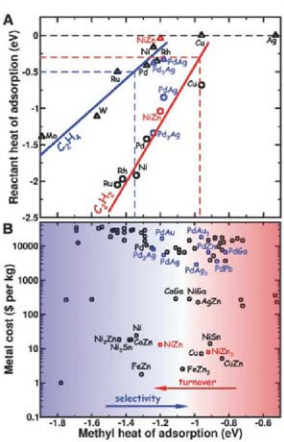

Fig. 2. **(A)** Heats of adsorption for acetylene (C_2H_2) and ethylene (C_2H_4) plotted against the heat of adsorption for methyl (CH_3). The adsorption energies are defined as the total energy of the surface with adsorbed species minus the sum of the total energy of the surface and the adsorbate in vacuum. The solid lines show the predicted acetylene (red line) and ethylene (blue line) adsorption energies from scaling. The dotted lines define the region of interest, where the ethylene binding energy is less than the barrier for further hydrogenation (blue) and where the reactivity of the acetylene hydrogenation step equals 1 s^{-1} per site (red). The adsorption geometry of ethylene on Ni and Rh has been accounted for by specifically choosing the methyl binding site to be on top of Ni and Rh (even though the most stable adsorption site is threefold), which corresponds to the site of adsorption of the carbons in ethylene. **(B)** Price (in 2006) of 70 binary intermetallic compounds plotted against the calculated methyl binding energies. The smooth transition between regions of low and high selectivity (blue) and high and low reactivity (red) is indicated.

the Pd-based catalysts is that they are extremely expensive, we have included the cost of raw materials of the catalysts as a parameter in Fig. 2B. Apart from Cu, which is known to be selective (*16*, *17*), Co-Ga, Fe-Zn, and Ni-Zn alloys stand out in this plot as particularly interesting. We have also calculated the stability of the different alloys, and here the Co-Ga and Ni-Zn alloys stand out, with heats of formation that are very exothermic, below –0.9 eV (87 kJ/mol). We have chosen the cheaper of the two, the Ni-Zn compounds, for further study.

Both NiZn and $NiZn_3$ are predicted to have good selectivity (Fig. 2B). For $NiZn_3$, we have not performed complete DFT calculations, because the correct structure according to the phase diagram (*18*) should be $Ni_{16}Zn_{53}$, but for the NiZn alloy we have made a complete DFT calculation of the reaction path for the close-packed (110) surface on the experimentally observed body-centered cubic (bcc) structure. The full potential energy diagram for the reaction (Fig. 1B) shows that NiZn should be active and quite selective. In Fig. 3, the acetylene and ethylene adsorption structures on the NiZn intermetallic compound are shown. The adsorbents bind to the Ni sites, showing that the change in adsorption properties is not the result of bonding to the Zn. Rather, Zn changes the electronic properties of Ni in the surface (*19*, *20*). We have also examined the segregation properties of the NiZn intermetallic compound. Segregation of Ni and Zn to the surface of NiZn in the bcc (110) structure costs 1.23 and 0.33 eV, respectively. This result means that the NiZn bimetallic compound is quite stable, which is expected for such a highly ordered alloy (*21*, *22*). We have concentrated here on the close-packed surfaces. Steps and other low-coordinated sites on catalyst surfaces will bind ethylene and acetylene more strongly and would be able to break the C-C bonds (*23*). We therefore expect those sites to be poisoned here.

Although calculations can point to possible candidates, many properties apart from activity and selectivity determine whether a particular material is suited as a catalyst. We have already mentioned intrinsic stability and segregation properties, and we can add resistance to coking and poisoning by other molecules in the reaction mixture, sintering properties, particle size distribution, and the ability to dissociate hydrogen. For example, Cu has been found to deactivate rapidly (*24*, *25*). Thus, experiments are needed to verify the suitability of a given candidate material.

We synthesized a series of Ni-Zn alloy catalysts on $MgAl_2O_4$ spinel supports that had a Zn content between 45 and 75% and tested their selectivity in the hydrogenation of acetylene in a gas mixture of 1.33% ethylene, 0.0667% acetylene, and 0.67% hydrogen (*26*). The ethane production as a function of acetylene conversion is shown in Fig. 4. A highly selective catalyst will have very low ethane production, even at high conversion, where the amount of acetylene in the reactants is small. We compared different Ni-Zn catalysts with the well-established Pd-Ag system. Pure Ni has rather poor selectivity, as also observed for pure Pd. The Pd-Ag alloy, on the other hand, shows a very good selectivity under high conversion. As expected from Fig. 2B, the selectivity increases substantially as the amount of Zn is increased. The Ni-Zn catalyst with the highest Zn content had an even greater selectivity than the best Pd-Ag catalyst we tested. The Ni-Zn catalysts we studied appeared to be more stable than has been reported for Cu (*23*–*25*). We know of no previous mention of NiZn alloy catalysts for selective hydrogenation. There are reports of Ni catalysts supported on $ZnAl_2O_4$ spinels (*27*), but these catalysts are reported to not contain a NiZn alloy.

The width of the interesting range of methyl binding energies in Fig. 2B is quite broad, ~0.5 eV, which is relatively large compared to both typical DFT– generalized gradient approximation errors (~0.2 eV) and the scatter in scaling plots such as Fig. 2A (~0.15 eV). It shows that even with the present accuracy of our theoretical treatment, it can be used as guidance toward new catalysts.

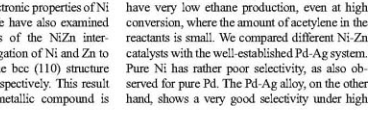

Fig. 3. Modeling of the NiZn catalyst in the bcc-B2 (110) structure. The unit cell is repeated twice in the *x* and *y* directions. The Ni atoms are shown as blue and Zn as gray. The adsorption of acetylene (left) and ethylene (right) is shown (small black and white structures).

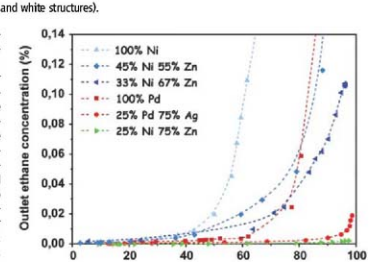

Fig. 4. Measured concentration of ethane at the reactor outlet as a function of acetylene conversion for seven catalysts. Ethane production is a measure of the selectivity of acetylene hydrogenation, and zero ethane corresponds to the most-selective catalyst. At the reactor inlet, the gas contained 1.33% ethylene, 0.0667% acetylene, and 0.67% hydrogen, with the remainder made up of Ar and N_2 in a total pressure of 1 bar. Experimental details are given in the supporting online material.

References and Notes

1. N. S. Schbib, M. A. García, C. E. Gigola, A. F. Errazu, *Ind. Eng. Chem. Res.* **35**, 1496 (1996).
2. A. N. R. Bos, K. R. Westerterp, *Chem. Eng. Process.* **32**, 1 (1993).
3. B. M. Collins, U.S. Patent, 4,126,645 (1978).
4. C. N. Thanh, B. Didillon, P. Sarrazin, C. Cameron, U.S. Patent 6,054,409 (2000).
5. P. A. Sheth, M. Neurock, C. M. Smith, *J. Phys. Chem. B* **107**, 2003 (2003).
6. P. A. Sheth, M. Neurock, C. M. Smith, *J. Phys. Chem. B* **109**, 12449 (2005).
7. D. Mei, P. Sheth, M. Neurock, C. M. Smith, *J. Catal.* **242**, 1 (2006).
8. Z.-P. Liu, P. Hu, *J. Am. Chem. Soc.* **125**, 1958 (2003).
9. G. C. Bond, *Catalysis by Metals* (Academic Press, New York, 1962).
10. F. Abild-Pedersen *et al.*, *Phys. Rev. Lett.* **99**, 016105 (2007).
11. E. Shustorovich, A. T. Bell, *Surf. Sci.* **205**, 492 (1988).
12. K. Kowalz *et al.*, *Sci. Technol. Adv. Mater.* **8**, 420 (2007).
13. M. A. Volpe, P. Rodríguez, C. E. Gigola, *Catal. Lett.* **61**, 27 (1999).
14. T. V. Choudhary, C. Sivadinarayana, A. K. Datye, D. Kumar, D. W. Goodman, *Catal. Lett.* **86**, 1 (2003).
15. S. A. Blankenship, R. W. Voight, J. A. Perkins, J. E. Fried, U.S. Patent 6,509,292 (2003).
16. L. K. Freivel, L. J. Kressley, U.S. Patent 3,912,789 (1975).
17. M. C. Convillon, U.S. Patent 4,440,956 (1984).
18. G. Nover, K. Schubert, *J. Less Common Met.* **75**, 51 (1980).
19. B. Hammer, J. K. Nørskov, *Nature* **376**, 238 (1995).
20. B. Hammer, J. K. Nørskov, *Adv. Catal.* **45**, 71 (2000).
21. L. V. Pourovskii, A. V. Ruban, B. Johansson, I. A. Abrikosov, *Phys. Rev. Lett.* **90**, 026105 (2003).
22. A. V. Ruban, *Phys. Rev. B* **65**, 174201 (2002).
23. R. T. Vang *et al.*, *Nat. Mater.* **4**, 160 (2005).
24. J. T. Wehrli, D. J. Thomas, D. L. Trimm, M. S. Wainwright, N. W. Cant, *Appl. Catal.* **66**, 199 (1990).
25. J. T. Wehrli, D. J. Thomas, M. S. Wainwright, D. L. Trimm, N. W. Cant, *Appl. Catal.* **70**, 253 (1991).
26. Details of the experimental studies are available as supporting material on *Science* Online.

27. J. C. Rodríguez, A. J. Marchi, A. Borgna, A. Monzón, *J. Catal.* **171**, 268 (1997).
28. Funding from the Lundbeck Foundation, the Danish National Research Foundation, the Danish Research Councils (STVF), and the Danish Center for Scientific Computing is gratefully acknowledged.

Supporting Online Material

www.sciencemag.org/cgi/content/full/320/5881/1320/DC1
SOM Text
References

19 February 2008; accepted 1 May 2008
10.1126/science.1156660

The Aftershock Signature of Supershear Earthquakes

Michel Bouchon[1]* and Hayrullah Karabulut[2]

Recent studies show that earthquake faults may rupture at speeds exceeding the shear wave velocity of rocks. This supershear rupture produces in the ground a seismic shock wave similar to the sonic boom produced by a supersonic airplane. This shock wave may increase the destruction caused by the earthquake. We report that supershear earthquakes are characterized by a specific pattern of aftershocks: The fault plane itself is remarkably quiet whereas aftershocks cluster off the fault, on secondary structures that are activated by the supershear rupture. The post-earthquake quiescence of the fault shows that friction is relatively uniform over supershear segments, whereas the activation of off-fault structures is explained by the shock wave radiation, which produces high stresses over a wide zone surrounding the fault.

Although supershear rupture was theoretically predicted more than 30 years ago (*1*–*3*) and first reported over two decades ago (*4*), the realization that it may be common during earthquakes has come only in the past few years (*5*–*13*). This phenomenon can occur only in mode II rupture; that is, when the fault slips in the direction in which rupture propagates. This is the mode of rupture prevalent in large crustal earthquakes. When a fault breaks at supershear speed, the earthquake ground motion is considerably modified (*14*, *15*). We report here that all the faults on which supershear rupture has been inferred have in common a specific pattern of aftershocks: The fault itself is remarkably free of aftershocks, which cluster off the fault on secondary structures that are activated by the supershear rupture.

The 1999 moment magnitude (M_w) = 7.4 Izmit earthquake ruptured about 150 km of the North Anatolian fault (NAF) in Turkey. Rupture began near the middle of the fault (Fig. 1) and propagated eastward at supershear speed for about 50 km before decelerating to sub-Rayleigh velocity (*6*). To the west of the epicenter, where the fault broke at classical sub-Rayleigh velocity, the aftershocks defined an E-W linear band that followed the fault under Izmit Bay and the eastern Marmara Sea (Fig. 1 and fig. S2A), except for two aftershock clusters located near the termination of the fault and associated with geothermal activity and branching (*16*, *17*).

To the east of the epicenter, the aftershock pattern was different. All along the supershear segment, few aftershocks occurred near the fault trace itself. Instead, they were spread over a broad area surrounding the fault (Fig. 1 and fig. S2B). Between Izmit and Sapanca, the aftershock clusters displayed a NE-SW trend. This orientation follows the lineaments of the old faulting system that characterized the deformation of the region before the development of the NAF (*18*). The aftershock pattern shows that some of these paleofaults, previously thought to be inactive, were partly reactivated by the earthquake. Farther east, between Sapanca and Akyazi, the aftershocks occurred to the south of the rupture on the complex fault system produced by the splaying of the two branches of the NAF. This system consists of a series of short normal faults, bounded to the south and east by strike-slip faults (Fig. 1) (*18*, *19*). The spreading of the aftershocks over the whole area, confirmed by focal mechanisms (*20*), indicates that the whole fault system was activated by the earthquake. The quiescence of the rupture plane itself, which bounds this area to the north, is striking, particularly when one considers that it was the region of highest slip (*21*). Seismic activity reached its peak just beyond the termination of the supershear segment. Farther east, the fault system becomes simpler and, like in the west, aftershocks formed a relatively narrow band parallel to the rupture trace of the slightly north-dipping Karadere segment.

The 1999 M_w = 7.2 Düzce earthquake occurred 3 months after the Izmit earthquake and extended the 150-km-long rupture 40 km eastward. Like the Izmit earthquake, it was a bilateral event nucleating near the middle of the fault (Fig. 2), and near-field recordings show that while rupture propagated westward from the hypocenter at sub-Rayleigh velocity, the average eastward velocity was supershear (*6*, *22*). Aftershocks occurred to the north of the surface rupture, as expected because, unlike the quasi-vertical Izmit rupture, the E-W striking Düzce fault dips about 65° northward (*22*). To the west of the epicenter, except along the fringe of the rupture trace (which corresponds to the shallow part of the fault), aftershocks were distributed rather evenly over the fault plane for a distance of

[1]Centre National de la Recherche Scientifique et Université Joseph Fourier, Grenoble, Laboratoire de Géophysique Interne et Tectonophysique, Boîte Postale 53, 38041 Grenoble, France. [2]Kandilli Observatory and Earthquake Research Institute, Bogaziçi University, Istanbul Kandilli Observatory, 81220 Cengelköy, Istanbul.

*To whom correspondence should be addressed. E-mail: Michel.Bouchon@ujf-grenoble.fr

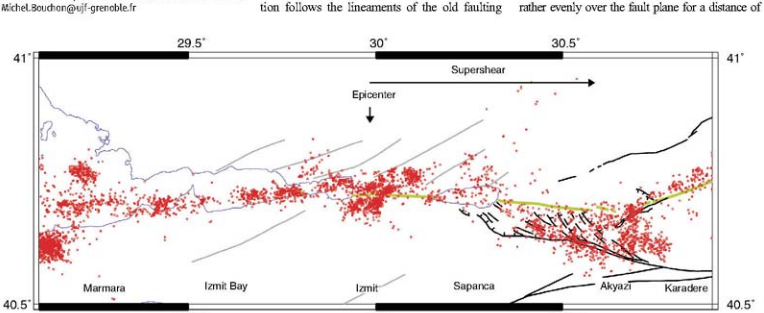

Fig. 1. Map of Izmit aftershocks (red dots) for the period from 17 August to 12 November 1999, relocated after combining all the available data recorded in the region (fig. S1). The surface rupture is in yellow, the active faults in black, and the ones thought to be inactive in gray (*19*).

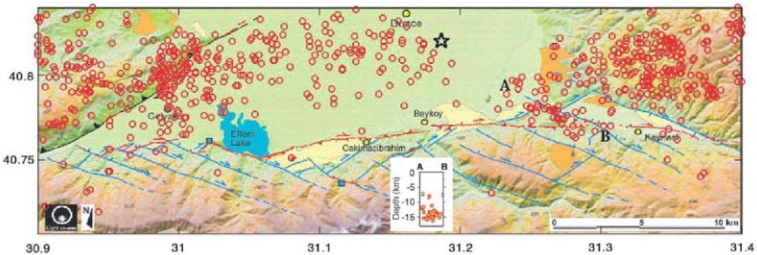

Fig. 2. Map of the Düzce aftershocks (red circles). The epicenters (*37*) are drawn on a background tectonic map (*23*) showing the surface rupture (red) and the plioquaternary fault system (blue). The main shock epicenter is shown by a star. The inset in the middle is the vertical cross-section between A and B.

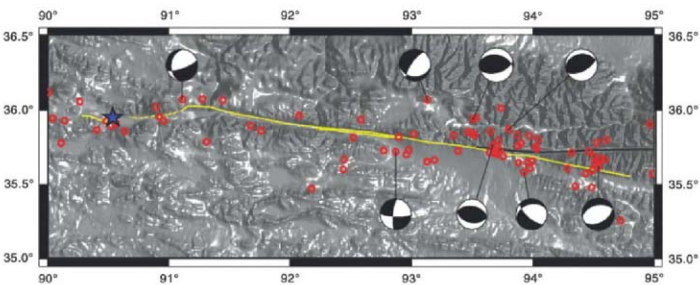

Fig. 3. Map of the Kunlunshan aftershocks of magnitude 4 and higher (red circles), with the focal mechanisms of the largest ones (balloons). The surface rupture is in yellow and the unbroken segment of the Kunlun fault in black. The epicenter is shown by a star.

about 15 km. Beyond this distance, which corresponds to a sharp drop in surface slip (*23*), the density of aftershocks increased, probably reflecting the complex mechanical interaction between the diverging Düzce and Karadere faults in this area.

To the east of the epicenter, the aftershock pattern was notably different. For about 5 km eastward from the hypocenter, the rupture plane was free of aftershocks. Beyond this gap, some aftershock epicenters clustered near the surface trace of the rupture. A cross-section of this cluster (Fig. 2, inset), however, shows that these events occurred at depth and not on the Düzce fault, which is shallow in this area. This WNW-ESE–trending cluster paralleled the old fault system that prevailed in the region before the development of the Düzce fault (*23*) and indicates that the earthquake reactivated some of these paleofaults. Farther east, the number of aftershocks increased near and beyond the termination of the surface break. This area also corresponds to the eastern termination of the mapped trace of the Düzce fault. Beyond it lies the complex 15-km-wide zone of deformation that separates the Düzce fault from the eastern single trace of the NAF.

The 2001 M_w = 7.9 Kunlunshan (Tibet) earthquake produced the longest surface rupture ever observed (Fig. 3), a nearly continuous break extending for about 425 km (*24*). Most of the rupture—about 300 km—occurred at supershear speed (*7*, *10*). In spite of its large magnitude, the earthquake was followed by few aftershocks (*10*, *25*). The strongest one reached a M_w of only 5.6, much lower than the value of about 6.8 typically expected for an event of this size. Only 17 aftershocks had a body wave magnitude m_b of 5 or higher, whereas on average for the magnitude of the main shock, more than 70 could have been expected (*26*). Another unusual feature of the Kunlunshan sequence is that out of the eight largest aftershocks for which focal mechanism could be determined (*27*, *28*), only one event of relatively small magnitude (M_w = 5.1) had a mechanism similar to that of the main shock (Fig. 3). Although the absence of local stations prevents precise locations, this is a strong indication that most of the aftershocks occurred not on the rupture plane, but on secondary structures off the main fault. The fact that the longest surface rupture ever observed was directly the source of so few aftershocks of such small magnitude is astonishing. Seismic activity, although small, clustered in two areas: the mechanically complex zone where the rupture splayed off the main Kunlun fault and the near-termination of the surface rupture. Thus, like at Izmit and Düzce, the long supershear segment of the Kunlunshan earthquake was quiet. The small aftershock activity of the region was concentrated near the junction of the rupture plane with other faults and near the termination of the supershear rupture.

The 2002 M_w = 7.9 Denali fault (Alaska) earthquake produced a surface rupture of about 340 km. Rupture started on a 48-km-long north-dipping thrust fault, the Sustina Glacier fault, then propagated eastward for nearly 300 km as a

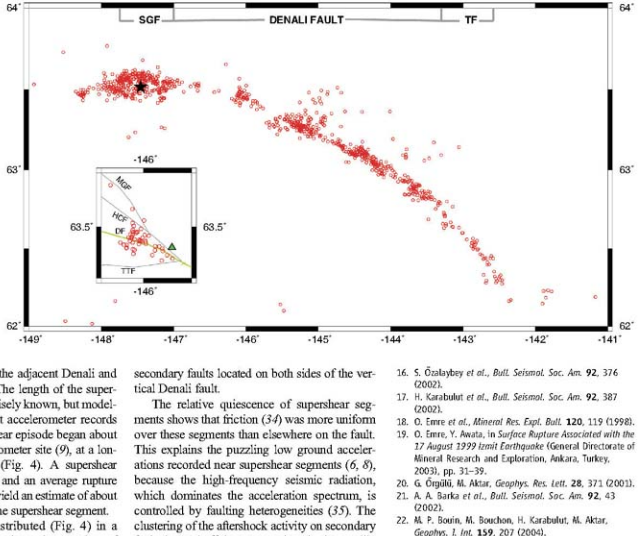

Fig. 4. Map of the Denali aftershocks of magnitude 3 and higher (red circles). The epicenter is shown by a star (SGF, Sustina Glacier fault; TF, Totschunda fault). The inset is a zoom of the 146° cluster, with the surface rupture in yellow and the fault nest in gray (MGF, McGinnis Glacier fault; HCF, Hines Creek fault; DF, Denali fault; TTF, Talkeetna fault). The accelerometer location is indicated by a triangle.

strike-slip rupture along the adjacent Denali and Totschunda faults (*29*). The length of the supershear segment is not precisely known, but modeling of the lone near-fault accelerometer records suggests that the supershear episode began about 35 km before the accelerometer site (*9*), at a longitude of about 146.5° (Fig. 4). A supershear speed of 5.5 km/s (*8*, *9*) and an average rupture velocity of 3.3 km/s (*30*) yield an estimate of about 60 km for the length of the supershear segment.

Aftershocks were distributed (Fig. 4) in a nearly continuous band along the 340 km of rupture, with the notable exception of the fault stretch between 146.5° and 145.5°. Except for a cluster of events centered around 146°, this stretch lacked aftershocks. This cluster was associated with a nest of faults (Fig. 4, inset) that merge there with the Denali fault. Geophysical investigations of this area (*31*, *32*) show that the aftershocks clustered on these secondary faults, principally the south-dipping Hines Creek fault and the north-dipping Talkeetna thrust fault, located respectively north and south of the Denali fault. In this zone, the Denali fault is nearly vertical and was almost free of aftershocks (*31*, *32*). Farther east, between 145.5° and 145°, where supershear is inferred to have ended, a broad aftershock cluster was present. There again, geophysical imaging has shown that these aftershocks clustered, not on the vertical Denali fault but on two shallow-dipping secondary faults, the McCallum Creek–State Creek and the Donnelly Dome–Granite Mountain thrust faults located on opposite sites of the Denali fault (*31*). Focal mechanisms of events in this cluster confirm that most of them, including the largest aftershock of the earthquake, had thrust mechanisms (*33*). Along the inferred supershear stretch, few aftershocks are associated with the Denali fault itself. Aftershocks in this zone cluster on well-recognized secondary faults located on both sides of the vertical Denali fault.

The relative quiescence of supershear segments shows that friction (*34*) was more uniform over these segments than elsewhere on the fault. This explains the puzzling low ground accelerations recorded near supershear segments (*6*, *8*), because the high-frequency seismic radiation, which dominates the acceleration spectrum, is controlled by faulting heterogeneities (*35*). The clustering of the aftershock activity on secondary faults located off the rupture plane is also readily explained: The shock wave radiated by the supershear rupture produces high stresses over a wide zone surrounding the fault (*36*). In this area the stress carried on the Mach cone is nearly the same as that which occurs on the fault (*36*). The width of this zone is comparable to the depth of faulting, in agreement with the present observations.

References

1. R. Burridge, *Geophys. J.* **35**, 439 (1973).
2. D. J. Andrews, *J. Geophys. Res.* **81**, 5679 (1976).
3. S. Das, K. Aki, *Geophys. J. R. Astron. Soc.* **50**, 643 (1977).
4. R. J. Archuleta, *J. Geophys. Res.* **89**, 4559 (1984).
5. S. Das, *Science* **317**, 905 (2007).
6. M. Bouchon *et al.*, *Geophys. Res. Lett.* **28**, 2723 (2001).
7. M. Bouchon, M. Vallée, *Science* **301**, 824 (2003).
8. W. L. Ellsworth *et al.*, *Earthquake Spectra* **20**, 597 (2004).
9. E. M. Dunham, R. J. Archuleta, *Bull. Seismol. Soc. Am.* **94**, S256 (2004).
10. D. P. Robinson, C. Brough, S. Das, *J. Geophys. Res.* **111**, B08303 (2006).
11. A. J. Rosakis, O. Samudrala, D. Coker, *Science* **284**, 1337 (1999).
12. K. Xia, A. J. Rosakis, H. Kanamori, J. R. Rice, *Science* **308**, 681 (2005).
13. X. Lu, N. Lapusta, A. J. Rosakis, *Proc. Natl. Acad. Sci. U.S.A.* **104**, 18931 (2007).
14. B. T. Aagaard, T. H. Heaton, *Bull. Seismol. Soc. Am.* **94**, 2064 (2004).
15. P. Bernard, D. Baumont, *Geophys. J. Int.* **162**, 431 (2005).
16. S. Özalaybey *et al.*, *Bull. Seismol. Soc. Am.* **92**, 376 (2002).
17. H. Karabulut *et al.*, *Bull. Seismol. Soc. Am.* **92**, 387 (2002).
18. O. Emre *et al.*, *Mineral Res. Expl. Bull.* **120**, 119 (1998).
19. O. Emre, Y. Awata, in *Surface Rupture Associated with the 17 August 1999 Izmit Earthquake* (General Directorate of Mineral Research and Exploration, Ankara, Turkey, 2003), pp. 31–39.
20. G. Örgülü, M. Aktar, *Geophys. Res. Lett.* **28**, 371 (2001).
21. A. A. Barka *et al.*, *Bull. Seismol. Soc. Am.* **92**, 43 (2002).
22. M. P. Bouin, M. Bouchon, H. Karabulut, M. Aktar, *Geophys. J. Int.* **159**, 207 (2004).
23. S. Pucci, thesis (Universita degli Studi di Perugia, Italy, 2006).
24. Y. Klinger *et al.*, *Bull. Seismol. Soc. Am.* **95**, 1970 (2005).
25. M. Antolik, R. E. Abercrombie, G. Ekström, *Bull. Seismol. Soc. Am.* **94**, 1173 (2004).
26. P. A. Reasenberg, L. M. Jones, *Science* **243**, 1173 (1989).
27. www.globalcmt.org.
28. P. Hao *et al.*, *Acta Seismol. Sinica* **17**, 31 (2004).
29. D. Eberhart-Phillips *et al.*, *Science* **300**, 1113 (2003).
30. D. D. Oglesby *et al.*, *Bull. Seismol. Soc. Am.* **94**, S214 (2004).
31. T. M. Brocher *et al.*, *Bull. Seismol. Soc. Am.* **94**, S85 (2004).
32. M. A. Fisher *et al.*, *Bull. Seismol. Soc. Am.* **94**, S107 (2004).
33. N. A. Ratchkovski, S. Wiemer, R. A. Hansen, *Bull. Seismol. Soc. Am.* **94**, S156 (2004).
34. R. Madariaga, *Science* **316**, 842 (2007).
35. R. Madariaga, *Ann. Geophys.* **1**, 17 (1983).
36. H. S. Bhat *et al.*, *J. Geophys. Res.* **112**, B06301 (2007).
37. S. Özalaybey *et al.*, paper presented at the 27th General Assembly of the European Seismological Commission, Lisbon, Portugal, 10 September 2000.

Supporting Online Material

www.sciencemag.org/cgi/content/full/320/5881/1323/DC1
SOM Text
Figs. S1 and S2
References

9 January 2008; accepted 5 May 2008
10.1126/science.1155030

Multipartite Entanglement Among Single Spins in Diamond

P. Neumann,[1]* N. Mizuochi,[2]* F. Rempp,[1] P. Hemmer,[3] H. Watanabe,[4] S. Yamasaki,[5] V. Jacques,[1] T. Gaebel,[1] F. Jelezko,[1] J. Wrachtrup[1]†

Robust entanglement at room temperature is a necessary requirement for practical applications in quantum technology. We demonstrate the creation of bipartite- and tripartite-entangled quantum states in a small quantum register consisting of individual ^{13}C nuclei in a diamond lattice. Individual nuclear spins are controlled via their hyperfine coupling to a single electron at a nitrogen-vacancy defect center. Quantum correlations are of high quality and persist on a millisecond time scale even at room temperature, which is adequate for sophisticated quantum operations.

Schrödinger coined the term "entanglement" to mean a peculiar mutual quantum interaction in which the properties of two or more physical objects can be correlated, even when separated. Since then, the generation and retrieval of entanglement among several qubits have become of fundamental importance in quantum science and technology. Quantum teleportation error correction, computation, and communication all benefit from (or require) entanglement. One current challenge for the field of quantum information processing has been to engineer a sufficiently large and complex controllable system in which questions related to entanglement can be precisely explored. Hence, proving entanglement among an increasing number of qubits is typically a benchmark for physical systems, in demonstrating their relevance to engineer quantum states. On the level of single quantum systems, entanglement has been proven for photons (*1*), ions (*2*, *3*), atoms (*4*), and superconductors (*5*). All solid-state qubit devices require low temperature to achieve sufficiently long entanglement lifetime. Whereas single electron spins can be accessed by charge transport (*6*) or optically (*7*), nuclei are more promising for quantum engineering because of their long coherence times, even under ambient conditions. Because of their weak interaction with the environment, nuclear spins are not directly affected by (for example) lattice phonons, which are a prominent source for dephasing in most solid-state systems. In ensemble studies, (pseudo)entanglement among nuclei has been demonstrated (*8*–*10*), but this has not been confirmed for single nuclear spins so far.

For the present experiments, ^{13}C nuclei coupled to a single nitrogen-vacancy (NV) defect center in diamond (Fig. 1A) were chosen. This system allows for high-fidelity polarization and detection of single electron and nuclear spin states, even under ambient conditions (*11*–*16*). The NV center's electron spin ($S = 1$) exhibits extraordinarily slow relaxation, with a longitudinal relaxation time T_1 (i.e., the time for spontaneous transition between pure states) on the order of milliseconds (*17*). The phase memory time T_2 is found to be around 0.6 ms (*18*). Hence, this defect has been identified as a prominent candidate for engineering quantum states and quantum information processing (*19*–*22*), as well as for high-resolution magnetometry (*23*). Scalability toward larger-scale quantum registers was proposed, for example, through optical interactions between NV centers. Alternatively, probabilistic entanglement based on photonic channels can provide efficient scaling up (*24*).

The NV center is a point defect (Fig. 1A): That is, the electron spin is mostly localized at the defect site. However, about 11% of its electron spin density is distributed over the nearest-neighbor carbon atoms (*25*), mostly those at the dangling bonds caused by the vacancy. As a result, substantial hyperfine and dipolar coupling are detectable for single nuclei localized close to the defect (*26*, *27*). Here, we use such coupling (Fig. 1B) to effectively control two nuclear spins on an individual basis, and by using this technique, we are able to demonstrate entanglement of two ^{13}C nuclear spins (N_1, N_2) in the first coordination shell of the vacancy. All four maximally entangled states, namely the Bell states

$$\Phi^{\pm} = 1/\sqrt{2}(|00\rangle \pm |11\rangle) \quad (1)$$

$$\Psi^{\pm} = 1/\sqrt{2}(|01\rangle \pm |10\rangle) \quad (2)$$

are generated, where "0" and "1" denote the two possible nuclear spin orientations ($m_I = -1/2 \mapsto |0\rangle$, $m_I = +1/2 \mapsto |1\rangle$, $|N_1N_2\rangle$) (Fig. 1B).

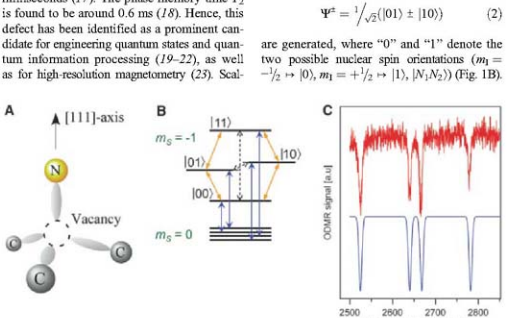

Fig. 1. (**A**) Atomic structure of the NV center. The nitrogen atom, vacancy, and three nearest-neighbor carbon atoms are shown. Two of the carbon atoms are ^{13}C isotopes with nuclear spin 1/2. (**B**) Energy-level scheme of electronic ground state of the NV center. Two of three hyperfine split electron spin sublevels ($m_S = 0,-1$) are depicted. Allowed transitions are shown by solid arrows (blue, electron spins; orange, nuclear spins). Zero and double quantum transitions are shown as dashed arrows. For further information, see (*15*). (**C**) ODMR spectrum (red curve) showing the $m_S = 0 \leftrightarrow -1$ transition. The simulated spectrum (blue curve) accounts for the hyperfine splitting of a single electron spin with two nearest-neighbor ^{13}C atoms. a.u., arbitrary units.

Table 1. Fidelity and entanglement measures for Bell, *GHZ*, and *W* states. Dashes indicate that the respective coherence measures were not calculated.

Coherence measure → / Bell state ↓	Fidelity	Concurrence	Partial transpose
Ψ^+	0.80 ± 0.07	$0.65^{+0.15}_{-0.08}$	$-0.31^{+0.05}_{-0.06}$
Ψ^-	0.81 ± 0.06	0.59 ± 0.11	$-0.32^{+0.04}_{-0.05}$
Φ^+	0.98 ± 0.05	$0.96^{+0.04}_{-0.09}$	$-0.49^{+0.04}_{-0.02}$
Φ^-	0.96 ± 0.05	$0.92^{+0.07}_{-0.08}$	−0.47 ± 0.46
GHZ	0.87 ± 0.06	—	—
W	$0.85^{+0.05}_{-0.1}$	—	—

[1]3. Physikalisches Institut, Universität Stuttgart, Pfaffenwaldring 57, D-70550 Stuttgart, Germany. [2]Graduate School of Library, Information and Media Studies, University of Tsukuba, 1-2 Kasuga, Tsukuba-City, Ibaraki 305-8550, Japan. [3]Department of Electrical and Computer Engineering, Texas A&M University, College Station, TX 77843, USA. [4]Diamond Research Center, National Institute of Advanced Industrial Science and Technology (AIST), Tsukuba Central 2, Tsukuba, 305-8568, Japan. [5]Nanotechnology Research Institute AIST, Tsukuba Central 2, Tsukuba, 305-8568, Japan.

*These authors contributed equally to this work.
†To whom correspondence should be addressed. E-mail: wrachtrup@physik.uni-stuttgart.de

These entangled states cannot be achieved by independently bringing the spins into an individual superposition state: Instead, they are global states of the two spins. To demonstrate even tripartite entanglement, we take the NV center's electron spin (E) into account and generate maximally entangled states such as the Greenberger-Horne-Zeilinger (*GHZ*) states, as well as the so-called *W* state

$$GHZ = {}^{1}/_{\sqrt{2}}(|000\rangle + e^{i\varphi}|111\rangle) \quad (3)$$

$$W = {}^{1}/_{\sqrt{3}}(|110\rangle + e^{i\varphi}|101\rangle + e^{i\theta}|011\rangle) \quad (4)$$

where φ and θ are arbitrary phases. Again, "0" and "1" denote the two possible spin states of all three spins ($m_S = 0 \leftrightarrow |0\rangle$, $m_S = -1 \leftrightarrow |1\rangle$, $|E\,N_1N_2\rangle$).

The measured optically detected magnetic resonance (ODMR) spectrum of the electron spin of a single center is shown in Fig. 1C. Four lines separated by hyperfine splittings are observed in each $m_S = 0 \leftrightarrow -1$ and $0 \leftrightarrow 1$ transition (*15*). The Bell states $\Phi^{\pm}$ and $\Psi^{\pm}$ are prepared as follows (Fig. 2A). After initialization by optical pumping, the system is set in the $m_S = 0$ state. The nuclear spin states, however, are undetermined. To initialize a specific nuclear spin starting state, we applied a transition-selective microwave (MW) π pulse and transferred $|E\,N_1N_2\rangle = |000\rangle$ into $|100\rangle$. If the system was in $|000\rangle$ after the laser irradiation, a pure $|00\rangle$ ($=|100\rangle$) state is created. If the system was in another state after laser irradiation, a subsequent MW excitation to $|00\rangle$ does not occur, and no observable signal is visible. To increase the success rate of initialization, one can, in principle, apply additional preparation steps (*27*).

Generation of Bell states proceeds in two steps. At first, a coherent superposition of states $|01\rangle$ and $|00\rangle$ is generated with a $\pi/2$ pulse on one radio frequency (rf) transition, which yields ${}^{1}/_{\sqrt{2}}(|00\rangle + |01\rangle)$. By the application of a frequency-selective π pulse in resonance with the $|01\rangle$ and $|11\rangle$ transition, eventually $\Phi^- = {}^{1}/_{\sqrt{2}}(|00\rangle - |11\rangle)$ is formed. The remaining Bell

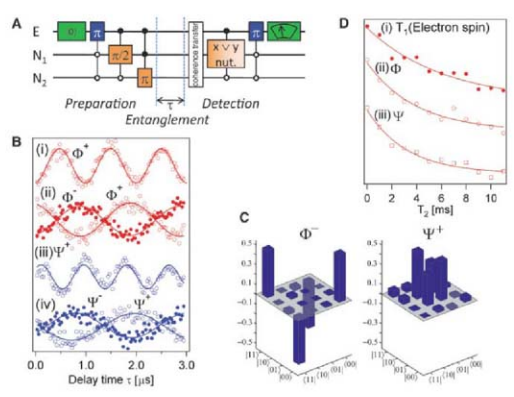

Fig. 2. **(A)** Pulse sequence for Bell state generation (Φ^-) among two nuclear spins. Spin-selective pulses are represented by squares, operating on a target qubit. Vertical lines represent logical connections. The control qubit state $|1\rangle$ and the state $|0\rangle$ are displayed as closed and open circles, respectively. For example, an open circle indicates that the pulse is applied to the target qubit if the quantum state of the controlling qubit is $|0\rangle$. Bell states evolve during time τ followed by state tomography. During six different transfer steps, the six possible coherences among the four nuclear spin states are unitarily mapped onto nuclear spin N_1. Each coherence is completely analyzed by performing two nutations (nut.) with two 90° phase-shifted rf fields. The results are the density matrix elements. **(B)** Ramsey fringes of Bell states: (i) Φ^-, (ii) Φ^+ and Φ^-, (iii) Ψ^+, and (iv) Ψ^+ and Ψ^-. The frequency offsets of rf1 ($\Delta\omega_1$), rf2 ($\Delta\omega_2$), and fitted curve (ω_{fit}) are: (i) $\Delta\omega_1 = 0.5$, $\Delta\omega_2 = 0.5$, and $\omega_{fit} = 1.0$ MHz ≈ $\Delta\omega_1+\Delta\omega_2$; (ii) $\Delta\omega_1 = 0$, $\Delta\omega_2 = 0.5$, and $\omega_{fit} = 0.5$ MHz ≈ $\Delta\omega_1+\Delta\omega_2$; (iii) $\Delta\omega_1 = -0.3$, $\Delta\omega_2 = 1.0$, and ω_{fit} = 1.3 MHz ≈ $\Delta\omega_2-\Delta\omega_1$; and (iv) $\Delta\omega_1 = 0$, $\Delta\omega_2 = 0.4$, and $\omega_{fit} = 0.4$ MHz ≈ $\Delta\omega_2-\Delta\omega_1$. **(C)** Density matrix reconstruction (real part) of states Φ^- and Ψ^+. Imaginary parts are found in (*15*). The high absolute values of the main off-diagonal elements (Φ^-: $|00\rangle\langle 11|$, $|11\rangle\langle 00|$; Ψ^+: $|10\rangle\langle 01|$, $|01\rangle\langle 10|$) prove that these are, in fact, entangled states and not just incoherent mixtures (otherwise, all off-diagonal elements would be zero). **(D)** Coherence time of Bell states as compared with the relaxation time of the electron T_1.

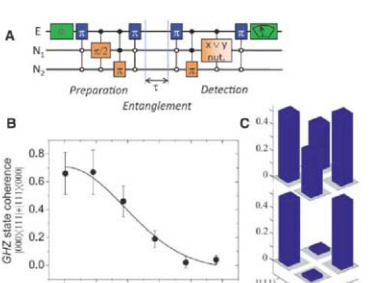

Fig. 3. **(A)** Pulse sequence for generation and detection of the *GHZ* state. The preparation sequence is similar to that of Bell states, followed by a selective MW pulse. For readout, a tomography is performed for the ideally nonzero density matrix elements. **(B)** Ramsey fringes of the *GHZ* coherence quantified by showing the sums of the respective off-diagonal elements of the density matrix ($\rho_{1,8}+\rho_{8,1}$ = $|000\rangle\langle 111| + |111\rangle\langle 000|$). The decay is fitted to $\exp[-(\nu/T_2{}^*)^2]$, with $T_2{}^* = 1.3 \pm 0.2$ μs. Error bars indicate the accuracy of the measured data points. **(C)** Tomogram of *GHZ* state's main density matrix entries. Unmeasured elements are discarded. The top graph shows the density matrix for evolution time τ = 0 μs, whereas the bottom graph shows the decay of off-diagonal elements for τ = 2.4 μs.

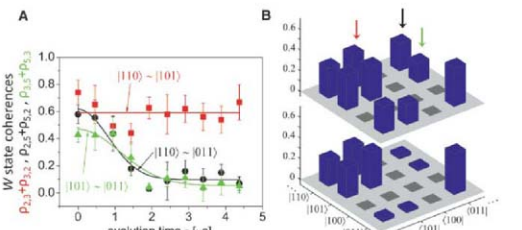

Fig. 4. (A) Ramsey fringes of all three coherences [sum of the corresponding off-diagonal elements: for example, $\rho_{5,2}+\rho_{2,5} = |011\rangle\langle 110| + |110\rangle\langle 011|$]. The respective off-diagonal elements are marked with a correspondingly colored arrow in (**B**). Only coherence between the two energy eigenstates containing the same electron spin orientation ($\rho_{3,2} = |101\rangle\langle 110|$, $\rho_{2,3} = |110\rangle\langle 101|$) shows no decay during the observation time. The others decay within 2 μs. The decay is fitted to $\exp[-(\tau/T_2^*)^2]$, with $T_2^* = 1.2 \pm 0.2$ μs for the circles and $T_2^* = 1.6 \pm 0.3$ μs for the triangles. The straight line for the squares is a guide to the eye. Error bars indicate the accuracy of the measured data points. (**B**) Tomograms of the main entries of the *W* state. The top and bottom graphs display the density matrix right after preparation and after 4.4 μs, respectively. Gray density matrix elements have not been measured.

states are prepared in a similar fashion (*28*). Having arranged the Bell states, we proved their generation via Ramsey fringes: that is, letting the Bell state evolve freely for a certain time τ and analyzing its phase afterwards (*15*). Phases of different Bell states evolve differently under rotation around the quantization axis (*28*). Φ and Ψ are characterized by an angular frequency $\Delta\omega_{\Phi,\Psi} = \Delta\omega_1+\Delta\omega_2$ and $\Delta\omega_2-\Delta\omega_1$, respectively (Fig. 2B), where $\Delta\omega_1$ and $\Delta\omega_2$ are detunings from resonance of the two radio frequency fields rf1 and rf2 involved in generation and detection of the respective Bell states. The "+" and "–" states are distinguishable by their phase with respect to the phase of the driving rf field (Fig. 2B).

A standard procedure to quantify the amount of entanglement is density matrix tomography. By measuring the probabilities to find the nuclear spins in a certain eigenstate and revealing coherent phases among them (e.g., $|00\rangle + |11\rangle$), researchers have performed density matrix tomography for all Bell states (*26*) (Fig. 2A). Tomography results are plotted in Fig. 2C. For brevity, only the real part of Φ and Ψ^+ is shown. Concurrence and the negative eigenvalue of the partial transpose were calculated (Table 1). To compare the measured density matrix ρ with the ideally expected one σ, we estimated the fidelity $F = \{\mathrm{tr}[(\sigma^{1/2}\rho\sigma^{1/2})^{1/2}]\}^2$ [$F = \mathrm{tr}(\sigma\rho)$ for pure states σ], where tr is the trace of a matrix. As demonstrated in Table 1, especially for $\Phi^\pm$, the respective values get close to ideal. It has been shown that a state ρ of two qubits is entangled if and only if its partial transpose ρ^{pt} has a negative eigenvalue (*29*, *30*). As shown in Table 1, this is indeed the case for all four states. We also have measured the coherence decay time T_2 of Φ and Ψ (Fig. 2D). Both types of Bell states decay on a time scale of 3 to 5 ms, which is similar to the relaxation time of the electron spin ($T_1 = 6$ ms).

After entangling two nuclear spins, the next step is to generate a tripartite entangled state via the electron spin of the NV center itself as the third qubit. The easiest tripartite entangled state to generate is the *GHZ* state. For its generation, we start off with a nuclear $\Phi^\pm$ state and apply a nuclear spin state–selective π pulse on the electron transition (Fig. 3A). For *W* state generation and further details of state preparation and readout, see (*15*). Tomography of these tripartite entangled states can be performed in a fashion similar to that of the Bell states. Note that these three spin coherences are directly observable in our spin resonance experiment. In the present work, we restricted our measurements to the main (ideally nonzero) density matrix entries of the respective entangled states (Figs. 3B and 4B). It can be shown that these elements are sufficient to calculate the fidelity $F = \mathrm{tr}(\sigma\rho)$ (*15*) (Table 1).

Because, for both states, an electron spin is now involved in the entangled states, one would expect the coherences to decay much faster than those where only nuclear spins were involved. Indeed, by measuring Ramsey fringes of *GHZ* coherence after a waiting time of 2 μs, we find that only an incoherent mixture of $|111\rangle$ and $|000\rangle$ is left (Fig. 3, B and C). The Ramsey fringe decay time is determined by inhomogeneities caused by slow spectral diffusion. Refocusing such inhomogeneities or decoupling these interactions will greatly lengthen the respective coherence time. Interaction with other spin impurities limits T_1 and T_2 of the NV center's electron spin [highest reported values: $T_1 = 380$ s, (*31*); $T_2 = 350$ μs, (*18*)]. Thus, the *GHZ* state prepared here would be an even more robust resource for quantum state engineering in a purer lattice environment.

The aforementioned *GHZ* decoherence is only expected to be due to the electron spin. This is reflected in the dephasing behavior of the *W* state. After the electron spin coherence has decayed, the remaining *W* state is written as an incoherent mixture of states $|0\rangle|11\rangle$ and $|1\rangle(|10\rangle + |01\rangle)$. Thus, for the electron spin measured to be in state $|1\rangle$, nuclear spin entanglement is expected to be found, namely the Ψ^+ nuclear spin Bell state. Observation of Ramsey fringes of all *W* state coherences indeed shows the expected behavior. The two coherences involving electron spin states decay within 2 μs, whereas the coherence with mainly nuclear spin character ($\langle 1|\Psi^+\rangle$) persists on this time scale (Fig. 4, A and B). Nuclear spin coherence outlasts electron spin decoherence.

Given the long decoherence times found for nuclear spin entangled states, there is ample opportunity to create even higher entangled states: for example, by including the nitrogen nuclear spin that is present in the defect but which was not used here. Large-scale networks may be achieved by entangling distant defects through emitted photons. Proposals similar to this have been published (*22*). Finally, we note that *GHZ*-type spin states are ideal candidates for quantum-improved measurements. In magnetometry applications, they outperform mixed states in signal-to-noise ratio by a factor of $\sqrt{N}$, where N is the number of entangled spins (*32*). Entangled spin states in a diamond-based magnetometer thus might enhance sensitivity considerably.

References and Notes

1. J. L. O'Brien, *Science* **318**, 1567 (2007).
2. C. F. Roos *et al.*, *Phys. Rev. Lett.* **92**, 220402 (2004).
3. C. F. Roos *et al.*, *Science* **304**, 1478 (2004).
4. J. Volz *et al.*, *Phys. Rev. Lett.* **96**, 030404 (2006).
5. M. Steffen *et al.*, *Science* **313**, 1423 (2006).
6. J. M. Elzerman *et al.*, *Nature* **430**, 431 (2004).
7. J. Berezovsky *et al.*, *Science* **314**, 1916 (2006).
8. T. S. Mahesh, N. Rajendran, X. H. Peng, D. Suter, *Phys. Rev. A* **75**, 062303 (2007).
9. H. G. Krojanski, D. Suter, *Phys. Rev. Lett.* **93**, 090501 (2004).
10. L. M. K. Vandersypen *et al.*, *Nature* **414**, 883 (2001).
11. J. Harrison, M. J. Sellars, N. B. Manson, *J. Lumin.* **107**, 245 (2004).
12. A. Beveratos, R. Brouri, T. Gacoin, J. P. Poizat, P. Grangier, *Phys. Rev. A* **64**, 061802 (2001).
13. C. Kurtsiefer, S. Mayer, P. Zarda, H. Weinfurter, *Phys. Rev. Lett.* **85**, 290 (2000).
14. A. Gruber *et al.*, *Science* **276**, 2012 (1997).
15. Supporting material is available on *Science* Online.
16. L. Childress *et al.*, *Science* **314**, 281 (2006).
17. D. A. Redman, S. Brown, R. H. Sands, S. C. Rand, *Phys. Rev. Lett.* **67**, 3420 (1991).
18. T. Gaebel *et al.*, *Nat. Phys.* **2**, 408 (2006).
19. J. Wrachtrup, S. Y. Kilin, A. P. Nizovtsev, *Opt. Spectrosc.* **91**, 429 (2001).
20. L. Childress, J. M. Taylor, A. S. Sorensen, M. D. Lukin, *Phys. Rev. Lett.* **96**, 070504 (2006).
21. R. J. Epstein, F. M. Mendoza, Y. K. Kato, D. D. Awschalom, *Nat. Phys.* **1**, 94 (2005).
22. S. D. Barrett, P. Kok, *Phys. Rev. A* **71**, 060310 (2005).
23. B. M. Chernobrod, G. P. Berman, *J. Appl. Phys.* **97**, 014903 (2005).

24. L. M. Duan, R. Raussendorf, *Phys. Rev. Lett.* **95**, 080503 (2005).
25. J. H. N. Loubser, J. A. van Wyk, *Diamond Res.* **11**, 4 (1977).
26. F. Jelezko *et al.*, *Phys. Rev. Lett.* **93**, 130501 (2004).
27. M. V. G. Dutt *et al.*, *Science* **316**, 1312 (2007).
28. M. Mehring, J. Mende, W. Scherer, *Phys. Rev. Lett.* **90**, 153001 (2003).
29. A. Peres, *Phys. Rev. Lett.* **77**, 1413 (1996).
30. M. Horodecki, P. Horodecki, R. Horodecki, *Phys. Lett. A* **223**, 1 (1996).
31. J. Harrison, M. J. Sellars, N. B. Manson, *Diamond Relat. Mater.* **15**, 586 (2006).
32. V. Giovannetti, S. Lloyd, L. Maccone, *Science* **306**, 1330 (2004).
33. We acknowledge financial support by the European Union (QAP, EQUIND, and NEDQIT) and Deutsche Forschungsgemeinschaft (SFB/TR21 and the JPN-GER cooperative program). N.M. is supported by the program KAKENHI (grant no. 18740175), and V.J. is supported by the Humboldt Foundation. We thank D. Twitchen from Element Six (UK) Ltd. for providing us with ultrapure chemical vapor deposition diamond samples.

Supporting Online Material

www.sciencemag.org/cgi/content/full/320/5881/1326/DC1
Materials and Methods
Figs. S1 to S4
Tables S1 to S3
References

3 March 2008; accepted 8 May 2008
10.1126/science.1157233

Strong Dissipation Inhibits Losses and Induces Correlations in Cold Molecular Gases

N. Syassen,[1] D. M. Bauer,[1] M. Lettner,[1] T. Volz,[1]* D. Dietze,[1]† J. J. García-Ripoll,[1,2] J. I. Cirac,[2] G. Rempe,[1] S. Dürr[1]‡

Atomic quantum gases in the strong-correlation regime offer unique possibilities to explore a variety of many-body quantum phenomena. Reaching this regime has usually required both strong elastic and weak inelastic interactions because the latter produce losses. We show that strong inelastic collisions can actually inhibit particle losses and drive a system into a strongly correlated regime. Studying the dynamics of ultracold molecules in an optical lattice confined to one dimension, we show that the particle loss rate is reduced by a factor of 10. Adding a lattice along the one dimension increases the reduction to a factor of 2000. Our results open the possibility to observe exotic quantum many-body phenomena with systems that suffer from strong inelastic collisions.

Strong interactions are responsible for many interesting quantum phenomena in many-body systems: high-temperature superconductivity (*1*), excitations with fractional statistic (*2*), topological quantum computation (*3*), and a plethora of exotic behaviors in magnetic systems (*4*). One of the main physical mechanisms that gives rise to strong correlations for bosonic particles can be understood as follows. At low temperatures and for strong elastic repulsive interactions, particles tend to stay far away from each other in order to keep the energy low. That is, the wave function describing the particles tends to vanish when two of them coincide at the same position. In order to fulfill these constraints, this wave function has to be highly entangled at all times, which may give rise to counterintuitive effects both in the equilibrium properties as well as in the dynamics. In one dimension, for example, this occurs in the so-called Tonks-Girardeau gas (TGG) (*5*, *6*), where the set of allowed wave functions for bosonic particles coincide (up to some transformation) with those of free fermions. Despite being bosons, the excitation spectrum, the evolution of the density distribution, etc. correspond to those of fermionic particles. In two dimensions, the same mechanism leads to the fractional quantum Hall effect (*7*), where the ground state as well as the low energy excitations fulfill the above-mentioned constraint, giving rise to the existence of anyons, which behave neither like bosons nor fermions but have fractional statistics (*2*).

We show that inelastic interactions can be used to reach the strong correlation regime with bosonic particles: This may seem surprising because inelastic collisions are generally associated with particle losses. This behavior can be understood by using an analogy in classical optics, where light absorption is expressed by an imaginary part of the refractive index. If an electromagnetic wave impinges perpendicularly on a surface between two media with complex refractive indices n_1 and n_2, then a fraction $|(n_1 - n_2)/(n_1 + n_2)|^2$ of the intensity will be reflected. In the limit $|n_2| \to \infty$, the light is perfectly reflected off the surface, irrespective of whether n_2 is real or complex. In our case, bosons interacting with large imaginary (*8*, *9*) scattering length almost perfectly reflect off each other for an analogous reason, thereby giving rise to the same constraints in the particles' wave function as the ones corresponding to elastic collisions and thus to the same physical phenomena. In our experiment, the correlations manifest themselves in a strong suppression of the rates at which particles are lost because of inelastic collisions.

Our experiment used molecules confined to one dimension by an optical lattice, both with and without a periodic potential along the one dimension. We started with the transfer of a Bose-Einstein condensate (BEC) of ^{87}Rb atoms into a three-dimensional (3D) optical lattice in such a way that the central region of the resulting Mott insulator contains exactly two atoms at each lattice site. A Feshbach resonance at 1007.4 G (*10*) was used to associate the atom pairs to molecules (*11*). Subsequently, the magnetic field was held at 1005.5 G. Atoms remaining after the association were removed with blast light. This procedure prepared a quantum state that contains one molecule at each site of a 3D optical lattice (*12*, *13*). The optical-lattice potential seen by a molecule is $-V_x\cos^2(kx) - V_z\cos^2(ky) - V_\parallel\cos^2(kz)$, where $\lambda = 2\pi/k = 830.440$ nm is the light wavelength. At the end of the state preparation, $V_\parallel$ is equal to $V_{\perp}$,

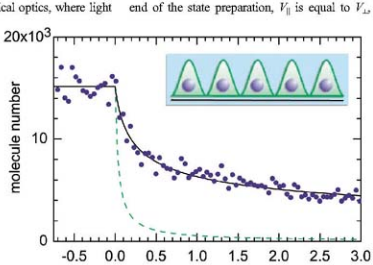

Fig. 1. Time-resolved loss of molecules at $V_\parallel = 0$. The loss begins at $t = 0$. The solid line shows a fit of Eq. 2 to the experimental data (•) with $t \leq 1$ ms. The best-fit value is $\gamma n^3(0) = 4.3$/ms, corresponding to $K_{3D} = 2.2 \times 10^{-10}$ cm^3/s and, at $t = 0$, to $g^{(2)} = 0.11$. The dashed line shows the expectation for an uncorrelated system. The observed loss is much slower than the dashed line because of strong correlations.

[1]Max-Planck-Institut für Quantenoptik, Hans-Kopfermann-Straße 1, 85748 Garching, Germany. [2]Universidad Complutense, Facultad de Físicas, Ciudad Universitaria s/n, 28040 Madrid, Spain.

*Present address: Institute of Quantum Electronics, Eidgenössische Technische Hochschule (ETH)–Hönggerberg, 8093 Zürich, Switzerland.

†Present address: Institut für Photonik, Technische Universität Wien, Gußhausstraße 25-29, 1040 Wien, Austria.

‡To whom correspondence should be addressed. E-mail: stephan.duerr@mpq.mpg.de

which equals $127E_r$, where $E_r = \hbar^2k^2/2m$ is the molecular recoil energy and m is the mass of one molecule.

After state preparation, $V_\parallel$ was linearly ramped down to its final value. After this ramp, we have an array of tubes of 1D gases. We chose a ramp duration of 0.5 ms. For much faster ramps, we observed a substantial broadening of the momentum distribution along the tubes. For much slower ramps, particle loss during the ramp became noticeable. After the ramp, the system was allowed to evolve for a variable hold time at the final value of $V_\parallel$. During this hold time, molecules collided inelastically, leading to loss. After the hold time, all molecules were dissociated (*11*) into atom pairs by using the Feshbach resonance. The dissociation terminated the loss. Lastly, the magnetic field and the lattice light were switched off simultaneously, and the number of atoms was determined from a time-of-flight absorption image.

The experimental data represent an average over a large number of tubes of different lengths. This is not critical because the initial 1D density, $n(0) = 2/\lambda$, is identical in all tubes. The lattice beams that create $V_\perp$ have a finite waist. This results in a harmonic confinement with angular frequency $\omega_\parallel = 2\pi \times 71$ Hz along the tubes. This is negligible as long as we evaluate the loss only for much faster time scales. In the decay of the molecule number as a function of hold time at $V_\parallel = 0$ (Fig. 1), the ramp-down of $V_\parallel$ begins at $t = -0.5$ ms and ends at $t = 0$. The data do not show noticeable loss during the ramp-down. In order to avoid complications because of the harmonic confinement $\omega_\parallel$ along the tubes, we processed only data for $t \leq 1$ ms.

A quantitative understanding of the loss process is based on the 1D particle density n, which evolves according to (*14*)

$$\frac{dn}{dt} = -Kn^2 g^{(2)} \tag{1}$$

where $g^{(2)} = \langle n^2 \rangle / \langle n \rangle^2$ is the pair correlation function that gives the reduction factor of the loss rate compared with an uncorrelated state where $g^{(2)} = 1$. K is the 1D loss rate coefficient, which can be related to the 3D scattering properties as follows: First, the scattering potential can be modeled as a delta interaction with 1D interaction strength g, yielding $K = -2\mathrm{Im}(g)/\hbar$ (*14*). Second, extending the arguments of (*15*) to the case of a complex-valued 3D scattering length a, one obtains $g = 2\hbar^2 a / \{ma_\perp^2 [1 + a\zeta(\frac{1}{2})/\sqrt{2}a_\perp]\}$, where $a_\perp$ is the size of the gas in the perpendicular direction and ζ denotes the Riemann zeta function with $\zeta(1/2) \approx -1.46$. The real and imaginary parts of a, $\mathrm{Re}(a)$ and $\mathrm{Im}(a)$, represent elastic and inelastic scattering, respectively.

For the ground state of the TGG, we can derive an analytic expression for $g^{(2)}$. By introducing a dimensionless interaction strength $\gamma = mg/\hbar^2 n$ and using the same techniques as in (*16*, *17*), we obtain $g^{(2)} = 4\pi^2/|\gamma|^2$ in the limit $|\gamma| >> 1$. Inserting this expression in Eq. 1, we obtain

$$\frac{dn}{dt} = -\chi n^4 \tag{2}$$

where $\chi = 4\pi^2\hbar^4 K/3m^2|g|^2$. This equation gives a prediction for the particle losses for a low-energy

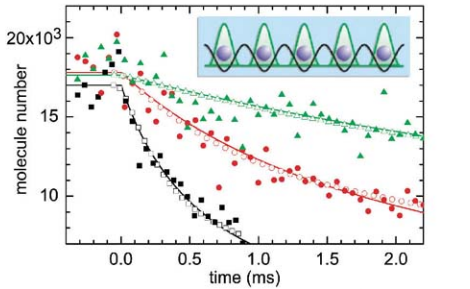

Fig. 2. Loss at $V_\parallel \neq 0$. Solid lines show fits of Eq. 3 to the experimental data (solid symbols). Open symbols show results of our numerical calculations. Black squares, red circles, and green triangles correspond to $V_\parallel/E_r$ values of 1.8, 3.9, and 6.0, respectively.

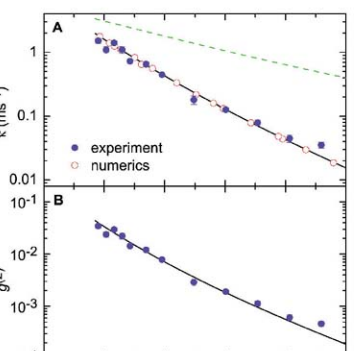

Fig. 3. Loss at different lattice depths $V_\parallel$. **(A)** Fits as in Fig. 2 yield the experimental results (•) for κ. A fit of Eq. 4 to the data yields the solid line. The best-fit value is $K_{3D} = 1.7 \times 10^{-16}$ cm^3/s. The experimental data and the analytic model agree well with results of our numerical calculations (○). For comparison, the dashed line shows the naïve estimate $2|I|/\hbar$, which is nowhere close to the data. Error bars indicate one statistical standard error. **(B)** Pair correlation function $g^{(2)} = \kappa/\Gamma$ calculated from the data in (**A**).

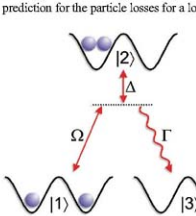

Fig. 4. Particle losses in a 1D lattice. The initial level $|1\rangle$ contains exactly one particle at each lattice site. State $|2\rangle$ is obtained after one tunneling process. Population in state $|2\rangle$ decays incoherently into state $|3\rangle$ with rate Γ. The tunneling coupling between states $|1\rangle$ and $|2\rangle$ can be described by a Rabi frequency Ω and a detuning Δ. In the limit $\Gamma >> \Omega$, the effective decay rate from $|1\rangle \rightarrow |3\rangle$ is $\Gamma_{\mathrm{eff}} = \Omega^2/\{\Gamma[1 + (2\Delta/\Gamma)^2]\}$, and the population of level $|2\rangle$ after a time $t >> 1/\Gamma$ is $\Gamma_{\mathrm{eff}}/\Gamma$ times that of level $|1\rangle$ (*29*). The parameters are related to the Bose-Hubbard parameters by $\Gamma = -2\mathrm{Im}(U)/\hbar$, $\Delta = \mathrm{Re}(U)/\hbar$, and $\Omega = \sqrt{8}J/\hbar$.

TGG. Similar considerations apply to inelastic three-body collisions (*18*–*20*). Note that a TGG at finite temperature has recently been observed experimentally (*21*–*23*) but for the known case of strong elastic interactions.

A fit of Eq. 2 to the data in Fig. 1 with $t \leq 1$ ms yields $\mathrm{Im}(1/a) = 1/(24\ \mathrm{nm})$. Combined with $|\mathrm{Re}(a)| \ll |\mathrm{Im}(a)|$ (*14*), this yields $g^{(2)} = 0.11 \pm 0.01$ at $t = 0$. This shows that the loss rate is strongly reduced because of correlations. $g^{(2)} \propto n^2$ decreases with time, so that the loss rate is reduced even further.

From these results, we can determine the two-body loss coefficient for a BEC, $K_{3D} = -8\pi\hbar\,\mathrm{Im}(a)/m = 2.2 \times 10^{-10} \pm 0.2 \times 10^{-10}\ \mathrm{cm}^3/\mathrm{s}$. This agrees fairly well with the measurements discussed below and with a previous measurement (*24*) at 1005.8 G that yielded $K_{3D} = 1.5 \times 10^{-10}\ \mathrm{cm}^3/\mathrm{s}$. For comparison we note that, if losses were not inhibited, that is, $g^{(2)} = 1$, then the loss should follow the dashed line, which is calculated with K_{3D} from (*24*). Clearly, the loss rate is reduced.

This reduction is directly related to the fact that the spatial wave functions of the particles do not overlap, and thus they become strongly correlated. Further support for this conclusion comes from the time dependence of our data. If the system were weakly correlated, then $g^{(2)} \approx 1$ would be time independent. Equation 1 would then predict that the number of particles N follows $dN/dt \propto N^2$ instead of $dN/dt \propto N^4$ if we are close to the TGG ground state (*14*). We fit $dN/dt \propto N^p$ with an arbitrary power p to the data with $t \leq 1$ ms. This yields $p = 4.3 \pm 0.6$, in good agreement with $p = 4$.

We now turn to a situation with a lattice potential along the 1D tubes with $V_0 \ll V_\perp$. The motion perpendicular to the tubes remains frozen out as before, but the motion along the tubes is now described as hopping between discrete lattice sites. This is a natural way of amplifying the effects due to interactions and thus reaching more deeply into the strong-correlation regime (*25*, *21*). Apart from that, many paradigmatic models in solid state and other fields of physics assume a lattice structure. We performed measurements (Fig. 2) similar to that in Fig. 1 for various values of the lattice depth V_0. Here, the temporal change of $g^{(2)}$ is negligible (*14*). Spatial integration of Eq. 1 yields

$$\frac{dN}{dt} = -\frac{\kappa}{N(0)} N^2(t) \qquad (3)$$

where we abbreviated $\kappa = K n(0)\, g^{(2)}$. We fit this to the data with $N(t) \geq N(0)/2$ in order to neglect the harmonic confinement along the tube. The best-fit values for the loss rate κ obtained for different lattice depths V_0 are shown in Fig. 3A.

A prediction for κ can be developed starting from the Lieb-Liniger Hamiltonian (*16*, *14*). In the presence of a periodic potential in the tight-binding limit, we obtain a Bose-Hubbard model (*26*) with tunneling amplitude J and on-site interaction $\mathrm{Re}(U)$. J and U can be expressed in terms of m, a_s, and a Wannier function. $\Gamma = -2\mathrm{Im}(U)/\hbar$ is the rate at which two particles at the same site are lost. In this model, losses occur when two particles occupy neighboring sites and one of them hops to the other's site. For strong inelastic interactions ($J/\hbar\Gamma \ll 1$), we obtain an effective loss rate Γ_{eff} for two neighboring particles (Fig. 4). An extension of this double-well model to many sites yields $\kappa = 4\Gamma_{\mathrm{eff}}$ (*14*) so that

$$\kappa = \frac{32J^2}{\hbar^2\Gamma}\left\{1 + \left[\frac{\mathrm{Re}(a)}{\mathrm{Im}(a)}\right]^2\right\}^{-1} \qquad (4)$$

This coefficient shows again that for strong inelastic interactions ($\Gamma \to \infty$) particle losses are inhibited. For large, finite values of Γ one can, as before, observe such an inhibition by looking at the particle losses. We fit Eq. 4 to the data in Fig. 3A. With $|\mathrm{Re}(a)| \ll |\mathrm{Im}(a)|$ there is only one free fit parameter. The best-fit value is $K_{3D} = 1.7 \times 10^{-10} \pm 0.3 \times 10^{-10}\ \mathrm{cm}^3/\mathrm{s}$, which is close to the result of Fig. 1. As $V_\parallel/E_r$ increases from 1.7 to 10, Γ increases from 45/ms to 82/ms.

In order to test the quality of this analytic model, we performed extensive numerical calculations by solving the master equation (*14*) with use of matrix product density operators (*27*). They reveal that the system maps to a very good approximation to a fermionized gas and that it loses its memory about the initial state in a time $\sim 1/\Gamma$. During this very short time, only little loss occurs, and after this short transient the loss is well described by a time-independent $g^{(2)}$ with κ from Eq. 4. We find good agreement between experimental data, analytic model, and numerical results in Figs. 2 and 3.

For $|\mathrm{Re}(a)| \ll |\mathrm{Im}(a)|$, Eq. 4 tells us that the larger the loss coefficient Γ, the smaller the actual loss rate κ. This means that fast on-site loss tends to preserve the initial state and thus suppresses tunneling in the many-body system. This can be interpreted as a manifestation of the continuous quantum Zeno effect (*28*): Fast dissipation freezes the system in its initial state. Without this Zeno effect, one might naïvely estimate that tunneling would occur at a rate $\sim 2J/\hbar$. If such tunneling event would lead to immediate loss, then $2J/\hbar$ should set the time scale for the loss, but that estimate is too naïve, as the dashed line in Fig. 3A shows.

The value of K_{3D} extracted from Fig. 3A is used to calculate Γ and thus $g^{(2)} = \kappa/\Gamma$ (*14*) for each experimental data point. The results (Fig. 3B) agree well with the theoretical expectation (solid line) based on the same value of K_{3D}. The smallest measured value of $g^{(2)} = 4.6 \times 10^{-4} \pm 0.7 \times 10^{-4}$ represents an improvement of more than two orders of magnitude over previous experiments (*23*). Note that a noninteracting gas has $g^{(2)} = 1$ at any lattice depth. The observed suppression of $g^{(2)}$ is caused by the inelastic interactions, not by the lattice itself. Moreover, the strength of the correlations in our experiment is determined by the interparticle interactions. This situation differs fundamentally from experiments in very deep lattices where tunneling is negligible on the time scale of the experiment, interactions are irrelevant, and bosonic symmetrization of the wave function is possible but has no detectable consequences.

The mechanism introduced here could also give rise to other strongly correlated states, such as a Laughlin state (*7*) or one with anyonic excitation (*2*). The present paper opens up the possibility of observing exotic quantum many-body phenomena in systems that suffer from strong inelastic collisions. Furthermore, the rate coefficients for those collisions may be artificially increased by using photoassociation or Feshbach resonances, thus further reducing the actual loss rate in the strongly correlated regime.

References and Notes

1. P. W. Anderson, *Science* **235**, 1196 (1987).
2. F. Wilczek, *Phys. Rev. Lett.* **48**, 1144 (1982).
3. A. Y. Kitaev, *Ann. Phys. (N.Y.)* **303**, 2 (2003).
4. A. Auerbach, *Interacting Electrons and Quantum Magnetism* (Springer, Berlin, 1994).
5. L. Tonks, *Phys. Rev.* **50**, 955 (1936).
6. M. Girardeau, *J. Math. Phys.* **1**, 516 (1960).
7. H. L. Stormer, D. C. Tsui, A. C. Gossard, *Rev. Mod. Phys.* **71**, S298 (1999).
8. B. J. Verhaar, *Laser Phys.* **4**, 1050 (1994).
9. J. L. Bohn, P. S. Julienne, *Phys. Rev. A* **56**, 1486 (1997).
10. A. Marte *et al.*, *Phys. Rev. Lett.* **89**, 283202 (2002).
11. S. Dürr, T. Volz, A. Marte, G. Rempe, *Phys. Rev. Lett.* **92**, 020406 (2004).
12. T. Volz *et al.*, *Nat. Phys.* **2**, 692 (2006).
13. S. Dürr *et al.*, in *Atomic Physics 20: XXth International Conference on Atomic Physics*, C. Roos, H. Häffner, R. Blatt, Eds., American Institute of Physics (AIP) Conference Proceedings No. 869 (AIP, New York, 2006), pp. 278–283.
14. Modeling details are available on *Science* Online.
15. M. Olshanii, *Phys. Rev. Lett.* **81**, 938 (1998).
16. E. H. Lieb, W. Liniger, *Phys. Rev.* **130**, 1605 (1963).
17. D. M. Gangardt, G. V. Shlyapnikov, *Phys. Rev. Lett.* **90**, 010401 (2003).
18. Y. Kagan, B. V. Svistunov, G. V. Shlyapnikov, *J. Exp. Theor. Phys. Lett.* **42**, 209 (1985).
19. E. A. Burt *et al.*, *Phys. Rev. Lett.* **79**, 337 (1997).
20. B. Laburthe Tolra *et al.*, *Phys. Rev. Lett.* **92**, 190401 (2004).
21. B. Paredes *et al.*, *Nature* **429**, 277 (2004).
22. T. Kinoshita, T. Wenger, D. S. Weiss, *Science* **305**, 1125 (2004); published online 29 July 2004 (10.1126/science.1100700).
23. T. Kinoshita, T. Wenger, D. S. Weiss, *Phys. Rev. Lett.* **95**, 190406 (2005).
24. N. Syassen, T. Volz, S. Teichmann, S. Dürr, G. Rempe, *Phys. Rev. A* **74**, 062706 (2006).
25. T. Stöferle, H. Moritz, C. Schori, M. Köhl, T. Esslinger, *Phys. Rev. Lett.* **92**, 130403 (2004).
26. D. Jaksch, C. Bruder, J. I. Cirac, C. W. Gardiner, P. Zoller, *Phys. Rev. Lett.* **81**, 3108 (1998).
27. F. Verstraete, J. J. García-Ripoll, J. I. Cirac, *Phys. Rev. Lett.* **93**, 207204 (2004).
28. B. Misra, E. C. G. Sudarshan, *J. Math. Phys.* **18**, 756 (1977).
29. C. Cohen-Tannoudji, J. Dupont-Roc, G. Grynberg, *Atom-Photon Interactions* (Wiley, New York, 1992), pp. 49–59.

30. We acknowledge financial support of the German Excellence Initiative via the program Nanosystems Initiative Munich and of the Deutsche Forschungsgemeinschaft via SFB 631. J.J.G.-R. acknowledges financial support from the Ramon y Cajal Program and the Spanish projects FIS2006-04885 and CAM-UCM/910758.

Supporting Online Material

www.sciencemag.org/cgi/content/full/320/5881/1329/DC1
SOM Text

16 January 2008; accepted 15 April 2008
10.1126/science.1155309

Subdiffraction Multicolor Imaging of the Nuclear Periphery with 3D Structured Illumination Microscopy

Lothar Schermelleh,[1]* Peter M. Carlton,[2]* Sebastian Haase,[2,4] Lin Shao,[2] Lukman Winoto,[2] Peter Kner,[2] Brian Burke,[3] M. Cristina Cardoso,[4] David A. Agard,[2] Mats G. L. Gustafsson,[5] Heinrich Leonhardt,[1]† John W. Sedat[2]†

Fluorescence light microscopy allows multicolor visualization of cellular components with high specificity, but its utility has until recently been constrained by the intrinsic limit of spatial resolution. We applied three-dimensional structured illumination microscopy (3D-SIM) to circumvent this limit and to study the mammalian nucleus. By simultaneously imaging chromatin, nuclear lamina, and the nuclear pore complex (NPC), we observed several features that escape detection by conventional microscopy. We could resolve single NPCs that colocalized with channels in the lamin network and peripheral heterochromatin. We could differentially localize distinct NPC components and detect double-layered invaginations of the nuclear envelope in prophase as previously seen only by electron microscopy. Multicolor 3D-SIM opens new and facile possibilities to analyze subcellular structures beyond the diffraction limit of the emitted light.

Light microscopy is a key technology in modern cell biology and, in combination with immunofluorescence, fluorescent protein fusions, or in situ hybridization, allows the specific localization of nearly all cellular components. A fundamental limitation of optical microscopy is its low resolution relative to the scale of subcellular structures. This limitation occurs because light traveling through a lens cannot be focused to a point but only to an Airy disk (*1*) with a diameter of about half the wavelength of the emitted light (*2*, *3*). Because the wavelengths of visible light range from 400 to 700 nm, objects closer than 200 to 350 nm apart cannot be resolved but appear merged into one.

Improving resolution beyond the 200-nm diffraction limit while retaining the advantages of light microscopy and the specificity of molecular imaging has been a long-standing goal. Here, we present results demonstrating that this goal can be achieved with the use of a microscope system that implements three-dimensional structured illumination microscopy (3D-SIM) (*4*) in an easy-to-use system that makes no extra demands on experimental procedures. Structured illumination microscopy (SIM) resolves objects beyond the diffraction limit by illuminating with multiple interfering beams of light (*5*). The emitted light then contains higher-resolution image information, encoded by a shift in reciprocal (Fourier, or frequency) space into observable modulations of the image, in a manner similar to the formation of Moiré patterns (fig. S1). This extra information can be decoded to reconstruct fine details, resulting in an image with twice the resolution of a conventional image taken on the same microscope (Fig. 1 and fig. S2). The 3D-SIM method extends previous 2D SIM methods by using three beams of interfering light, which generate a pattern along the axial (z) direction as well as the lateral (x and y) directions. We implemented 3D-SIM in a custom-built microscope designed for

[1]Center for Integrated Protein Science, Department of Biology, Ludwig Maximilians University Munich, 82152 Planegg-Martinsried, Germany. [2]Department of Biochemistry and Biophysics, University of California, San Francisco, CA 94143, USA. [3]Department of Anatomy and Cell Biology, University of Florida, Gainesville, FL 32610, USA. [4]Max Delbrück Center for Molecular Medicine, 13125 Berlin, Germany. [5]Department of Physiology and Program in Bioengineering, University of California, San Francisco, CA 94143, USA.

*These authors contributed equally to this work.
†To whom correspondence should be addressed. E-mail: h.leonhardt@lmu.de (H.L.); sedat@msg.ucsf.edu (J.W.S.)

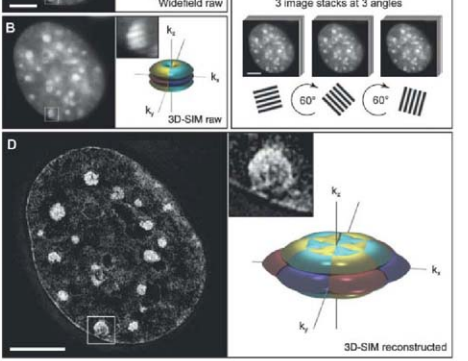

Fig. 1. Subdiffraction resolution imaging with 3D-SIM. (**A** and **B**) Cross section through a DAPI-stained C2C12 cell nucleus acquired with conventional wide-field illumination (**A**) and with structured illumination (**B**), showing the striped interference pattern (inset). The renderings to the right illustrate the respective support of detection in frequency space. The axes k_x, k_y, and k_z indicate spatial frequencies along the x, y, and z directions. The surfaces of the renderings represent the corresponding resolution limit. The depression of the frequency support ("missing cone") in z direction in (**A**) indicates the restriction in axial resolution of conventional wide-field microscopy. With 3D-SIM, the axial support is extended but remains within the resolution limit. (**C**) Five phases of the sine wave pattern are recorded at each z position, allowing the shifted components to be separated and returned to their proper location in frequency space. Three image stacks are recorded with the diffraction grating sequentially rotated into three positions 60° apart, resulting in nearly rotationally symmetric support over a larger region of frequency space. (**D**) The same cross section of the reconstructed 3D-SIM image shows enhanced image details compared with the original image (insets). The increase in resolution is shown in frequency space on the right, with the coverage extending two times farther from the origin. Scale bars indicate 5 μm.

ease of use so that slides prepared for conventional microscopes can be imaged without any further treatment, and operation of the microscope is similar to any modern commercial system. Although several subdiffraction-resolution optical microscopy methods have been developed in the past decade (*6*–*8*) and have been used to address specific biological questions (*9*, *10*), they still present limitations, such as the restriction of the resolution enhancement to either the lateral or the axial direction or to the near or evanescent field, limited multicolor and 3D sectioning abilities, and the requirement of unusual dyes. 3D-SIM is currently the only subdiffraction-resolution imaging technique that allows detection of three (and potentially more) wavelengths in the same sample, using standard fluorescent dyes, with 3D optical sectioning and enhancement of resolution in both lateral (x and y) and axial (z) directions.

We used 3D-SIM to probe higher-order chromatin structure and the relative localization of nuclear pores, the nuclear lamina, and chromatin at the nuclear periphery in mammalian tissue culture cells (*11*). The vertebrate nuclear pore complex (NPC) is a ~120 MD protein complex (*12*) that mediates communication and selective exchange between the nucleoplasm and cytoplasm. The relation between chromatin, the NPC, and other components of the nuclear envelope, such as the nuclear lamina, has been extensively studied (*13*, *14*). Electron microscopy (EM) has been instrumental in determining the fine structure of the NPC (*12*, *15*–*17*), but it cannot provide a global 3D view of the entire nucleus with specific labeling of the molecular components. 3D-SIM can bridge this technology gap and shed light on the nuclear periphery.

We first tested the ability of 3D-SIM to resolve the fine structure of interphase chromatin in three-dimensionally preserved formaldehyde-fixed mouse C2C12 myoblast cells stained with 4′,6-diamidino-2-phenylindole (DAPI). For comparison we recorded a reference image stack with conventional wide-field epifluorescence microscopy and applied constrained iterative deconvolution (*18*) to reduce out-of-focus blur (Fig. 2). In the 3D-SIM image, chromatin shows a more evidently fibrous substructure, and a brighter rim of heterochromatin staining is visible near the nuclear envelope as observed by EM. These chromatin-dense regions are surrounded by chromatin-poor regions, consistent with the interchromatin compartment observed by combined fluorescence and electron microscopic studies (*19*).

Unexpectedly, in 3D-SIM images of the nuclear periphery, we observed thousands of well-defined holes in DAPI staining, which could not be observed in the corresponding wide-field epifluorescence images (Fig. 2B). The size, number, and position of these holes suggested that they represented the exclusion of DNA from NPCs. To test this hypothesis and the potential of 3D-SIM for simultaneous multicolor 3D imaging of various nuclear structures, we co-immunostained these cells with NPC-specific antibodies and antibodies against lamin B. For comparison we recorded 3D image stacks of cells from the same sample with state-of-the-art confocal laser scanning microscopy (CLSM) and applied deconvolution (Fig. 3, A and B). The intermediate filament protein lamin B is a major component of the nuclear lamina that lines and stabilizes the nuclear envelope (*20*). The NPC antibodies used here (referred to as αNPC) are directed against the FG-repeat domain common to several nuclear pore proteins and mainly detect Nup62, Nup214, and Nup358, which are located in the center and at the cytoplasmic side of the NPC (*21*) with a minor signal from Nup153. In lateral cross sections of 3D-SIM image stacks, we consistently observed the peripheral heterochromatin rim outlined by a fine heterogeneous layer of the nuclear lamina and nuclear pore signals further above the lamina. This clear triple-layered organization was not resolvable with CLSM (Fig. 3A). For comparison, we also used a monoclonal antibody specific for Nup153, which is located on the nucleoplasmic side of the NPC (*21*) and obtained a pore signal in the same plane as the lamin B signal, demonstrating the potential of 3D-SIM to resolve subtle differences of epitope locations within the NPC (Fig. 3C). In apical cross sections, we found that NPC foci strictly localize within DAPI voids (Fig. 3B and movie S1). With very few exceptions, every DAPI void contained a focus of NPC staining and vice versa, suggesting that most if not all NPCs exclude chromatin from their immediate vicinity.

We calculated the density of NPC foci in 3D-SIM and confocal images (Fig. 3 and fig. S3) by using automatic detection with identical criteria.

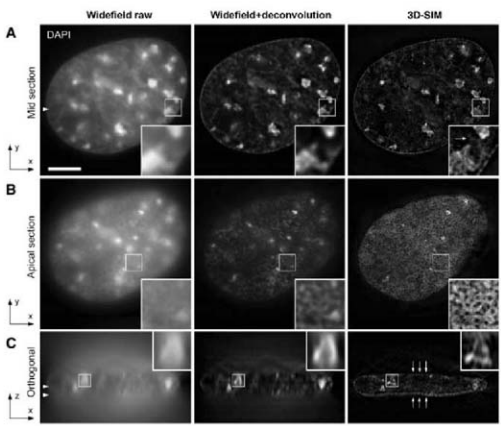

Fig. 2. Comparison of wide-field imaging and 3D-SIM in resolving interphase chromatin fine structure. 3D image stacks of the same DAPI-stained C2C12 cell nucleus were recorded with conventional wide-field illumination (left) and with 3D-SIM (right). Deconvolution was applied to the wide-field data set (middle). Scale bar, 5 μm. Arrowheads indicate the position of the respective cutting planes. **(A)** Mid cross section shows brightly stained chromocenters of clustered (peri-)centromeric heterochromatin. (Insets) Higher-detail information of chromatin substructures when recorded with 3D-SIM. Arrow points to a less-bright chromatin structure that has been spuriously eroded by the deconvolution procedure. **(B)** Projection of four apical sections (corresponding to a thickness of 0.5 μm) taken from the surface of the nuclear envelope closest to the coverslip. Whereas the raw image shows diffuse DAPI staining, the deconvolved image shows more pronounced variations in fluorescence intensities. Image data with 3D-SIM extended-resolution information reveal a punctuated pattern of regions devoid of DAPI staining. **(C)** Orthogonal cross-section through the entire 3D image stack demonstrates the low sectioning capability of conventional wide-field microscopy, which cannot be mitigated solely by deconvolution. In contrast, clear layers of peripheral heterochromatin can be resolved with 3D-SIM (arrows).

The 3D-SIM image showed an average (±SD) of 5.6 ± 3.3 foci per μm^2, whereas only 2.8 ± 1.1 foci per μm^2 were detected in the confocal image. By comparison, 12 ± 1.8 NPCs per μm^2 have been observed in mouse liver nuclei by freeze-fracture EM (*22*). Although the numbers cannot be directly compared because of cell type and cell cycle–dependent variations (*23*), they still indicate that 3D-SIM detects and resolves most NPCs and outperforms CLSM.

Although the discrete chromatin voids at NPCs are not visible in confocal or standard wide-field images, the intensity of DAPI staining should still show fluctuations that anticorrelate with NPC foci. We also reasoned that, even though the lamina does not show a striking one-to-one exclusion from NPCs under any of our methods, it should still be anticorrelated with the NPCs. To pursue these questions, we examined the average environment of an NPC focus in our images (fig. S4). Sub-images were cropped from the data set centered on the peak intensities of NPC foci, which were automatically detected in 3D. Intensity profiles through the center of each sub-image show a drop in intensity in DAPI staining, centered on the NPC focus, in all confocal and 3D-SIM images. A similar drop in intensity of the lamin signal is seen only in the case of 3D-SIM. In composites of the sub-images, a central hole can be seen in the DAPI channel. This indicates that the expected intensity fluctuations are present in all cases. The composite lamina image recorded by 3D-SIM also shows a hole, which was not detected by confocal microscopy. The width of the NPC signal was determined from intensity profiles by measuring the full width at half maximum. With CLSM this width was ~200 nm (192 ± 17 and 192 ± 11 nm before and after deconvolution, respectively), which essentially reflects the point spread function (PSF) of CLSM. In contrast, the measured width of NPC signal recorded with 3D-SIM was 120 ± 3 nm, which is in good agreement with EM measurements (*15*).

Many of the nuclei we imaged contained invaginations of the nuclear envelope that are especially prominent near the centrosome during prophase. These invaginations have been shown by EM studies to be tubular extensions of both nuclear envelopes (*24*), but because their width is generally smaller than the diffraction limit they appear as a single line by conventional microscopy. We investigated these nuclear invaginations in prophase nuclei by CLSM and 3D-SIM (Fig. 4) and could resolve the bilaminar structure of these invagination only with 3D-SIM (movie S2). This detailed substructure of nuclear

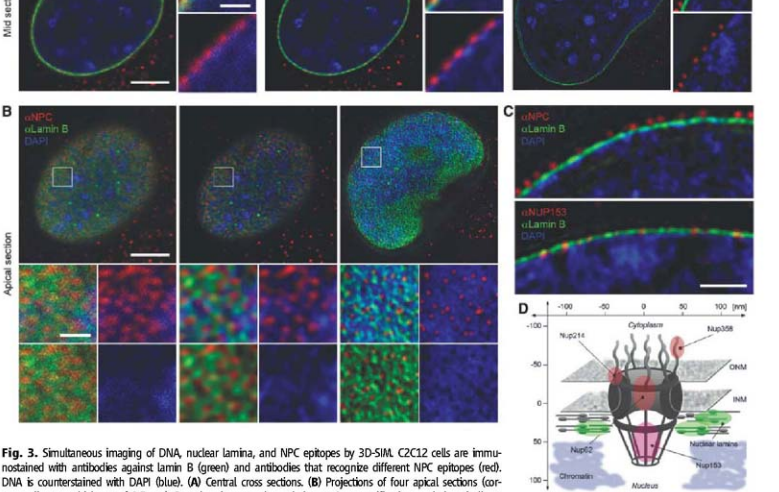

Fig. 3. Simultaneous imaging of DNA, nuclear lamina, and NPC epitopes by 3D-SIM. C2C12 cells are immunostained with antibodies against lamin B (green) and antibodies that recognize different NPC epitopes (red). DNA is counterstained with DAPI (blue). **(A)** Central cross sections. **(B)** Projections of four apical sections (corresponding to a thickness of 0.5 μm). Boxed regions are shown below at 4× magnification; scale bars indicate 5 μm and 1 μm, respectively. (A) CLSM and deconvolution still show partially overlapping signals. In contrast, with 3D-SIM the spatial separation of NPC, lamina, and chromatin and chromatin-free channels underneath nuclear pores are clearly visible. (B) Top view on the nuclear envelope. Whereas CLSM fails to resolve close nuclear pores, 3D-SIM shows clearly separated NPC signals at voids of peripheral chromatin and surrounded by an irregular network of nuclear lamina. **(C)** Mid sections comparing stainings with an antibody that mainly reacts with Nup214, Nup358, and Nup62 (αNPC) and one specifically recognizing Nup153 (αNup153). The αNPC signal is above the lamina (140 ± 8 nm), whereas the αNup153 pore signal is at the same level as the lamina (−15 ± 20 nm). Scale bars 1 μm. **(D)** Schematic outline of the NPC, showing the relative position of Nup proteins and surrounding structures. ONM, outer nuclear membrane; INM, inner nuclear membrane.

invaginations has so far only been detected by transmission electron microscopy (TEM) (fig. S5). We also quantified the width of the lamin B signal in interphase nuclei in lateral and axial directions by fitting Gaussian curves to the measured intensities. Because the thickness of the lamina is in the range of 20 to 50 nm, the obtained values should reflect the resolution limit of either of the applied methods. With 3D-SIM we determined a width of threads in the lamin network with an upper limit of 98 ± 12 nm laterally and 299 ± 22 nm axially, whereas confocal images showed more than twofold higher values (243 ± 30 nm laterally and 736 ± 225 nm axially). Subsequent deconvolution of CLSM data/images did not improve the lateral (231 ± 28 nm) but did improve the axial (418 ± 26 nm) resolution, which is mostly due to an increased signal-to-noise ratio by removing out-of-focus blur and suppression of background (*2*). This 3D imaging of complex biological structures demonstrates about twofold enhanced resolution of 3D-SIM over conventional fluorescence imaging techniques in lateral and axial directions.

Many cellular structures and macromolecular complexes, including the nuclear envelope and its pores, fall just below the diffraction limit of conventional light microscopy, preventing quantitative analysis. In doubling the resolution of conventional microscopy in three dimensions, 3D-SIM was able to resolve individual nuclear pores, detect and measure the exclusion of chromatin and the nuclear lamina from nuclear pores, and accurately image invaginations of the nuclear envelope caused by the formation of the mitotic spindle. We have demonstrated both an increase in quantitative precision of measurement and the detection of novel cytological features, by imaging to a resolution approaching 100 nm. Although this level of resolution is less than that afforded by other techniques such as stimulated emission depletion (STED), photoactivated localization (PALM), or stochastic optical reconstruction (STORM) microscopy (*25*–*29*), 3D-SIM is currently the only subdiffraction-resolution imaging technique that can produce multicolor 3D images of whole cells with enhancement of resolution in both lateral and axial directions. Notably, these results were obtained with standard cytological methods, without the need for unconventional fluorescent dyes or coverslips, and on a microscope platform designed to be no more difficult to use than a conventional commercial microscope. The possibility of using 3D-SIM with well-established standard labeling techniques and to simultaneously locate different molecules or structures in the 3D cellular context opens interesting new perspectives for molecular cell biology.

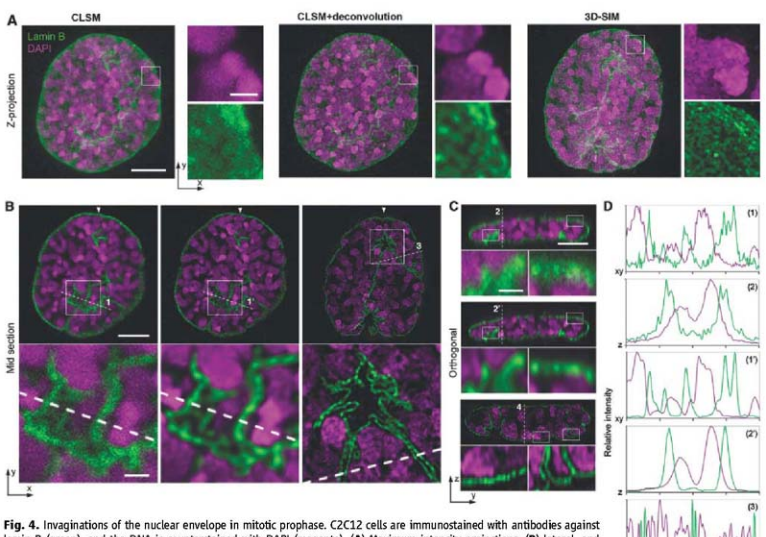

Fig. 4. Invaginations of the nuclear envelope in mitotic prophase. C2C12 cells are immunostained with antibodies against lamin B (green), and the DNA is counterstained with DAPI (magenta). **(A)** Maximum intensity projections, **(B)** lateral, and **(C)** orthogonal cross sections. Scale bars, 5 µm. Inset boxes are shown below at 4× magnification (scale bars, 1 µm). 3D-SIM reveals the globular substructure of condensed chromosomes and the fine-structured fibrillar network of the nuclear lamina (movie S2). **(D)** Lateral and axial line profiles of dashed lines in (B) and (C), respectively. Whereas the lateral peak widths are only slightly decreased in the lateral direction (1 versus 1′), the axial profiles show clearly decreased peak widths after deconvolution, indicating a substantial improvement of axial resolution (2 versus 2′). With 3D-SIM, the peak widths of the lamin B signal are about halved with respect to the deconvolved confocal image in lateral and axial directions, and double peaks are resolved where only single peaks are seen in the confocal profiles. Similarly, DAPI staining shows multiple small peaks, which again reflects the increase of image details in 3D-SIM.

References and Notes

1. M. Born, E. Wolf, Eds., *Principle of Optics* (Cambridge Univ. Press, Cambridge, 1998).
2. J. B. Pawley, Ed., *Handbook of Biological Confocal Microscopy* (Springer, New York, ed. 3, 2006).
3. S. Abbe, *Arch. Mikrosk. Anat.* **9**, 413 (1873).
4. M. G. Gustafsson *et al.*, *Biophys. J.*, in press; published online 7 March 2008 (10.1529/biophysj.107.120345).
5. M. G. Gustafsson, *J. Microsc.* **198**, 82 (2000).
6. R. Heintzmann, G. Ficz, *Brief. Funct. Genomics Proteomics* **5**, 289 (2006).
7. S. W. Hell, *Nat. Biotechnol.* **21**, 1347 (2003).
8. S. W. Hell, *Science* **316**, 1153 (2007).
9. R. J. Kittel *et al.*, *Science* **312**, 1051 (2006); published online 13 April 2006 (10.1126/science.1126308).
10. K. I. Willig, S. O. Rizzoli, V. Westphal, R. Jahn, S. W. Hell, *Nature* **440**, 935 (2006).
11. Material and methods are available on *Science* Online.
12. R. Reichelt *et al.*, *J. Cell Biol.* **110**, 883 (1990).
13. B. Burke, C. L. Stewart, *Nat. Rev. Mol. Cell Biol.* **3**, 575 (2002).
14. M. R. Paddy, A. S. Belmont, H. Saumweber, D. A. Agard, J. W. Sedat, *Cell* **62**, 89 (1990).
15. M. Beck *et al.*, *Science* **306**, 1387 (2004); published online 28 October 2004 (10.1126/science.1104808).
16. M. Beck, V. Lucic, F. Forster, W. Baumeister, O. Medalia, *Nature* **449**, 611 (2007).
17. D. Stoffler *et al.*, *J. Mol. Biol.* **328**, 119 (2003).
18. D. A. Agard, Y. Hiraoka, P. Shaw, J. W. Sedat, *Methods Cell Biol.* **30**, 353 (1989).
19. H. Albiez *et al.*, *Chromosome Res.* **14**, 707 (2006).
20. L. Gerace, A. Blum, G. Blobel, *J. Cell Biol.* **79**, 546 (1978).
21. B. Fahrenkrog *et al.*, *J. Struct. Biol.* **140**, 254 (2002).
22. R. Tonini, F. Grohovaz, C. A. Laporta, M. Mazzanti, *FASEB J.* **13**, 1395 (1999).
23. M. Winey, D. Yarar, T. H. Giddings Jr., D. N. Mastronarde, *Mol. Biol. Cell* **8**, 2119 (1997).
24. M. Fricker, M. Hollinshead, N. White, D. Vaux, *J. Cell Biol.* **136**, 531 (1997).
25. M. Bates, B. Huang, G. T. Dempsey, X. Zhuang, *Science* **317**, 1749 (2007); published online 15 August 2007 (10.1126/science.1146598).
26. E. Betzig *et al.*, *Science* **313**, 1642 (2006); published online 9 August 2006 (10.1126/science.1127344).
27. G. Donnert *et al.*, *Proc. Natl. Acad. Sci. U.S.A.* **103**, 11440 (2006).
28. B. Huang, W. Wang, M. Bates, X. Zhuang, *Science* **319**, 810 (2008); published online 2 January 2008 (10.1126/science.1153529).
29. M. J. Rust, M. Bates, X. Zhuang, *Nat. Methods* **3**, 793 (2006).

30. This work was supported by grants from the Bavaria California Technology Center, the Center for NanoScience, the Nanosystems Initiative Munich, and the Deutsche Forschungsgemeinschaft to L. Schermelleh, M.C.C., and H.L.; by NIH grant GM-2501–25 to J.W.S.; by the David and Lucile Packard Foundation; and by NSF through the Center for Biophotonics, an NSF Science and Technology Center managed by the University of California, Davis, under cooperative agreement no. PHY 0120999. P.M.C. is partially supported by the Keck Laboratory for Advanced Microscopy at the University of California, San Francisco. We thank A. Copič, K. Weis, and F. Spada for comments on the manuscript and helpful discussions. P.M.C., L. Shao, L.W., and P.K. have performed limited paid consulting for Applied Precision, which is planning a commercial microscope system using three-dimensional structured illumination. The University of California holds patents for structured illumination microscopy.

Supporting Online Material

www.sciencemag.org/cgi/content/full/320/5881/1332/DC1
Materials and Methods
Figs. S1 to S6
References and Notes
Movies S1 and S2

25 February 2008; accepted 13 May 2008
10.1126/science.1156947

Intersection of the RNA Interference and X-Inactivation Pathways

Yuya Ogawa, Bryan K. Sun, Jeannie T. Lee*

In mammals, dosage compensation is achieved by X-chromosome inactivation (XCI) in the female. The noncoding *Xist* gene initiates silencing of the X chromosome, whereas its antisense partner *Tsix* blocks silencing. The complementarity of Xist and Tsix RNAs has long suggested a role for RNA interference (RNAi). Here, we report that murine Xist and Tsix form duplexes in vivo. During XCI, the duplexes are processed to small RNAs (sRNAs), most likely on the active X (Xa) in a Dicer-dependent manner. Deleting *Dicer* compromises sRNA production and derepresses *Xist*. Furthermore, without Dicer, Xist RNA cannot accumulate and histone 3 lysine 27 trimethylation is blocked on the inactive X (Xi). The defects are partially rescued by truncating Tsix. Thus, XCI and RNAi intersect, down-regulating *Xist* on Xa and spreading silencing on Xi.

X-chromosome inactivation (XCI) (*1*) balances X-chromosome dosages between XX and XY individuals. XCI is initiated by *Xist* (*2*, *3*) and opposed by *Tsix* (*4*). How *Xist* induces XCI on inactive X (Xi) and how *Tsix* stably silences *Xist* on active X (Xa) remain two unanswered questions. A role for RNA interference (RNAi) has long been speculated. RNAi refers to the repressive influence of double-stranded RNA (dsRNA) on gene transcription and transcript stability (*5*, *6*). Numerous similarities, including the involvement of noncoding RNAs, can be found between XCI and RNAi silencing of constitutive heterochromatin. However, a deficiency of Dicer (Dcr) has no obvious effect on maintaining Xi in T cells (*7*) and, although Xist and Tsix RNAs are perfectly complementary, dsRNAs had never been observed in vivo.

Here, we formally explore a role for RNAi in XCI. To search for small RNAs (sRNAs) within *Xist/Tsix*, we performed Northern analysis in mouse embryonic stem (ES) cells, a model that recapitulates XCI during cell differentiation ex vivo; and in mouse embryonic fibroblasts (MEFs), post-XCI cells that faithfully maintain one Xi. At repeat A, a region of *Xist* required for silencing (*8*), we observed sRNAs at ~30 nucleotides (nt) and ~37 nt in the Tsix orientation and at ~25 and ~35 nt in the Xist orientation (Fig. 1A). At *Xist* exon 7, sRNAs occurred between 24 and 42 nt on the Tsix strand and at ~25 and ~35 nt on the Xist strand (Fig. 1B). At the promoter, robust quantities of Tsix-strand sRNAs were observed (Fig. 1C). sRNAs were also seen on the Xist strand, implying that low-level sense transcription must occur at the promoter. The integrity of all Northern blots was confirmed by micro RNA 292-as (miRNA292-as) and tRNA controls (Fig. 1 and fig. S1). The sRNAs were developmentally regulated, being unmeasurable in the pre-XCI [day 0 (d0)] and post-XCI (MEF) states and detectable only during XCI (d4 and d10). Furthermore, sRNAs occurred in both XX and XY cells. For discussion purposes, we call them xiRNA for their X-inactivation center origin, distinct from the smaller small interfering RNA (siRNAs) and miRNAs.

To determine whether xiRNA production depends on antisense expression, we investigated ES cells in which *Tsix* was deleted ($Tsix^{\Delta CpG}$) (*4*) and the *Tsix* regulator *Xite* ($Xite^{\Delta L}$) (*9*). Deleting *Tsix* resulted in a dramatic reduction in antisense-strand xiRNA (Fig. 1D). A residual level of xiRNA was still detectable, consistent with cryptic promoter activity in $Tsix^{\Delta CpG}$ (*4*). Deleting *Xite* likewise reduced antisense xiRNA levels, consistent with a requirement for *Xite* in trans-activating *Tsix* (*9*). In the sense orientation, both deletions also compromised xiRNA production. Thus, sRNAs are indeed generated from *Xist/Tsix* and depend on *Tsix* and *Xite* expression.

The presence of xiRNAs implied that Tsix and Xist must exist as long duplex precursors. However, the developmental timing of xiRNA appearance is paradoxical: Although Tsix and Xist are biallelically expressed on d0, they become monoallelically expressed on opposite Xs during XCI (*4*). On d0, three to five copies per chromosome of Xist RNA are present, whereas Tsix occurs at >10-fold molar excess (*10*–*12*). Upon XCI, Tsix is down-regulated on Xi as Xist up-regulates >30-fold. On Xa, Tsix persists as Xist is down-regulated. How would dsRNA form when Tsix and Xist, both cis-limited, are on opposite chromosomes during XCI?

Department of Molecular Biology, Massachusetts General Hospital; Department of Genetics, Harvard Medical School; and Howard Hughes Medical Institute, Boston, MA 02114, USA.

*To whom correspondence should be addressed. E-mail: tee@molbio.mgh.harvard.edu

To determine whether Tsix and Xist formed dsRNA, we devised an in vivo ribonuclease (RNase) protection assay based on differential susceptibility of single-stranded RNA (ssRNA) and dsRNAs to RNase A/T1. We permeabilized replicate preparations of d0 ES cells in a non-denaturing buffer containing deoxyribonuclease I (DNase I) and RNase, and performed strand-specific reverse transcription polymerase chain reaction (RT-PCR) on the protected RNAs. To confirm assay sensitivity, a positive control into which one copy per cell of in vitro–transcribed

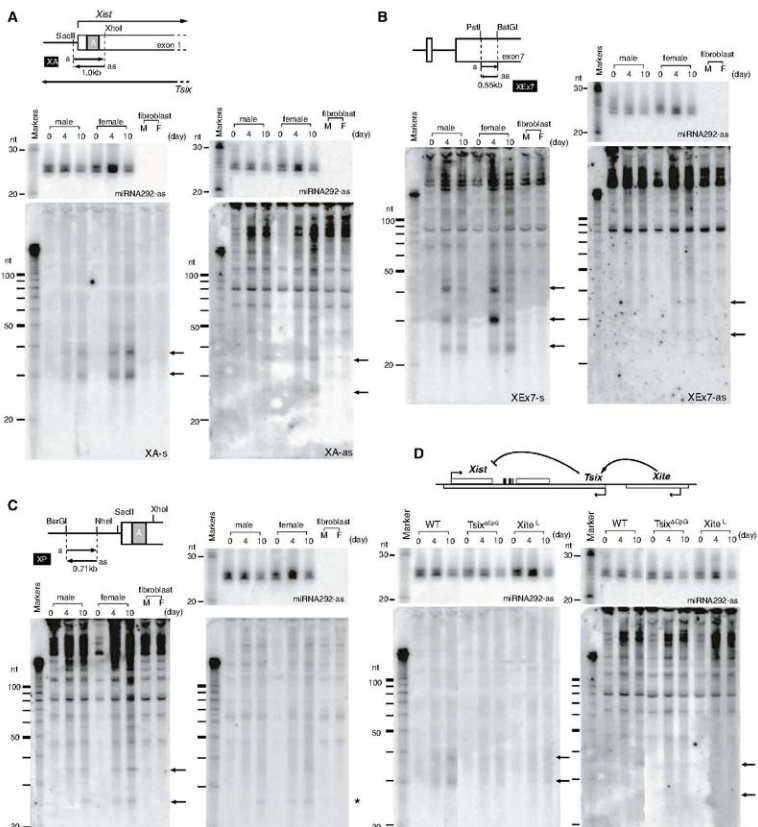

Fig. 1. sRNAs derived from *Tsix/Xist*. **(A)** xiRNAs from *Xist* repeat A (XA) region (map) detected by Northern analysis. Sense (s) and antisense (as) riboprobes detected Tsix and Xist, respectively. miR292-as controls are shown on the same blots. M, male; F, female. **(B)** Northern analysis of xiRNAs from *Xist* exon 7 (XEx7). **(C)** Northern analysis of *Xist* promoter (XP) region. **(D)** Northern analysis of mutant cells. WT lanes are identical to those in (A) (concurrent analysis).

and annealed Tsix:Xist dsRNA was spiked could readily be detected with this protocol (Fig. 2, A and B). The abundant single-stranded ribonuclease M2 (Rrm2) and glyceraldehyde-3-phosphate dehydrogenase (Gapdh) transcripts were not amplified, indicating that our assay was specific for dsRNA. We consistently observed RNase-protected Xist and Tsix RNA strands in XX and XY ES cells, suggesting the presence of dsRNA (Fig. 2B). Real-time RT-PCR quantitation showed that ~16% of Xist and ~13% of Tsix strands were protected (Fig. 2C). As expected of duplexes, approximately equal stoichiometric ratios of the two strands were present in the RNase-protected fraction. Kinetic analysis revealed decreasing amounts of dsRNA during differentiation in XX and XY cells (Fig. 2D). Thus, steady-state quantities of both dsRNA and xiRNA are developmentally regulated, but in an opposite manner.

The inverse correlation over time raised the possibility that dsRNA is processed to xiRNA. To address potential allelic differences, we performed allele-specific RNase protection assays using two genetically marked female ES cell lines: wild-type (WT) 16.7, which carries Xs from *Mus castaneus* (X^{cas}) and *M. musculus* (X^{mus}) and undergoes random XCI [with a natural 30:70 specific-specific bias (*13*)], and *Tsix*$^{\Delta CpG/+}$ mutants, which harbor a *Tsix* deletion on X^{mus} (*4*) and therefore always inactivate X^{mus} in the 16.7 background. Total Tsix RNA (with no RNase treatment) decreased >10-fold over time, but a low residual level could still be detected at d4 and d10 as expected (*4, 9, 14*). From this residual pool, using single-nucleotide polymorphism (SNP)–based allele-specific primers at position 3, we unexpectedly found that duplexed Tsix (RNase-protected) in *Tsix*$^{\Delta CpG/+}$ cells predominantly originated from Xi (X^{mus}) (Fig. 2E), the X on which the major *Tsix* promoter is deleted. Likewise, the Xist strand found in duplex form originated from Xi. Thus, Tsix:Xist duplexes are detected primarily from Xi.

Duplexes may form only on Xi, or they may form on both Xs but be stable only on Xi. The latter possibility is notable, considering the inverse kinetic relationship between the appearance of long dsRNA versus xiRNA. Could dsRNA be processed to xiRNA on Xa? Several observations favored this idea. First, dsRNA was selectively lost from Xa. Second, xiRNA production depended on *Tsix*, a gene expressed from Xa from d4 to d10. Finally, despite lacking Xi, XY cells produced xiRNAs.

Because dsRNAs are substrates for Dcr, we tested Dcr's role by deleting *Dcr*'s RNAseIII domain in female ES cells (*15*) (fig. S2). Because Dcr-deficient ($Dcr^{-/-}$) cells are known to grow poorly (*15*), we introduced a *Dcr* transgene expressed at <<5% of WT levels (Fig. 3, A and B) and improved the growth of $Dcr^{-/-}$ clones (henceforth referred to as $Dcr^{-/-}$). Northern analysis revealed diminished xiRNA levels (Fig. 3, C and D), suggesting that xiRNA production depends on Dcr. All tested *Dcr*-deficient clones behaved similarly. *Xist* expression prematurely increased 5- to 10-fold in pre-XCI cells (Fig. 3B), implying increased *Xist* transcription or greater RNA stability. Male $Dcr^{-/-}$ clones likewise showed significant Xist derepression on d4 (fig. S3). Thus, Dcr regulates xiRNA levels and antagonizes *Xist* upregulation in ES cells.

RNA immunofluorescence in situ hybridization (immunoFISH) analysis showed that Dcr has

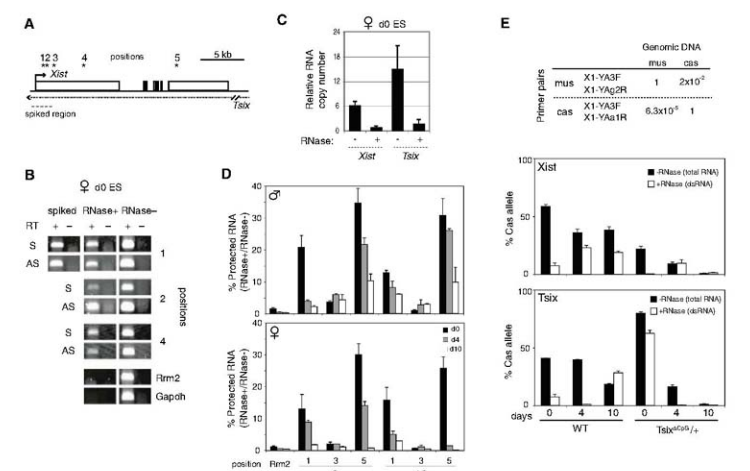

Fig. 2. Tsix and Xist RNA form long duplexes in vivo. **(A)** Map of *Tsix*/*Xist* and primer pairs (asterisks). **(B)** In vivo RNAse protection assay. **(C)** Relative quantities of Xist and Tsix in duplexes measured at position 2 (base pairs 1206 to 1337 of *Xist*) by strand-specific real-time RT-PCR of protected RNA ($RNase^+$) as compared with total levels ($RNase^-$). Quantities are standardized to Xist in the Xist-Tsix duplex (for Xist, $RNase^+ = 1$). Error bars indicate 1 SD in triplicate reactions. **(D)** Quantities of protected Tsix or Xist RNAs ($RNase^+$) relative to total Tsix or Xist ($RNase^-$) for in vivo RNase protection assays. Error bars indicate 1 SD in triplicate reactions. **(E)** In vivo RNase protection assays to test allelic origin of dsRNA using strand-specific, allele-specific real-time RT-PCR with SNP-based primers for X^{cas} or X^{mus} alleles (top). PCR of control genomic DNA shows high specificity (98% for mus and >99.99% for cas). Error bars indicate 1 SD in triplicate reactions. For test samples, the mus and cas fractions were amplified separately, normalized to genomic DNA (X^{cas}:X^{mus} = 1:1), and plotted as a function of time. Percent of Cas = [X^{cas} RNA/(X^{cas} RNA + X^{mus} RNA)] × 100. Because the bars show relative allelic fractions, quantities are only comparable within a single time point.

additional XCI effects. Despite elevated Xist levels, Xist could not "coat" the X nor induce heterochromatic changes (Fig. 3E). On d10, Xist RNA accumulation occurred in only 0.4% of cells (n = 278 cells) and histone 3 (H3) lysine 27 (K27) trimethylation (H3-3meK27) in 0.7% of cells (n = 278 cells). By contrast, in *Dcr* 2lox/[heterozygous Dcr knockout carrying one conditional allele (2loxP sites) and one deleted allele] controls, Xist accumulated in 56.8% and H3-3meK27 in 83.1% of cells (n = 148 cells). Moreover, the X-linked *Mecp2* gene failed to be dosage-compensated in $Dcr^{-/-}$ cells, whereas it appropriately decreased 1.5- to twofold in controls (Fig. 3A). Therefore, in addition to local effects on *Xist*, Dcr also affected Xi globally, because the formation of Xist and H3-3meK27 domains was compromised without Dcr.

Because XCI and cell differentiation are linked (*16*, *17*), the XCI defects might be explained by Dcr's pleiotropic effects on differentiation (*15*, *18*) rather than specific effects on XCI. Indeed, $Dcr^{-/-}$ clones differentiated poorly and continued to express Oct4 and Nanog pluripotency factors on d10 (Fig. 3, A and F, fig. S3). To determine whether Dcr specifically affects XCI, we truncated Tsix by inserting a polyadenylate cassette in $Dcr^{-/-}$ cells (fig. S4), reasoning that disabling *Tsix*, which negatively regulates *Xist*, might overcome the failure to accumulate Xist RNA. As expected, $Dcr^{-/-}Tsix^{\Delta}$ double mutants (Dcr-TST) and $Tsix^{\Delta}$ controls (TST) showed truncated Tsix expression from X^{mus} and highly skewed XCI patterns (Fig. 4A). Although Dcr-TST cells continued to differentiate poorly (fig. S5), total Xist levels were restored to nearly WT levels during differentiation (Fig. 4B). Furthermore, disabling Tsix partially restored Xist localization to Xi (Fig. 4C). Therefore, Dcr's effect on XCI can be genetically separated from its effect on cell differentiation.

Additionally, to the extent that Xist levels and localization were restored in Dcr-TST cells, H3-3meK27 was only partly rescued in Xist$^+$ cells (Fig. 4D). In WT and TST controls, Xist accumulation was almost always accompanied by robust H3-3meK27. In contrast, 30 to 40% of Xist$^+$ Dcr-TST cells displayed weak or no H3-3meK27 foci, implying that H3-3meK27 also depends on Dcr. These data showed that Xist accumulation and H3-K27 methylation are genetically separable. We conclude that Dcr intersects XCI in several ways. Locally, Dcr controls xiRNA and Xist expression. Globally, it regulates Xist accumulation and H3-3meK27 on Xi.

In aggregate, our data suggest specific effects of RNAi on XCI (Fig. 4E). *Dcr* and *Tsix*/*Xist* genetically interact, and a second-site mutation in *Tsix* partially suppresses the $Dcr^{-/-}$ effect on *Xist*. We propose that Tsix:Xist duplexes initially form on both Xs. During XCI, continued expression of Tsix on Xa would lead to dsRNA processing to xiRNAs, which would locally repress *Xist* in cis, an idea reminiscent of transcriptional gene silencing (TGS) (*6*, *19*–*21*). Consistent with allele-specific TGS at *Xist*, RNA-directed DNA methyl-

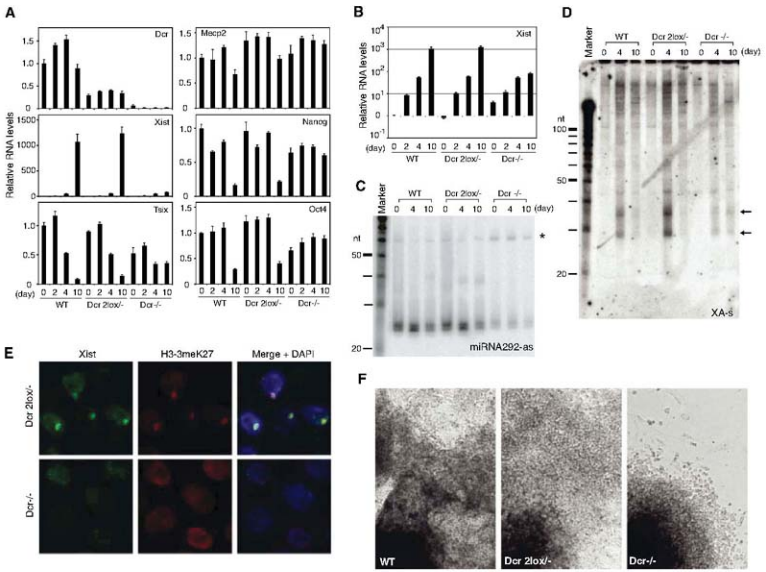

Fig. 3. *Dcr* deficiency impairs xiRNA production and XCI. **(A)** Quantitative real-time RT-PCR of indicated transcripts normalized to β-actin. **(B)** Xist quantitation plotted on a log scale. **(C** and **D)** Northern analyses of miRNA292-as control **(C)** and xiRNAs **(D)** in mutant cells. There is an accumulation of miRNA292-as precursors (asterisk) in $Dcr^{-/-}$ cells. **(E)** Immuno-RNA FISH for Xist and H3-3meK27 on d10. 4′,6′-diamidino-2-phenylindole (DAPI), blue. **(F)** Phase contrast images of d10 embryoid bodies (EB).

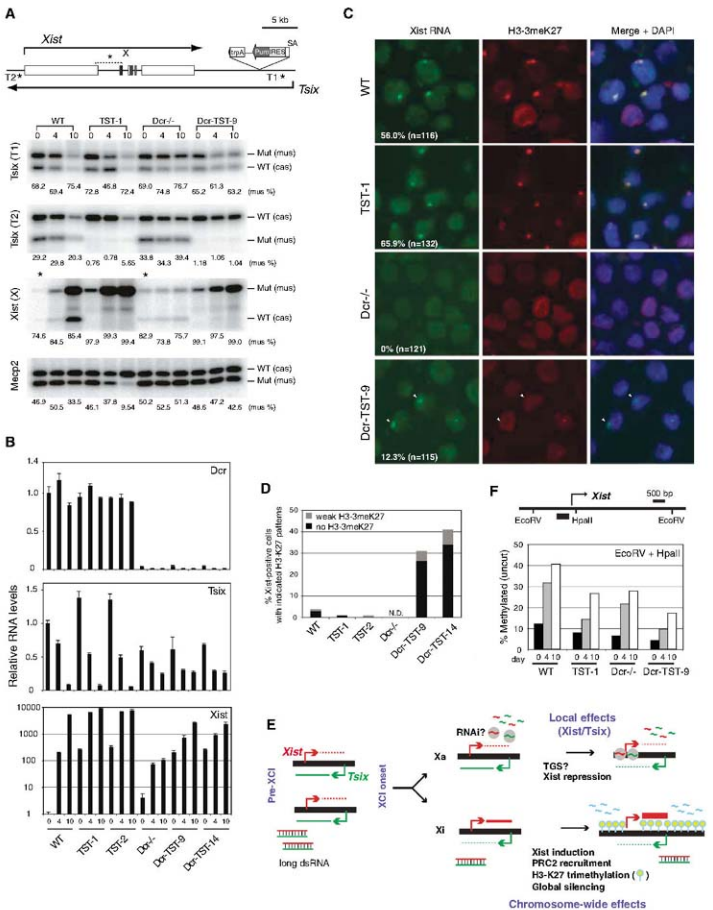

Fig. 4. *Tsix* genetically interacts with *Dcr*. (**A**) Allele-specific RT-PCR analysis. All RT reactions were negative (not shown in figure). Xist d0 samples (asterisks) were 10-fold overloaded to visualize low expression. trpA, triple poly-A cassette; Puro, puromycin; IRES, internal ribosome site; SA, splice acceptor. (**B**) Real-time RT-PCR of indicated transcripts, each normalized to β-actin. (**C**) Immuno-RNA FISH for Xist and H3-3meK27 domains (arrowheads) on d10. *n*, sample size. (**D**) Frequency of aberrant H3-3meK27 enrichment in the Xist$^+$ subpopulation of indicated cell lines. *n* = 100 to 150 cells. (**E**) Model of the intersection of RNAi and XCI. (**F**) Methylation-sensitive restriction analysis of the *Xist* promoter. Genomic DNA was digested with EcoRV or Eco RV+Hpa II. The percent of uncut (methylated) DNA at Hpa II is plotted.

ation by *Tsix* has been proposed (*10*). Here we found that abrogating Dcr and/or Tsix resulted in decreased methylation at the 5′ end of *Xist* (Fig. 4F). By our model, extremely low Tsix and Xist expression might be sufficient to maintain TGS on Xa in post-XCI cells (*19*). On Xi, chromosome-wide accumulation of Xist RNA and H3-3meK27 depends on Dcr. These ideas support the emerging concept of nuclear RNAi processes in mammals (*20*, *21*). Because Dcr is not known to cleave RNAs to 25 to 42 nt, the observed effects on XCI may be partially indirect. Alternatively, Dcr may have properties yet to be discovered in mammals. XCI now provides a new system in which to investigate RNAi processes.

References and Notes

1. M. F. Lyon, *Nature* **190**, 372 (1961).
2. C. J. Brown *et al.*, *Cell* **71**, 527 (1992).
3. G. D. Penny, G. F. Kay, S. A. Sheardown, S. Rastan, N. Brockdorff, *Nature* **379**, 131 (1996).
4. J. T. Lee, N. Lu, *Cell* **99**, 47 (1999).
5. A. Fire *et al.*, *Nature* **391**, 806 (1998).
6. S. I. Grewal, S. C. Elgin, *Nature* **447**, 399 (2007).
7. B. S. Cobb *et al.*, *J. Exp. Med.* **201**, 1367 (2005).
8. A. Wutz, T. P. Rasmussen, R. Jaenisch, *Nat. Genet.* **30**, 167 (2002).
9. Y. Ogawa, J. T. Lee, *Mol. Cell* **11**, 731 (2003).
10. B. K. Sun, A. M. Deaton, J. T. Lee, *Mol. Cell* **21**, 617 (2006).
11. C. H. Buzin, J. R. Mann, J. Singer-Sam, *Development* **120**, 3529 (1994).
12. S. Shibata, J. T. Lee, *Hum. Mol. Genet.* **12**, 125 (2003).
13. P. Avner *et al.*, *Genet. Res.* **72**, 217 (1998).
14. S. Shibata, J. T. Lee, *Curr. Biol.* **14**, 1747 (2004).
15. E. P. Murchison, J. F. Partridge, O. H. Tam, S. Cheloufi, G. J. Hannon, *Proc. Natl. Acad. Sci. U.S.A.* **102**, 12135 (2005).
16. M. Monk, M. I. Harper, *Nature* **281**, 311 (1979).
17. J. T. Lee, *Science* **309**, 768 (2005).
18. C. Kanellopoulou *et al.*, *Genes Dev.* **19**, 489 (2005).
19. T. A. Volpe *et al.*, *Science* **297**, 1833 (2002).
20. D. H. Kim, L. M. Villeneuve, K. V. Morris, J. J. Rossi, *Nat. Struct. Mol. Biol.* **13**, 793 (2006).
21. K. V. Morris, S. W. Chan, S. E. Jacobsen, D. J. Looney, *Science* **305**, 1289 (2004).

22. We thank G. Hannon for the *Dcr* targeting construct and Dcr2lox/− male ES cells; N. Lau for technical advice; and M. Anguera, J. Erwin, S. Namekawa, B. Payer, and J. Zhao for careful critique of the manuscript. Y.O. is especially indebted to A. Ogawa for her support. This work is funded by the Medical Scientist Training Program (B.K.S.), NIH, and the Howard Hughes Medical Institute (J.T.L.).

Supporting Online Material

www.sciencemag.org/cgi/content/full/320/5881/1336/DC1
Materials and Methods
Figs. S1 to S5
References

12 March 2008; accepted 30 April 2008
10.1126/science.1157676

Fission Yeast Pot1-Tpp1 Protects Telomeres and Regulates Telomere Length

Tomoichiro Miyoshi, Junko Kanoh, Motoki Saito, Fuyuki Ishikawa*

Telomeres are specialized chromatin structures that protect chromosomal ends. Protection of telomeres 1 (Pot1) binds to the telomeric G-rich overhang, thereby protecting telomeres and regulating telomerase. Mammalian POT1 and TPP1 interact and constitute part of the six-protein shelterin complex. Here we report that Tpz1, the TPP1 homolog in fission yeast, forms a complex with Pot1. Tpz1 binds to Ccq1 and the previously undiscovered protein Poz1 (Pot1-associated in *Schizosaccharomyces pombe*), which protect telomeres redundantly and regulate telomerase in positive and negative manners, respectively. Thus, the Pot1-Tpz1 complex accomplishes its functions by recruiting effector molecules Ccq1 and Poz1. Moreover, Poz1 bridges Pot1-Tpz1 and Taz1-Rap1, thereby connecting the single-stranded and double-stranded telomeric DNA regions. Such molecular architectures are similar to those of mammalian shelterin, indicating that the overall DNA-protein architecture is conserved across evolution.

Telomeres consist of long arrays of double-stranded (ds) G-rich telomeric repeats terminated by G-rich single-stranded (ss) overhangs at the 3′-terminus (G-tail). The *Oxytricha nova* telomere end–binding protein (TEBP)–α and –β heterodimers are prototypes of G-tail–binding proteins (*1*, *2*). TEBP-α and -β contain oligonucleotide/oligosaccharide-binding (OB) fold domains involved in DNA binding and protein-protein interaction (*3*). Protection of telomeres 1 (Pot1), the homolog of TEBP-α, binds to the G-tail and is essential for telomere protection (*4*, *5*). Mammalian POT1 and the TEBP-β homolog TPP1 form a complex that protects telomeres and regulates telomerase (*6*–*9*). POT1 and TPP1 constitute the shelterin complex together with TIN2, RAP1, and ds telomeric DNA–binding proteins TRF1 and TRF2 (*10*). It has been proposed that mammalian POT1 transduces signals from TRF1 to negatively control telomerase reaction (*11*).

To elucidate how fission yeast Pot1 functions, we purified proteins associated with Pot1. We identified Ccq1 and two uncharacterized proteins, encoded SPAC19G12.13 and SPAC6F6.16, by mass spectrometry of Pot1 immunoprecipitates (fig. S1 and table S1). Ccq1 is a telomere protein that recruits a Snf2/histone deacetylase (HDAC)–containing repressor complex (SHREC) (*12*, *13*). SPAC19G12.13 produces the previously undiscovered Pot1 complex component Poz1 (Pot1-associated in *Schizosaccharomyces pombe*) (GenBank accession number AB433171). We found that the presence of introns in SPAC6F6.16 resulted in encoding a protein larger than that predicted in the database (fig. S2). Secondary structure–based fold-recognition programs predicted that the N terminus of the SPAC6F6.16 product (residues 1 to 158) contains an OB fold domain that is most closely related to those of TEBP-β and human TPP1 (fig. S2 and table S3). Moreover, the product and Pot1 form a complex that protects telomeres and regulates telomerase. We therefore conclude that SPAC6F6.16 encodes the fission yeast Tpp1 homolog. Because the gene name *tpp1*$^{+}$ is already being used by another gene in fission yeast, we will call this gene *tpz1*$^{+}$ (*TPP1 homolog* in Schizosaccharomyces pombe) (GenBank accession number AB433170).

The physical association between Pot1 and Ccq1, Tpz1, or Poz1 was confirmed by immunoprecipitation (Fig. 1A). Immunofluorescence experiments showed that Ccq1, Tpz1, and Poz1 colocalize with Pot1 (fig. S3). A chromatin immunoprecipitation (ChIP) assay also demonstrated that Ccq1, Tpz1, and Poz1 are specifically bound to telomeres (Fig. 1B). Thus, Ccq1, Tpz1, and Poz1 are closely associated with Pot1 at telomeres. Ccq1 directly associates with Clr3, an HDAC in SHREC (*12*) (fig. S4). However, Clr3 was not detected in the Pot1-precipitated fraction and is not involved in controlling telomere length, indicating that the Pot1 complex identified in this study is distinct from SHREC.

We used a yeast two-hybrid assay to examine interactions between Tpz1 and Pot1, Ccq1, or Poz1. Tpz1 associated with Pot1, Ccq1, and Poz1 (Fig. 1C). However, we did not observe any substantial interaction between Poz1 and Pot1 or Ccq1 (fig. S5). Deletion analyses revealed that the N terminus of Tpz1 (amino acids 2 to 223) is sufficient for the interaction with Pot1 but not with Ccq1 or Poz1 [Pot1-binding domain (PBD)]. The N-terminal OB fold (OB1) of Pot1 (amino acids 1 to 138) is dispensable for the interaction. In contrast, the C terminus of Tpz1 (amino acids 379- to 508) interacts with Ccq1 and Poz1 but not with Pot1[Ccq1/Poz1-binding domain (CPBD)]. Taken together, Tpz1 is the core molecule interacting with Pot1, Ccq1, and Poz1. The relative positions of the regions responsible for Pot1-Tpz1 interaction in Pot1 and Tpz1 are similar to those in TEBP-α/β and human TPP1 and POT1

Department of Gene Mechanisms, Graduate School of Biostudies, Kyoto University, Yoshida-Konoe-cho, Sakyo-ku, Kyoto 606-8501, Japan.

*To whom correspondence should be addressed. E-mail: fishikaw@lif.kyoto-u.ac.jp

(fig. S12). In fission yeast, telomere-defective cells can survive by self-circularizing the three chromosomes. Pot1-Flag was coimmunoprecipitated with Ccq1-Myc in telomerase-defective cells [*telomerase reverse transcriptase-1Δ* (*trt1Δ*); *trt1*$^{+}$ encodes the catalytic subunit of telomerase] that maintain circular chromosomes lacking telomeric repeat sequences (*14*, *15*), suggesting that the Pot1 complex is formed independently of the presence of either ds or ss telomeric DNAs or physical chromosomal ends (Fig. 1D). When *tpz1*$^{+}$ was deleted, the Pot1-Ccq1 association was abolished in circular chromosome–containing cells, indicating that Tpz1 plays a crucial role in complex assembly.

tpz1Δ cells did not grow or formed very small colonies (fig. S2). In the surviving haploid *tpz1Δ* cells, telomeric signals were completely lost (Fig. 2A), chromosome I–derived telomere-containing Not I fragments (I and L) disappeared in pulsed-field gel electrophoresis (PFGE), and a band corresponding to I+L–fused fragments was detected (Fig. 2B and fig. S6D). Such findings are diagnostic of self-circularized chromosomes, a hallmark of telomere deprotection (*15*), and are observed in *pot1Δ* cells (*4*), indicating that *tpz1*$^{+}$ is also essential for telomere protection. To test whether Tpz1 protects telomeres independently of Pot1, a glutathione *S*-transferase (GST)–fused N-terminal fragment of Tpz1 (amino acids 2 to 223) containing PBD was overproduced. GST-Tpz1 (amino acids 2 to 223) interacted with Pot1, and the interaction between endogenous Tpz1 and Pot1 was substantially reduced (fig. S6). In this condition, telomeric DNA was completely lost and self-circularized chromosomes appeared, indicating that the physical interaction between Pot1 and Tpz1 is required for end protection, as was reported for mammalian POT1 and TPP1 (*9*, *16*). In contrast to *tpz1Δ*, *poz1Δ* and *ccq1Δ* single mutants grew normally. Poz1 and Ccq1 are recruited to telomeres independently of each other (fig. S7). However, when *ccq1*$^{+}$ and *poz1*$^{+}$ were simultaneously deleted, cells rapidly lost telomeres and survived by forming self-circularized chromosomes (Fig. 2, A and B). Therefore, the Pot1-Tpz1 complex is essential to protect telomeres from fusions, and Ccq1 and Poz1 contribute redundantly to this pathway.

poz1Δ and *ccq1Δ* cells possessed elongated (up to 2 kilo–base pair long) and shortened (by ~200 base pairs) telomeres, respectively (Fig. 2A) (*13*). Therefore, Poz1 and Ccq1 regulate telomere length negatively and positively, respectively. Tpz1 immunoprecipitates exhibited telomerase activity that gave rise to products similar to those of Trt1 immunoprecipitates (Fig. 2C). The Tpz1-associated telomerase activity was abrogated in *ccq1Δ* but not in *poz1Δ* cells. Moreover, *ccq1Δtrt1Δ* cells showed similar telomere length to *trt1Δ* cells (fig. S8). The *ccq1*$^{+}$ deletion did not affect the activity of Trt1 immunoprecipitates (Fig. 2C). These results suggest that Ccq1 promotes telomere elongation by facilitating telomerase recruitment or stabilizing the Tpz1-telomerase complex but is not required for the catalytic activity of telomerase per se.

Telomeric DNA is maintained primarily by telomerase. Telomere elongation in *poz1Δ* cells was abolished by the deletion of *trt1*$^{+}$ (Fig. 3A). These results indicate that telomeres in *poz1Δ* cells are elongated by telomerase and suggest that Poz1 negatively regulates telomerase. Taz1, the homolog of vertebrate ds telomeric DNA-binding proteins TRF1 and TRF2, associates with Rap1. Telomeres are elongated in *taz1Δ* or *rap1Δ* cells (*17*–*19*), and the elongation in *taz1Δ* cells depends on telomerase (*14*). *taz1Δ* or *rap1Δ* is epistatic to *poz1Δ* in telomere-length control (Fig. 3B). The yeast two-hybrid assay showed that Poz1 specifically interacts with Rap1 but not Taz1 (Fig. 3C). Coimmunoprecipitation experiments demonstrated that Poz1 interacts with Rap1 in a Taz1-independent manner in vivo (Fig. 3D). These results suggest that Poz1 acts as a transducer downstream of the Taz1-Rap1 pathway so as to negatively control telomerase.

To examine how the Pot1 complex is recruited to telomeres, telomeric repeats were inserted into self-circularized chromosomes lacking original telomere repeats in the *trt1Δ* background (Fig. 3E). ChIP assays demonstrated that Poz1 and Pot1 associate with the internal telomeric repeats in a Taz1- and Rap1-dependent manner,

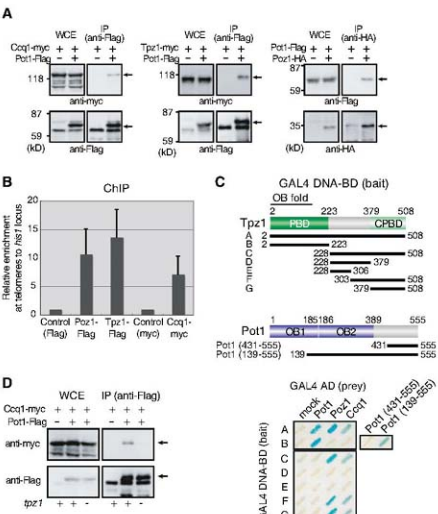

Fig. 1. *S. pombe* Pot1, Ccq1, Tpz1, and Poz1 form a complex at telomeres. **(A)** Pot1 interacts with Ccq1, Tpz1, and Poz1. Immunoprecipitates (IP) were obtained from whole-cell extracts (WCEs) with the use of indicated antibodies and analyzed by immunoblotting. Arrows indicate positions of tagged proteins. HA, hemagglutinin. **(B)** Tpz1, Poz1, and Ccq1 are bound to telomeres. The ChIP assay was performed with subtelomeric and *histidine 1*$^{+}$ (*his1*$^{+}$) gene primer sets. Relative enrichment at telomeres as compared with the *his1*$^{+}$ locus in the precipitated fractions was determined by the quantitative polymerase chain reaction system. Error bars represent SD (n = 3 individual experiments). **(C)** Physical association between Tpz1 and Ccq1, Pot1, or Poz1. Protein interaction was detected by the yeast two-hybrid assay. The GAL4 DNA-binding domain (GAL4 DNA-BD) and GAL4 activation domain (GAL4 AD) were fused to indicated peptides. OB1 and OB2 refer to the OB fold domains that were experimentally established and predicted, respectively (*5*, *20*). **(D)** Tpz1 is required for Pot1 complex formation. WCEs were prepared from strains expressing the indicated tagged proteins in the presence or absence of *tpz1*$^{+}$ in *trt1Δ* cells harboring self-circularized chromosomes.

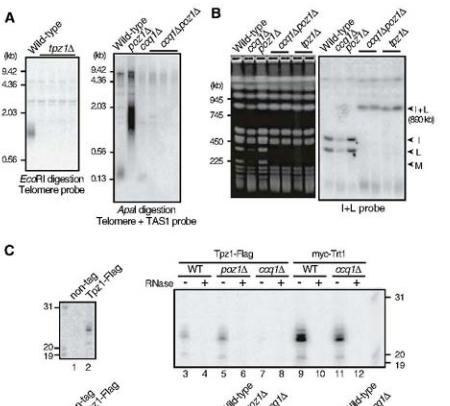

Fig. 2. The Pot1 complex protects telomeres and associates with telomerase activity. **(A)** Telomere length in *tpz1Δ*, *ccq1Δ*, *poz1Δ*, and *ccq1Δpoz1Δ*. Digested genomic DNAs from indicated strains were subjected to Southern hybridization with indicated probes (*21*). **(B)** Chromosome circularization in *tpz1Δ* and *ccq1Δpoz1Δ*. Not I–digested DNAs were separated by PFGE. The ethidium bromide–stained gel (left) and Southern hybridization with probes specific for I and L fragments (right) are shown. **(C)** Tpz1 coimmunoprecipitates telomerase activity in a Ccq1-dependent manner. Telomerase activity was measured in the precipitates prepared from strains expressing indicated proteins in the presence or absence of ribonuclease as described in (*22*) (top). ^{32}P-labeled 19-, 20-, and 31-nucleotide oligomers served as size markers. Amounts of precipitated proteins were determined by immunoblotting (bottom).

indicating that the Pot1 complex can be recruited by ds telomeric DNA in the absence of ss telomeric DNA or physical DNA ends. These results also suggest that Taz1-Rap1 is responsible for bridging ds telomeric DNA and the Pot1 complex. Conversely, we observed that Poz1 and Pot1 are bound to native telomeric ends in *taz1Δ* or *rap1Δ* cells (fig. S9), indicating that the Pot1 complex is recruited to telomeres in a Taz1-Rap1–independent manner. We did not observe complete loss of telomeric DNA in *ccq1Δtaz1Δ* or *ccq1Δrap1Δ* cells, in contrast to *ccq1Δpoz1Δ* cells (fig. S10), suggesting that Poz1 is recruited to and protects telomeres independently of Taz1 or Rap1. Taken together, we suggest that Pot1 is recruited to telomeres by two distinct modes: in ds telomeric DNA–dependent and G-tail–dependent manners.

We found that *ccq1Δpoz1Δ* cells lost telomeres much more rapidly than *trt1Δpoz1Δ* cells did (Figs. 2A and 3A), raising the possibility that Ccq1 maintains telomeres in a telomerase-independent manner in addition to its role in regulating elongation by telomerase. Telomeres are recognized as double-strand breaks in *ccq1Δ* cells to activate the DNA damage checkpoint (fig. S11). *trt1Δ* cells cultured in liquid medium showed progressive telomere shortening and poor growth. Then, the cells resumed growth by amplifying terminal DNAs containing telomeric repeats and subtelomeric sequences [telomere-associated sequence (TAS)] via homologous recombination (HR) (*14*). *ccq1Δtrt1Δ* cells started to show amplified telomere+TAS signals earlier than *trt1Δ* cells, suggesting that *ccq1Δ* accelerates HR-mediated telomere lengthening in the *trt1Δ* background (fig. S11). Although telomere signals persisted in *rhp55Δ*, *rhp51Δ*, and *ccq1Δ* single mutants, the concomitant deletion of *ccq1*$^+$ and *rhp55*$^+$ or *rhp51*$^+$ led to the com-

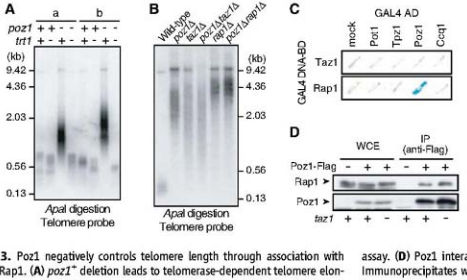

Fig. 3. Poz1 negatively controls telomere length through association with Taz1-Rap1. **(A)** *poz1*$^+$ deletion leads to telomerase-dependent telomere elongation. Genomic DNAs were prepared from indicated haploid cells derived from heterozygous *poz1Δ/poz1*$^+$ *trt1Δ/trt1*$^+$ diploid cells (results from two independent tetrads a and b are shown) and subjected to Southern hybridization. **(B)** *tazΔ* or *rapΔ* is epistatic to *pozΔ* in telomere-length control. **(C)** Poz1 and Rap1 protein interaction was detected by the yeast two-hybrid assay. **(D)** Poz1 interacts with Rap1 in a Taz1-independent manner in vivo. Immunoprecipitates were obtained from WCEs using antibodies to Flag and analyzed by immunoblotting. **(E)** Poz1 and Pot1 are localized at internal ds telomeric repeats in a Taz1- or Rap1-dependent manner. A cassette containing TAS-*ura4*$^+$-telomeric repeats was inserted into the *ade6* locus of circular chromosome III. Fold enrichments of *ura4*$^+$ and *lys1*$^+$ in indicated immunoprecipitates in a ChIP assay are shown.

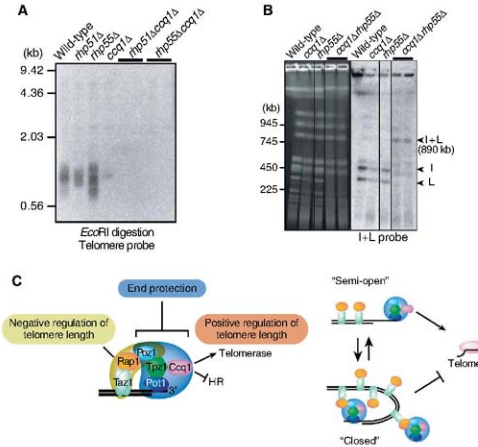

Fig. 4. Ccq1 inhibits HR at telomeres. **(A)** Telomeres are lost in *ccq1Δrhp51Δ* and *ccq1Δrhp55Δ*. **(B)** HR prevents chromosome circularization in *ccq1Δ*. Not I–digested chromosomal DNAs were fractionated by PFGE, stained with ethidium bromide (left), and subjected to Southern hybridization (right). **(C)** Model of Pot1-complex–mediated switching between closed and semi-open telomere configurations. The Pot1 complex exists at telomeres in two distinguishable modes (closed and semi-open configurations) that regulate telomerase in opposite manners. In both cases, Ccq1 and Poz1 protect telomeres from degradation, HR, and fusion.

plete loss of telomeric DNA and chromosome circularization (Fig. 4, A and B), indicating that terminal DNAs in *ccq1Δ* cells are maintained via HR. Thus, Ccq1 protects telomeres from HR. In *ccq1Δ* cells, the deregulated HR activity at telomeres contributes to the survival of cells without circular chromosome formation.

We propose that the Pot1 complex exists at telomeres in two distinguishable modes. When telomeres are relatively long, the Pot1 complex associates with ds telomeric DNA-Taz1-Rap1 via Poz1 because of a high concentration of local Taz1-Rap1 proteins, leading to inhibition of telomerase action (a closed configuration). When telomeres shorten, the Pot1 complex is dissociated from Taz1-Rap1, facilitating telomerase action aided by Ccq1 (a semi-open configuration). The structure and function of fission yeast telomeres revealed in this study highlight the conservation of major features of the shelterin complex across a wide evolutionary distance (fig. S12). We also predict that shelterin functions by recruiting unidentified effector molecules in higher eukaryotes, similar to the recruitment of Ccq1 in fission yeast.

References and Notes

1. D. E. Gottschling, V. A. Zakian, *Cell* **47**, 195 (1986).
2. C. M. Price, T. R. Cech, *Genes Dev.* **1**, 783 (1987).
3. M. P. Horvath, V. L. Schweiker, J. M. Bevilacqua, J. A. Ruggles, S. C. Schultz, *Cell* **95**, 963 (1998).
4. P. Baumann, T. R. Cech, *Science* **292**, 1171 (2001).
5. M. Lei, E. R. Podell, P. Baumann, T. R. Cech, *Nature* **426**, 198 (2003).
6. L. Wu *et al.*, *Cell* **126**, 49 (2006).
7. D. Hockemeyer, J. P. Daniels, H. Takai, T. de Lange, *Cell* **126**, 63 (2006).
8. F. Wang *et al.*, *Nature* **445**, 506 (2007).
9. H. Xin *et al.*, *Nature* **445**, 559 (2007).
10. T. de Lange, *Genes Dev.* **19**, 2100 (2005).
11. D. Loayza, T. de Lange, *Nature* **423**, 1013 (2003).
12. T. Sugiyama *et al.*, *Cell* **128**, 491 (2007).
13. M. R. Flory, A. R. Carson, E. G. Muller, R. Aebersold, *Mol. Cell* **16**, 619 (2004).
14. T. M. Nakamura, J. P. Cooper, T. R. Cech, *Science* **282**, 493 (1998).
15. T. Naito, A. Matsuura, F. Ishikawa, *Nat. Genet.* **20**, 203 (1998).
16. D. Hockemeyer *et al.*, *Nat. Struct. Mol. Biol.* **14**, 754 (2007).
17. J. P. Cooper, E. R. Nimmo, R. C. Allshire, T. R. Cech, *Nature* **385**, 744 (1997).
18. J. Kanoh, F. Ishikawa, *Curr. Biol.* **11**, 1624 (2001).
19. Y. Chikashige, Y. Hiraoka, *Curr. Biol.* **11**, 1618 (2001).
20. J. E. Croy, E. R. Podell, D. S. Wuttke, *J. Mol. Biol.* **361**, 80 (2006).
21. Materials and methods are available as supporting material on *Science* Online.

22. C. H. Haering, T. M. Nakamura, P. Baumann, T. R. Cech, *Proc. Natl. Acad. Sci. U.S.A.* **97**, 6367 (2000).
23. We thank M. Tamura and A. Hagiwara for technical assistance; P. Baumann, T. M. Nakamura, M. Yanagida, M. Shirakawa, and M. Katahira for discussions and materials; and A. Katayama and M. Sasaki for assistance. This work was supported by a Grant-in-Aid for Scientific Research on Priority Areas (J.K.) and for Cancer Research (F.I.) from the Ministry of Education, Culture, Sports, Science and Technology, Japan.

Supporting Online Material

www.sciencemag.org/cgi/content/full/320/5881/1341/DC1
Materials and Methods
Figs. S1 to S12
Tables S1 to S3
References

4 January 2008; accepted 10 April 2008
10.1126/science.1154819

The Transcriptional Landscape of the Yeast Genome Defined by RNA Sequencing

Ugrappa Nagalakshmi,[1]* Zhong Wang,[1]* Karl Waern,[1] Chong Shou,[2] Debasish Raha,[1] Mark Gerstein,[2,3] Michael Snyder[1,2,3]†

The identification of untranslated regions, introns, and coding regions within an organism remains challenging. We developed a quantitative sequencing-based method called RNA-Seq for mapping transcribed regions, in which complementary DNA fragments are subjected to high-throughput sequencing and mapped to the genome. We applied RNA-Seq to generate a high-resolution transcriptome map of the yeast genome and demonstrated that most (74.5%) of the nonrepetitive sequence of the yeast genome is transcribed. We confirmed many known and predicted introns and demonstrated that others are not actively used. Alternative initiation codons and upstream open reading frames also were identified for many yeast genes. We also found unexpected 3′-end heterogeneity and the presence of many overlapping genes. These results indicate that the yeast transcriptome is more complex than previously appreciated.

A major challenge in genomics is to identify all genes and exons and their boundaries. This information is crucial in order to understand the functional elements of the genome and determine when they are expressed and how they are regulated. Often, genes are identified

through the presence of large open reading frames (ORFs), sequence conservation, or cDNA probing of DNA tiling microarrays (*1*–*5*). These methods often fail to identify short exons, do not precisely reveal the boundaries of untranslated regions (UTRs), and/or have high false-positive rates.

In order to better map the transcribed regions of the yeast genome, we developed the RNA-Seq approach presented in Fig. 1. Briefly, polyadenylate [poly(A)] RNA was isolated from yeast cells grown in rich media (*6*) and used to generate double-stranded cDNA by reverse transcription with either random hexamers or oligo(dT) primers. The double-stranded cDNA was fragmented and subjected to high-throughput Illumina sequencing in which 35 base pairs (bp) of sequence were determined from one end of each fragment. Two technical and two biological replicates were performed for each hexamer and oligo(dT)-primed cDNA sample for a total of 15,787,335 and 14,125,182 reads, respectively. These sequence reads were analyzed with an algorithm that maps unique (that is, single-copy) sequences to the genome and allows for up to two mismatches (*6*). Of 29,912,517 total reads, 15,870,540 (56%) were mapped to unique genomic regions (fig. S1A and table S1).

We assessed our results by several criteria. First, none of the 29,912,517 sequence reads matched the deleted 3.5-kb regions of the genome (Fig. 1C), and very few, if any, matched the nontranscribed centromeres (fig S1B) (*6*); thus, our method is specific. Second, our replicates were in close agreement with one another, having a 0.99 Pearson correlation coefficient for technical replicates and a 0.93 to 0.95 coefficient for biological replicates (fig. S2). The data generated from hexamers and oligo(dT) primers also were closely correlated (0.97) and showed similar patterns of expression (fig. S2). Therefore, we merged all of these data sets, and the subsequent analyses were performed using the merged data.

RNA-Seq analyses revealed extensive expression of the whole yeast genome (Fig. 2A); 74.5% of the genome was expressed as RNA-Seq tags (Fig. 2B). We detected more reads from the 3′ ends than from the 5′ ends of annotated genes (fig. S3), presumably due to the enrichment of 3′ sequences during poly(A) purification as well as enhanced priming at the 3′ ends. Despite this bias, the deep sequencing allowed the detection of signals across the entire gene. Overall, 85% of the bases detected as expressed by RNA-Seq overlapped with those found with DNA-tiling microarrays (*7*).

We investigated the overall transcriptional activity and found that 4666 of the 5099 annotated ORFs (91.5%) in the Saccharomyces Genome Database (SGD) were expressed as tags above background (*6*). For this analysis, we removed 1178 ORFs whose 3′ ends lie within 100 bp of one another and whose transcripts might overlap. In addition, 327 ORFs that were not unique in their 3′ ends were not analyzed. We observed high expression for 20% of the genes; Gene Ontology (GO) analysis revealed that genes involved in biosynthetic pathways and ion transport were specifically enriched in the highly expressed category ($P < 2.3 \times 10^{-58}$; see table S2 for a complete list). Medium and low expression levels were observed for 39 and 33% of the genes, respectively. As expected, we did not detect the expression of genes involved in meiosis, mating, cell differentiation, sugar transport, or vitamin metabolism, the functions of which are not required during vegetative growth (*8*).

The majority of yeast genes have been annotated primarily with ORFs and, to a lesser extent, with cDNA sequencing (*9*); thus, the 5′ and 3′ boundaries and UTRs of most yeast genes have not been precisely defined. To map the 5′ ends of genes with RNA-Seq, the 5′ ends of 1331 genes were first determined by generating and sequencing rapid amplification of cDNA ends (RACE) polymerase chain reaction (PCR) products (table S3). We then used 125 RACE ends to optimize parameters for determining 5′ ends by searching RNA-Seq data for a sharp signal reduction in the transcribed region; applying these parameters revealed the 5′ boundary regions for 4665 transcribed genes. Genes with very low levels of expression were excluded from the analysis. Comparison of these results with 1025 boundaries mapped with 5′ RACE showed that both methods identified 5′ boundaries within 50 bp of one another for 786 genes (77.9%) (Fig. 3A). Combining the 5′ RACE results with the RNA-Seq results defined the 5′ boundaries of 4835 yeast genes (Fig. 3B). The median length of 5′ UTRs was 50 bp with a range of 0 to 990 bp (Fig. 3A, top right). Two hundred forty-one genes contained a start codon (ATG) less than 10 bp from the 5′ end; we do not know if these ATGs represent true initiation codons.

We also globally mapped the 3′ boundaries of yeast genes by searching for a rapid transition in the RNA-Seq signal as well as by identifying end tags with poly(A) sequences containing a novel stretch of three or more consecutive As lying next to a genomic yeast sequence (*6*). Using these methods, we mapped the 3′ boundaries of 5212 transcribed genes and deduced the transcribed strand (Fig. 3, C and D, and table S4). The end tags allowed the precise assignment of 3′ boundaries even when transcripts were overlapping at their 3′ ends (Fig. 4). We found evidence that the transcription of a large number of yeast genes overlaps with transcription from the other strand. Of 4646 verified expressed ORFs, 275 transcribed pairs (11.8% of expressed genes) contained overlapping 3′ ends. Pervasive overlapping transcripts may be unique to *Saccharomyces cerevisiae* and other organisms lacking microRNA/small interfering RNA–processing components that might otherwise degrade double-stranded RNAs. Moreover, overlapping transcription at 3′ ends could be a form of gene regulation by which neighboring genes can potentially influence (positively or negatively) the expression of one another.

The median length of yeast 3′ UTRs is 104 bp, with a range of 0 to 1461 bp (Fig. 3A). Although most yeast genes have a single precise 3′ end (within 1 to 2 bp), many genes had heterogeneous 3′-end sequences. These occurred either in localized regions (usually 2 to 10 bp), suggesting some variability in 3′-end processing at the poly(A) signal, or, in 540 genes, in multiple peaks greater than 10 bp apart, suggesting that more than one poly(A) site is used (fig. S4).

In yeast, the first ATG at the 5′ end of an ORF is usually annotated as the start codon. However, in some databases the second ATG is annotated when the predicted amino-terminal protein–coding sequence is not conserved (*10*, *11*). RNA-Seq analysis revealed 35 genes with 5′ ends upstream of an ATG that is 5′ and in-frame to the annotated ATG initiation codon, suggesting that these proteins are potentially longer than predicted. We also found 29 genes whose 5′ end is located downstream of the annotated ATG, suggesting that these proteins are shorter than previously predicted; the 5′ ends of four of the latter genes were confirmed by RACE sequencing.

We also examined our data for the presence of introns; in yeast, introns are typically identified on the basis of sequence conservation, microarray analyses, or other studies. We detected 240 of 306 known introns with an algorithm that detects introns through the presence of discontinuous sequences whose boundaries contain GT and AG/AC and also detects sequence tags that span the intron boundary, which indicates that transcripts from these genes are spliced. For the 66 introns not validated with the algorithm, we examined 30 whose genes were expressed. In four cases, the intron sequences were clearly expressed at levels similar to those of the adjacent exons (Fig. 3E and fig. S5), and unspliced products, but not splice junction tags, were identified. Thus, transcripts from these genes are probably not spliced at appreciable levels in vegetative cells [see also (*12*)]. In two of these cases, the presence or lack of an intron affected the predicted protein sequence.

Recent analysis predicts that many eukaryotic 5′ UTRs may contain upstream ORFs (uORFs) (*13*). uORFs have been shown to regulate protein expression (*14*) and mRNA degradation (*15*) and have been annotated for 17 yeast genes. Our data predict uORFs upstream of the start codon for 321 (6%) of the yeast gene transcripts (Fig. 5 and table S6). GO analysis of these genes revealed that genes encoding DNA-binding proteins [$P < 0.0027$, false discovery rate (FDR)–adjusted] and anatomical structure and development (for example, sporulation; $P < 0.0045$, FDR-adjusted) were significantly enriched in uORFs (Fig. 5B). The presence of uORFs in DNA binding proteins suggests that these important genes are likely to be highly regulated.

[1]Department of Molecular, Cellular, and Developmental Biology, Yale University, New Haven, CT 06520, USA. [2]Program in Computer Science and Computational Biology, Yale University, New Haven, CT 06520, USA. [3]Department of Molecular, Biophysics and Biochemistry, Yale University, New Haven, CT 06520, USA.

*These authors contributed equally to this work.
†To whom correspondence should be addressed. E-mail: michael.snyder@yale.edu

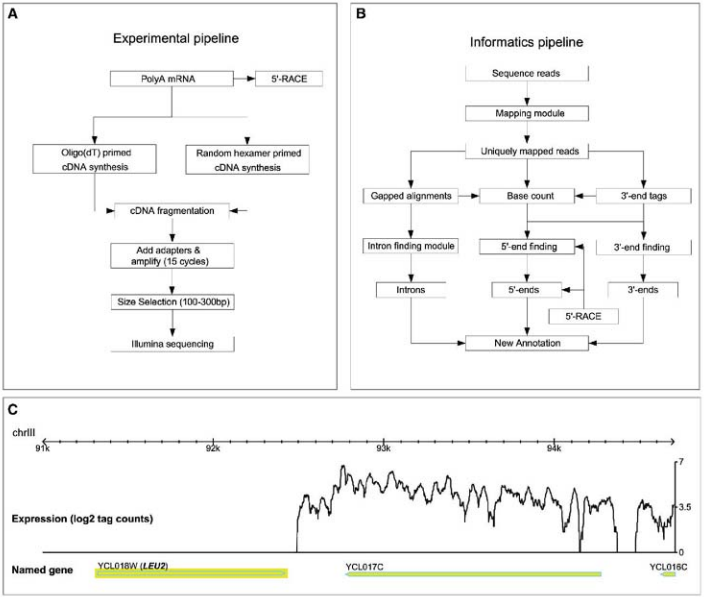

Fig. 1. (**A** and **B**) Flowcharts of the RNA-Seq method. (**C**) RNA-Seq signals are not evident at a deleted gene (*LEU2*) but are abundant at an expressed neighboring gene (*YCL017C*).

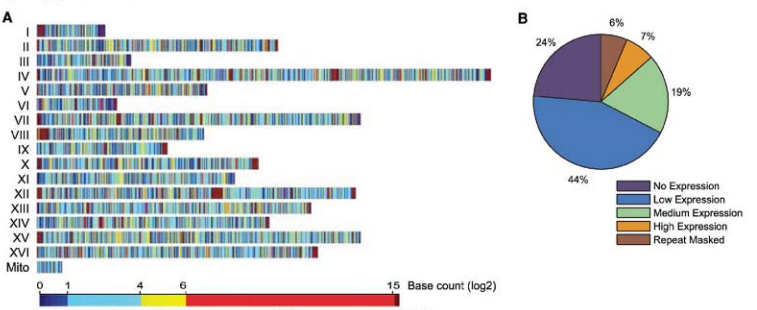

Fig. 2. (**A**) The genome distribution of transcribed regions in yeast. Colors represent different transcription levels for each base (log2 tag count). Numbers of chromosome regions are shown on the left. Mito, mitochondria. (**B**) A summary of the transcription level of the transcriptome.

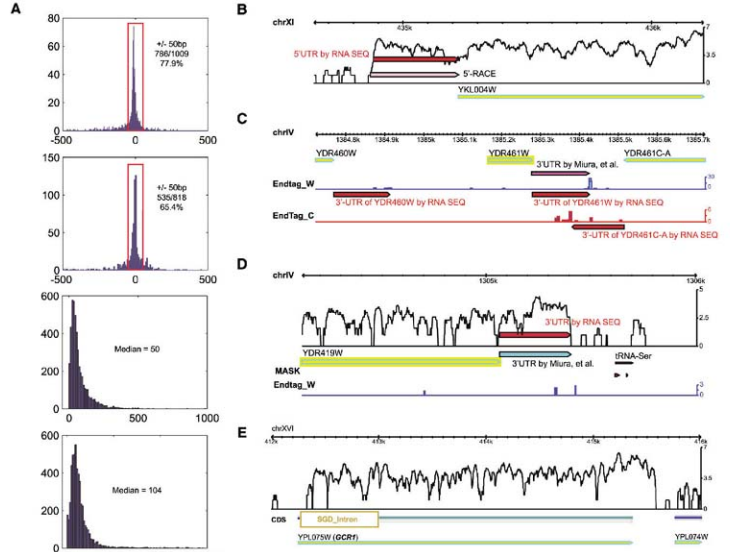

Fig. 3. **(A)** Size differences between mapped 5′-UTR data with RNA-Seq and RACE (top) and 3′-UTR data with RNA-Seq and cDNA sequencing (*9*) (second from top) next to the size distributions of the 5′ UTR (second from bottom) and 3′ UTR (bottom). **(B)** The 5′ UTR as determined by RNA-Seq and by 5′ RACE for gene *YKL004W*. In all figures, a colored box represents an ORF and an arrow indicates the transcription direction. chrXI, chromosome XI. **(C)** 3′ UTR determined by RNA-Seq on the basis of end tags for genes *YDR460W*, *YDR461W*, and *YDR461C-A*, or for *YDR461W* by cDNA sequencing (*9*). Endtag_W (blue) and Endtag_C (red) represent RNA-Seq reads containing poly(A) tails on either Watson or Crick strands, respectively, and the bars represent confidence scores of each 3′ end (*6*). **(D)** 3′ UTR determined by RNA-Seq based on a sharp expression decrease as compared with cDNA data (*9*). MASK, repeated mask sequence. **(E)** An SGD-annotated intron (box in brown color) in *GCR1* not supported by RNA-Seq. CDS, coding sequence.

We also searched for transcription in intergenic regions (Fig. 5D) by identifying stretches of 150 bp or greater with significant expression above that of surrounding regions (Fig. 5F) (*6*). Of 487 expressed regions identified, 204 had not been observed by microarray analyses or cDNA studies (*7*, *9*). For 18 regions found by RNA-Seq but not other methods, we tested expression with real-time quantitative PCR (QPCR) and confirmed transcription in 16 cases (table S5).

Because RNA-Seq is a quantitative method, it can potentially be used to quantify RNA levels. We determined the median signal in a 30-bp window located immediately upstream of the 3′ ends of the annotated stop codon (table S4) after removing genes with overlapping 3′ ends in this region. The expression levels of 34 genes predicted to be expressed at a range of high, medium, and low levels were measured with QPCR. We found a strong correlation ($R = 0.98$) between the QPCR and RNA-Seq data (fig. S6A). As expected, discrepancies were the largest among the genes expressed at a low level and were better than those obtained with standard microarrays ($R = 0.72$) (fig. S6C) (*16*) or tiling DNA-microarray analysis ($R = 0.48$) (fig. S6B) (*7*). Moreover, the dynamic range of RNA-Seq is at least 8000-fold,

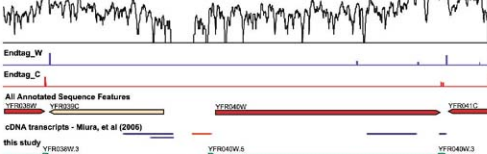

Fig. 4. New annotations of UTRs in a relatively poorly annotated chrVI region. ORFs identified by this study are denoted by dotted lines, and arrows denote the transcription direction. Green-shaded boxes are UTRs. cDNA transcripts in red are of high confidence and those in blue are of low confidence [defined in (*9*)].

compared with ~60-fold for DNA microarrays (see the scale of fig. S6, B and C).

RNA-Seq offers several advantages as compared with other technologies. First, it allows interrogation of all unique sequences of the genome, including those that are closely related, as long as unique bases exist that can be monitored. Second, because a large number of reads can readily be obtained, the method is very sensitive and offers a large dynamic range. Thus, RNA-Seq can detect and quantify levels of RNAs expressed at very low levels as compared with DNA microarrays; the sensitivity of the latter is probably reduced because of cross-hybridization effects. Third, RNA-Seq allows accurate determination of exon boundaries. Although we precisely mapped 3′ ends of many yeast genes using RNA-Seq, we did not attempt to determine the nucleotide reso-

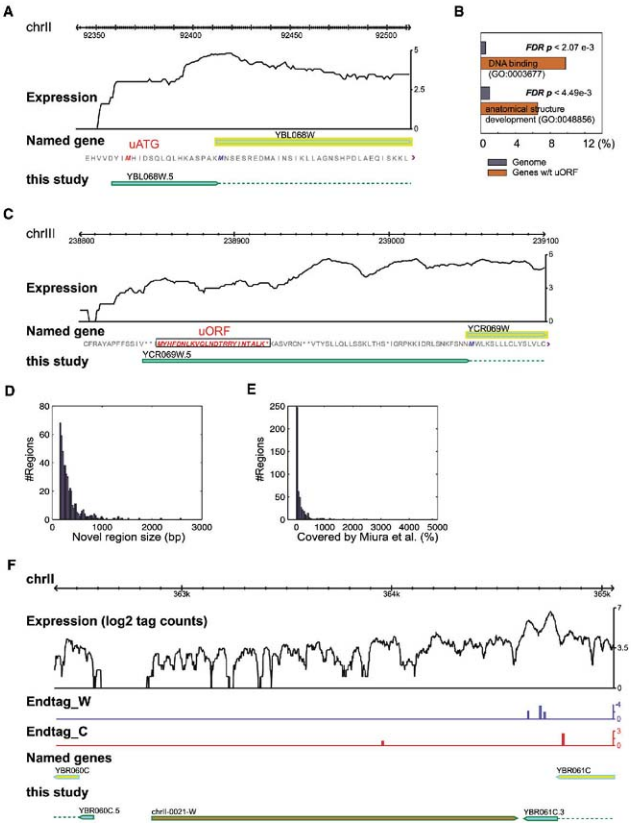

Fig. 5. (**A**) RNA-Seq reveals putative upstream start codons (uATG, in red) relative to existing annotations (blue ATG). (**B**) Significantly more upstream uORFs were found relative to annotated ORFs for certain biological functions. *P* values are FDR–adjusted. (**C**) An example of an uORF (boxed and in red). (**D**) Size distribution of previously undescribed transcribed regions. (**E**) Transcribed regions previously covered by cDNA sequencing (*9*) in percentages. (**F**) An example of a previously undescribed transcribed region containing a poly(A) signal (shaded in red).

lution of 5′ boundaries because yeast 5′ ends are often heterogeneous (*9*, *17*) and we performed an amplification step. Instead, an approximate location was deduced by a sharp transition in signal over a small interval. Nonetheless, overall, RNA-Seq provides a useful map of exon boundaries. Our RNA-Seq method allowed us to map the transcriptional landscape of the yeast genome and define UTRs and previously unknown transcribed regions. In the future, application of this method should help to precisely determine the transcriptional landscape of other genomes.

References and Notes

1. M. Snyder, M. Gerstein, *Science* **300**, 258 (2003).
2. M. B. Gerstein *et al.*, *Genome Res.* **17**, 669 (2007).
3. M. D. Adams *et al.*, *Nature* **377**, 3 (1995).
4. P. Kapranov *et al.*, *Science* **296**, 916 (2002).
5. P. Bertone *et al.*, *Science* **306**, 2242 (2004).
6. Materials and methods are available as supporting material on *Science* Online.
7. F. Perocchi, Z. Xu, S. Clauder-Münster, L. M. Steinmetz, *Nucleic Acids Res.* **35**, e128 (2007).
8. L. David *et al.*, *Proc. Natl. Acad. Sci. U.S.A.* **103**, 5320 (2006).
9. F. Miura *et al.*, *Proc. Natl. Acad. Sci. U.S.A.* **103**, 17846 (2006).
10. M. Kellis, N. Patterson, M. Endrizzi, B. Birren, E. S. Lander, *Nature* **423**, 241 (2003).
11. P. Clifton *et al.*, *Science* **301**, 71 (2003).
12. K. Juneau, C. Palm, M. Miranda, R. W. Davis, *Proc. Natl. Acad. Sci. U.S.A.* **104**, 1522 (2007).
13. F. Mignone, C. Gissi, S. Liuni, G. Pesole, *Genome Biol.* **3**, REVIEWS0004 (2002).
14. A. G. Hinnebusch, *Annu. Rev. Microbiol.* **59**, 407 (2005).
15. M. J. Ruiz-Echevarría, S. W. Peltz, *Cell* **101**, 741 (2000).
16. F. C. Holstege *et al.*, *Cell* **95**, 717 (1998).
17. C. F. Albright, R. W. Robbins, *J. Biol. Chem.* **265**, 7042 (1990).
18. We thank S. P. Dinesh-Kumar for comments. Funded by two grants from NIH and one from the Connecticut Stem Cell Fund (06SCE01). The Gene Expression Omnibus accession number for sequences is GSE11209.

Supporting Online Material

www.sciencemag.org/cgi/content/full/1158441/DC1
Materials and Methods
Figs. S1 to S6
Tables S1 to S6
References

31 March 2008; accepted 22 April 2008
Published online 1 May 2008;
10.1126/science.1158441
Include this information when citing this paper.

The Transcription/Migration Interface in Heart Precursors of *Ciona intestinalis*

Lionel Christiaen,[1]* Brad Davidson,[1]† Takeshi Kawashima,[2] Weston Powell,[1] Hector Nolla,[3] Karen Vranizan,[4] Michael Levine[1]*

Gene regulatory networks direct the progressive determination of cell fate during embryogenesis, but how they control cell behavior during morphogenesis remains largely elusive. Cell sorting, microarrays, and targeted molecular manipulations were used to analyze cardiac cell migration in the ascidian *Ciona intestinalis*. The heart network regulates genes involved in most cellular activities required for migration, including adhesion, cell polarity, and membrane protrusions. We demonstrated that fibroblast growth factor signaling and the forkhead transcription factor FoxF directly upregulate the small guanosine triphosphatase RhoDF, which synergizes with Cdc42 to contribute to the protrusive activity of migrating cells. Moreover, RhoDF induces membrane protrusions independently of other cellular activities required for migration. We propose that transcription regulation of specific effector genes determines the coordinated deployment of discrete cellular modules underlying migration.

There has been considerable progress in elucidating the gene regulatory networks controlling cell fate specification during animal development (*1*–*3*). In parallel, traditional in vitro assays coupled with more-recent proteome analyses have characterized the protein interaction networks controlling dynamic cellular processes, such as actin-based membrane protrusions (*4*) and adhesion (*5*). Comparatively little is known about how transient regulatory states interface with the dynamic cellular processes underlying morphogenesis. We investigated this problem using the migrating heart precursors of the ascidian *Ciona intestinalis* as a relatively simple model. The ascidian heart develops from the B7.5 pair of blastomeres that specifically express the basic helix-loop-helix transcription factor Mesp in response to the T-box factor Tbx6 (*6*, *7*). Subsequently, a fibroblast growth factor (FGF) signal activates the Ets1/2 transcription factor, a presumed Mesp target, and induces heart specification and cell migration of the anteriormost B7.5 granddaughter cells (Fig. 1A) (*8*). As a consequence, the heart precursors, called trunk ventral cells (TVCs), migrate into the trunk, whereas their sibling cells form anterior tail muscles (ATMs) (Fig. 1B). FGF signaling upregulates the forkhead box transcription factor FoxF in the TVCs. Interfering with FoxF function inhibits cell migration, but not heart muscle differentiation, showing that TVC migration is predominantly controlled by FGF signaling and the FoxF transcription factor (*9*).

To determine how FGF and FoxF control TVC migration, we developed a method for lineage-specific transcription profiling using fluorescence-activated cell sorting (FACS) and microarray analysis. The cis-regulatory DNAs from *Mesp* and the myogenic differentiation *MyoD* were used to express green and yellow fluorescent proteins in the B7.5-lineage and surrounding mesodermal cells, respectively [Fig. 1B; Mesp, green fluorescent protein (GFP) transgenes; MyoD, yellow fluorescent protein (YFP) transgenes]. B7.5-lineage cells were sorted based on their GFP fluorescence, after targeted manipulations of Mesp, FoxF, and FGF signaling using the *Mesp* cis-regulatory DNA (Fig. 1, A to C) (*7*–*9*). Targeted expression of a dominant-negative FGF receptor (dnFGFR) converts the entire B7.5 lineage into ATMs (*8*) and is therefore expected to inhibit the expression of TVC-specific genes (Fig. 1A and fig. S3). In addition, modified versions of Mesp and FoxF (Mesp:VP16 and FoxF:WRPW, respectively; both are fusion proteins) block TVC migration but not cardiomyocyte differentiation (*7*, *9*), thereby providing an opportunity to identify migration-specific genes (Fig. 1, A and E).

Microarray assays captured differential expression of known TVC- and tail muscle–specific marker genes (Fig. 1D and table S1). Moreover, at least 130 genes were found to be downregulated in all three conditions that inhibit TVC migration as compared with wild-type samples (Fig. 1E, fig. S4, and table S2). Transcriptional profiling of late gastrula stage B7.5 cells (LG sample) and whole tailbud embryos (whole sample) indicated that these 130 genes are upregulated in wild-type TVCs at the onset of migration (fig. S4). In situ hybridization assays validated the experimental design: 51 of 56 randomly selected candidate genes were expressed in migrating TVCs (Fig. 1, F and G, and fig. S3). Candidate migration genes include a broad spectrum of functional classes [for example, the RhoDF small Ras-homolog guanosine triphosphatase (Rho GTPase) and wunen-like phospholipid phosphohydrolase] (Fig. 1, F and G, and table S2). This diversity supports the view that many facets of cell migration are controlled transcriptionally (*10*, *11*).

Specific gene families and biological processes have been implicated in directed cell migration, such as polarity, cell-matrix adhesion, and actin dynamics regulators (figs. S7 to S9). We compared the expression levels of individual genes in wild-type and dnFGFR samples, which permitted the identification of genes specifically upregulated in either TVCs or ATMs (Fig. 1A and figs. S5 and S9). Cell type–specific genes were found to func-

[1]Department of Molecular and Cell Biology, Division of Genetics, Genomics and Development, Center for Integrative Genomics, University of California, Berkeley, CA 94720, USA. [2]Department of Energy Joint Genome Institute, Walnut Creek, CA 94598, USA. [3]Cancer Research Laboratory, University of California, Berkeley, CA 94720, USA. [4]Functional Genomics Laboratory, University of California, Berkeley, CA 94720, USA.

*To whom correspondence should be addressed. E-mail: lionelchristiaen@berkeley.edu (L.C.); mlevine@berkeley.edu (M.L.)

†Present address: Department of Molecular and Cellular Biology, Molecular Cardiovascular Research Program, University of Arizona, Tucson, AZ 85724, USA.

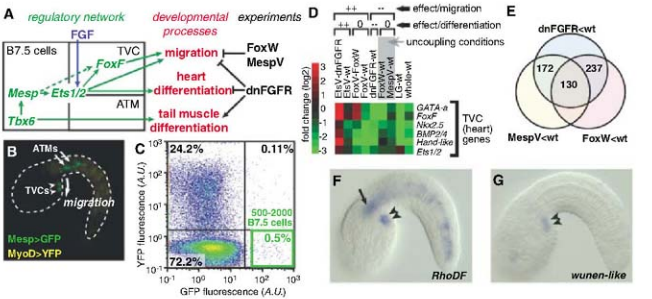

Fig. 1. Transcription profiling of heart precursors. **(A)** Regulatory network controlling developmental processes in the B7.5 lineage. Expression of dnFGFR, MespV, or FoxW inhibits cell migration. **(B)** Embryo expressing Mesp-GFP and MyoD-YFP transgenes. **(C)** FACS plot. Mesp-GFP– and MyoD-YFP–expressing cells are distinguished by their green or yellow fluorescence, respectively. The GFP-only quadrant (green box) was used to select B7.5-lineage cells. A.U., arbitrary units. **(D)** Experimental design and profiling of TVC marker genes. Effects on heart differentiation and cell migration are shown [for example, in column six FoxW inhibits migration (—), but not heart differentiation (0). Ets1/2:VP16, EtsV, and FoxF:VP16, FoxV have opposite effects from those of dnFGFR and FoxW, respectively; both enhance migration (++)]. wt, wild type. **(E)** Identification of 130 candidate migration genes downregulated in conditions inhibiting cell migration as compared with wild-type samples (for example, dnFGFR<wt indicates genes showing reduced expression in dnFGFR as compared with wt samples). **(F** and **G)** In situ hybridization of selected candidate migration genes (*RhoDF* and *wunen-like*). Arrowheads indicate TVCs; arrow indicates *RhoDF* expression in the notochord.

tion in each of the aforementioned cellular processes (figs. S7 to S9). For example, integrin-β3 and talin are upregulated in TVCs, possibly contributing to the changes in cell adhesion required for their migration. Conversely, ATM-specific upregulation of myosin light-chain kinase (MLCK) and myosin regulatory light chain (MRLC) may enhance actomyosin contraction in tail muscles (fig. S9). Thus, the identified network may control most of the cellular processes underlying TVC and ATM morphogenesis.

Many components in the above pathways do not exhibit differential regulation in TVCs and ATMs, suggesting constitutive expression in the B7.5 lineage (Fig. 2A and figs. S6 to S9). For example, about two-thirds of the actin dynamics regulators are constitutively expressed in both cell types (fig. S8). *RhoDF* is the only Rho GTPase that is specifically upregulated in the TVCs (Fig. 2A and fig. S8). Taken together, these observations suggest that the heart network controls individual cellular processes by regulating subsets of effector genes.

Cell culture experiments demonstrated that the formation of membrane protrusions at the leading edge of migrating cells is powered by polarized actin polymerization (*12*, *13*). In mammalian cells, both RhoD and RhoF/Rif were shown to directly activate the Diaphanous-related formin mDia2, which promotes the directed growth of actin filaments (*14*, *15*). Our observations suggest that Mesp, FGF, and FoxF might control this process primarily through the transcriptional activation of *RhoDF* (Fig. 2A and fig. S9).

As a first step toward testing this model, we characterized *RhoDF* cis-regulatory sequences. A RhoDF lacZ fusion gene recapitulated endogenous *RhoDF* expression, including expression in TVCs and notochord cells, as well as inhibition by FoxF:WRPW (FoxW) (Fig. 2B and figs.

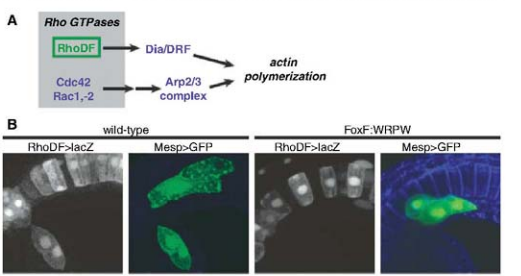

Fig. 2. The heart network regulates subsets of migration effectors. **(A)** Selected protein interactions promoting actin polymerization (extracted from fig. S9). Microarray analysis indicates that the Rho GTPase RhoDF is upregulated in the TVCs downstream of FGF and FoxF (green box and label). Diaphanous and Diaphanous-related formin (Dia/DRF); members of the Arp2/3 complex; and the Rho GTPases Rac1, Rac2, and Cdc42, are not differentially expressed between TVCs and ATMs (blue labels). Cdc42, Rac1, and Rac2 activate the Arp2/3 complex indirectly (successive arrows) (SOM text, section 6.4, and fig. S9). **(B)** RhoDF-lacZ (gray) expression in B7.5-lineage cells (marked by Mesp-GFP) is lost upon FoxF:WRPW coexpression. Blue indicates Alexa-phalloidin staining.

S10 and S11). Separate cis-regulatory modules control *RhoDF* expression in the notochord and TVCs (fig. S11). The minimal 425–base pair TVC enhancer contains putative Ets1/2- and FoxF-binding sites (fig. S11). Mutational analysis and cis-trans complementation assays demonstrated that both Ets1/2 and FoxF provide direct regulatory inputs for *RhoDF* upregulation in the TVCs (fig. S12). Therefore, FGF, FoxF, and RhoDF constitute a feed-forward circuit within the heart gene regulatory network.

The function of RhoDF in TVC migration was examined by injection of antisense morpholino oligonucleotides (MOs) and targeted expression of dominant-negative (dn) and constitutively active (ca) mutants. MOs were coinjected with brachyury-GFP (*16*) and Mesp–GFP-moesin transgenes to visualize notochord cells and TVCs, respectively (Fig. 3A). Injection of a translation-blocking MO (ATG-MO) led to the formation of multicellular spheres (Fig. 3C). This severe phenotype presumably results from the inhibition of maternal mRNAs and suggests that RhoDF is essential for cell movements during early embryogenesis [supporting online material (SOM) text, section 8.2]. A splicing-inhibitor MO (E2I2) was used to inves-

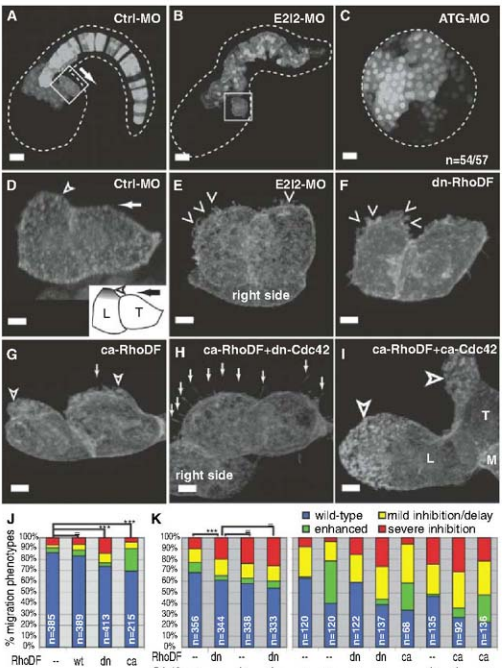

Fig. 3. RhoDF and Cdc42 synergy in TVC migration and protrusive activity. (**A** to **C**) Embryos injected with brachyury-GFP, Mesp–GFP-moesin, and indicated MOs. Scale bars, 20 μm. (**D** and **E**) Magnified apical views of TVCs from (**A**) and (**B**). The arrows in (**A**) and (**D**) indicate the direction of migration. (**F** to **I**) TVCs expressing the indicated Rho GTPase mutants. Shown are apical views from three-dimensional projections (arrows, filopodia; solid arrowhead, lateral protrusion; open arrowheads, disrupted protrusion; L, leader; T, trailer; M, muscle cells; $n > 10$ embryos for each condition. Scale bars, 5 μm.). (**J** and **K**) Migration phenotypes. Histograms are from different pools of experiments (n is the number of B7.5 clusters scored. In χ^2 tests, for "=" $P > 0.05$ and for "≠" $P < 0.001$. $n > 3$ replicate experiments).

tigate the specific function of zygotic *RhoDF* transcripts (fig. S14). The E2I2 MO perturbed both TVC migration and notochord intercalation (Fig. 3B and fig. S14). Targeted expression of dn-RhoDF caused mild but statistically significant TVC migration defects, whereas ca-RhoDF appeared to enhance migration (Fig. 3J).

Detailed observations of the TVCs using an actin-binding GFP-moesin reporter (*17*) revealed that the leading cell (L) exhibits lateral protrusions enlarging its leading edge, whereas the trailing cell (T) is constricted at the trailing edge (Fig. 3D and fig. S13). Upon MO injection or dn-RhoDF expression, the cell contour was irregular and lateral protrusions appeared disrupted (Fig. 3, E and F). In contrast, ca-RhoDF induced a dramatic enlargement of lateral protrusions (Fig. 3G). Taken together, these observations suggest that RhoDF contributes to optimal TVC migration, possibly through the regulation of actin-based protrusions.

The ubiquitous Rho GTPase Cdc42, which also regulates actin-based protrusions, may function redundantly and/or in concert with RhoDF (*18*, *19*). We investigated these possibilities by coexpressing dn and ca forms of RhoDF and Cdc42 (Fig. 3, F to I and K, and fig. S15). dn-Cdc42 and dn-RhoDF produced similar migration and protrusion phenotypes, whether expressed separately or together, suggesting that they function synergistically in TVCs (Fig. 3, F and K, and fig. S15). ca-Cdc42 induced actin-rich protrusions that failed to extend upon coexpression of dn-RhoDF (fig. S15). More strikingly, dn-Cdc42 reduced the width of the ca-RhoDF–induced protrusions, often causing the formation of multiple filopodia (Fig. 3H). Finally, ca-RhoDF and ca-Cdc42 coexpression disrupted the TVCs' polarity and produced protrusions that often covered the entire leading edge (Fig. 3I and fig. S15).

The simplest interpretation is that Cdc42 promotes actin-filament branching through indirect activation of the actin-related protein 2/3 (Arp2/3) complex (*20*, *21*), whereas RhoDF induces actin filament elongation through the activation of Diaphanous-related formins (Fig. 2A). The precise balance of microfilament branching and elongation would then pattern the actin meshwork underlying membrane protrusion [Fig. 4B, fig. S15F, and (*13*)].

The preceding results suggest that upregulation of *RhoDF* by FGF and FoxF is sufficient to promote actin-based protrusions in TVCs because *RhoDF* works in concert with Cdc42 and other constitutive activators of actin polymerization (Fig. 2A). Additional epistasis assays were performed to determine whether RhoDF is indeed the only missing factor. Targeted expression of FoxF:WRPW, dnFGFR, or Ets:WRPW [a constitutive repressor form of Ets1/2 (*8*)] consistently blocked migration and the formation of lateral protrusions (Fig. 4A and fig. S16). Both wild-type and activated forms of RhoDF were sufficient to induce lateral protrusions in nonmigrating B7.5 cells expressing FoxF:WRPW (Fig. 4A and fig. S16). Cells coexpressing Ets:WRPW and ca-RhoDF formed smaller protrusions and filopodia, whereas dnFGFR eliminated the ability of ca-RhoDF to induce protrusions (fig. S16). These observations indicate that FGF signaling provides as-yet-unidentified inputs required for RhoDF/Cdc42–induced protrusive activity (Fig. 4B and fig. S16). The formation of RhoDF-induced protrusions in the FoxF:WRPW background indicates that FoxF controls membrane protrusion essentially through *RhoDF* upregulation and shows that protrusive activity is separable from other processes required for migration.

Our results illuminate previously unrecognized characteristics of the transcription/cell behavior interface. The heart gene network impinges on most of the individual cellular processes required for migration by regulating subsets of effector genes that function together with constitutively expressed proteins. These shared regulatory inputs probably contribute to the coordination of different cellular processes, which could nevertheless be uncoupled from one another, thus highlighting the intrinsically modular nature of cell behavior.

TVC-specific expression of *RhoDF* depends on FGF, Ets1/2, FoxF, and as-yet-unidentified

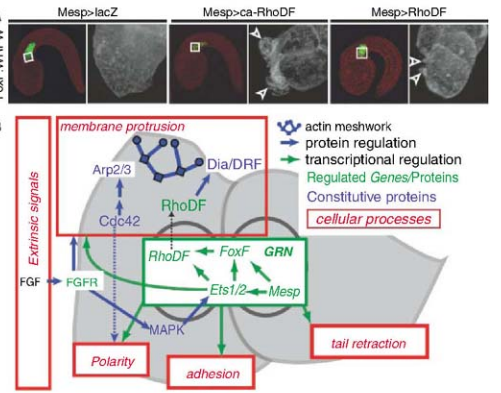

Fig. 4. RhoDF induces membrane protrusion in nonmigrating cells. **(A)** B7.5-lineage cells coexpressing FoxF:WRPW and lacZ, ca-RhoDF, or RhoDF. [Whole embryos and close-up views (boxes) are shown. Red indicates Alexa-phalloïdin counterstaining.] Arrowheads indicate protrusions. **(B)** Summary model. The gene regulatory network (GRN) influences polarity, adhesion, tail retraction, and membrane protrusion. Membrane protrusion is controlled in part by FoxF- and Ets1/2-mediated upregulation of RhoDF, which functions together with constitutively expressed Cdc42, Dia/DRF (blue circles), and Arp2/3 (blue squares).

inputs, stressing the fact that RhoDF-induced protrusive activity is regulated by multiple inputs from the heart specification network (Fig. 4B and figs. S10 to S12). A separate enhancer controls *RhoDF* expression in the notochord (fig. S11). In principle, this modular organization of the *RhoDF* cis-regulatory elements permits activation by distinct gene regulatory networks in the notochord and TVCs. RhoDF contributes to the formation of protrusions in migrating TVCs and probably also in intercalating notochord cells (Fig. 3B and fig. S14). Unlike TVCs, notochord cells maintain adhesive contacts with their neighbors. In *laminin-α3/4/5* mutants, these adhesive contacts are disrupted and notochord cells migrate away from their normal location, displaying dynamic protrusions reminiscent of those induced by ca-RhoDF (*22*) (fig. S15). Thus, the notochord and TVCs deploy different suites of shared (such as protrusions) and tissue-specific (such as adhesive properties) cellular modules. We propose that tissue-specific gene networks control the distinct combinations of cellular modules underlying the morphogenetic diversity observed during evolution and development.

References and Notes

1. A. Stathopoulos, M. Levine, *Dev. Cell* **9**, 449 (2005).
2. E. H. Davidson *et al.*, *Science* **295**, 1669 (2002).
3. K. S. Imai, M. Levine, N. Satoh, Y. Satou, *Science* **312**, 1183 (2006).
4. C. Bakal, J. Aach, G. Church, N. Perrimon, *Science* **316**, 1753 (2007).
5. R. Zaidel-Bar, S. Itzkovitz, A. Ma'ayan, R. Iyengar, B. Geiger, *Nat. Cell Biol.* **9**, 858 (2007).
6. Y. Satou, K. S. Imai, N. Satoh, *Development* **131**, 2533 (2004).
7. B. Davidson, W. Shi, M. Levine, *Development* **132**, 4811 (2005).
8. B. Davidson, W. Shi, J. Beh, L. Christiaen, M. Levine, *Genes Dev.* **20**, 2728 (2006).
9. J. Beh, W. Shi, M. Levine, B. Davidson, L. Christiaen, *Development* **134**, 3297 (2007).
10. L. Borghese *et al.*, *Dev. Cell* **10**, 497 (2006).
11. X. Wang *et al.*, *Dev. Cell* **10**, 117 (2006).
12. S. A. Koestler, S. Auinger, M. Vinzenz, K. Rottner, J. V. Small, *Nat. Cell Biol.* **10**, 306 (2008).
13. C. Yang *et al.*, *PLoS Biol.* **5**, e317 (2007).
14. P. A. Randazzo, *Dev. Cell* **4**, 287 (2003).
15. S. Pellegrin, H. Mellor, *Curr. Biol.* **15**, 129 (2005).
16. J. C. Corbo, M. Levine, R. W. Zeller, *Development* **124**, 589 (1997).
17. K. A. Edwards, M. Demsky, R. A. Montague, N. Weymouth, D. P. Kiehart, *Dev. Biol.* **191**, 103 (1997).
18. S. Ellis, H. Mellor, *Curr. Biol.* **10**, 1387 (2000).
19. C. D. Nobes, A. Hall, *Cell* **81**, 53 (1995).
20. R. Rohatgi *et al.*, *Cell* **97**, 221 (1999).
21. L. Ma, R. Rohatgi, M. W. Kirschner, *Proc. Natl. Acad. Sci. U.S.A.* **95**, 15362 (1998).
22. M. T. Veeman *et al.*, *Development* **135**, 33 (2007).
23. Microarray data available at ArrayExpress; accession number, E-MEXP-1478. We thank J. Beh, A. Philips, and P. Lemaire for sharing constructs; M. Blanchette and V. Peng for help with microarrays; Y. Satou for expressed sequence tag sequences and annotations; and W. Shi, K. Imai, and U. Rothbacher for help with microinjections. Authors' contributions were as follows: L.C. designed the project, performed and analyzed experiments, and prepared the figures; B.D. and T.K. designed the custom microarray; L.C. and W.P. performed in situ hybridizations; L.C. and H.N. performed the FACS experiments; L.C. and K.V. analyzed the microarray data; and L.C. and M.L. wrote the paper. This work was funded by NSF grant IOB 0445470 and NIH grant 1RB-106681 to M.L., a grant from the Gordon and Betty Moore Foundation to the Center for Integrative Genomics, and an American Heart Association fellowship (0625042Y) to B.D.

Supporting Online Material

www.sciencemag.org/cgi/content/full/320/5881/1349/DC1
Materials and Methods
SOM Text
Figs. S1 to S16
Tables S1 and S2
References

21 March 2008; accepted 9 May 2008
10.1126/science.1158170

High Impulsivity Predicts the Switch to Compulsive Cocaine-Taking

David Belin,[1]* Adam C. Mar,[1] Jeffrey W. Dalley,[1,2] Trevor W. Robbins,[1] Barry J. Everitt[1]*

Both impulsivity and novelty-seeking have been suggested to be behavioral markers of the propensity to take addictive drugs. However, their relevance for the vulnerability to compulsively seek and take drugs, which is a hallmark feature of addiction, is unknown. We report here that, whereas high reactivity to novelty predicts the propensity to initiate cocaine self-administration, high impulsivity predicts the development of addiction-like behavior in rats, including persistent or compulsive drug-taking in the face of aversive outcomes. This study shows experimental evidence that a shift from impulsivity to compulsivity occurs during the development of addictive behavior, which provides insights into the genesis and neural mechanisms of drug addiction.

Compulsive cocaine use has been hypothesized to result from a failure in top-down executive control over maladaptive habit learning (*1*, *2*). In neural terms, this may reflect the diminishing influence of prefrontal cortical function, as behavioral control devolves from ventral to dorsal striatum (*1*). In behavioral terms, we predict that the development of addiction reflects a shift from impulsivity to compulsivity (*3*).

Human studies have implicated individual differences in different forms of impulsivity and sensation-seeking in vulnerability to drug use and abuse (*4*–*6*). However, whether the enhanced impulsivity observed in drug addicts (*7*, *8*) predates the onset of compulsive drug use or is a consequence of protracted exposure to drugs has not been fully established. In addressing this issue experimentally, we operationalized these human traits in

experimental animals as an inability to wait before performing an appropriate response, one phenotype of impulsivity (*9*) measured as premature responses in a five-choice serial reaction-time task (5-CSRTT) of sustained visual attention (*10*), as distinct from locomotor reactivity to a novel environment, a sensation-seeking phenotype (*11*). These animal models support the existence of a "vulnerable phenotype" that predisposes to drug addiction. Thus, outbred rats exhibiting high levels of novelty-induced locomotor activity, called high responder (HR), show increased sensitivity to the reinforcing effects of addictive drugs and self-administer lower doses of psychostimulants than low-responder (LR) littermates (*11*). Impulsivity, on the other hand, correlates with ethanol intake (*12*) and predicts instead the escalation of cocaine self-administration (*10*, *13*), which may be more indicative of a necessary stage in the transition to compulsive drug-seeking. Although these studies have addressed the initiation of drug-taking, they have not captured the essential feature of addiction, namely, the persistence of drug-seeking in the face of negative consequences, a characteristic incorporated into recent animal models based on the DSM-IV criteria for substance dependence (*14*, *15*). Therefore, we have used a model of addiction based on individual differences in compulsive cocaine use (*14*) to investigate the contrasting contribution of high impulsivity (HI) and high reactivity to novelty (HR) to the development of compulsive drug-taking.

In this model, we have operationally defined three addiction-like criteria in rats that correspond to those of the DSM-IV description of substance dependence (*16*), namely, (i) increased motivation to take the drug, (ii) an inability to refrain from drug-seeking, and (iii) maintained drug use despite aversive consequences [see (*17*) for details]. Thus, rats positive for none of the three criteria (zero-criteria rats) are resistant to addiction, whereas rats that have three addiction-like criteria (three-criteria rats) are considered "addicted," and represent 15 to 20% of the population initially exposed to cocaine (*14*), a proportion that is similar to that observed in human populations (*18*).

To compare the propensity of HI and HR rats both to acquire cocaine self-administration and to make the transition to compulsive cocaine-taking, we first identified HI and LI rats in the 5-CSRTT (*10*), then HR and LR rats in a novelty-induced locomotor activity procedure (*11*). Subsequently, we compared the propensity of these different groups to acquire cocaine self-administration and to develop the three addiction-like criteria following protracted self-administration (*17*). HI and LI rats did not differ in their novelty-induced locomotor activity; conversely, HR and LR rats were not impulsive (Fig. 1, A and B). As predicted (*11*), HR rats were more prone to acquire cocaine self-administration than LR rats, showing an upward shift in the cocaine dose-response curve (Fig. 2). However, HI rats did not differ from LI rats in their acquisition of cocaine self-administration.

After 40 days of cocaine self-administration, we measured the three addiction-like behaviors in a cohort of 23 rats (*17*), so that each rat was defined as showing none or one, two, or three of these behaviors (table S2), as well as an addiction score, calculated as the sum of the standardized

[1]Behavioural and Clinical Neuroscience Institute and Department of Experimental Psychology, University of Cambridge, Downing Street, Cambridge CB2 3EB, UK. [2]Department of Psychiatry, University of Cambridge, Addenbrooke's Hospital, Hills Road, Cambridge CB2 2QQ, UK.

*To whom correspondence should be addressed. E-mail: bdb26@cam.ac.uk (D.B.); bje10@cam.ac.uk (B.J.E.)

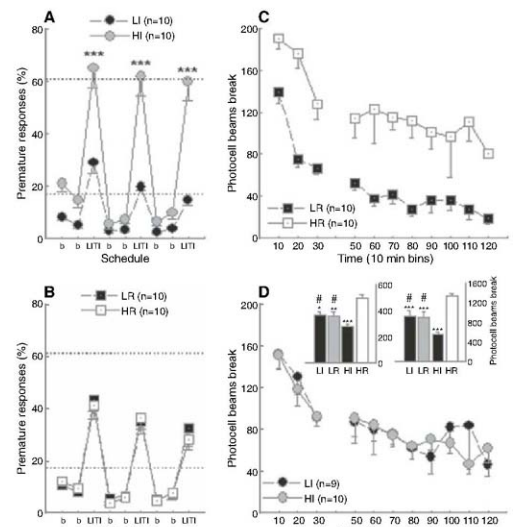

Fig. 1. Impulsivity and novelty-induced locomotor activity: two distinct phenotypes. On two baseline days (b), premature responses in the 5-CSRTT were measured. (**A** and **B**) During long intertrial intervals (LITIs), HI rats showed more premature responses than LI rats (Group: $F_{1,34} = 14.4$, $P < 0.01$; Schedule: $F_{8,288} = 130.22$, $P < 0.01$; Schedule × Group: $F_{24,288} = 7.01$, $P < 0.01$) (***$P < 0.001$) (**A**) and HR ($P < 0.01$) or LR rats ($P < 0.05$) (**B**). HR rats did not differ from LR rats or from LI subjects (**B**). (**C** and **D**) HR rats were more reactive to novelty than LR rats for the first 30 min (left histogram, inset) or the total duration of the session (right histogram) (Group: $F_{1,35} = 12.17$, $P < 0.01$ and $F_{1,35} = 17.63$, $P < 0.01$, respectively; Group × Time: $F_{6,70} = 1.26$, not significant, and $F_{30,350} < 1$, $P < 0.001$, respectively). (Inset) HI and LI subjects differed from both HR ($P < 0.01$) and LR rats (#, $P < 0.01$) but never from each other. *Comparison with HR: *$P < 0.05$, **$P < 0.01$, ***$P < 0.001$. (D) Black and gray dotted lines represent the average premature responses during the last two long intertrial intervals for HI and LI rats, respectively.

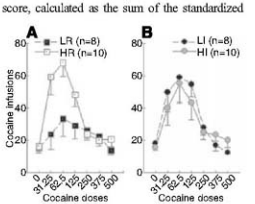

Fig. 2. Novelty-induced locomotor activity predicts the propensity to acquire cocaine self-administration. (**A**) HR rats showed an upward shift of the cocaine dose-response curve compared with LR littermates (Group: $F_{1,16} = 4.9$, $P < 0.05$; Dose: $F_{6,96} = 11.73$, $P < 0.01$; and Group × Dose: $F_{6,96} = 4.39$, $P < 0.01$). HR rats infused more cocaine at the lowest three doses than vehicle ($P < 0.01$). (**B**) HI and LI subjects did not differ in their number of self-administered cocaine infusions (Group: $F_{1,16} < 1$; Dose: $F_{6,96} = 10.79$, $P < 0.01$; Group × Dose: $F_{6,96} < 1$).

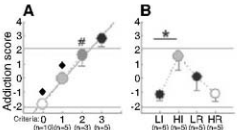

Fig. 3. HI rats closely resemble three-criteria rats. After protracted self-administration, rats with zero, one, two, or three criteria were identified. **(A)** When ranked on a linear addiction scale ($R^2 = 0.99$, Group: $F_{3,19} = 34.43$, $P < 0.01$), three-criteria rats had addiction scores (2.8 ± 0.6) above the standard deviation (2.1), and higher than all the other groups (versus zero- and one-criteria rats: ◆, $P < 0.01$, versus 2 criteria rats: #, $P \leq 0.05$). **(B)** HI rats displayed higher addiction scores than LI rats ($F_{1,9} = 7.55$, *$P < 0.05$), whereas HR rats did not differ from LR rats. Only HI rats did not differ from three-criteria rats for their addiction score ($F_{3,20} = 10.13$, $P < 0.01$) and displayed higher addiction scores than zero-criteria ($P < 0.01$) and HR rats ($P < 0.05$). HR, LR, and LI rats did not differ from zero-criteria rats.

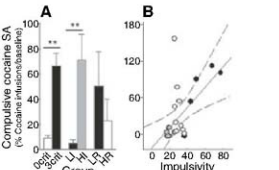

Fig. 4. Impulsivity predicts the transition to compulsivity. **(A)** HI rats receiving punishment (*17*) continued compulsive cocaine self-administration (SA). HI rats ($n = 5$) displayed higher resistance to punishment than LI rats ($n = 6$) ($F_{1,9} = 12.79$, $P < 0.01$), whereas HR ($n = 5$) rats did not differ from LR rats ($n = 5$). When compared with zero- and three-criteria rats for their resistance to punishment (Group: $F_{5,30} = 10.13$, $P < 0.01$), only HI rats were similar to three-criteria rats; they showed greater resistance to punishment than zero-criteria, LI, and HR rats ($P < 0.05$). LI and HR rats differed from three-criteria, but not from zero-criteria, rats (A. **$P < 0.01$. **(B)** Impulsivity predicts compulsive cocaine self-administration ($R = 0.42$, $P < 0.05$). Gray and black shadings represent LI and HI rats, respectively.

scores of each of the addiction-like criteria (*17*). Thus, rats with zero, one, two, or three criteria were linearly distributed along an addiction scale, corresponding operationally to the Addiction Severity Index (ASI) in humans (*17*, *19*). On this scale, three-criteria rats had scores higher than all the other groups (Fig. 3A), especially when compared with zero-criteria animals, from which they differed for each of the addiction-like behaviors (fig. S1). Only the zero-criteria rats had highly negative addiction scores.

Although reactivity to novelty predicts the vulnerability to acquire cocaine self-administration, it is high impulsivity that predicts the transition from controlled to compulsive cocaine-taking. HI rats displayed higher addiction scores than LI rats whereas, in marked contrast, HR rats did not differ from LR rats (Fig. 3B). LI, HR, and LR rats were represented mainly in the zero- and one-criteria populations; however, HI rats were largely represented in the two- and three-criteria populations. Additionally, only HI rats were more frequently represented in the three-criteria group than in the zero-criteria group (table S1).

A factor analysis revealed that impulsivity and addiction-like behavior are explained by the same factor that was itself orthogonal to reactivity to novelty, thereby identifying an impulsivity-addiction construct (fig. S2). Thus, HI rats did not differ from three-criteria rats in any of their addiction-like behaviors (Fig. 4A and fig. S3).

More specifically, the high addiction score of HI rats derived from the development of compulsive cocaine self-administration. HI rats displayed greater resistance to punishment of the drug-taking response than did LI, HR, and LR rats (Fig. 4A), and at the population level, correlational analysis revealed that impulsivity predicts compulsivity (Fig. 4B). However, HI rats did not differ from LI, HR, or LR rats in their total intake of cocaine (fig. S3); therefore, the development of compulsive cocaine-taking observed specifically in the highly impulsive rats cannot be attributed to differential exposure to cocaine. Because clinical investigations generally compare addicted subjects with drug-naïve controls, we analyzed whether animals vulnerable and resistant to addiction differed in their impulsivity and locomotor reactivity to novelty before any exposure to cocaine. This analysis showed that three-criteria rats were more impulsive, but not more reactive to novelty, than zero-criteria rats before cocaine self-administration (fig. S4).

These data allow us to identify one variety of impulsivity, measured as an inability to wait and sample predictive stimuli before responding (*20*), as a key behavioral marker specific for the vulnerability to progress to compulsive cocaine use, the hallmark of addiction. Our results are in accord with observations that (i) highly impulsive humans are overrepresented in drug-addicted populations (*21*), (ii) impulsivity or sensation-seeking may predate compulsive drug use (*22*, *23*), and (iii) there is a high comorbidity between drug addiction and disorders characterized by impulsive behavior, such as attention deficit–hyperactivity disorder (ADHD) (*21*).

The results indicate that the relation between high impulsivity and addiction-like behavior is completely independent of the initial propensity to acquire cocaine self-administration (fig. S2) (*17*), an observation consistent with the demonstration that impulsivity is unrelated to the subjective effects of oral amphetamine administration (*24*). Instead, this early vulnerability to cocaine's reinforcing effects was predicted by high locomotor reactivity to novelty. Our observations further suggest that the subjective and behavioral responses to cocaine during initial exposure to the drug do not determine the subsequent progression to addiction, as might perhaps have been previously suspected (*11*).

Our study also provides experimental evidence that high levels of impulsivity can antedate the onset of compulsive drug use and, thereby, emphasizes the importance of preexisting impulsivity observed in addicts (*2*, *4*, *7*). Moreover, by demonstrating the link between impulsivity and compulsivity in the development of addiction, these data provide a major impetus for investigating the neurobiological mechanisms underlying this transition. One candidate is the apparent devolution of control over drug-seeking behavior from the ventral to the dorsal striatum (*25*), which has been shown to depend on the cascading, serial ascending circuitry that links these striatal domains via its regulatory dopaminergic innervation arising in the midbrain (*26*, *27*). This hypothesis is further supported by the observation that the early vulnerability to escalate cocaine intake shown by highly impulsive rats is predicted by low D2 and/or D3 dopamine receptor levels in the ventral, but not the dorsal, striatum (*10*). In contrast, chronic exposure to cocaine in monkeys (*28*) and drug-abusers (*29*) is associated with low D2 and/or D3 dopamine receptor availability, predominantly in the dorsal striatum.

References and Notes

1. B. J. Everitt, T. W. Robbins, *Nat. Neurosci.* **8**, 1481 (2005).
2. J. D. Jentsch, J. R. Taylor, *Psychopharmacology (Berlin)* **146**, 373 (1999).
3. G. F. Koob, M. Le Moal, *Neuropsychopharmacology* **24**, 97 (2001).
4. M. J. Kreek, D. A. Nielsen, E. R. Butelman, K. S. LaForge, *Nat. Neurosci.* **8**, 1450 (2005).
5. N. Chaloner, J. Doran, J. Swendsen, *Encephale* **30**, 564 (2004).
6. T. A. Wills, D. Vaccaro, G. McNamara, *J. Subst. Abuse* **6**, 1 (1994).
7. G. Dom, P. D'Haene, W. Hulstijn, B. Sabbe, *Addiction* **101**, 50 (2006).
8. M. L. Zilberman, H. Tavares, D. C. Hodgins, N. el-Guebaly, *J. Addict. Dis.* **26**, 79 (2007).
9. J. L. Evenden, *Psychopharmacology (Berlin)* **146**, 348 (1999).
10. J. W. Dalley *et al.*, *Science* **315**, 1267 (2007).
11. P. V. Piazza, J. M. Deminière, M. Le Moal, H. Simon, *Science* **245**, 1511 (1989).
12. C. X. Poulos, A. D. Le, J. L. Parker, *Behav. Pharmacol.* **6**, 810 (1995).
13. J. L. Perry, E. B. Larson, J. P. German, G. J. Madden, M. E. Carroll, *Psychopharmacology (Berlin)* **178**, 193 (2005).
14. V. Deroche-Gamonet, D. Belin, P. V. Piazza, *Science* **305**, 1014 (2004).
15. L. J. Vanderschuren, B. J. Everitt, *Science* **305**, 1017 (2004).
16. American Psychiatric Association, *Diagnostic and Statistical Manual of Mental Disorders: DSM-IV-TR* (American Psychiatric Association, Washington, DC, ed. 4, text revised, 2000).
17. Materials and methods are available as supporting material on *Science* Online.
18. J. C. Anthony, L. A. Warner, R. C. Kessler, *Exp. Clin. Psychopharmacol.* **2**, 244 (1994).
19. S. H. Rikoon, J. S. Cacciola, D. Carise, A. I. Alterman, A. T. McLellan, *J. Subst. Abuse Treat.* **31**, 17 (2006).
20. J. Evenden, *Psychopharmacology (Berlin)* **143**, 111 (1999).
21. J. T. Nigg *et al.*, *J. Am. Acad. Child Adolesc. Psychiatry* **45**, 468 (2006).
22. S. Dawe, N. J. Loxton, *Neurosci. Biobehav. Rev.* **28**, 343 (2004).

23. K. J. Sher, B. D. Bartholow, M. D. Wood, *J. Consult. Clin. Psychol.* **68**, 818 (2000).
24. T. L. White, D. C. Lott, H. de Wit, *Neuropsychopharmacology* **31**, 1064 (2006).
25. L. J. Vanderschuren, P. Di Ciano, B. J. Everitt, *J. Neurosci.* **25**, 8665 (2005).
26. D. Belin, B. J. Everitt, *Neuron* **57**, 432 (2008).
27. S. N. Haber, J. L. Fudge, N. R. McFarland, *J. Neurosci.* **20**, 2369 (2000).
28. M. A. Nader *et al.*, *Nat. Neurosci.* **9**, 1050 (2006).
29. N. D. Volkow *et al.*, *Synapse* **14**, 169 (1993).

30. This work has been supported by grants from the Foundation Fyssen to D.B. and the U.K. Medical Research Council (MRC) no. G9536855 to B.J.E. and was completed within the Behavioural and Clinical Neuroscience Institute, which is supported by a joint grant from the MRC and the Wellcome Trust. The authors thank D. Theobald for his assistance and M. Solinas and A. Rouscent for their comments on this manuscript. Behavioral experiments and statistical analyses were designed and performed by D.B. The manuscript was prepared by D.B., A.C.M., J.W.D., T.W.R., and B.J.E. The authors declare that they have no competing financial interests.

Supporting Online Material
www.sciencemag.org/cgi/content/full/320/5881/1352/DC1
Materials and Methods
SOM Text
Figs. S1 to S4
Tables S1 and S2
References

21 March 2008; accepted 7 May 2008
10.1126/science.1158136

Patches with Links: A Unified System for Processing Faces in the Macaque Temporal Lobe

Sebastian Moeller, Winrich A. Freiwald, Doris Y. Tsao*

The brain processes objects through a series of regions along the ventral visual pathway, but the circuitry subserving the analysis of specific complex forms remains unknown. One complex form category, faces, selectively activates six patches of cortex in the macaque ventral pathway. To identify the connectivity of these face patches, we used electrical microstimulation combined with simultaneous functional magnetic resonance imaging. Stimulation of each of four targeted face patches produced strong activation, specifically within a subset of the other face patches. Stimulation outside the face patches produced an activation pattern that spared the face patches. These results suggest that the face patches form a strongly and specifically interconnected hierarchical network.

An essential step to understand the neural mechanism underlying any percept is to identify its anatomical substrate. For example, many theoretical models of object recognition propose a hierarchical architecture (*1*, *2*), but it remains unclear if and how such hierarchical models are actually implemented by the brain.

The face-processing system of macaque monkeys provides an ideal preparation for dissecting the large-scale functional anatomy of object recognition. Almost all macaques have a set of face-selective regions that can be easily identified by functional magnetic resonance imaging (fMRI) (*3*, *4*) and readily targeted for anatomical experiments (*5*). Understanding the connectivity of these regions should provide insights into the large-scale circuitry used by the brain to perceive a complex form.

It is debated whether face processing relies on a sequence of dedicated processing stages (*6*) or whether it relies on distributed representations (*7*). The former model predicts that face-selective regions show strong connections to each other but not to surrounding non–face selective temporal cortex, whereas the latter predicts strong connections between face-selective regions and surrounding non–face selective temporal cortex (*8*).

Tracer injections made into the macaque temporal lobe reveal a patchy connectivity pattern (*9*–*14*). For example, Saleem *et al.* found that injections into TEO (a cytoarchitectonic area in posterior inferior temporal cortex) produce labeling in TE (a cytoarchitectonic area in anterior temporal cortex) in two to five discrete foci (*10*). However, the functional properties of cells at injection and termination sites were not identified in these studies. In general, to dissect functional anatomy, it is necessary to combine connectivity maps with functional topography (*15*, *16*). Specifically, the connections of the macaque face patches cannot be deduced from previous studies. To identify the anatomical connections of the macaque face patches, we used fMRI-guided electrical microstimulation combined with simultaneous fMRI (*17*–*19*).

Macaque monkeys typically have six discrete, bilateral patches of face-selective cortex (Fig. 1 and fig. S1). These patches are organized as follows: one posterior patch on the lateral surface of area TEO (which we will refer to as "PL," for posterior lateral); two middle face patches in posterior area TE, one located in the fundus of the superior temporal sulcus (STS) ("MF," for middle fundus) and one on the lower lip of the STS ("ML," for middle lateral); and three patches in anterior area TE, one located near the fundus of the STS ("AF," for anterior fundus), one on the lower lip of the STS and adjacent gyrus, in area TEad ("AL," for anterior lateral), and one more medially on the ventral surface, just lateral and anterior to the anterior middle temporal sulcus (AMTS), in area TEav ("AM," for anterior medial) (*20*).

We identified the locations of face patches in four monkeys (M1 through M4) by scanning them with a standard face-localizer stimulus (*5*). Individual animals and hemispheres exhibited slight variations on the prototypical pattern just described. Face patches in the left and right hemispheres of monkey M1 on flattened maps of the posterior two-thirds of the brain excluding prefrontal cortex and in coronal slices are shown in Fig. 1, A and B; this animal had five discrete face regions in the right hemisphere (PL and ML were confluent). Time courses from the face patches confirm the face selectivity of each patch (Fig. 1C). The face patches of the three other animals (M2 through M4) used in this study are shown in fig. S1.

We then targeted a subset of the face patches for microstimulation combined with simultaneous fMRI. We first verified that the electrode correctly targeted each face patch by recording spiking activity. We then transferred the animal to the scanner for microstimulation. We stimulated a total of four different face patches (ML, AL, AM, and AF); several inferotemporal sites neighboring the face patches; and a site in the upper bank of the STS (table S1).

We first targeted ML in monkey M1. Magnetic resonance images of the electrode descending into ML, in sagittal and coronal planes, are shown in Fig. 2A. The response profile of the last cell recorded from this patch before microstimulation is shown in Fig. 2B; this cell was highly face selective (as were neighboring ones above it). The location of the electrode tip, marked on the flat map, confirms that stimulation was within ML (Fig. 2C). Comparing activation with and without microstimulation revealed five discrete regions in the temporal lobe (Fig. 2C). Stimulation resulted in a large spread around the electrode tip, a stretch of 4 mm with little activity, and then three discrete anterior patches located 6 to 11 mm anterior to the stimulation site. These patches coincided with the three anterior face patches of this monkey (compare Fig. 1A with Fig. 2C, and Fig. 1B with Fig. 2D). This activation pattern was reproducible across scan sessions and was not sensitive to the choice of significance threshold (fig. S2). Time courses from the six face patches confirm strong activation during microstimulation epochs (Fig. 2E).

The results of stimulating ML in two additional animals (M2 and M3) are shown in fig. S3. In monkey M2, stimulation in ML elicited activation in three other face patches: MF, PL, and AL. In monkey M3, stimulation in ML elicited activation in two other face patches: PL and AL. Results from the three animals show that ML is strongly connected to PL and AL and more variably to the remaining face patches.

Institute for Brain Research and Center for Advanced Imaging, University of Bremen, Post Office Box 330440, D-28334 Bremen, Germany.

*To whom correspondence should be addressed. E-mail: doris@nmr.mgh.harvard.edu

If fMRI activity is driven principally by the energy demands of transmitter release during synaptic activity (*21*, *22*), then these electrical stimulation–induced activations likely reflect orthodromic (rather than antidromic) spike propagation. Activations could result from direct or indirect connections (*23*).

Microstimulation-induced activations were usually much stronger in the hemisphere ipsilateral to the stimulation site, but we sometimes observed activation in contralateral face patches as well. Contralateral activations induced by stimulation in the right hemisphere ML of monkeys M1 and M2 are shown in fig. S4. These contralateral activations were confined to the face patches PL, ML, and MF.

ML was strongly connected to AL in all three animals. To follow the circuit, we next targeted AL (Fig. 3A). The last cell recorded before moving the animal to the scanner was face selective (Fig. 3B). In addition to spread around the stimulation site, stimulation in AL produced strong activation in ML, MF, and AF, and weak activation in AM (Fig. 3, C to E). In contrast to stimulation in ML, stimulation in AL produced no activation in PL. In a second animal (M4), stimulation of AL elicited activation in ML, MF, and AM, but not AF or PL (fig. S5). Thus AL appears to be robustly connected to ML, MF, and AM, and more variably to AF.

We next targeted AM, the most anterior of the six face patches. In monkey M1, stimulation in AM induced activity in ML, AL, and AF (fig. S6, A to E). In monkey M2, stimulation in AM induced activity in ML and AL (fig. S6, F to J; this animal lacked an AF in the stimulated hemisphere, see fig. S1A). Thus AM appears to be robustly connected to AL and ML.

Finally, we stimulated the third of the anterior face patches, AF, in one animal (M1, fig. S7). This experiment showed that AF is strongly connected to MF and, more weakly, to ML.

In the experiments described so far, the animal fixated on a blank gray screen during microstimulation. To test for interactions between microstimulation and visual stimulation (*24*, *25*), we combined electrical and visual stimulation in a stimulus sequence of six conditions: faces, faces + microstimulation, objects, objects + microstimulation, blank, and blank + microstimulation. Two monkeys (M1 and M2) were tested with this stimulus sequence, while we microstimulated in ML. This experiment revealed that (i) the strength of activation elicited in the face patches by microstimulation in ML was comparable to that elicited by viewing faces, and (ii) there was only a weak interaction between responses to microstimulation and those to visual stimulation (supporting online text).

If the circuitry of the inferior temporal cortex (ITC) follows a single scheme, then stimulating just outside a face patch should yield an activation pattern similar to that obtained by stimulating inside a face patch. If, on the other hand, the

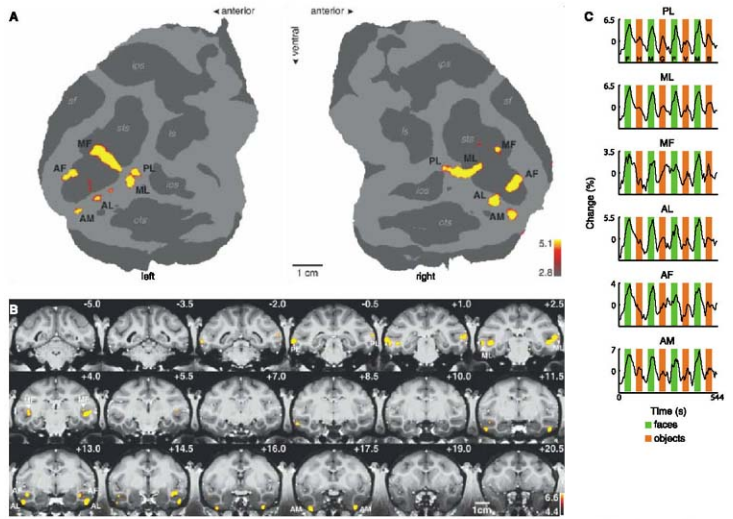

Fig. 1. Face-selective patches in monkey M1. (**A**) The flattened cortical surfaces ("flatmaps") from both hemispheres show regions significantly more activated by faces than by other objects. Computational flattening involves distorting the spatial arrangement of the data and underestimates the size of the sulci (shown in dark gray). Anatomical labels: *ips*, intraparietal sulcus; *sf*, Sylvan fissure; *sts*, superior temporal sulcus; *ls*, lunate sulcus; *ios*, inferior occipital sulcus; and *ots*, occipitotemporal sulcus. All color scale bars show the significance of the contrast maps as negative common logarithm of the probability of error. (**B**) The same contrast overlaid on high-resolution coronal slices from monkey M1. The anterior-posterior position of each slice in mm relative to the interaural line is given in the top right corner; the left hemisphere is shown on the left. (**C**) Mean time courses extracted from the six face patches of the right hemisphere. Three different visual stimulation conditions were presented as follows (see letters on bars for PL): faces (green epochs: F, human faces; M, monkey faces), objects (orange epochs: H, hands; G, gadgets; V, vegetables and fruits; B, human bodies), and scrambled versions of the same images (white epochs).

face patches constitute a unique system within ITC, then stimulating outside the face patches may yield a qualitatively different activation pattern. In particular, a distributed mechanism for coding nonface objects might predict that stimulation outside a face patch should lead to widespread activity throughout ITC.

We therefore stimulated three different sites just outside the face patches. First, we stimulated a site just posterior to ML, on the lower lip of the STS, in monkey M1 (Fig. 4A). The last cell recorded from this site responded only to scrambled patterns (Fig. 4B). Stimulation at this site produced a large spread of activity within the STS around the stimulation site (which spared both PL and ML), as well as a discrete patch of activity in the lower bank of the STS, anterior to ML and 7 mm anterior to the stimulation site (Fig. 4, C to E). This result suggests that ITC outside the face patches also exhibits discrete patchy connectivity, consistent with previous anatomical tracer studies (*10*, *13*, *26*). The result of microstimulating outside ML in monkey M2 is shown in fig. S8. In addition to a large spread around the stimulation site (which included PL, but largely spared ML), there was activity in a discrete region just posterior to AL, on the outer surface of the inferotemporal gyrus. Finally, the result of stimulating just posterior to AM in monkey M2 is shown in fig. S9. This produced spread around the stimulation site, as well as activity in a discrete posterior projection site within the ventral bank of the STS and a discrete anterior projection site within the fundus of the STS.

Face cells have been found in both the upper and lower banks of the STS (*27*). To compare connections of the upper with the lower banks of the STS, we stimulated a site in the upper bank of the STS in monkey M1 at approximately the same AP position as ML (fig. S10, A to E). Stimulation at this site produced a different activation pattern from stimulation in the lower bank; instead of discrete clusters of activation, we observed a large swath of activity extending from −5 to +20 within the upper bank and fundus of the STS, as well as activation in cingulate and somatomotor cortex (fig. S10, F to J, second monkey). This experiment shows that the technique of fMRI combined with microstimulation is capable of detecting highly distributed connectivity patterns. Furthermore, the result suggests that microstimulation is capable of activating cells more than one synapse away (it seems unlikely that all of the activated areas in fig. S10 were directly connected to the stimulation site). If true, this strengthens our main finding concerning the specificity of connections between face patches, because it implies that cells two synapses or more away from the stimulation site were also located within the face patch system.

We did not observe any other cortical regions consistently activated besides those described (*28*). However, we did consistently observe stimulation-induced activation in three subcortical regions: the amygdala, claustrum, and pulvinar. Stimulation in AM elicited activation in the lateral

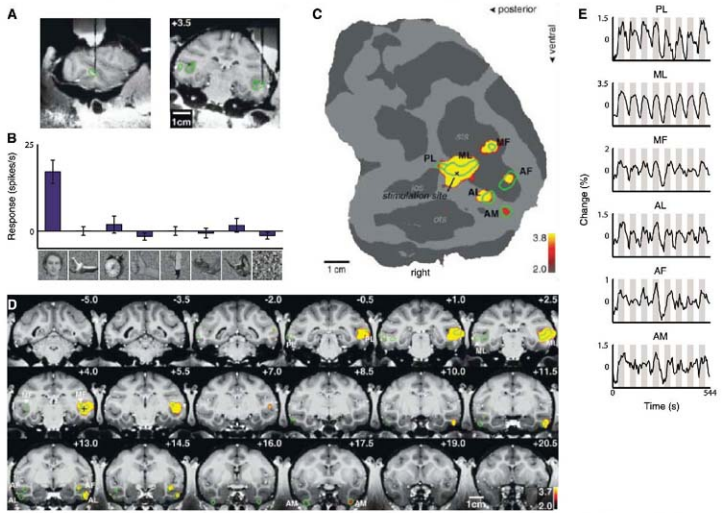

Fig. 2. Brain regions activated by microstimulation in face patch ML of monkey M1. **(A)** The position of the electrode in relation to the face patches (indicated by green outlines) in sagittal and coronal MRI slices; the tip of the electrode was located 3.5 mm anterior to the interaural line. **(B)** Selectivity profile of the last neuron recorded before stimulation. The bars show the mean response of this unit to images from eight different image categories (faces, fruits, gadgets, hands, bodies, monkey body parts, monkey bodies, and scrambles); error bars show 95% confidence intervals. **(C)** Areas significantly activated by microstimulation versus no microstimulation overlaid on the flatmap. The face patches (compare Fig. 1) are indicated by the green outlines. The stimulation site inside ML is marked by an "x." **(D)** The same functional contrast overlaid on coronal slices. The face patches are indicated by green outlines. The "+" indicates the approximate stimulation site (the slice containing the actual stimulation site, at +3.5, is not included in this mosaic). **(E)** Mean time courses from the six face patches in the right hemisphere. Microstimulation blocks (gray epochs) were interleaved with fixation only blocks (white epochs).

nucleus of the amygdala and laterally adjacent claustrum in both monkeys tested (fig. S11, A and B). Stimulation outside, but close to, AM also activated the lateral amygdala and claustrum (fig. S9C, slice at +20.5), which suggests that these two structures receive inputs from a larger region within ventral ITC (*29*).

We observed activation of the inferior pulvinar in response to microstimulation of both ML (fig. S11C) and AL (fig. S11D), as well as inferotemporal foci outside the face patches. Thus, the inferior pulvinar appears to be strongly connected to a large portion of ITC (*9*). Because the pulvinar, claustrum, and amygdala were the only non–face selective brain structures consistently activated by stimulation of the face patches, we hypothesize that these structures may constitute three bottlenecks for communication between the face patches and other regions of the brain (*30*).

In this study, we imaged brain regions activated by microstimulation of four different macaque face patches (ML, AL, AM, and AF). The results suggest that the six macaque face patches form a tightly and specifically interconnected system (summarized in fig. S12 and table S2). The existence of an interconnected circuit consisting of six nodes, likely dedicated to coding the same Gestalt form, shows that functional specialization in the inferior temporal lobe exists not only at the level of isolated columns (*31*) or patches (*5*), but extends to the level of connected, distributed networks.

Our results extend previous findings of functional specialization in early visual cortex, where modules processing the same visual attribute have been shown to be specifically connected (*32*), for example, color-specific blobs in area V1 with color-specific thin stripes in area V2 (*33*). The face patch network likely represents a stable structural network, because the connections were apparent across three very different functional states: without visual stimulation, with visual stimulation by faces, and with visual stimulation by nonface objects (supporting online text). However, functional connectivity within the face patch system and between the face patches and other brain areas may be modulated by behavioral and perceptual state (*24*, *34*).

Of all the face patches, we know most about the functional properties of the two middle ones, ML and MF. Single-unit recordings show that almost all visually responsive cells in this region are face selective (*5*), which implies that the step of face detection has been accomplished. Microstimulation of ML activated three anterior face patches (Fig. 2C), which suggests the existence of a sequence of dedicated face-processing stages following face detection. Such an architecture would be consistent with computational models of object recognition in which a detection stage precedes individual recognition (*35*). However, our results suggest an important role for feedback in face-processing. Stimulation of AL led to feedback activation of ML (Fig. 3) with a strength and spatial precision comparable to the feed-forward activation of AL by ML stimulation (Fig. 2).

Is the circuitry of the face patches unique or a theme that is recapitulated in surrounding non–face selective cortex? The results of microstimulating outside the face patches (Fig. 4 and figs. S8 and S9) suggest that there do exist largely self-contained networks of modules, outside the face patches, for processing shape. Because nonface objects elicit highly distributed fMRI response patterns in ITC (*7*), these networks of nonface modules likely represent aspects of form present in almost all objects, such that any object would activate multiple networks. But given their size, there may exist only a finite set of macroscopic shape-processing networks.

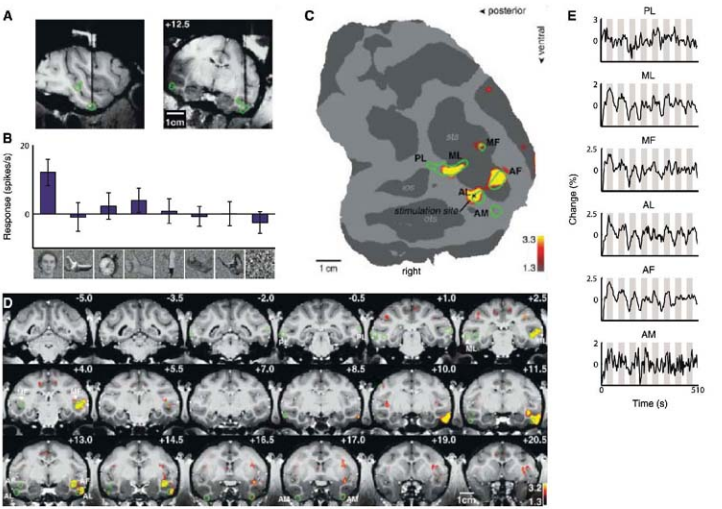

Fig. 3. Brain regions activated by microstimulation in face patch AL of monkey M1. Same conventions as in Fig. 2. **(A)** Electrode position in AL. **(B)** Example of neuronal selectivity. **(C)** The contrast between microstimulation and no microstimulation revealed microstimulation-induced activity in four discrete patches in the temporal lobe coinciding with AL (the stimulation site), AF, ML, and MF, as well as a fifth patch of faint activation coinciding with AM. PL was the only face patch not activated. **(D)** The same contrast overlaid on coronal slices. **(E)** Time courses from the six face patches of the right hemisphere.

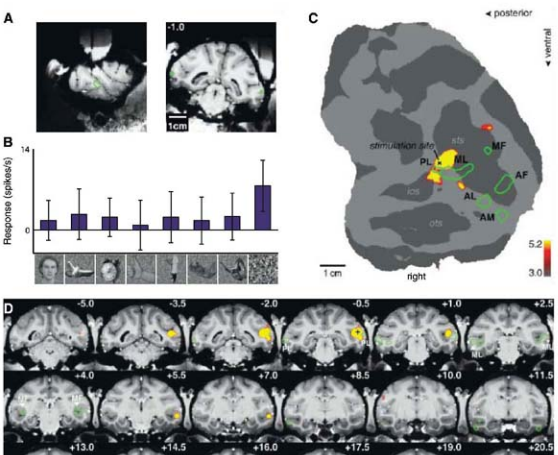

Fig. 4. Brain regions activated by microstimulation outside face patch ML in monkey M1. Same conventions as Fig. 2. **(A)** Electrode position just posterior to ML. **(B)** Example of neuronal selectivity. **(C)** The contrast microstimulation versus no microstimulation revealed microstimulation-induced activity around the stimulation site, as well as in a distinct patch anterior to ML. **(D)** The same contrast overlaid on coronal slices. Note how the activation spared most of PL and the other face patches. **(E)** Time courses from the patch just anterior to ML and from ML.

References and Notes

1. S. Ullman, *Trends Cognit. Sci.* **11**, 58 (2007).
2. M. Riesenhuber, T. Poggio, *Nat. Neurosci.* **2**, 1019 (1999).
3. D. Y. Tsao, W. A. Freiwald, T. A. Knutsen, J. B. Mandeville, R. B. Tootell, *Nat. Neurosci.* **6**, 989 (2003).
4. M. A. Pinsk, K. DeSimone, T. Moore, C. G. Gross, S. Kastner, *Proc. Natl. Acad. Sci. U.S.A.* **102**, 6996 (2005).
5. D. Y. Tsao, W. A. Freiwald, R. B. H. Tootell, M. S. Livingstone, *Science* **311**, 670 (2006).
6. V. Bruce, A. Young, *Br. J. Psychol.* **77**, 305 (1986).
7. J. V. Haxby *et al.*, *Science* **293**, 2425 (2001).
8. J. D. Cohen, F. Tong, *Science* **293**, 2405 (2001).
9. M. J. Webster, J. Bachevalier, L. G. Ungerleider, *J. Comp. Neurol.* **335**, 73 (1993).
10. K. S. Saleem, K. Tanaka, K. S. Rockland, *Cereb. Cortex* **3**, 454 (1993).
11. K. S. Saleem, K. Tanaka, *J. Neurosci.* **16**, 4757 (1996).
12. K. Cheng, K. S. Saleem, K. Tanaka, *J. Neurosci.* **17**, 7902 (1997).
13. K. S. Saleem, W. Suzuki, K. Tanaka, T. Hashikawa, *J. Neurosci.* **20**, 5083 (2000).
14. W. Suzuki, K. S. Saleem, K. Tanaka, *J. Comp. Neurol.* **422**, 206 (2000).
15. W. H. Bosking, Y. Zhang, B. Schofield, D. Fitzpatrick, *J. Neurosci.* **17**, 2112 (1997).
16. L. C. Sincich, G. G. Blasdel, *J. Neurosci.* **21**, 4416 (2001).
17. A. S. Tolias *et al.*, *Neuron* **48**, 901 (2005).
18. L. B. Ekstrom, G. Bonmassar, R. B. H. Tootell, P. R. Roelfsema, W. Vanduffel, paper presented at the Society for Neuroscience Annual Meeting, Washington, DC, 12 to 16 November 2005.
19. This technique is not as sensitive as classic tracer injection followed by post mortem histology and may therefore miss weak, diffuse projections. But as an in vivo method, it has several important advantages for correlating anatomy to function: (i) because the results come in the form of fMRI activity maps, they can be precisely compared with the pattern of fMRI-identified face patches; (ii) the technique allows for repetitions; (iii) it allows for combination with electrophysiological experiments; and (iv) it allows for the use of many stimulation sites in the same animal, enabling a detailed, sequential characterization of connectivity.
20. K. S. Saleem, N. K. Logothetis, *A Combined MRI and Histology Atlas of the Rhesus Monkey Brain in Stereotaxic Coordinates* (Elsevier, London, 2007).
21. C. Mathiesen, K. Caesar, N. Akgoren, M. Lauritzen, *J. Physiol.* **512**, 555 (1998).
22. N. K. Logothetis, J. Pauls, M. Augath, T. Trinath, A. Oeltermann, *Nature* **412**, 150 (2001).
23. For example, in Fig. 2C, the activation in AM could be due to a direct connection from ML to AM or to an indirect connection from ML to AL to AM.
24. S. L. Fairhall, A. Ishai, *Cereb. Cortex* **17**, 2400 (2007).
25. When the animal is viewing nonface objects, cortex representing nonface objects could exert a strong inhibitory influence on the face patches, thereby reducing or eliminating the effect of microstimulation on the face patches. Alternatively, if processing within face patches and non–face selective cortex proceeds in parallel, then viewing nonface stimuli should not strongly affect microstimulation-induced activity within the face patch system.
26. B. Seltzer, D. N. Pandya, *J. Comp. Neurol.* **290**, 451 (1989).
27. G. C. Baylis, E. T. Rolls, *Exp. Brain Res.* **65**, 614 (1987).
28. Tracer studies show that ITC is connected to ventrolateral prefrontal cortex (36) and area V4 (37). Prefrontal connections may have been missed in the current study because prefrontal cortex was not covered by the slice prescription during AM stimulation (prefrontal cortex was covered during stimulation of ML in monkeys M3 and M4, and stimulation of AL in monkey M4). Tracer studies show that connections between V4 and TEO are stronger than those between V4 and TE (*14*, *37*). Thus, V4 connections may have been missed because PL (located in TEO) was not stimulated.
29. M. J. Webster, L. G. Ungerleider, J. Bachevalier, *J. Neurosci.* **11**, 1095 (1991).
30. J. M. Chein, W. Schneider, *Brain Res. Cognit. Brain Res.* **25**, 607 (2005).
31. K. Tanaka, *Annu. Rev. Neurosci.* **19**, 109 (1996).
32. D. J. Felleman, Y. Xiao, E. McClendon, *J. Neurosci.* **17**, 3185 (1997).
33. M. S. Livingstone, D. H. Hubel, *J. Neurosci.* **4**, 309 (1984).
34. C. Summerfield *et al.*, *Science* **314**, 1311 (2006).
35. B. Epshtein, S. Ullman, paper presented at the IEEE Computer Society Conference on Computer Vision and Pattern Recognition (CVPR), New York, 17 to 22 June 2006.
36. M. J. Webster, J. Bachevalier, L. G. Ungerleider, *Cereb. Cortex* **4**, 470 (1994).
37. L. G. Ungerleider, T. W. Galkin, R. Desimone, R. Gattass, *Cereb. Cortex* **18**, 477 (2008).

38. We are grateful to the late David Freeman and to M. Livingstone, who programmed and designed the visual stimulus presentation software RF3; to N. Schwers, K. Thoss, and R. Hakizimana for technical support; to S. Everling for advice on microstimulation; to M. Livingstone and K. S. Saleem for comments on the manuscript; and to Guerbet for providing Sinerem. This work was supported by a Sofia Kovalevskaya Award from the Alexander von Humboldt Foundation; by the German Science Foundation (DFG FR1437/3-1); and by the German Ministry of Science (grant no. 01GO0506, Bremen Center for Advanced Imaging).

Supporting Online Material

www.sciencemag.org/cgi/content/full/320/5881/1355/DC1
Materials and Methods
SOM Text
Figs. S1 to S12
Tables S1 to S2
References and Notes

6 March 2008; accepted 7 May 2008
10.1126/science.1157436

Hotter Than Hot:
Combining RNAi and Stem Cells

Ten years ago, RNA interference was an interesting but arcane phenomenon that excited a small group of researchers working on *Caenorhabditis elegans*. At the same time, embryonic stem cells were a useful but cumbersome system for engineering targeted gene deletions in mice. Neither tool seemed to have much use beyond its narrowly defined specialty. What a difference a decade makes.
By Alan Dove

Today, RNA interference, or RNAi, is simultaneously one of the hottest techniques in molecular biology and a bold new frontier in the study of gene regulation. Stem cells, meanwhile, are the subjects of loud protests, presidential campaign discussions, and multibillion-dollar funding initiatives.

Besides their simultaneous climbs to fame, RNAi and stem cells have something else in common: researchers are increasingly combining the two. Indeed, RNAi has quickly become an important tool for probing the nature of stem cells, as well as engineering "knockdowns" of animal genes. Stem cells modified with RNAi techniques may also enable the slowly developing field of tissue engineering to break into the clinic.

Equipment and reagent manufacturers have been quick to cater to scientists using both stem cells and RNAi, offering everything from nucleic acids with special modifications for RNAi work to complete kits for popular types of stem cell studies. Both technologies are still in their infancy, though, and both present numerous pitfalls for researchers who combine them.

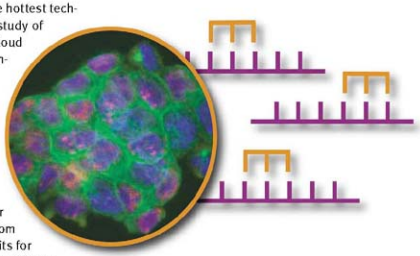

CREDIT: IMAGE KINDLY PROVIDED BY FRANK BUCHHOLZ

Searching for Self-renewal

When molecular biologists refer to RNAi, they often mean using synthetic small interfering RNA (siRNA) molecules to silence specific genes in a cell. As cultured cells take up the siRNA, the molecule binds complementary messenger RNA, targeting it for destruction by a highly conserved—and very efficient—pathway. In a mouse embryonic stem cell line, this enables investigators to generate targeted disruptions of nearly any gene product much faster than with traditional recombinant DNA techniques.

"The biggest advantage of using RNAi, not only in embryonic stem cells but also in other cells, is the speed at which you can deplete the protein product," says Frank Buchholz, a group leader at the **Max Planck Institute of Molecular Cell Biology and Genetics** in Dresden, Germany.

The catch is that siRNA-based gene silencing is often not as precise or thorough as a traditional gene deletion. Rather than targeting a particular genetic locus, an siRNA floats freely in the cell, often binding not only its primary target, but other messenger RNAs as well. These off-target effects often produce spurious results.

In addition, an siRNA is unlikely to shut down its primary target completely. "With RNAi technology, it's always a knockdown, it's probably never really a 100 percent knockout, so there may be differences in phenotypes that one may observe," says Buchholz. That drawback can be an advantage for some studies. Many gene products exhibit dose-dependent effects, and Buchholz says the continued >

> "The biggest advantage of using RNAi is the speed at which you can deplete the protein product."

Look for these Upcoming Articles
Structural Proteomics — August 1
Genomics: qPCR — September 19
Lab on a Chip/Microfluidics — Nov 7

Inclusion of companies in this article does not indicate endorsement by either AAAS or Science, nor is it meant to imply that their products or services are superior to those of other companies.

"Although miRNAs have been known for many years, tools to manipulate miRNAs in cells have been around only for the last couple of years."

ability to generate different degrees of knockdowns with siRNA has helped researchers study that phenomenon. Those hoping to use siRNA as a shortcut to making a complete knockout animal, however, need to interpret their results cautiously.

Nonetheless, Buchholz and his colleagues have already used siRNA for an initial survey of the genes involved in maintaining "stemness," or stem cells' ability to self-renew and form all tissue types. "RNAi of course offers an ideal technique to find the molecules or to find the genes that are involved in this differentiation process," says Buchholz.

Taking advantage of the speed of siRNA compared to traditional gene knockouts, the researchers knocked down each mouse gene in the genome. They then monitored the cells' subsequent expression of Oct-4, a marker for the stem cell state. The result was a list of candidate genes involved in maintaining self-renewal.

Despite combining two relatively new technologies, the experiment was surprisingly straightforward. "Of course working with stem cells requires certain skills, because you always have to treat them nicely," says Buchholz. But he adds that "we actually were able to very rapidly establish a transfection protocol, which established very good knockdown levels in mouse embryonic stem cells by lipofection."

Indeed, stem cells seem particularly suited for siRNA-based studies. "Stem cells are fairly amenable to lipid-mediated delivery. As the cell becomes more differentiated, it becomes harder to transfect," says Devin Leake, director of research and development for the life science research group at **Thermo Fisher Scientific** in Milford, Massachusetts.

It's the Network

Things get trickier when researchers try to probe the cells' own RNAi system, in which endogenous microRNA, or miRNA, molecules silence specific gene targets. In recent years, the miRNA system has emerged as a fundamental and evolutionarily conserved component of gene regulation, at least as important as transcriptional silencing. Each endogenous miRNA can regulate multiple genes. The silencing pattern often targets multiple components of a single metabolic pathway, raising hopes that miRNAs will both illuminate new biology and point the way to promising new drugs.

In stem cells, miRNA-mediated gene regulation is clearly one of the major mechanisms controlling differentiation, but scientists have only recently gained access to the tools to probe this system. "Although miRNAs have been known for many years, tools to manipulate miRNAs in cells have been around only for the last couple of years," says Eric Lader, director of research and development at **Qiagen** in Germantown, Maryland.

The first step of a typical miRNA experiment—exposing cells to a particular set of conditions and then isolating their expressed miRNAs—is usually the easiest. Because miRNAs are just short RNA molecules, researchers can simply modify traditional RNA isolation methods or, for even greater convenience, buy an appropriate kit. "Qiagen has adapted our RNA isolation techniques to quantitatively recover small RNAs in the total RNA prep, and to also allow further enrichment," says Lader. Qiagen is just one of many kit makers that offer reagents for miRNA isolation.

Characterizing and quantifying the isolated miRNAs can be more challenging, but several companies offer validated assays for all known miRNAs in popular model systems. Thermo Fisher, for example, offers a microarray for profiling all of the miRNAs in human cells, which could be particularly useful for stem cell researchers. "With this microarray, you can detect the endogenous levels of miRNAs in an undifferentiated cell or a differentiated cell, and look at the differences between those two," says Leake. Not to be outdone, Qiagen targets the same market with a completely different technique: a quantitative miRNA RT-PCR kit.

After identifying some miRNAs that might regulate a particular process, such as stem cell differentiation, researchers typically try to perturb those miRNAs to confirm their functions. Often, that brings them back to siRNAs, which can be custom-built to either inhibit or mimic specific miRNAs. Unfortunately, the process is not as simple as noting the miRNA sequence and targeting it with a complementary siRNA. Leake explains that to mimic or inhibit an endogenous miRNA, the artificial siRNA must be highly specific, capable of directing its target to the cell's RNA degradation machinery, and able to survive in the cell without being broken down itself.

The final challenge is that, even if investigators generate a perfect mimic or inhibitor for a given miRNA, the results can be difficult to interpret. "The difficulty is figuring out what's going on, because a single microRNA can affect the expression of any number of genes, and sometimes it exerts that effect coordinately with other microRNAs," says Lader.

Target Practice

Because of the miRNA system's enormous complexity, researchers inevitably turn to computers for help dissecting these tangled regulatory networks. In theory, one should be able to predict any miRNA's targets given nothing but the miRNA's sequence and the genome sequence of the organism. In practice, bioinformatics researchers are still struggling with the problem.

"Target prediction is one of the most unresolved issues in the field of miRNAs," says Søren Møller, chief scientific officer at **Exiqon** in Vedbaek, Denmark. While Exiqon focuses on improving the chemical specificity of synthetic siRNAs, Møller has also followed the problem of miRNA target prediction closely. "You can analyze miRNAs in a lot of different ways, but the next step, moving from miRNA differential expression to what signaling pathways are affected, is a key focus of many of our customers' research," he says.

The good news about miRNA target prediction is that there are numerous computer algorithms available to tackle the problem, and because most of them have been developed by basic continued >

researchers in academic labs, they are generally free, with published source code. The bad news is that the different algorithms often disagree with each other. "We advise [researchers] to use as many different target prediction algorithms as are out there, and look at the output and correlate that to the biology that they are familiar with," says Møller. In stem cell research, where both the basic biology and the functions of individual miRNAs are unclear, researchers should be especially skeptical of the computer's predictions.

Weaknesses in the software stem mainly from gaps in scientists' current understanding of the miRNAs themselves. Some algorithms, for example, require perfect complementarity between specific miRNA bases and a potential target messenger RNA, while others allow more room for noncanonical targets. The former strategy can miss targets that are biologically important, while the latter can yield spurious leads. As molecular biologists develop a clearer understanding of the underlying rules of miRNA targeting, bioinformaticians will be able to find a better balance in the algorithms.

A simpler version of the target prediction problem comes up when investigators design artificial siRNAs, and most companies offering siRNA-production services now provide free access to their proprietary siRNA prediction algorithms online. Typically, these programs take several sequence parameters of a target messenger RNA and build an siRNA or a set of siRNAs that should bind it.

While relatively basic siRNA algorithms are adequate for many uses, they still have room to improve. For example, using a mathematical technique called support vector machines (SVMs), software developers in **Applied Biosystems' Ambion** division in Austin, Texas, recently released a new application, which they claim produces siRNAs with substantially better efficacy. "I think one of the important differences is that we do take into account the local folding structure of the target messenger RNA, as well as looking at the sequence parameters of siRNAs themselves," says Kathy Latham director of the Ambion RNAi product line. The algorithm itself is proprietary, but researchers can access it for free through the company's website.

Featured Participants

Applied Biosystems/Ambion
www.ambion.com

Exiqon
www.exiqon.com

Max Planck Institute
www.mog.de/english

Qiagen
www.qiagen.com

Thermo Fisher
www.thermofisher.com

Better Binding through Chemistry

Ambion's new SVM-based algorithm is aimed at addressing an underappreciated problem in siRNA research: inconsistent silencing. While the field has focused extensively on reducing off-target effects, siRNAs can also confuse experimenters by failing to silence their primary targets.

"A really good siRNA might give you 90–95 percent silencing, but an okay siRNA might only give you 80 percent silencing," says Latham. That difference may be irrelevant for some experiments, but in differentiating stem cells, many regulatory gene products work like switches, moving the developmental process forward at a particular threshold of gene expression. For these genes, a partially active siRNA may be the same as no siRNA at all. "Differences in phenotypes are often attributed to off-target effects; however, differences in phenotypes can also be due to inconsistent silencing, which is why we combined chemical modifications to improve specificity with the new algorithmic approaches," says Ambion's Latham.

The specific siRNA chemical modification Ambion is using is the Locked Nucleic Acid design, which the company licensed recently from Exiqon. While Ambion now markets Locked Nucleic Acid–based siRNAs, Exiqon still develops and sells a variety of other products that use the same chemistry. "Based on our technology, we have developed a set of detection techniques for analysis of miRNAs in cells, but also some functional products that can down-regulate or knock down specific miRNAs in cells," says Exiqon's Møller.

For miRNA detection, Exiqon offers different kits based on quantitative PCR, microarrays, and Northern blots, and some of these may offer distinct advantages for stem cell researchers. Investigators looking at later stages of development may find Locked Nucleic Acids particularly attractive as probes for miRNA expression in tissues. Regular DNA or RNA oligonucleotides cannot detect miRNAs by in situ hybridization, but the more specific Locked Nucleic Acid oligonucleotides can. "A tissue is not a homogeneous set of cells. It's very diverse, and we've seen when we look in situ that different cell types express different miRNAs," says Møller.

Exiqon and Ambion are not the only companies offering chemically modified siRNAs, and investigators should shop around for the specific characteristics they need. Those hoping for easy delivery of siRNAs to target cells may find Thermo Fisher's new Accell siRNAs particularly useful. "Accell siRNAs are chemically modified to promote cellular uptake, without any kind of formulation, any kind of instrumentation," says Leake. Rather than encapsulating siRNAs in lipid-based delivery compounds, researchers simply add their custom-built siRNAs to a proprietary cell culture medium, then bathe the cells in it.

Regardless of the specific techniques they use, scientists combining stem cells with RNAi have good reason to be hopeful. Looking ahead to the next few years, Buchholz sees both techniques yielding major breakthroughs. "In the lab, I think we will learn a lot more about stem cells and the pathways that are driving [development]," he says, adding that "this is a prerequisite to really move the knowledge that we gain there closer to the clinic."

Alan Dove is a science writer and editor based in Massachusetts.

DOI: 10.1126/science.opms.p0800026

New Products

RNAi Cell Cycle Screening

The Acumen eX3 offers higher throughput for RNA interference (RNAi) cell cycle screening compared with traditional flow cytometry methods. It can read an entire 384-well plate in less than 10 minutes, including multiplexing the assay with other biomarkers. Acumen eX3 can analyze adherent cells in situ, unlike flow cytometry, which requires cell suspensions. This preserves morphological changes that may occur during drug treatment and gives important toxicity information.

TTP Labtech
For information 617-494-9794
www.ttplabtech.com

Gene Silencing

Thermo Scientific Dharmacon Accell siRNA is a novel form of short-interfering RNA (siRNA) that is absorbed directly by cells without the use of conventional delivery methods such as transfection reagents, viruses, or electroporation. It effectively silences genes in all cell types tested to date. Previous technologies for delivering siRNA into difficult cell types, such as primary cells, suspension cells, stem cells, and neurons, were often ineffective and resulted in high levels of cell death. Dharmacon Accell siRNA has been able to penetrate every cell type tested, without the need for delivery reagents that can skew experimental results. The siRNA is simply mixed with the optimized Accell delivery medium then added to cultured cells. The easy, two-step process avoids the experimental variability caused by toxicity and off-target effects of conventional siRNA delivery methods.

Thermo Fisher
For information 781-622-1000
www.thermo.com/dharmacon

Automated Stem Cell Culture

Velocity11 has released a data sheet that describes a high throughput, automated stem cell culture and screening system using its Filtered Plus Biocel platform. The automated platform was developed to use stem cells as the basis of high throughput assays and drug discovery programs to increase throughput and find more promising lead compounds. The system maintains a temperature of 37°C inside the Biocel, with air filtered to a class 100 specification, creating an optimized environment for plate-based cell maintenance and cell-based assays. With a novel method for controlling air velocity and ultralow penetration air filters, the system achieves increased turnover in filtered air, reducing the number of foreign particles and cell contamination. The automated procedure involves seeding plates from a bulk culture, adding compounds to cell plates, and transferring supernatant or cell lysate to an assay plate.

Velocity11
For information +44-1763-269110
www.velocity11.com

Advertisers of RNAi- or Stem Cell-related products

Applied Biosystems
www.appliedbiosystems.com/stemcells

Exiqon
www.exiqon.com

Bio-Rad
www.bio-rad.com

Synthetic miRNA Mimics and Inhibitors

New synthetic microRNAs (miRNAs) from Qiagen, including the miScript miRNA Mimics and the miScript miRNA Inhibitors, are ready-to-transfect to carry out gene regulation and cellular pathway analysis for applications from in vitro to animal models. These molecules are based on all known human, mouse, and rat miRNAs in the latest version of miRBase, the Sanger Institute's database for miRNA. These mimics and inhibitors are available in flexible formats, from single tubes to 96-well or 384-well plates. They are available in scales of 1 nmol and 5 nmol for in vitro use and 20 nmol for animal studies.

Qiagen
For information +49-2103-29-16115
www.qiagen.com/miRNA

RNAi Vectors

Two new vectors are available from Invitrogen for RNA interference (RNAi) research. The Block-iT HiPerform Lentiviral PolII miR RNAi Expression System with Emerald Green Fluorescent Protein offers the ability to deliver to nondividing, primary, and hard-to-transfect cells with lentiviral technology coupled to multisite technology for promoter flexibility, making it suitable for difficult applications, including in vivo RNAi. It contains a messenger RNA stabilizing sequence and a nuclear import sequence that generate up to five-fold higher virus titers and fluorescent protein expression than previous versions. The Block-iT Inducible PolII miR RNAi Expression System makes use of a tetracycline-inducible promoter that allows researchers to knock down even genes that are essential to the function of a cell.

Invitrogen
For information 800-955-6288
www.invitrogen.com/rnai

Media Preparation System

The Mediajet vario is a versatile petri dish filler that can be used to fill 35 mm, 55/60 mm, and 90/100 mm dishes. With a compact footprint of only 70 cm by 70 cm, it fits conveniently on the laboratory bench and can fill 900 petri dishes per hour. It features walk-away automation with novel feed-in and stack-out technology. When working with 35-mm petri dishes, it can perform automated production of thousands of agar plates on which to cultivate the nematode *C. elegans*. This nematode is a popular geneticists' tool because the simplicity, transparency, and speed of its biological functions facilitate studying genes and their functions.

Integra Biosciences
For information +41-81-286-9530
www.integra-biosciences.com

Electronically submit your new product description or product literature information! Go to **www.sciencemag.org/products/newproducts.dtl** for more information.

Newly offered instrumentation, apparatus, and laboratory materials of interest to researchers in all disciplines in academic, industrial, and governmental organizations are featured in this space. Emphasis is given to purpose, chief characteristics, and availability of products and materials. Endorsement by *Science* or AAAS of any products or materials mentioned is not implied. Additional information may be obtained from the manufacturer or supplier.